Redefining the Silver Lining of Selective Oxidation: Oxygen Speciation and Ni Promotion in Ag(111)-Catalyzed Ethylene Epoxidation

A dissertation submitted by:

Elizabeth E. Happel

In partial fulfillment of the requirements for the degree of:

Doctor of Philosophy, Chemistry: Chemical Physics

Tufts University

August 2025

Advisor: Professor E. Charles H. Sykes

Abstract

Silver-based catalysts remain the cornerstone of industrial ethylene epoxidation, yet fundamental questions persist regarding the identity and structure of active oxygen species and the mechanisms underpinning selective oxidation. In this thesis, I employ a suite of surface-sensitive techniques—ambient-pressure X-ray photoelectron spectroscopy (AP-XPS), scanning tunneling microscopy (STM), and density functional theory (DFT) benchmarking—to elucidate oxygen speciation and surface reactivity on Ag(111), both with and without Ni promotion.

Initial AP-XPS measurements under near-industrial conditions revealed that Ag(111) maintains a predominantly metallic character with limited carbonate formation, establishing realistic surface coverage benchmarks for modeling catalytic intermediates. Complementary DFT studies demonstrated systematic underestimation of O 1s binding energies for weakly bound oxygen species, particularly those associated with electrophilic oxygen, highlighting the limitations of conventional theory. To overcome this, STM imaging provided direct evidence for distinct oxygen configurations: a low-temperature ring-like phase, consistent with electrophilic oxygen and potentially a precursor to the oxametallacycle (OMC) intermediate, and a higher-temperature nucleophilic reconstruction.

Expanding on these insights, I developed and evaluated a novel Ni-doped Ag catalyst (NiAg) that activates O_2 more readily than bare Ag while maintaining moderate oxygen binding strength. Ni was found to preferentially stabilize nucleophilic oxygen, enhance selectivity for ethylene oxide, and promote spillover and speciation of oxygen via a newly identified class of "Ni-philic" oxygen. Operando XPS revealed that Ni sustains nucleophilic oxygen even under reducing conditions and facilitates the formation of industrially relevant carbonate and subsurface oxygen species.

This work not only resolves longstanding ambiguities surrounding electrophilic oxygen on Ag but also introduces a chlorine-free promoter system capable of rivaling conventional promoters in selectivity and stability. These findings pave the way for environmentally benign catalysts in partial oxidation reactions and set the stage for future investigations of Ni-philic oxygen in broader oxidation chemistries.

Acknowledgements

There have been many people who deserve credit for getting me to the place to submit this dissertation not the least of which is my PI, Charlie Sykes, who had endless patience for my constant nervousness about experimental results. His guidance and feedback were consistently kind and honest and I am grateful for the time he took to be a mentor and pushing me to try things I could have never imagined. In a similar vein, I would like to thank my committee members Art Utz and Roger Tobin who both pushed me to approach my research from different perspectives. A special thank you to Art for consistency fostering my love of teaching and always having an anecdote about whatever UHV related situation I was in.

I would like to thank Dr. Ira Waluyo, whose seemingly never-ending knowledge about XPS and generosity with her end station allowed me to enter a whole new world out of UHV (and into ambient pressures)! Thank you so much for your guidance as I figured out peak fitting and for your willingness to try to quantify such tiny amounts of Ni at the surface.

I'd like to thank my collaborators Professor Phil Christopher and Professor Matt Montemore both of whom had such patience for me getting up to speed on a project with years of background. I am so grateful to both of you for your constant willingness to "hear me out" about my "probably not the best" ideas and having the patience to listen to my less than coherent verbal descriptions of STM images and XPS spectra that I wish I could say got better from my first year to my last. I appreciate both of you for how much you have taught me. And a special thank you to Matt Montemore for being my external committee member and for answering so many emails about DFT.

I would never have been able to finish this thesis without the help of their students Anika Jalil, Sarah Stratton, and Toghrul Azizli who were instrumental in many of the projects herein. I'd like to thank my lab mates many of whom have shown me, in their own ways, the kind of scientist I aspire to be. A special thank you to Avery and Cole for several long trips to the beam line, sitting in my small car, and getting fajitas at El Potro — it's been fun! I would be remiss not to thank my other current lab mates including: Vinita who always started every day with a smile, Nipun and Nima who had to learn about UHV from me (*sorry guys*) but who manage to be good scientists anyway, and to Dr. Dennis whose help over the past few months has been instrumental in maintaining my sanity as I finished up this degree. Thank you to the folks in the Utz group past and present who were always kind enough to indulge my ideas about why something *might* magically fix itself by the morning and always letting me crawl around the infinity compressor.

While I did spend a lot of time over the past years in the basement, I would like to thank my friends who kept me sane especially to Laurin, Jess, Lee, and Haley for hearing me out about so many experimental failures and broken UHV equipment. Special thank you to Colleen and Marissa who consistently reminded me about the world outside of science. I cannot express enough how much your friendships mean to me both in the last five years and beyond.

I have my family to thank. And to embrace all the cliches since they exist for a reason: Words simply cannot explain the love I have for these folks. To my Dad (my "plus one") whose

excitement to always teach me new things, especially even the things I am most scared of, has pushed me to believe in myself and at the very least just give it a try. And to my Mom who is always there to pick me up when I have tried and failed (which has happened so many times). I am so beyond lucky to have a mom who can just get it and "look into my eyes" and know what I am thinking. I look forward to Euchre more often now that I'll hopefully have more weekends free. Thank you both, for everything.

I'd like to thank my Aunt, Dr. Mary Kriner who is continuously with me in spirit from the day I joined the Sykes lab. While this degree couldn't be less similar to hers, she always understood me and my desire to sign up for more school. While I wish I could celebrate with you now, you will forever be an inspiration of all the kindness one person can share with the world.

Finally, I have to thank my partner Will, who never stopped reminding me that running away to the mountains was on the table when I got overwhelmed. Thank you for listening to me talk about my day for too long every single day and picking me up after yet another piece of equipment broke. I am so lucky to have had you to keep me whole. I promise I'll be better with words on our wedding day, but for now thank you for always believing in me, even on Tuesdays.

List of Figures

List of Tables

Contents

Chapter 1: Introduction

Heterogeneous catalysts are used in over 80% of industrial processes which account for the production of over 10 trillion dollars' worth of goods annually.[1,2] Therefore small improvements in catalysts can result in massive energy savings and in the reduction of pollution. These catalysts are typically in the solid phase, while the reactants are gaseous, making recovery of catalytic material easier than in homogenous systems.[3,4] Additionally, their extensive use in industry can be partially attributed to their thermal stability.[5] However, unlike in a homogenous system, where each catalytic species acts as a single and identical active site, heterogenous catalysts are often comprised of multifaceted oxides or metal particles with many potentially active sites, which poses a challenge in both design and implementation.[3,5]

Catalyst design has been limited by the Brønsted–Evans–Polanyi (BEP) relationship which dictates that there is a linear dependance between the activation barrier and the binding strength in a chemical transformation.[6,7] A consequence of this is that the choice of catalytic metal mandates a compromise between low activation barriers (which yield faster reaction rates) and weak binding of reaction intermediates (which can yield high reaction selectivity).

The Sykes lab designs single site catalysts called single-atom alloys (SAA) that use small amounts of catalytically active elements like the Pt group metals alloyed with less reactive but more selective host metals such as copper.[8] Excitingly, these materials have been observed to deviate from linear scaling relationships and can also be designed from first principles due to their well-defined structure. However, nearly all the reported reactions on these materials are under reducing conditions.[8–10] I am expanding upon this previous work by applying this approach to oxidation reactions on NiAg alloys as many major industrial transformations occur under oxidizing conditions (sulfuric acid, ethylene oxide, etc.).[11,12]

1.1 Linear Scaling and the BEP

While catalysts are not consumed in a reaction, they offer an alternate reaction pathway with a lower activation barrier thereby increasing reaction rate (Figure 1.1A). In heterogeneous catalysis, the surface of a catalyst can make chemical bonds to a gas phase reactant which helps to break intramolecular bonds and form new ones. Adsorption strength of the molecule to the surface is among the most important aspects of determining both rate and selectivity of a specific reaction. This idea is articulated by the Sabatier principle which states that the binding energy

between a catalyst and reactant must be neither too strong nor too weak. If a bond is too weak, a catalyst will not react but if the bond is too strong the product will not desorb from the catalyst surface effectively limiting the reaction.[13]

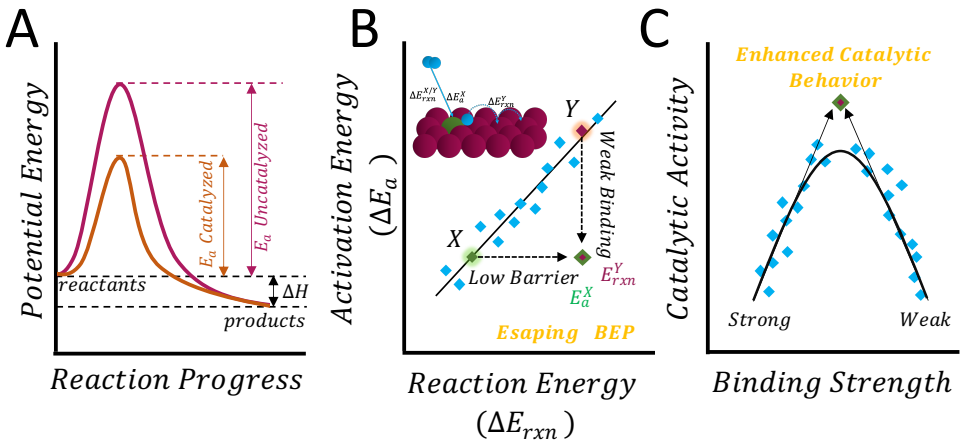

Figure 1.1. An overview of catalysis and guiding principles. (A) The effect of a catalyst on a potential energy diagram. **(B)** A plot showing the BEP relationship of the activation energy as a linear function of the reaction energy for chemical conversion. A favorable deviation from linearity is shown (purple/green point) in which the reaction activation energy is lowered in conjunction with more positive reaction energy (that is typically associated with weak binding); with an inset diagram of a single-atom alloy dissociating a molecule at a more reactive metal center (X, green) with a low activation energy (E_a) and intermediate reaction energy (ΔE_{Rxn}) before subsequent spillover onto a multitude of weak-binding host metal atoms (Y, purple). **(C)** The corresponding Sabatier volcano curve of the catalytic activity as a function of binding strength showing enhancement in the catalytic performance above what can be predicted by systems that are bound by linear scaling.

In 1912, Sabatier won a Nobel Prize for his theory which is now shown visually in 'volcano plots' where binding adsorbate strength is plotted against turn over frequency (TOF). [14–16] Similarly, the Bronsted-Evans-Polyani relationship describes this phenomenon as a linear dependence between the activation barrier and the reaction energy (Figure 1.1).[7,17] Both of these principles describe the compromise which must be made between low activation energy and weak binding strength for a catalytically active metal. However, bimetallic catalysts can result in a combination of each metals' properties. Thus, alloying acts to modify the bonding strength of the intermediate and moves the catalyst to a new position along the linear BEP.

1.2 Single Atom Alloys (SAAs)

The remarkable ability of bimetallic alloys to break linear scaling relationships is the key to their success as superior catalysts for many industrial reactions. A class of these alloys referred to as "near-surface alloys" has proven to supersede the Sabatier optimum by combining weak binding and lower activation energy than predicted. For example, Mavrikakis et al describe alloys that follow BEP relationships for H_2 activation with shifted activation energies that depend on the dopant metals Pt and Pd. The dopant metals form a monolayer on host metal surfaces which produce a catalyst which deviates from the BEP scaling associated with the pure metals.[18]

More recently, SAAs have been experimentally proven to break these linear scaling relationships and have become an increasingly popular area of research. [17,19] In fact, concentrations as low as ~0.01 ML of Pd on a Cu(111) crystal have been shown to substantially lower the activation barrier for hydrogen uptake and desorption from the Cu host surface.[9] The alloy combines the facile dissociation of hydrogen from Pd with the weak binding to Cu, which is very selective for the desired products. This is just one example of how an atomically dispersed dopant metal can significantly change the chemistry a host metal can perform.

The ability of density functional theory (DFT) to calculate activation energies for different chemical reactions on single metal and alloy surfaces affords surface scientists the opportunity to explore breaking linear scaling in model systems. The interdisciplinary work between experimental and theory groups has given rise to novel models being derived for single atom alloys resistant to coke formation and carbon monoxide poising for example.[20,21] The well-defined nature of SAAs has even given rise to theory-led discovery of a single atom catalyst, RhCu for propane dehydrogenation.[8] The RhCu system proved to go beyond model systems and work on larger scale reactor studies suggesting even more promise for later industrial applications.

1.3 D-band Theory

With these linear scaling relationships so well defined, binding energies can be quantified using the d-band model, which relates the d-band center of a catalytic metal to adsorption strength. Density of states of a transition metal can be a good indication of binding strength of the surface.[23] The adsorbate valance states interact with the s and d of the transition metal, and this coupling causes broadening to the adsorbate state; the result of which is a very broad half-filled s band. [24] However, the differences in transition metals comes from the formation of bonding and antibonding states between the valance and metal d states. Because the antibonding states are always above the the d states, the center of the d-states relative to the Fermi level is a good indicator of bond strength: the higher the d states are in energy relative to the Fermi level, the higher in energy the antibonding states are and the stronger the bonds are.[24,25] Generally, observations of changes to density of states can provide guidance for understanding adsorbate binding strength and electronic structure of transition metal samples (Figure 1.2).

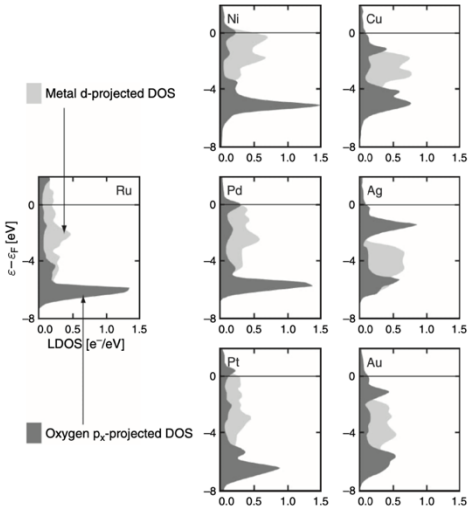

Figure 1.2. The density of states projected onto the d states of surface atoms for a range of close packed transition metal surfaces.[22]

It is important to understand how pure metals behave on their own to better predict the behavior of alloy surfaces.[26] There are two main sources of differences between bimetallic alloys and their individual component parts: ligand and ensemble effects. Ensemble effects result from geometric changes induced by alloying, while ligand effects are electronic perturbations of a metal that affect reactivity.[23,25,26] D band theory is helpful in that it provides a good approximation of ligand effects.

Most simply, when a larger metal atom is compressed into a lattice of smaller atoms, the d band is broadened and shifted to a lower energy away from the Fermi level. This results in a less reactive dopant atom compared to its reactivity among its own lattice. In the opposite scenario,

when a smaller atom is substituted into a larger host lattice the d band will compress and shift to a higher energy.[25]

Ensemble effects manifest as changes in reactivity as a result of the arrangement of surface atoms. In the case of bimetallic catalysts, this usually means changes in dispersion of the dopant metal in the host surface and whether it manifests as clusters or single atoms.[21,25] Changes to experimental conditions like partial pressures of reactants has been shown to help to control ensemble effects by selectively creating single atoms, dimers/trimers, or even larger clusters. [21]

1.4 Reactions of Interest: Ethylene Epoxidation

Ethylene oxide (EO) is a critical intermediate in the synthesis of plastics, polyesters, and a variety of glycols, most notably ethylene glycol. The partial oxidation of ethylene to EO is one of the most economically significant catalytic processes in the chemical industry, with global demand projected to exceed $65 billion annually by 2026.[27] This reaction is emblematic of a kinetically controlled selective oxidation, where the formation of EO is strongly favored over thermodynamically more stable combustion products such as CO_2 and H_2O. [28–30] The industrial catalyst for this reaction is silver, which is notably used for several partial oxidation in general and is also used for the conversion of methanol to formaldehyde.

Unpromoted silver surfaces achieve moderate EO selectivities of ~50%, but extensive industrial and academic research has increased this to ~90% through the incorporation of promoters such as Cl, Cs and Re.[28,31,32] However, this improvement comes at a significant environmental and safety cost. Chlorine, in particular, is a hazardous and corrosive gas that introduces considerable operational challenges. Nonetheless, its use is ubiquitous and effectively indispensable in modern EO catalysis. Cl is not only a promoter alone but is also required to enable the promotional effects of other elements. For instance, Cs alone does not enhance EO selectivity unless Cl is co-fed, and Re only becomes effective when both Cs and Cl are present.[31–34] This co-dependence has made the mechanistic interpretation of individual promoter roles exceedingly difficult. The prevailing hypotheses suggest that promoters alter the quantity, accessibility, or electronic character of reactive oxygen species, but no consensus has emerged.[31,35–40]

The underlying mechanism of ethylene epoxidation on Ag has been studied extensively using model single-crystal systems, particularly under ultra-high vacuum (UHV) conditions.[28] However, these studies face inherent limitations due to the difficulty of generating sufficiently oxidized Ag surfaces in UHV. For example, Campbell and co-workers demonstrated that mildly oxidized Ag(110) surfaces produced only combustion products, indicating that low coverages of atomic oxygen are insufficient for selective epoxidation.[41] Subsequent work highlighted the importance of achieving highly oxidized surface regions, particularly on Ag(111), to facilitate EO production.[42,43]

It is accepted that there are two main types of surface oxygen species that form on Ag: electrophilic oxygen ($O^{\delta+}$) and nucleophilic oxygen ($O^{\delta-}$). Electrophilic oxygen, observed at ~530.4 eV in X-ray photoelectron spectroscopy (XPS), is typically associated with selective epoxidation pathways via attack on the C=C double bond of ethylene, enabling ring closure to the epoxide.[44–47] Conversely, nucleophilic oxygen, appearing at ~528.2 eV is associated with total oxidation, attacking the C–H bond to initiate hydrogen abstraction.[39,48,49] The presence of nucleophilic oxygen is consistently correlated with reduced EO selectivity, and it is generally accepted to drive combustion toward CO_2 formation. Therefore, it is generally agreed upon that the distribution of surface species present largely govern product distribution for ethylene epoxidation.[44,50]

Despite this bifurcation in oxygen behavior, there is still a lack of understanding about the structures of both surfaces. Nucleophilic oxygen tends to be assigned as an oxygen induced reconstruction, most commonly the p(4x4).[46,51–53] And while there remains some debate about the exact unit cell of this structure there is an overarching agreement that nucleophilic oxygen is some surface reconstruction.[29,39,46] Similar agreements have yet to have been made about electrophilic oxygen whose structural identity, despite being thought to be isolated oxygen atoms for many years, remains especially perplexing to experimentalists and theorists alike.

The dynamic behavior of oxygen on Ag surfaces, including its coordination geometry, binding strength, and charge state, all depend sensitively on variables such as temperature, pressure, and surface coverage. Computational modeling, particularly density functional theory (DFT), has attempted to characterize this electrophilic species, yet discrepancies persist. Calculated binding

energies of isolated atomic oxygen on Ag(111) do not correspond to those measured experimentally for electrophilic oxygen. This mismatch has led to alternative hypotheses, including that the active species may be surface-adsorbed SO_4^{2-} moieties formed from trace sulfur impurities, which align better with XPS signatures.[48,54]

Other proposals highlight the possible role of subsurface oxygen, which may act either as a reactive intermediate or as a stabilizing background species that modulates surface reactivity.[55–59] Still more recent studies propose that molecular oxygen or peroxide-like $O_2^{\delta-}$ species may contribute directly to EO formation, particularly under reaction conditions mimicking industrial environments.[60–62] It is increasingly plausible that a combination of surface, subsurface, and molecularly bound oxygen species dynamically contribute to the reaction, depending on catalyst structure and gas-phase composition.[39] Operando and near-ambient pressure experiments, such as those conducted by Guo et al., have revealed multiple oxygen species coexisting under realistic conditions, including lattice oxygen, dioxygen, and subsurface oxygen. These studies underscore the ongoing debate over whether the catalytically active silver surface is metallic, partially oxidized, or covered with a mixture of atomic and molecular species.[56,61,63–65]

The lack of definitive mechanistic insight is further compounded by unresolved questions regarding the microkinetics of the reaction. A simplified elementary step mechanism is often proposed as follows: [66]

$$O_2(g) + * \rightarrow O_2* \quad (1)$$

$$O_2* + * \rightarrow 2O* \quad (2)$$

$$C_2H_4(g) + * \rightarrow C_2H_4* \quad (3)$$

$$C_2H_4* + O* \rightarrow C_2H_4O* + * \quad (4)$$

$$C_2H_4O* \rightarrow EO(g) + * \quad (5)$$

$$C_2H_4O* \rightarrow AA(g) + * \quad (6)$$

Here, adsorbed O* oxygen reacts with ethylene to form a surface-bound oxametallacycle (OMC) intermediate, which can subsequently decompose to either EO or acetaldehyde (AA). The fate of this intermediate—and thus the selectivity of the process—is determined by the nature of the

oxygen environment. Weakly bound, mono-coordinated O* favors EO, while stronger-binding, multi-coordinated species promote C–H bond activation and AA formation.

A foundational study by Linic and Barteau employed both DFT and experimental surface science to demonstrate that the OMC intermediate is common to both EO and AA pathways.[38]Their work has since been corroborated by others and is widely used to explain the dual reaction pathways.[42,67–70] Nonetheless, this model still depends critically on the identity of the surface oxygen species involved, which remains the key unresolved variable in EO catalysis.

Given the persistent uncertainties surrounding both oxygen speciation and promoter mechanisms, the discovery of new promoters, particularly those that are chlorine-free, presents a major opportunity for innovation. Despite the extensive industrial relevance of EO production, few new promoter systems have been identified in recent decades. Current academic efforts remain largely focused on Ag surfaces with canonical industrial promoters. This stagnation is partly due to the lack of molecular-level understanding of how promoters modulate surface reactivity and oxygen speciation. A rational, theory-guided strategy for promoter discovery is therefore needed.

The Sykes lab has demonstrated that single-atom alloys (SAAs) offer a powerful platform for tuning catalytic properties with atomic precision.[9,10,21,71–90] In this context, we propose a NiAg SAA system as a promising new catalyst for ethylene epoxidation. Ni is known to dissociate O_2 readily, even at cryogenic temperatures (as low as 8 K on Ni(111)), whereas Ag exhibits weak oxygen binding, which is thought to be critical for epoxide selectivity.[91] By alloying these two metals, we aim to combine the superior oxygen activation properties of Ni with the selective oxidation characteristics of Ag, creating a bifunctional surface that facilitates O_2 activation while avoiding overbinding. This design has the potential to yield a chlorine-free, high-selectivity catalyst for EO production.

1.5 References

(1) Wang, A.; Li, J.; Zhang, T. Heterogeneous Single-Atom Catalysis. *Nature Reviews Chemistry* **2018**, *2* (6), 65–81. https://doi.org/10.1038/s41570-018-0010-1.

(2) Adams, C. Applied Catalysis: A Predictive Socioeconomic History. *Topics in Catalysis* **2009**, *52* (8), 924–934. https://doi.org/10.1007/s11244-009-9251-z.

(3) Copéret, C.; Chabanas, M.; Petroff Saint-Arroman, R.; Basset, J.-M. Homogeneous and Heterogeneous Catalysis: Bridging the Gap through Surface Organometallic Chemistry. *Angewandte Chemie Interntational Edition* **2003**, *42* (2).

(4) Marcinkowski, M. D. Single Atom Alloys for Efficient and Selective Bond Activations: A Model Surface Chemistry Approach, Tufts University, 2016.

(5) Nørskov, J. K.; Bligaard, T.; Hvolbæk, B.; Abild-Pedersen, F.; Chorkendorff, I.; Christensen, C. H. The Nature of the Active Site in Heterogeneous Metal Catalysis. *Chemical Society Reviews* **2008**, *37* (10), 2163–2171. https://doi.org/10.1039/b800260f.

(6) Nilsson, A.; Pettersson, L. G. M.; Hammer, B.; Bligaard, T.; Christensen, C. H.; Nørskov, J. K. The Electronic Structure Effect in Heterogeneous Catalysis. *Catalysis Letters* **2005**, *100* (3–4), 111–114. https://doi.org/10.1007/s10562-004-3434-9.

(7) Michaelides, A.; Liu, Z. P.; Zhang, C. J.; Alavi, A.; King, D. A.; Hu, P. Identification of General Linear Relationships between Activation Energies and Enthalpy Changes for Dissociation Reactions at Surfaces. *Journal of the American Chemical Society* **2003**, *125* (13), 3704–3705. https://doi.org/10.1021/ja027366r.

(8) Ryan T. Hannagan, Georgios Giannakakis, Romain Réocreux, Julia Schumann, Jordan Finzel, Yicheng Wang, Angelos Michaelides, Prashant Deshlahra, Phillip Christopher, Maria Flytzani-Stephanopoulos, Michail Stamatakis, E. C. H. S. First-Principles Design of a Single-Atom-Alloy Propane Dehydrogenation Catalyst. *Science* **2021**, *372*, 1444–1447.

(9) Kyriakou, G.; Boucher, M. B.; Jewell, A. D.; Lewis, E. A.; Lawton, T. J.; Baber, A. E.; Tierney, H. L.; Flytzani-Stephanopoulos, M.; Charles, E.; Sykes, H. Isolated Metal Atom Geometries as a Strategy for Selective Heterogeneous Hydrogenations. *Science* **2012**, *335* (6073).

(10) Tierney, H. L.; Baber, A. E.; Kitchin, J. R.; Sykes, E. C. H. Hydrogen Dissociation and Spillover on Individual Isolated Palladium Atoms. *Physical Review Letters* **2009**, *103* (24), 1–4. https://doi.org/10.1103/PhysRevLett.103.246102.

(11) Group, V. *Sulfuric acid – Manufacturing process of Sulfuric acid*. https://www.valcogroup-valves.com/faq-2/sulfuric-acid-manufacturing-process-of-sulfuric-acid/.

(12) Miller, J. H.; Joshi, A.; Li, X.; Bhan, A. Catalytic Degradation of Ethylene Oxide over Ag/α-Al2O3. *Journal of Catalysis* **2020**, *389*, 714–720. https://doi.org/10.1016/j.jcat.2020.07.008.

(13) Nilsson, A.; Pettersson, L. G. M.; Hammer, B.; Bligaard, T.; Christensen, C. H.; Nørskov, J. K. The Electronic Structure Effect in Heterogeneous Catalysis. *Catalysis Letters* **2005**, *100* (3–4), 111–114. https://doi.org/10.1007/s10562-004-3434-9.

(14) Sabatier, P. *The Method of Direct Hydrogenation by Catalysis*. Nobel Lecture.

(15) Ooka, H.; Huang, J.; Exner, K. S. The Sabatier Principle in Electrocatalysis: Basics, Limitations, and Extensions. *Frontiers in Energy Research* **2021**, *9* (May), 1–20. https://doi.org/10.3389/fenrg.2021.654460.

(16) KOLASINSKI, KURT W. (Department of Chemistry, West Chester University, West Chester, PA, U. *Surface Science: Foundations of Catalysis and Nanoscience*, 3rd ed.; John Wiley & Sons, Ltd, 2012. https://doi.org/10.1002/9781119941798.
(17) Darby, M. T.; Stamatakis, M.; Michaelides, A.; Sykes, E. C. H. Lonely Atoms with Special Gifts: Breaking Linear Scaling Relationships in Heterogeneous Catalysis with Single-Atom Alloys. *Journal of Physical Chemistry Letters* **2018**, *9* (18), 5636–5646. https://doi.org/10.1021/acs.jpclett.8b01888.
(18) Greeley, J.; Mavrikakis, M. Alloy Catalysts Designed from First Principles. *Nature Materials* **2004**, *3* (11), 810–815. https://doi.org/10.1038/nmat1223.
(19) Hannagan, R. T.; Giannakakis, G.; Flytzani-Stephanopoulos, M.; Sykes, E. C. H. Single-Atom Alloy Catalysis. *Chemical Reviews*. American Chemical Society November 11, 2020. https://doi.org/10.1021/acs.chemrev.0c00078.
(20) Darby, M. T.; Réocreux, R.; Sykes, E. C. H.; Michaelides, A.; Stamatakis, M. Elucidating the Stability and Reactivity of Surface Intermediates on Single-Atom Alloy Catalysts. *ACS Catalysis* **2018**, *8* (6), 5038–5050. https://doi.org/10.1021/acscatal.8b00881.
(21) Darby, M. T.; Sykes, E. C. H.; Michaelides, A.; Stamatakis, M. Carbon Monoxide Poisoning Resistance and Structural Stability of Single Atom Alloys. *Topics in Catalysis* **2018**, *61* (5–6), 428–438. https://doi.org/10.1007/s11244-017-0882-1.
(22) Anders, N.; Petterson, L. G. M.; Norskov, J. K. *Chemical Bonding at Surfaces and Interfaces*; Elsevier B.V., 2008.
(23) Hammer, B.; Nørskov, J. K. Electronic Factors Determining the Reactivity of Metal Surfaces. *Surface Science* **1995**, *343* (3), 211–220. https://doi.org/10.1016/0039-6028(96)80007-0.
(24) Nørskov, J. K.; Abild-Pedersen, F.; Studt, F.; Bligaard, T. Density Functional Theory in Surface Chemistry and Catalysis. *Proceedings of the National Academy of Sciences of the United States of America* **2011**, *108* (3), 937–943. https://doi.org/10.1073/pnas.1006652108.
(25) A. Ruban , B. Hammer, P. Stoltze, H.L. Skriver, J. K. N. Surface Electronic Structure and Reactivity of Transition and Noble Metals. *Journal of Molecular Catalysis A: Chemical* **1997**, *115*, 421–429.
(26) Rodriguez, J. A.; Goodman, D. W. The Nature of the Metal-Metal Bond in Bimetallic Surfaces. *Science* **1992**, *257* (5072), 897–903. https://doi.org/10.1126/science.257.5072.897.
(27) *Global Ethylene Oxide Market - Forecast from 2021 to 2026*; 2021.
(28) Pu, T.; Tian, H.; Ford, M. E.; Rangarajan, S.; Wachs, I. E. Overview of Selective Oxidation of Ethylene to Ethylene Oxide by Ag Catalysts. *ACS Catalysis* **2019**, 10727–10750. https://doi.org/10.1021/acscatal.9b03443.
(29) Michaelides, A.; Reuter, K.; Scheffler, M. When Seeing Is Not Believing: Oxygen on Ag(111), a Simple Adsorption System? *Journal of Vacuum Science & Technology A: Vacuum, Surfaces, and Films* **2005**, *23* (6), 1487–1497. https://doi.org/10.1116/1.2049302.
(30) Grant, R. B.; Lambert, R. M. A Single Crystal Study of the Silver-Catalysed Selective Oxidation and Total Oxidation of Ethylene. *Journal of Catalysis* **1985**, *92* (2), 364–375. https://doi.org/10.1016/0021-9517(85)90270-2.
(31) Hwang, A.; Klaucke, J.; Lizandara-Pueyo, C.; Karpov, A.; Iglesia, E. Roles of Re and Cs Promoters and Organochlorine Moderators in the Synthesis of Ethylene Oxide on Ag-Based Catalysts. *ChemCatChem* **2023**. https://doi.org/10.1002/cctc.202301369.

(32) Diao, W.; Digiulio, C. D.; Schaal, M. T.; Ma, S.; Monnier, J. R. An Investigation on the Role of Re as a Promoter in Ag-Cs-Re/α-Al2O3 High-Selectivity, Ethylene Epoxidation Catalysts. *Journal of Catalysis* **2015**, *322*, 14–23. https://doi.org/10.1016/j.jcat.2014.11.007.
(33) Jankowiak, J. T.; Barteau, M. A. Ethylene Epoxidation over Silver and Copper-Silver Bimetallic Catalysts: I. Kinetics and Selectivity. *Journal of Catalysis* **2005**, *236* (2), 366–378. https://doi.org/10.1016/j.jcat.2005.10.018.
(34) Huš, M.; Hellman, A. Dipole Effect on Ethylene Epoxidation: Influence of Alkali Metals and Chlorine. *Journal of Catalysis* **2018**, *363*, 18–25. https://doi.org/10.1016/j.jcat.2018.04.008.
(35) Campbell, C. T. Chlorine Promoters in Selective Ethylene Epoxidation over Ag(111): A Comparison with Ag(110). *Journal of Catalysis* **1986**, *99* (1), 28–38. https://doi.org/10.1016/0021-9517(86)90195-8.
(36) Chen, C. J.; Harris, J. W.; Bhan, A. Kinetics of Ethylene Epoxidation on a Promoted Ag/α-Al2O3 Catalyst—The Effects of Product and Chloride Co-Feeds on Rates and Selectivity. *Chemistry - A European Journal* **2018**, *24* (47), 12405–12415. https://doi.org/10.1002/chem.201801356.
(37) Van Hoof, A. J. F.; Hermans, E. A. R.; Van Bavel, A. P.; Friedrich, H.; Hensen, E. J. M. Structure Sensitivity of Silver-Catalyzed Ethylene Epoxidation. *ACS Catalysis* **2019**, *9* (11), 9829–9839. https://doi.org/10.1021/acscatal.9b02720.
(38) Linic, S.; Barteau, M. A. Formation of a Stable Surface Oxametallacycle That Produces Ethylene Oxide. *Journal of the American Chemical Society* **2002**, *124* (2), 310–317. https://doi.org/10.1021/ja0118136.
(39) Carbonio, E. A.; Rocha, T. C. R.; Klyushin, A. Y.; Píš, I.; Magnano, E.; Nappini, S.; Piccinin, S.; Knop-Gericke, A.; Schlögl, R.; Jones, T. E. Are Multiple Oxygen Species Selective in Ethylene Epoxidation on Silver? *Chemical Science* **2018**, *9* (4), 990–998. https://doi.org/10.1039/c7sc04728b.
(40) Linic, S.; Barteau, M. A. Construction of a Reaction Coordinate and a Microkinetic Model for Ethylene Epoxidation on Silver from DFT Calculations and Surface Science Experiments. *Journal of Catalysis* **2003**, *214* (2), 200–212. https://doi.org/10.1016/S0021-9517(02)00156-2.
(41) Campbell, C. T.; Paffett, M. T. *Model Studies of Ethylene Epoxidation Catalyzed by the Ag(110) Surface*.
(42) Özbek, M. O.; Van Santen, R. A. The Mechanism of Ethylene Epoxidation Catalysis. *Catalysis Letters* **2013**, *143* (2), 131–141. https://doi.org/10.1007/s10562-012-0957-3.
(43) Su, D. S.; Jacob, T.; Hansen, T. W.; Wang, D.; Schlögl, R.; Freitag, B.; Kujawa, S. Surface Chemistry of Ag Particles: Identification of Oxide Species by Aberration-Corrected TEM and by DFT Calculations. *Angewandte Chemie* **2008**, *120* (27), 5083–5086. https://doi.org/10.1002/ange.200800406.
(44) Campbell, C. T.; Koel, B. E. Chlorine Promotion of Selective Ethylene Oxidation over Ag(110): Kinetics and Mechanism. *Journal of Catalysis* **1985**, *92* (2), 272–283. https://doi.org/10.1016/0021-9517(85)90261-1.
(45) Force, E. L.; Bell, A. T. The Relationship of Adsorbed Species Observed by Infrared Spectroscopy to the Mechanism of Ethylene Oxidation over Silver. *Journal of Catalysis* **1975**, *40* (3), 356–371. https://doi.org/10.1016/0021-9517(75)90267-5.

(46) Kaichev, V. V.; Bukhtiyarov, V. I.; Hävecker, M.; Knop-Gercke, A.; Mayer, R. W.; Schlögl, R. The Nature of Electrophilic and Nucleophilic Oxygen Adsorbed on Silver. *Kinetics and Catalysis* **2003**, *44* (3), 432–440. https://doi.org/10.1023/A:1024459305551.
(47) Bukhtiyarov, V. I.; Nizovskii, A. I.; Bluhm, H.; Hävecker, M.; Kleimenov, E.; Knop-Gericke, A.; Schlögl, R. Combined in Situ XPS and PTRMS Study of Ethylene Epoxidation over Silver. *Journal of Catalysis* **2006**, *238* (2), 260–269. https://doi.org/10.1016/j.jcat.2005.11.043.
(48) Jones, T. E.; Wyrwich, R.; Böcklein, S.; Carbonio, E. A.; Greiner, M. T.; Klyushin, A. Y.; Moritz, W.; Locatelli, A.; Menteş, T. O.; Niño, M. A.; Knop-Gericke, A.; Schlögl, R.; Günther, S.; Wintterlin, J.; Piccinin, S. The Selective Species in Ethylene Epoxidation on Silver. *ACS Catalysis* **2018**, *8* (5), 3844–3852. https://doi.org/10.1021/acscatal.8b00660.
(49) Stegelmann, C.; Schiødt, N. C.; Campbell, C. T.; Stoltze, P. Microkinetic Modeling of Ethylene Oxidation over Silver. *Journal of Catalysis* **2004**, *221* (2), 630–649. https://doi.org/10.1016/j.jcat.2003.10.004.
(50) Bukhtiyarov, V. I.; Hävecker, M.; Kaichev, V. V.; Knop-Gericke, A.; Mayer, R. W.; Schlögl, R. Atomic Oxygen Species on Silver: Photoelectron Spectroscopy and x-Ray Absorption Studies. *Physical Review B - Condensed Matter and Materials Physics* **2003**, *67* (23), 2354221–23542212. https://doi.org/10.1103/PhysRevB.67.235422.
(51) Schmid, M.; Reicho, A.; Stierle, A.; Costina, I.; Klikovits, J.; Kostelnik, P.; Dubay, O.; Kresse, G.; Gustafson, J.; Lundgren, E.; Andersen, J. N.; Dosch, H.; Varga, P. Structure of Ag(111)-p(4×4)-O: No Silver Oxide. *Physical Review Letters* **2006**, *96* (14), 1–4. https://doi.org/10.1103/PhysRevLett.96.146102.
(52) Li, W. X.; Stampfl, C.; Scheffler, M. Why Is a Noble Metal Catalytically Active? The Role of the O-Ag Interaction in the Function of Silver as an Oxidation Catalyst. *Physical Review Letters* **2003**, *90* (25), 4. https://doi.org/10.1103/PhysRevLett.90.256102.
(53) Campbell, C. T. Atomic and Molecular Oxygen Adsorption on Ag(111). *Surface Science* **1985**, *157* (1), 43–60. https://doi.org/10.1016/0039-6028(85)90634-X.
(54) Schiller, F.; Ali, K.; Makarova, A. A.; Auras, S. V.; García-Martínez, F.; Mohammed Idris Bakhit, A.; Castrillo Bodero, R.; Villar-García, I. J.; Ortega, J. E.; Pérez-Dieste, V. Near-Ambient Pressure Oxidation of Silver in the Presence of Steps: Electrophilic Oxygen and Sulfur Impurities. *ACS Catalysis* **2024**, 12865–12874. https://doi.org/10.1021/acscatal.4c02985.
(55) Guo, M.; Dongfang, N.; Iannuzzi, M.; van Bokhoven, J. A.; Artiglia, L. Structure and Reactivity of Active Oxygen Species on Silver Surfaces for Ethylene Epoxidation. *ACS Catalysis* **2024**, 10234–10244. https://doi.org/10.1021/acscatal.4c01566.
(56) Mize, C. J.; Crosby, L. D.; Isbill, S. B.; Roy, S. Insight into Subsurface Adsorption Derived from a Lattice-Gas Model and Monte Carlo Simulations. *Journal of Physical Chemistry C* **2022**, *126* (11), 5343–5353. https://doi.org/10.1021/acs.jpcc.2c00342.
(57) Xu, Y.; Greeley, J.; Mavrikakis, M. Effect of Subsurface Oxygen on the Reactivity of the Ag(111) Surface. *Journal of the American Chemical Society* **2005**, *127* (37), 12823–12827. https://doi.org/10.1021/ja043727m.
(58) Pawela-Crew, J.; Madix, R. J.; Stöhr, J. The Effect of Subsurface Oxygen on the Orientation of Molecular Oxygen on Ag(110). *Surface Science* **1995**, *339* (1–2), 23–28. https://doi.org/10.1016/0039-6028(95)00646-X.

(59) Chen, D.; Chen, L.; Zhao, Q. C.; Yang, Z. X.; Shang, C.; Liu, Z. P. Square-Pyramidal Subsurface Oxygen [Ag4OAg] Drives Selective Ethene Epoxidation on Silver. *Nature Catalysis* **2024**, *7* (5), 536–545. https://doi.org/10.1038/s41929-024-01135-2.
(60) Ercelik, M.; Zhang, L.; Kot, P.; Kim, J.; Chae, J.; Spree, L. E.; Guo, H.; Heinrich, A. J.; Bae, Y.; Borodin, D. Characterization of an Unexpected μ 3 Adsorption of Molecular Oxygen on Ag (100) with Low-Temperature STM. **2025**, No. 100. https://doi.org/10.1021/acs.jpcc.4c06572.
(61) Pu, T.; Setiawan, A.; Lis, B. M.; Zhu, M.; Ford, M. E.; Rangarajan, S.; Wachs, I. E. Nature and Reactivity of Oxygen Species on/in Silver Catalysts during Ethylene Oxidation. *ACS Catalysis* **2022**, *12*, 4375–4381. https://doi.org/10.1021/acscatal.1c05939.
(62) Chen, C. T.; Sviripa, A.; Verma, S.; Paolucci, C.; Flaherty, D. W. Reactions of Surface Peroxides Contribute to Rates and Selectivities for C2H4 Epoxidation on Silver. *ACS Catalysis* **2025**, 1387–1398. https://doi.org/10.1021/acscatal.4c06945.
(63) Özbek, M. O.; Önal, I.; Vansanten, R. A. Ethylene Epoxidation Catalyzed by Silver Oxide. *ChemCatChem* **2011**, *3* (1), 150–153. https://doi.org/10.1002/cctc.201000249.
(64) Ozbek, M. O.; Onal, I.; Van Santen, R. A. Effect of Surface and Oxygen Coverage on Ethylene Epoxidation. *Topics in Catalysis* **2012**, *55* (11–13), 710–717. https://doi.org/10.1007/s11244-012-9870-7.
(65) Pu, T.; Setiawan, A.; Foucher, A. C.; Guo, M.; Jehng, J. M.; Zhu, M.; Ford, M. E.; Stach, E. A.; Rangarajan, S.; Wachs, I. E. Revealing the Nature of Active Oxygen Species and Reaction Mechanism of Ethylene Epoxidation by Supported Ag/α-Al2O3 Catalysts. *ACS Catalysis* **2024**, *14* (1), 406–417. https://doi.org/10.1021/acscatal.3c04361.
(66) Li, H.; Cao, A.; Nørskov, J. K. Understanding Trends in Ethylene Epoxidation on Group IB Metals. *ACS Catalysis* **2021**, *11* (19), 12052–12057. https://doi.org/10.1021/acscatal.1c03094.
(67) Linic, S.; Barteau, M. A. Control of Ethylene Epoxidation Selectivity by Surface Oxametallacycles. *JACS* **2003**, *125* (2), 4034–4035. https://doi.org/10.1016/S0021-9517(02)00156-2.
(68) Saravanan, C.; Salazar, M. R.; Kress, J. D.; Redondo, A. Oxametallacycle Intermediates on Clean and Cs-Promoted Ag(111) Surfaces. *Journal of Physical Chemistry B* **2000**, *104* (36), 8685–8691. https://doi.org/10.1021/jp001030r.
(69) Jones, G. S.; Mavrikakis, M.; Barteau, M. A.; Vohs, J. M. *First Synthesis, Experimental and Theoretical Vibrational Spectra of an Oxametallacycle on a Metal Surface*; 1998.
(70) Zhou, L.; Madix, R. J. Oxidation of Styrene and Phenylacetaldehyde on Ag(111): Evidence for Transformation of Surface Oxametallacycle. *Journal of Physical Chemistry C* **2008**, *112* (12), 4725–4734. https://doi.org/10.1021/jp7119558.
(71) Tierney, H. L.; Baber, A. E.; Sykes, E. C. H. Atomic-Scale Imaging and Electronic Structure of Catalytic Sites on Pd/Cu Near Surface Alloys. *J. Phys. Chem. C* **2008**, *113* (17), 7246–7250. https://doi.org/10.1021/jp809766d.
(72) Bellisario, D. O.; Han, J. W.; Tierney, H. L.; Baber, A. E.; Sholl, D. S.; Sykes, E. C. H. Importance of Kinetics in Surface Alloying: A Comparison of the Diffusion Pathways of Pd and Ag Atoms on Cu(111). *Journal of Physical Chemistry C* **2009**, *113* (29), 12863–12869. https://doi.org/10.1021/jp903541k.
(73) Baber, A. E.; Tierney, H. L.; Lawton, T. J.; Sykes, E. C. H. An Atomic-Scale View of Palladium Alloys and Their Ability to Dissociate Molecular Hydrogen. *ChemCatChem* **2011**, *3* (3), 607–614. https://doi.org/10.1002/cctc.201000309.

(74) Marcinkowski, M. D.; Jewell, A. D.; Stamatakis, M.; Boucher, M. B.; Lewis, E. A.; Murphy, C. J.; Kyriakou, G.; Sykes, E. C. H. Controlling a Spillover Pathway with the Molecular Cork Effect. *Nature Materials* **2013**, *12* (6), 523–528. https://doi.org/10.1038/nmat3620.
(75) Boucher, M. B.; Zugic, B.; Cladaras, G.; Kammert, J.; Marcinkowski, M. D.; Lawton, T. J.; Sykes, E. C. H.; Flytzani-Stephanopoulos, M. Single Atom Alloy Surface Analogs in Pd0.18Cu15nanoparticles for Selective Hydrogenation Reactions. *Physical Chemistry Chemical Physics* **2013**, *15* (29), 12187–12196. https://doi.org/10.1039/c3cp51538a.
(76) Lucci, F. R.; Lawton, T. J.; Pronschinske, A.; Sykes, E. C. H. Atomic Scale Surface Structure of Pt/Cu(111) Surface Alloys. *Journal of Physical Chemistry C* **2014**, *118* (6), 3015–3022. https://doi.org/10.1021/jp405254z.
(77) Kyriakou, G.; Davidson, E. R. M.; Peng, G.; Roling, L. T.; Singh, S.; Boucher, M. B.; Marcinkowski, M. D.; Mavrikakis, M.; Michaelides, A.; Sykes, E. C. H. Significant Quantum Effects in Hydrogen Activation. *ACS Nano* **2014**, *8* (5), 4827–4835. https://doi.org/10.1021/nn500703k.
(78) Lucci, F. R.; Marcinkowski, M. D.; Lawton, T. J.; Sykes, E. C. H. H2 Activation and Spillover on Catalytically Relevant Pt-Cu Single Atom Alloys. *Journal of Physical Chemistry C* **2015**, *119* (43), 24351–24357. https://doi.org/10.1007/BF00305980.
(79) Lucci, F. R.; Liu, J.; Marcinkowski, M. D.; Yang, M.; Allard, L. F.; Flytzani-Stephanopoulos, M.; Sykes, E. C. H. Selective Hydrogenation of 1,3-Butadiene on Platinum-Copper Alloys at the Single-Atom Limit. *Nature Communications* **2015**, *6*, 1–8. https://doi.org/10.1038/ncomms9550.
(80) Lucci, F. R.; Darby, M. T.; Mattera, M. F. G.; Ivimey, C. J.; Therrien, A. J.; Michaelides, A.; Stamatakis, M.; Sykes, E. C. H. Controlling Hydrogen Activation, Spillover, and Desorption with Pd-Au Single-Atom Alloys. *Journal of Physical Chemistry Letters* **2016**, *7* (3), 480–485. https://doi.org/10.1021/acs.jpclett.5b02400.
(81) Shan, J.; Lucci, F. R.; Liu, J.; El-Soda, M.; Marcinkowski, M. D.; Allard, L. F.; Sykes, E. C. H.; Flytzani-Stephanopoulos, M. Water Co-Catalyzed Selective Dehydrogenation of Methanol to Formaldehyde and Hydrogen. *Surface Science* **2016**, *650*, 121–129. https://doi.org/10.1016/j.susc.2016.02.010.
(82) Liu, J.; Lucci, F. R.; Yang, M.; Lee, S.; Marcinkowski, M. D.; Therrien, A. J.; Williams, C. T.; Sykes, E. C. H.; Flytzani-Stephanopoulos, M. Tackling CO Poisoning with Single-Atom Alloy Catalysts. *Journal of the American Chemical Society* **2016**, *138* (20), 6396–6399. https://doi.org/10.1021/jacs.6b03339.
(83) Wang, Z. T.; Darby, M. T.; Therrien, A. J.; El-Soda, M.; Michaelides, A.; Stamatakis, M.; Sykes, E. C. H. Preparation, Structure, and Surface Chemistry of Ni-Au Single Atom Alloys. *Journal of Physical Chemistry C* **2016**, *120* (25), 13574–13580. https://doi.org/10.1021/acs.jpcc.6b03473.
(84) Marcinkowski, M. D.; Liu, J.; Murphy, C. J.; Liriano, M. L.; Wasio, N. A.; Lucci, F. R.; Flytzani-Stephanopoulos, M.; Sykes, E. C. H. Selective Formic Acid Dehydrogenation on Pt-Cu Single-Atom Alloys. *ACS Catalysis* **2017**, *7* (1), 413–420. https://doi.org/10.1021/acscatal.6b02772.
(85) Wang, Z. T.; Hoyt, R. A.; El-Soda, M.; Madix, R. J.; Kaxiras, E.; Sykes, E. C. H. Dry Dehydrogenation of Ethanol on Pt–Cu Single Atom Alloys. *Topics in Catalysis* **2018**, *61* (5–6), 328–335. https://doi.org/10.1007/s11244-017-0856-3.

(86) Liu, J.; Shan, J.; Lucci, F. R.; Cao, S.; Sykes, E. C. H.; Flytzani-Stephanopoulos, M. Palladium-Gold Single Atom Alloy Catalysts for Liquid Phase Selective Hydrogenation of 1-Hexyne. *Catalysis Science and Technology* **2017**, *7* (19), 4276–4284. https://doi.org/10.1039/c7cy00794a.
(87) Marcinkowski, M. D.; Darby, M. T.; Liu, J.; Wimble, J. M.; Lucci, F. R.; Lee, S.; Michaelides, A.; Flytzani-Stephanopoulos, M.; Stamatakis, M.; Sykes, E. C. H. Pt/Cu Single-Atom Alloys as Coke-Resistant Catalysts for Efficient C-H Activation. *Nature Chemistry* **2018**, *10* (3), 325–332. https://doi.org/10.1038/NCHEM.2915.
(88) Darby, M. T.; Réocreux, R.; Sykes, E. C. H.; Michaelides, A.; Stamatakis, M. Elucidating the Stability and Reactivity of Surface Intermediates on Single-Atom Alloy Catalysts. *ACS Catalysis* **2018**, *8* (6), 5038–5050. https://doi.org/10.1021/acscatal.8b00881.
(89) Lucci, F. R.; Zhang, L.; Thuening, T.; Uhlman, M. B.; Schilling, A. C.; Henkelman, G.; Charles, E. The Effect of Single Pd Atoms on the Energetics of Recombinative O2 Desorption from Au(111). *Surface Science* **2018**, *677* (June), 296–300. https://doi.org/10.1016/j.susc.2018.08.001.
(90) Darby, M. T.; Stamatakis, M.; Michaelides, A.; Sykes, E. C. H. Lonely Atoms with Special Gifts: Breaking Linear Scaling Relationships in Heterogeneous Catalysis with Single-Atom Alloys. *Journal of Physical Chemistry Letters* **2018**, *9* (18), 5636–5646. https://doi.org/10.1021/acs.jpclett.8b01888.
(91) Ceyer, J. D. B. Q. Y. Y. A. D. J. S. T. THE ADSORPTION OF CO AND O 2 ON Ni(Lll) AT 8 K. *Surface Science* **1988**, *195*, 77–93. https://doi.org/10.1016/0039-6028(88)90781-9.

Chapter 2: Experimental Methods and Techniques

Single crystals are a valuable tool as model systems to investigate industrial reactions. While these studies provide useful descriptions of reactions and other properties at the atomic level, they require a well characterized interface of known concentration and structure. Therefore, an ultrahigh vacuum environment (UHV) is required. For example, if there were an atmosphere of N_2 atoms at room temperature (T), the incident flux (Z_w) can be calculated from the Hertz-Knudsen equation:

$$Z_w = \frac{p}{(2\pi k_b T)^{1/2}} \qquad (1)$$

that at a pressure (p), $1x10^{-6}$ torr, if all the atoms to hit the surface were to stick, a monolayer could be formed in a single second.[1] The nature of single crystal model studies relies on observing surface reactions on well-defined atomic scale systems; thus, it is imperative that the samples remain free of unwanted adsorbates. Additionally, lower pressure environments increase a particle's mean free path (λ) as described by:

$$\lambda = \frac{k_b T}{2^{1/2}\sigma p} \qquad (2)$$

Where σ is the collision cross section.[1] Lower pressures also make it possible for electrons to travel to detectors without unwanted collisions along the way. Additionally, lower pressures minimize detector noise from electron multipliers, which is especially useful for electron spectroscopies like X-ray photoelectron spectroscopy. Ambient pressure XPS, for instance, must have its detector very physically close to a sample to overcome the lower mean free paths from higher pressure conditions.

2.1 X-Ray Photoelectron Spectroscopy

X-ray photoelectron spectroscopy (XPS) was first discovered by Heinrich Hertz in 1887, who initially referred to it as electron spectroscopy for chemical analysis (ESCA).[2] Based on the photoelectron effect, XPS irradiates a sample with mono energetic soft x-rays, and the kinetic energy of the emitted photoelectrons is analyzed.

The emission of the photoelectron is the result of the complete transfer of the x-ray's energy to a core level electron. This can be expressed:

$$h\nu = BE + KE + \phi_{spec} \qquad (3)$$

where the energy of the x-ray ($h\nu$) is equal to the sum of the binding (BE) and kinetic (KE) energies of the electron and the work function of the instrument (ϕ_{spec}). The binding energy refers to how tightly bound the electron is to the atom/orbital that it is attached to. Because binding energy is a material property, Equation 3 is often rearranged to:

$$BE = h\nu - KE - \phi_{spec} \qquad (4)$$

This binding energy scale is used because it allows for uniform and straightforward comparisons of chemical states. If presented on a kinetic energy scale, the X-ray source energy used to collect the data would need to be known to compare chemical states across sources on account of the varying kinetic energy of the emitted photoelectron.

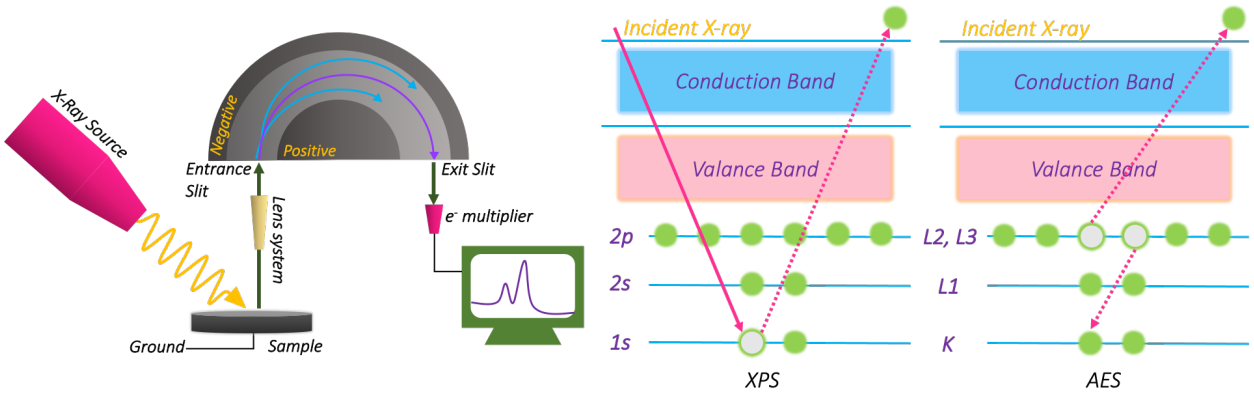

Figure 2.1. An overview of XPS. Schematic representation of XPS experimental set up and processes that result from x-ray bombardment including emission of photoelectrons and auger electron emission.

Any electron with a binding energy less than that of the source should be emitted and observed with XPS (Figure 2.1). The result of this electron loss is a hole which leads to a release of energy by either x-ray, fluorescence, or Auger electron emission. While relaxation via fluorescence is not detected in XPS spectra, Auger emissions are detected and can be used for qualitative analysis.

The Auger process involves a three-electron transition where the kinetic energy measured depends on the binding energies of the specific orbitals in the atom from which it originates. Therefore, unlike photoelectron emission, the kinetic energy of Auger electrons remains constant

across x-ray sources. Coupling the constant binding energy of an emitted photoelectron with the changing binding energy of Auger electrons is useful for spectral overlaps from the two different emissions.[2]

A major advantage to using XPS is the ability to determine the chemical environment of atoms in a sample; for example, nearest neighbors and oxidation states both affect photoelectron peaks.[2] Conducting this spectroscopy in UHV conditions removes adsorbed gases and other possible contaminants from the sample, prevents arcing and high voltage breakdown, and increases the mean free path for electrons and photons. While these conditions are advantageous for clean and sensitive analysis, they limit the range of experiments run. For example, studying single atom alloys as model systems for industrial reactions: XPS can explore their surface reactivity, but UHV limits the simulation of industrial reaction conditions, thus ambient pressure XPS at synchrotron lab sources is particularly useful to the studies presented herein.

2.2 Scanning Tunneling Microscopy

Scanning tunneling microscopy (STM) relies on the quantum mechanical phenomenon of electron tunneling and allows for incredibly detailed investigations of surface structures as well as the manipulation of atoms and molecules on surfaces. The discovery of STM is accredited to Binnig and Rohrer who won the Nobel Prize in 1987.[3]

When two metals are brought close together without electrical connection each of their Fermi energies remain characteristic of their individual values (Figure 2.2A). The offset of the Fermi energies is equal to the difference in the workfunctions of the two metals:[1]

$$\Phi_c = E_F^L - E_F^R \qquad (5)$$

By bringing the metals closer together and electrically connecting them, the Fermi energies line up and the vacuum level shifts so the potential between the metals is no longer constant and an electric field exists in the vacuum between the metals (Figure 2.2B). In this case, all states up to the Fermi energy are full and above are empty so no current will flow between the metals as there is no empty states to fill. However, when a bias is applied to the metals in electrical contact the direction of the flow of current can be controlled by adjusting the potential difference between the two.

In Figure 2.2 C the left-hand metal is biased positively with respect to the right-hand metal, thereby lowering the left metal's Fermi energy. The occupied states of the right metal are at the same energy as the unoccupied states of the left metal meaning if they are brought sufficiently close electrons will be able to tunnel. While classically no current will flow because of the potential barrier, the tunneling current is exponentially proportional to distance (d):

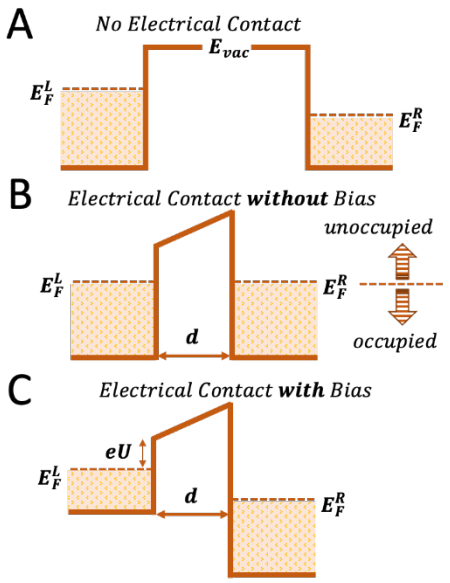

Figure 2.2. An overview of tunneling as it applies to STM. Illustrations of the Fermi and vacuum level positions for two metals separated by distance *d*. **(A)** Isolated metals. **(B)** After electrical contact, in the absence of an applied bias. **(C)** Biasing shifts the relative positions of the Fermi levels and makes available unoccupied states in an energy window eU into which electrons can tunnel.

$$I \propto e^{-2kd} \qquad (6)$$

where k is

$$k^2 = \frac{2m}{\hbar^2}(eU_b - E) \quad (7)$$

and eU_b is the barrier height and E is the energy state from which tunneling occurs; thus when the metals are brought in close enough current will be detected. These tunneling currents are on the order of nano amps or less, and as per Equation 6, the sensitivity of the tunneling current to distance allows for sub angstrom resolution.

A central component of STM is an atomically sharp probe tip typically made from W or a Pt/Ir alloy that is moved by three perpendicular piezoelectric transducers (typically labeled in cartesian coordinates). The transducers expand and contract when a voltage is applied allowing the tip to scan the xy plane/surface of the crystal (Figure 2.3). There is also a coarse move option in the z direction that can macroscopically move the tip towards or away from the crystal face. Though, the z piezo is responsible for the fine adjustment of moving the tip and sample within angstroms of each other.

Once sufficiently approached, the electron wavefunction of the tip overlaps with the wavefunction of the surface and a tunneling conductance is generated. A bias voltage is then applied between the tip and the sample and tunneling current is generated. The bias voltage (V) is the sample voltage, thus if $V > 0$ electrons are tunneling from the occupied sites of the tip to the empty states of the sample. While a $V < 0$ means the electrons are tunneling from the occupied sample states to the unoccupied states of the tip.

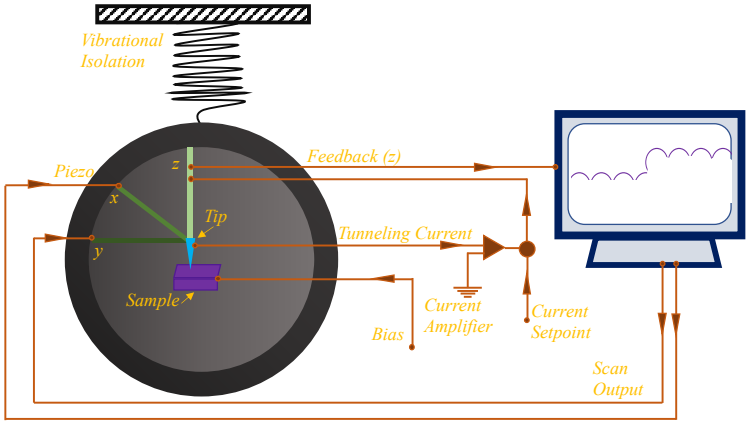

Figure 2.3 The essential components of a scanning tunneling microscope.

The tunneling is converted to a voltage by a current amplifier that is compared with a reference value to provide feedback to the tip. If the absolute tunneling current is greater than the reference value, the voltage applied to the z piezo will withdraw the tip from the sample and vice versa. As the tip traverses the surface, a 2D array of equilibrium z positions forms representing a contour plot of equal tunneling current. The topography of the surface is displayed: depressions with low z values and protrusions with high z values, providing a visual representation of the crystal surface. Therefore, STM does not actually image atoms, it images electronic states.

Because of the sensitivity of this technique, experiments are often run below 100 K. Low temperature STM (LT-STM) is commonly used for its better signal to noise ratio than room temperature instruments, and other effects like superconducting or the Kondo effect are also minimized. (31)

Additionally, manipulation of atoms or especially high resolution imaging can be more easily realized at low temperatures.[4] While the benefits of low temperature imaging are plentiful, these temperatures are often achieved with liquid nitrogen or helium which can be expensive to maintain.

2.3 The Infinity STM

I was responsible for the installation and initial setup of the prototype Infinity STM by Scienta Omicron (Figure 2.4). This instrument is uniquely designed to use a closed-cycle compression of liquid helium to cool the STM head, recycling the same volume of helium without the need for refilling a dewar.

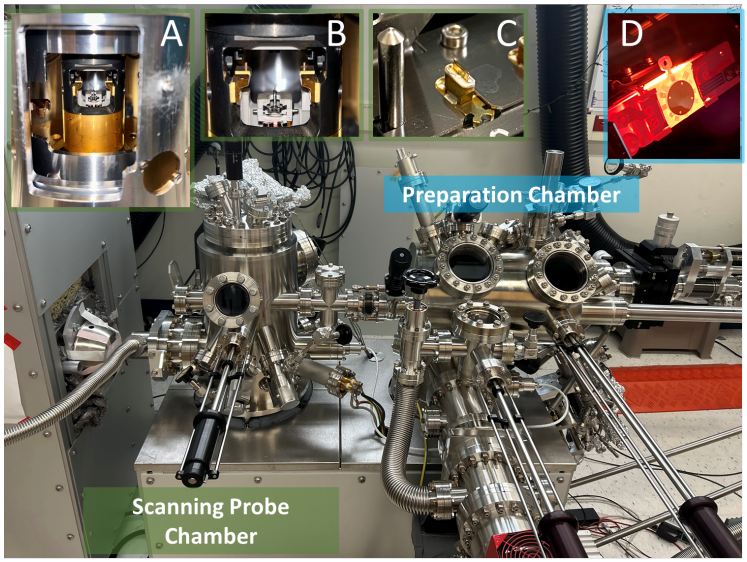

Figure 2.4 The Infinity STM. The Infinity is divided into two chambers: the scanning probe chamber which hosts the STM head **(A)** which can host either etched W STM tips **(B)** or q-plus AFM cantilevers **(C).** The preparation chamber is where sample cleaning and annealing take place specifically on the manipulator at the back of the chamber **(D).**

The Infinity STM consists of two distinct chambers separated by a small manual VAT gate valve. The preparation chamber is dedicated to sample cleaning and preparation and is equipped with both a RBD hot filament sputter gun and an Omicron Cold Cathode sputter gun. These sputter guns are positioned to enable perpendicular bombardment of the sample surface. This is facilitated by a manipulator located at the rear of the preparation chamber. The manipulator can hold both a sample plate and a tip holder, allowing for treatment of both prior to imaging. The manipulator offers precise movement of the sample in the X, Y, Z, and θ directions, ensuring optimal positioning for various experimental preparations. It also houses a Pyrolytic Boron Nitride heater capable of annealing samples to temperatures up to 1000 K. Additionally, the chamber is equipped with high-precision leak valves and e-beam evaporation sources for introducing gas-phase adsorbates and metal dopants to the system.

The preparation chamber is pumped by both an ion pump and a turbomolecular pump, which can be isolated using a large gate valve. New samples are introduced via a load lock that is isolated from the main chamber by a small gate valve. This load lock can be differentially pumped by the turbo pump before opening to allow introduction of new samples or tips into the chamber. Samples are transferred within the chamber using magnetic wobble sticks, which position the

samples on a central magnetic rod. From there, samples can be moved into the preparation chamber or transitioned into the scanning probe chamber. They can also be removed from the magnetic rod and transferred to the manipulator setup for further preparation.

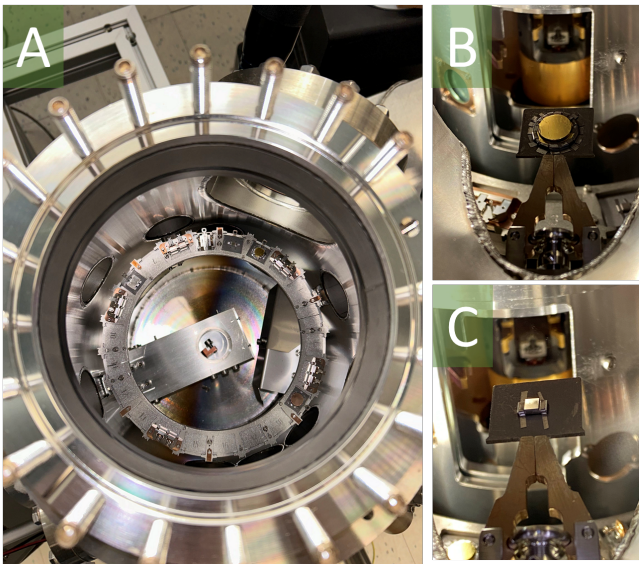

Figure 2.5 Sample and their storage in the Infinity STM. (A) Carousel of samples in the scanning chamber of the infinity. This chamber can support differently sized crystal samples **(B and C)** but care must be taken to leave a proper gap in along the edges to properly sit inside the STM head.

The scanning probe chamber is pumped solely by an ion pump unless it is open to the preparation chamber. This chamber houses a carousel surrounding the central SPM head, capable of holding up to 22 samples. Specialty positions are equipped with holders for both q-plus atomic force microscopy (AFM) and STM tips. Samples must be mounted on specialized Ta plates that are securely adhered to the crystal surface, as the plate must be inverted when introduced to the SPM head (note: the tip is located beneath the sample holder) (Figure 2.5).

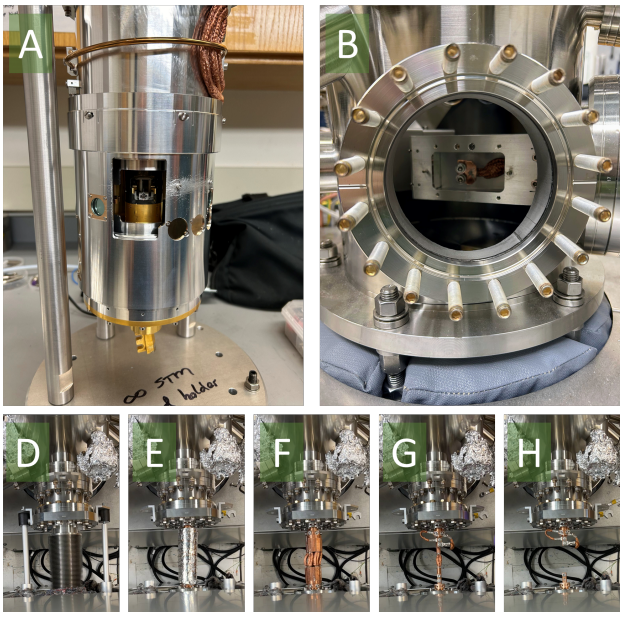

Figure 2.6 The connection of the STM head to the He chiller. (A) Shows the head of the STM outside of the chamber with the two-pronged golden hooks that connect to the copper thermal braids **(B)** that sit below the carousel. There are a series of layers of connection and isolation between the He chiller box and the STM head that must be connected for cooling and disconnected for maintenance and baking. Starting with protective bellows and support bars **(D)**, thin aluminum insulation **(E)**, the first external layer of copper braids **(F)**, the internal cooling braids **(G)** and finally complete isolation **(H).**

The SPM head is continuously cooled by liquid helium and, with the cold shields in place, can achieve minimum sample temperatures of approximately 11 K. Thermal contact is established by connecting the gold-colored hooks at the bottom of the SPM head to copper feedthroughs, which are directly linked to the chiller box (Figure 2.6). Proper contact between the SPM head and the chiller box is critical in determining the minimum achievable temperature. Hence, ensuring good thermal contact and isolating the copper braids effectively is essential for efficient cooling.

2.4 Temperature Programmed Desorption

The desorption of adsorbed atoms and molecules is one of the fundamental surface kinetic processes that can provide important information about interactions between a surface and the adsorbed species. Temperature programmed desorption (TPD) is a technique where a linear temperature ramp is applied to a sample and the rate of molecular desorption is monitored by tracking the amount of desorbed species in the gas phase as a function of time. Thus, this technique is a useful way of studying reaction kinetics.

A typical experimental set up requires a method of sample heating where heating rate is linear with respect to time. Usually this calls for resistive heating where an electric current is passed through thin support wires that are spot welded or otherwise in contact with the sample. The wires heat the sample via conduction and temperature is measured by a thermocouple attached similarly to the sample. Then to measure the rate of desorption, a quadrupole mass spectrometer is tuned to the masses of the desorbing species and positioned close to the sample. Additionally, there is often a reservoir for liquid nitrogen for cooling the sample to temperatures low enough that small amounts of reactants can adsorb to the sample. This all occurs in a UHV chamber with the sample suspended centrally, see Figure 2.7A.

Desorption rate is directly proportional to the measured increase in background pressure. This thermal desorption follows the Arrhenius equation

$$k_d = Ae^{(-E_d/RT)} \qquad (8)$$

Where k_d is the rate constant, A is the pre-exponential factor, E_d is the desorption barrier, R is the gas constant and T is temperature. Thus, desorption has an exponential dependance on temperature. Combining the desorption rate with the Arrhenius equation results in the Polanyi Wigner equation which describes the

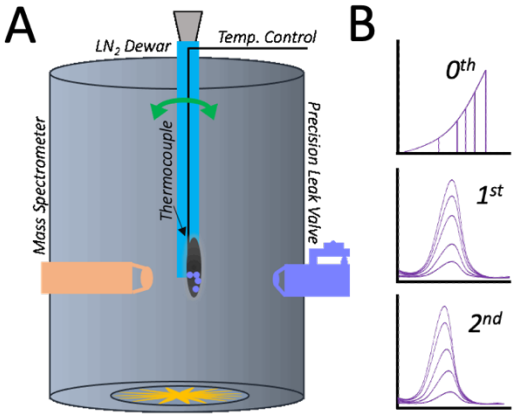

Figure 2.7. An overview of temperature programmed desorption. (A) The basic components and general set up for a TPD chamber. **(B)** The shape of desorption traces for different desorption orders.

relationship between desorption temperature and activation energy and can be rearranged to find the energy of desorption at a specific temperature.[5,6]

$$-\frac{d\Theta}{dT} = \frac{A}{\beta}\Theta^m exp\frac{-E_d}{RT} \quad (9)$$

The equation can be rearranged and is then referred to as the Redhead equation, where T_p is the maximum desorption temperature, ν is a frequency factor, and β is the heating rate (dT/dt). As previously stated, in TPD experiments a linear heating is applied to the sample, thus the ratio of E and T_p is linear in the range $10^{13} > \nu/\beta > 10^8$.[7]

$$\frac{E_d}{RT_p} = ln\left(\frac{\nu T_p}{\beta}\right) - 3.46 \qquad (10)$$

Most simply, peak shape and area under the curve can be used to determine reaction order and surface coverage. The three main types of desorption with distinct peak shapes can be seen in Figure 2.4B. A family of zeroth order desorption spectra will share the same leading edge, indicating that desorption is active at the same temperature regardless of coverage. Similarly, first order desorption is not dependent on coverages, and molecules desorb molecularly from the surface without combining with another surface molecule. In the case of second order however, atoms or molecules combine on the surface then desorb.[8]

While the Redhead analysis is the simplest of the choices for analysis, the pre-exponential factor is often assumed to be 10^{13} s^{-1}, despite a range of other values determined experimentally.[910] Other analysis methods include "complete" analysis, where ν and E_d are not assumed to be dependent on coverage, and "leading edge" analysis where the leading edge of the trace can be used to determine coverage so an Arrhenius plot can be obtained.[7] Complete and leading edge analyses are more complicated mathematically, and require very good signal to noise ratios to be effective (respectively).

2.5 References

(1) KOLASINSKI, KURT W. (Department of Chemistry, West Chester University, West Chester, PA, U. *Surface Science: Foundations of Catalysis and Nanoscience*, 3rd ed.; John Wiley & Sons, Ltd, 2012. https://doi.org/10.1002/9781119941798.

(2) Stevie, F. A.; Donley, C. L. Introduction to X-Ray Photoelectron Spectroscopy. *Journal of Vacuum Science & Technology A: Vacuum, Surfaces, and Films* **2020**, *38* (6), 063204. https://doi.org/10.1116/6.0000412.

(3) Binnig, G.; Rohrer, H. Scanning Tunneling Microscopy---from Birth to Adolescence. *Rev. Mod. Phys.* **1987**, *59* (3), 615–625. https://doi.org/10.1103/RevModPhys.59.615.

(4) Morgenstern, M.; Schwarz, A.; Schwarz, U. D. Low Temperature Scanning Probe Microscopy. In *Springer Handbook of Nanotechnology*; Bhushan, B., Ed.; Springer: Berlin, Heidelberg, 2004; pp 413–447. https://doi.org/10.1007/3-540-29838-X_14.

(5) Attard, G.; Barnes, C. *Surfaces*; Oxford Chemistry Primers, 1998.

(6) Thermal Desorption of Gases: P.A Redhead, Vacuum, 12 (4), July/Aug. 1962, 203–211. *Vacuum* **1962**, *12* (5), 274. https://doi.org/10.1016/0042-207X(62)90543-2.

(7) King, D. A. Thermal Desorption from Metal Surfaces: A Review. *Surface Science* **1975**, *47* (1), 384–402. https://doi.org/10.1016/0039-6028(75)90302-7.

(8) *Calorimetry and Thermal Methods in Catalysis*; Auroux, A., Ed.; Springer Series in Materials Science; Springer: Berlin, Heidelberg, 2013; Vol. 154. https://doi.org/10.1007/978-3-642-11954-5.

(9) Campbell, C. T.; Sellers, J. R. V. The Entropies of Adsorbed Molecules. *J. Am. Chem. Soc.* **2012**, *134* (43), 18109–18115. https://doi.org/10.1021/ja3080117.

(10) de Jong, A. M.; Niemantsverdriet, J. W. Thermal Desorption Analysis: Comparative Test of Ten Commonly Applied Procedures. *Surface Science* **1990**, *233* (3), 355–365. https://doi.org/10.1016/0039-6028(90)90649-S.

Chapter 3: Ag(111) Remains Significantly Reduced In Situ Under Simulated Ethylene Epoxidation Conditions

This chapter was modified from the following publication: Elizabeth E. Happel, Toghrul Azizli, Avery S. Daniels, Cole Easton, Adrian Hunt, Phillip Christopher, Iradwikanari Waluyo, Matthew M. Montemore, and E. Charles H. Sykes. Ag(111) Remains Significantly Reduced In Situ Under Simulated Ethylene Epoxidation Conditions. *Submitted JPCL* ***2025***

3.1 Abstract

The direct epoxidation of ethylene to ethylene oxide is among the highest value processes in the chemical industry, yet the mechanism of this reaction remains under debate. A central question concerns the state of the unpromoted Ag catalyst under reaction conditions—whether it is metallic or oxidized – as this is crucial for understanding the active oxidant species and reaction mechanism. Utilizing near-ambient pressure XPS at chemical potentials that simulate industrially relevant temperatures and pressures, we demonstrate that under purely oxidizing conditions, primarily nucleophilic oxygen (~0.8 ML) with some impurity carbonate species (~0.2 ML) form on Ag(111). However, upon switching to the industrially relevant 5:2 ethylene-to-oxygen ratio at 433 K, nucleophilic oxygen is rapidly consumed, leaving primarily surface-bound carbonate and bare Ag. Quantification of the carbonate coverage indicates that the Ag(111) surface has ~50% exposed metallic sites under simulated reaction conditions. This result indicates that proposed mechanisms involving a fully oxidized surface may not represent the state of the surface under relevant reaction conditions and that the bare Ag sites required to form the proposed oxametallacycle intermediate, thought to be responsible for selective epoxidation, are present.

3.2 Introduction

Ethylene oxide (EO) is a critical intermediate in the production of plastics, polyester, and various glycols, including ethylene glycol. The partial oxidation of ethylene to EO is among the highest-volume chemical processes in the industry, projected to reach approximately $65 billion/year by 2026.[1] This reaction exemplifies a kinetically controlled reaction, where EO is the main product despite the much greater thermodynamic stability of carbon dioxide and water.[2–4] Silver-based catalysts are primarily employed for this reaction, achieving a EO selectivity of around 50% when unpromoted. Extensive academic and industrial research has improved this selectivity to

90% through the use of promoters such as Cl, Re, and Cs.[2,5,6] Importantly, the nature of adsorbed oxygen on silver has been shown to significantly influence selectivity to EO.[7,8]

X-ray photoelectron spectroscopy (XPS) studies have identified two primary oxygen species on Ag: electrophilic and nucleophilic.[8–14] It is generally accepted that electrophilic oxygen predominates on Ag at lower temperatures and pressures, while nucleophilic oxygen forms at higher temperatures and pressures.[10,13,15–19] Both species were widely believed to be comprised of oxygen atoms with different coordination sites that lead to differing selectivities for EO formation. For instance, Bukhtiyarov et al. examined silver foils with surfaces that were oxidized using isotopically labeled temperature-programmed reaction (TPR) experiments and suggested that only electrophilic oxygen contributes to EO formation, while both electrophilic and nucleophilic oxygen generate CO_2.[20]

However, other work has suggested that O2 is responsible for EO formation. For instance, some of the earliest studies by Campbell and coworkers indicated that low coverage molecular O_2 is involved in the rate limiting step on a Ag(110) surface.[2,21] Later investigations instead suggested that more fully oxidized silver catalysts are essential for EO production.[22,23] Studies by Linic and Barteau showed evidence for an oxametallacycle (OMC) intermediate in which ethylene is bound to bare Ag and an O atom, suggesting that the OMC formation requires both bare Ag and O sites.[24–26]

In situ studies of the ethylene epoxidation mechanism have garnered increased interest. Guo et al. utilized near-ambient pressure x-ray photoelectron spectroscopy to characterize oxygen species present under near-ambient pressures of ethylene and oxygen, identifying several distinct oxygen species which were assigned as surface lattice oxygen, dioxygen oxygen, and subsurface oxygen species.[27] Most recently, investigations by Wachs, Flaherty, and others employing in situ Raman and XPS in conjunction with DFT have suggested that dioxygen oxygen or O_2-like species may be the active species for ethylene epoxidation.[28–31] These studies also suggest that while Ag surfaces may have high O coverages in purely oxidizing conditions there is a significant drop in this coverage once reductants like ethylene are present.

Nevertheless, the precise chemical state of silver under reaction conditions and the extent of surface oxidation remain open questions. While single crystal studies offer the ability to more

easily quantify the type and amount of surface oxygen, the difficulty in oxidizing Ag(111), which has a dissociative sticking probability of ~$5x10^{-6}$, has led to studies focusing on oxidizing conditions.[32] However, ethylene is a reductant and given that ethylene epoxidation is industrially performed in an ethylene-rich environment with ethylene:oxygen ratios of ~ 5:2, it is important to study the state of the Ag surface under this balance of oxidizing and reducing reactants.[33,34] Herein we demonstrate that at temperatures and pressures to simulate industrial conditions, ~80% of the Ag surface is oxidized under 0.2 Torr oxygen and 433 K, whereas when ethylene is introduced at a 5:2 ratio, the surface becomes reduced and is composed of bare Ag sites and surface-bound carbonate.

3.3 Results and Discussion

While AP-XPS cannot reach industrial pressures, one can study the adsorbates at the same chemical potential as Ag nanoparticle catalysts by working at a lower temperature that should yield equivalent surface coverages of the adsorbates at steady state. Here, we use 433 K to match the surface chemical potential of O/Ag at simulated reactor conditions (513 K, 0.1 Bar). Therefore, to characterize Ag(111) in a purely oxidizing environment, we first saturated the Ag(111) crystal with oxygen at 0.2 Torr and 433 K. After equilibration, the primary species observed was nucleophilic oxygen, with a binding energy around 528.4 eV (Fig. 3.1A). This species is often associated with the p(4x4) reconstruction on Ag(111) and this type of nucleophilic oxygen is generally thought to favor total combustion.[13,18,19] Additionally, a higher binding energy feature around 530.2 eV was detected, which can be attributed to either electrophilic oxygen or carbonate impurities.[10,15–17] Given the significant overlap in the binding energies of electrophilic oxygen and carbonate oxygen, we used C 1s spectra to quantify the amount of oxygen associated with carbonate vs. surface oxygen. As mentioned, the ~288.1 eV peak in the C 1s spectra is associated with carbonate and given the 3:1 ratio of oxygen to carbon in carbonate, our analysis (see appendix) indicates that the primary oxygen species resulting in a 530.2 eV feature is carbonate. Thus, under these conditions, assuming surface saturation as 0.375 monolayer (ML) in agreement with the saturation coverage of the p(4x4) reconstruction, ~17% of the surface is covered by carbonate and ~77% by nucleophilic oxygen, while ~6% of the surface remains bare. While there is not a deliberate addition of carbon to the gas environment, it is known that AP-XPS chambers in user facilities typically have a residual background pressure

of carbon-containing contaminants, which when oxygen is present, leads to the buildup of carbonate on otherwise clean surfaces.[35–37]

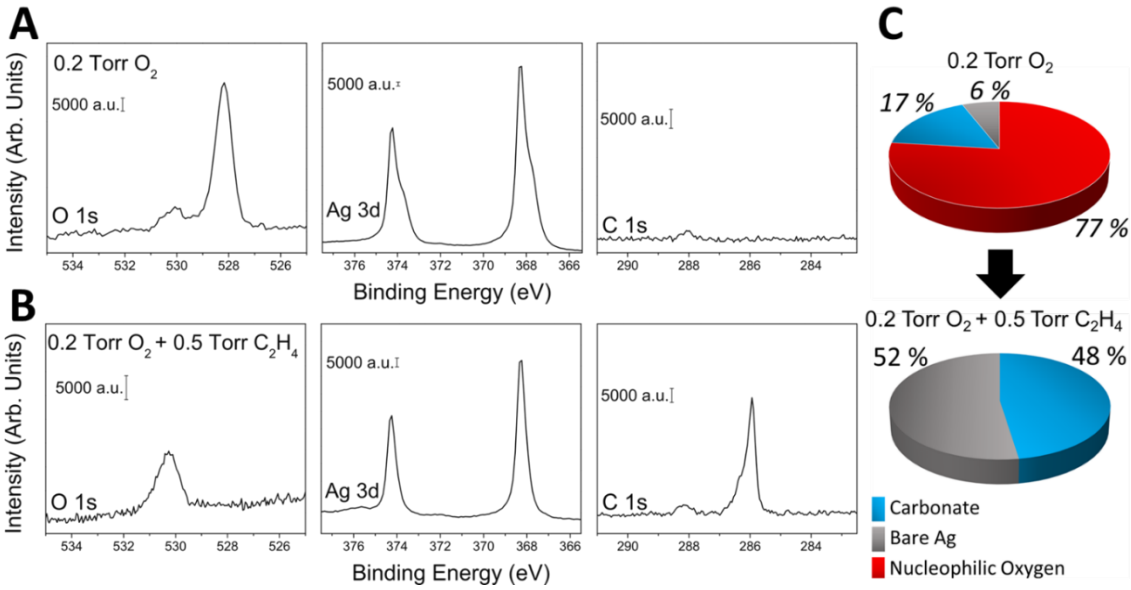

Figures 3.1. AP-XPS spectra showing surface species on Ag(111) in oxidizing vs. epoxidation conditions. C 1s, O 1s, and Ag 3d spectra of Ag(111) under **(A)** 0.2 Torr O_2 at 433 K and **(B)** 0.2 Torr O_2 and 0.5 Torr C_2H_4 at 433 K. The C 1s and Ag 3d spectra were taken at 500 eV and O 1s at 760 eV photon energies. Ag 3d were also corrected for the lower electron inelastic mean free path (IMFP) at higher background pressures (see appendix for additional fits of Ag $3d_{5/2}$ spectra). **(C)** shows the surface composition at 0.2 Torr oxygen followed by the composition at 0.2 Torr O_2 and 0.5 Torr C_2H_4.

Upon the introduction of 0.5 Torr of ethylene to the existing 0.2 Torr oxygen, a distinct gas phase ethylene feature appears at ~286 eV in the C 1s spectra (Fig 3.2B) and the coverage of nucleophilic oxygen decreases to zero as seen in Fig. 3.2A. It is also apparent from these XPS spectra that the total oxygen coverage decreases to ~50% and by quantifying the oxygen-to-carbon ratios we find that all of this oxygen is associated with carbonate species which appears at a binding energy of ~ 530.4 eV.[10,38] Notably, upon ethylene introduction, the carbonate coverage increases from 0.2 ML to 0.5 ML, in agreement with previous reports of carbonate formation under ethylene epoxidation conditions, which is often considered to be a spectator in the reaction.[35,37–39]

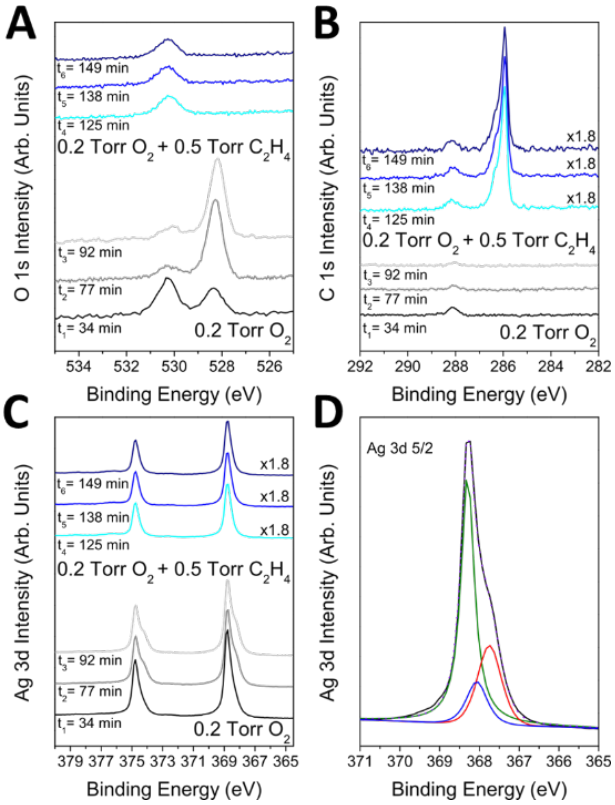

Figure 3.2. Equilibration of Ag(111) upon changing from purely oxidizing to simulated epoxidation conditions. The equilibration of O 1s, C 1s, and Ag 3d spectra over time are shown in (A), (B), and (C) respectively after initial equilibration of Ag(111) under 0.2 Torr oxygen and then with the simultaneous introduction of 0.5 Torr of ethylene to the environment at 433 K. (D) Fitted Ag $3d_{5/2}$ spectra after 92 min in 0.2 Torr oxygen at 433 K with the distinct shoulder at higher binding energy (red) assigned to an oxygen-induced Ag reconstruction and Ag in furrows below oxygen (blue).[40] Where noted, XPS peak intensity was corrected for the lower inelastic mean free path at increased chamber pressure.

Further investigation of the surface species present under simulated epoxidation reaction conditions was conducted by measuring the Ag 3d spectra. Under purely oxidizing conditions (0.2 Torr O_2), a lower binding energy shoulder at ~ 367.8 eV in the Ag 3d spectra was observed (Fig. 3.2). While oxide formation on Ag surfaces (i.e. Ag_2O) results in a shift to lower BEs (~ 367.3 eV), the binding energy of this shoulder at ~ 367.8 eV corresponds to the formation of a reconstructed surface oxide layer, such as the p(4x4) structure that is often associated with nucleophilic oxygen on Ag(111). [40,41] Thus, even under these purely oxidizing conditions at 433 K, the silver surface is reconstructed, but is never fully oxidized.

It is clear from Fig 3.2 that when ethylene is introduced to Ag(111) under 0.2 Torr oxygen, the nucleophilic oxygen is rapidly consumed and the Ag 3d spectra return to the same shape and BE as metallic Ag(111) with some carbonate (Fig A3.1). Specifically, low coverages of carbonate can lead to a small shoulder to Ag 3d spectra offset by only ~0.2 eV from the metallic peak.[37,38,42] The simultaneous loss of both nucleophilic oxygen species in the O 1s spectra and the reconstructed Ag shoulder of the Ag 3d spectra further confirms the assignment of this shoulder to a surface reconstruction like the p(4x4) associated with nucleophilic oxygen. Both shoulders associated with carbonate and nucleophilic oxygen always remain distinct from bulk oxide formation. Quantification of the carbonate coverage reveals that under simulated conditions with the industrially relevant 5:2 ethylene to oxygen ratio, the Ag surface is ~50% metallic with ~50% covered by carbonate. This is consistent with DFT which predicts saturation of carbonate on Ag(111) as ~67% coverage with respect to the known 0.375 ML saturation coverage of the p(4x4) reconstruction, this suggests under reaction conditions there are bare Ag sites available (see appendix for more on stability of carbonate coverages).

Table 3.1. The Effect of Temperature on Surface Coverage Under Reaction Conditions.

	Coverage, ML			
	Electrophilic Oxygen	**Nucleophilic Oxygen**	**Carbonate**	**Bare Ag**
0.2 Torr O_2 + 0.5 Torr C_2H_4 *418 K*	0.0 ±0.05	0.0 ±0.05	0.2 ±0.05	0.7 ±0.05
0.2 Torr O_2 + 0.5 Torr C_2H_4 *433 K*	0.0 ±0.05	0.0 ±0.05	0.5 ±0.05	0.5 ±0.05
0.2 Torr O_2 + 0.5 Torr C_2H_4 *463 K*	0.0 ±0.05	0.0 ±0.05	0.3 ±0.05	0.6 ±0.05

To account for differences in the exact surface chemical potential between our model studies and EO reaction conditions, we varied the surface temperature both above and below 433 K (Fig A3.2). Specifically, we performed experiments at 418 K (calculated to be +0.04 eV in chemical potential, relative to 433 K) and 463 K (-0.08 eV in chemical potential relative to 433 K). The thermodynamic modelling, which interpolates between experimental entropies and enthalpies, is expected to be more accurate than these variations. While temperature notably affects the distribution of oxygen species, the Ag consistently remains reduced (Table 3.1). Both higher and lower temperatures result in decreased carbonate coverages. Despite these increases, the total oxygen coverage remains low, and the Ag 3d spectra consistently indicate a metallic state.

To test whether DFT calculations are consistent with a metallic, carbonate-covered Ag surface being more stable than an oxidized surface under simulated reaction conditions, we constructed a phase diagram using ab initio atomistic thermodynamics as shown in Figure 3.3. This phase diagram is consistent with previous studies comparing the p-(4x4) reconstruction to adsorbed O and bare Ag.[46–48] Figure 3.3 shows that the DFT results are consistent with the experiment in that metallic Ag with carbonate is more stable than the p-(4x4) oxygen reconstruction under these experimental conditions.

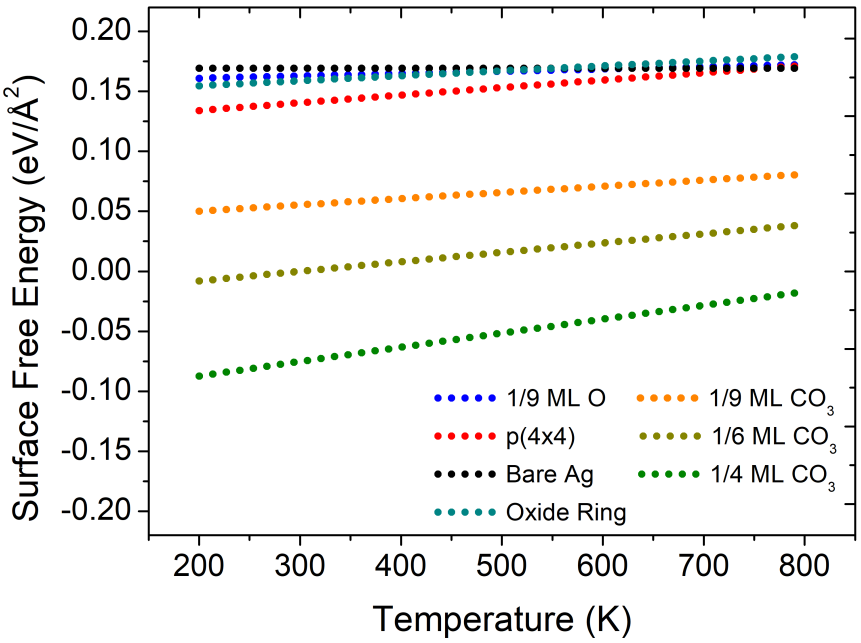

Figure 3.3. DFT-calculated phase diagram showing the stability of a metallic, carbonate-covered Ag surface under simulated reaction conditions. Surface free energies for bare Ag(111), O/Ag(111) at 1/9 ML, the p(4x4) reconstruction, and CO_3/Ag(111) at three different coverages. Conditions: pO_2 = 0.2 Torr, pC_2H_4 = 0.5 Torr, pH_2O = 0.01.

To test whether DFT-calculated energetics are consistent with a metallic, carbonate-covered Ag surface being more stable than an oxidized surface under simulated reaction conditions, we constructed a phase diagram using ab initio atomistic thermodynamics as shown in Figure 3.3. Our results are consistent with previous studies comparing the p(4x4) reconstruction to adsorbed O and bare Ag.[43–45] The DFT predictions are consistent with the experimental results in that

metallic Ag with carbonate is more stable than the p(4x4) oxygen reconstruction under these experimental conditions (see Figure 3.3).

3.4 Conclusion

This work demonstrates that under purely oxidizing conditions and at a chemical potential that is equivalent to that of the oxygen partial pressure and temperature of simulated industrial EO synthesis conditions, nucleophilic oxygen is the dominant species, consistent with an oxygen-induced Ag reconstruction, such as the p(4x4) structure. This nucleophilic oxygen coverage constitutes approximately 80% of a monolayer, leaving a small portion of exposed metallic silver. In contrast, upon the introduction of ethylene at the industrial oxygen:ethylene ratio, nucleophilic oxygen is rapidly consumed, resulting in a reduced Ag surface with only carbonate species that occupies approximately 50% of the Ag(111) surface. Together, these results indicate that at industrially relevant reactant ratios, ethylene acts as a powerful reductant, quickly consuming nucleophilic oxygen and leaving only carbonate on the otherwise bare metallic Ag surface. This suggests that mechanistic models of ethylene epoxidation on Ag should not assume the surface is fully oxidized; rather metallic Ag sites and carbonate appear to dominate the surface. Future studies are aimed at exploring the effect of common ethylene epoxidation promotors on the state of Ag.

3.5 References

(1) *Global Ethylene Oxide Market - Forecast from 2021 to 2026*; 2021.
(2) Pu, T.; Tian, H.; Ford, M. E.; Rangarajan, S.; Wachs, I. E. Overview of Selective Oxidation of Ethylene to Ethylene Oxide by Ag Catalysts. *ACS Catalysis* **2019**, 10727–10750. https://doi.org/10.1021/acscatal.9b03443.
(3) Michaelides, A.; Reuter, K.; Scheffler, M. When Seeing Is Not Believing: Oxygen on Ag(111), a Simple Adsorption System? *Journal of Vacuum Science & Technology A: Vacuum, Surfaces, and Films* **2005**, *23* (6), 1487–1497. https://doi.org/10.1116/1.2049302.
(4) Grant, R. B.; Lambert, R. M. A Single Crystal Study of the Silver-Catalysed Selective Oxidation and Total Oxidation of Ethylene. *Journal of Catalysis* **1985**, *92* (2), 364–375. https://doi.org/10.1016/0021-9517(85)90270-2.
(5) Hwang, A.; Klaucke, J.; Lizandara-Pueyo, C.; Karpov, A.; Iglesia, E. Roles of Re and Cs Promoters and Organochlorine Moderators in the Synthesis of Ethylene Oxide on Ag-Based Catalysts. *ChemCatChem* **2023**. https://doi.org/10.1002/cctc.202301369.
(6) Diao, W.; Digiulio, C. D.; Schaal, M. T.; Ma, S.; Monnier, J. R. An Investigation on the Role of Re as a Promoter in Ag-Cs-Re/α-Al2O3 High-Selectivity, Ethylene Epoxidation Catalysts. *Journal of Catalysis* **2015**, *322*, 14–23. https://doi.org/10.1016/j.jcat.2014.11.007.
(7) Bukhtiyarov, V. I.; Prosvirin, I. P.; Kvon, R. I. Study of Reactivity of Oxygen States Adsorbed at a Silver Surface towards C2H4 by XPS, TPD and TPR. *Surface Science* **1994**, *320* (1), L47–L50. https://doi.org/10.1016/0039-6028(94)00562-1.
(8) Kaichev, V. V.; Bukhtiyarov, V. I.; Hävecker, M.; Knop-Gercke, A.; Mayer, R. W.; Schlögl, R. The Nature of Electrophilic and Nucleophilic Oxygen Adsorbed on Silver. *Kinetics and Catalysis* **2003**, *44* (3), 471–480.
(9) Force, E. The Relationship of Adsorbed Species Observed by Infrared Spectroscopy to the Mechanism of Ethylene Oxidation over Silver. *Journal of Catalysis* **1975**, *40* (3), 356–371. https://doi.org/10.1016/0021-9517(75)90267-5.
(10) Bukhtiyarov, V. I.; Nizovskii, A. I.; Bluhm, H.; Hävecker, M.; Kleimenov, E.; Knop-Gericke, A.; Schlögl, R. Combined in Situ XPS and PTRMS Study of Ethylene Epoxidation over Silver. *Journal of Catalysis* **2006**, *238* (2), 260–269. https://doi.org/10.1016/j.jcat.2005.11.043.
(11) Carbonio, E. A.; Rocha, T. C. R.; Klyushin, A. Yu.; Píš, I.; Magnano, E.; Nappini, S.; Piccinin, S.; Knop-Gericke, A.; Schlögl, R.; Jones, T. E. Are Multiple Oxygen Species Selective in Ethylene Epoxidation on Silver? *Chem. Sci.* **2018**, *9* (4), 990–998. https://doi.org/10.1039/C7SC04728B.
(12) Jones, T. E.; Wyrwich, R.; Böcklein, S.; Carbonio, E. A.; Greiner, M. T.; Klyushin, A. Yu.; Moritz, W.; Locatelli, A.; Menteş, T. O.; Niño, M. A.; Knop-Gericke, A.; Schlögl, R.; Günther, S.; Wintterlin, J.; Piccinin, S. The Selective Species in Ethylene Epoxidation on Silver. *ACS Catal.* **2018**, *8* (5), 3844–3852. https://doi.org/10.1021/acscatal.8b00660.
(13) Stegelmann, C.; Schiødt, N. C.; Campbell, C. T.; Stoltze, P. Microkinetic Modeling of Ethylene Oxidation over Silver. *Journal of Catalysis* **2004**, *221* (2), 630–649. https://doi.org/10.1016/j.jcat.2003.10.004.
(14) Campbell, C. T.; Koel, B. E. Chlorine Promotion of Selective Ethylene Oxidation over Ag(110): Kinetics and Mechanism. *Journal of Catalysis* **1985**, *92*, 272–283.
(15) Campbell, C. T.; Koel, B. E. Chlorine Promotion of Selective Ethylene Oxidation over Ag(110): Kinetics and Mechanism. *Journal of Catalysis* **1985**, *92* (2), 272–283. https://doi.org/10.1016/0021-9517(85)90261-1.
(16) Force, E. L.; Bell, A. T. The Relationship of Adsorbed Species Observed by Infrared Spectroscopy to the Mechanism of Ethylene Oxidation over Silver. *Journal of Catalysis* **1975**, *40* (3), 356–371. https://doi.org/10.1016/0021-9517(75)90267-5.

(17) Kaichev, V. V.; Bukhtiyarov, V. I.; Hävecker, M.; Knop-Gercke, A.; Mayer, R. W.; Schlögl, R. The Nature of Electrophilic and Nucleophilic Oxygen Adsorbed on Silver. *Kinetics and Catalysis* **2003**, *44* (3), 432–440. https://doi.org/10.1023/A:1024459305551.
(18) Jones, T. E.; Wyrwich, R.; Böcklein, S.; Carbonio, E. A.; Greiner, M. T.; Klyushin, A. Y.; Moritz, W.; Locatelli, A.; Menteş, T. O.; Niño, M. A.; Knop-Gericke, A.; Schlögl, R.; Günther, S.; Wintterlin, J.; Piccinin, S. The Selective Species in Ethylene Epoxidation on Silver. *ACS Catalysis* **2018**, *8* (5), 3844–3852. https://doi.org/10.1021/acscatal.8b00660.
(19) Carbonio, E. A.; Rocha, T. C. R.; Klyushin, A. Y.; Píš, I.; Magnano, E.; Nappini, S.; Piccinin, S.; Knop-Gericke, A.; Schlögl, R.; Jones, T. E. Are Multiple Oxygen Species Selective in Ethylene Epoxidation on Silver? *Chemical Science* **2018**, *9* (4), 990–998. https://doi.org/10.1039/c7sc04728b.
(20) Bukhtiyarov, V. I.; Prosvirin, I. P.; Kvon, R. I. Study of Reactivity of Oxygen States Adsorbed at a Silver Surface towards C2H4 by XPS, TPD and TPR. *Surface Science* **1994**, *320* (1–2), 2–5. https://doi.org/10.1016/0039-6028(94)00562-1.
(21) Campbell, C. T.; Paffett, M. T. *Model Studies of Ethylene Epoxidation Catalyzed by the Ag(110) Surface*.
(22) van Santen, R. A.; de Groot, C. P. M. The Mechanism of Ethylene Epoxidation. *Journal of Catalysis* **1986**, *98* (2), 530–539. https://doi.org/10.1016/0021-9517(86)90341-6.
(23) Su, D. S.; Jacob, T.; Hansen, T. W.; Wang, D.; Schlögl, R.; Freitag, B.; Kujawa, S. Surface Chemistry of Ag Particles: Identification of Oxide Species by Aberration-Corrected TEM and by DFT Calculations. *Angewandte Chemie* **2008**, *120* (27), 5083–5086. https://doi.org/10.1002/ange.200800406.
(24) Linic, S.; Barteau, M. A. Construction of a Reaction Coordinate and a Microkinetic Model for Ethylene Epoxidation on Silver from DFT Calculations and Surface Science Experiments. *Journal of Catalysis* **2003**, *214* (2), 200–212. https://doi.org/10.1016/S0021-9517(02)00156-2.
(25) Ozbek, M. O.; Onal, I.; Van Santen, R. A. Effect of Surface and Oxygen Coverage on Ethylene Epoxidation. *Topics in Catalysis* **2012**, *55* (11–13), 710–717. https://doi.org/10.1007/s11244-012-9870-7.
(26) Kokalj, A.; Gava, P.; De Gironcoli, S.; Baroni, S. Activated Adsorption of Ethylene on Atomic-Oxygen-Covered Ag(100) and Ag(210): Formation of an Oxametallacycle. *Journal of Physical Chemistry C* **2008**, *112* (4), 1019–1027. https://doi.org/10.1021/jp0747961.
(27) Guo, M.; Dongfang, N.; Iannuzzi, M.; van Bokhoven, J. A.; Artiglia, L. Structure and Reactivity of Active Oxygen Species on Silver Surfaces for Ethylene Epoxidation. *ACS Catalysis* **2024**, 10234–10244. https://doi.org/10.1021/acscatal.4c01566.
(28) Ercelik, M.; Zhang, L.; Kot, P.; Kim, J.; Chae, J.; Spree, L. E.; Guo, H.; Heinrich, A. J.; Bae, Y.; Borodin, D. Characterization of an Unexpected μ 3 Adsorption of Molecular Oxygen on Ag (100) with Low-Temperature STM. **2025**, No. 100. https://doi.org/10.1021/acs.jpcc.4c06572.
(29) Pu, T.; Setiawan, A.; Lis, B. M.; Zhu, M.; Ford, M. E.; Rangarajan, S.; Wachs, I. E. Nature and Reactivity of Oxygen Species on/in Silver Catalysts during Ethylene Oxidation. *ACS Catalysis* **2022**, *12*, 4375–4381. https://doi.org/10.1021/acscatal.1c05939.
(30) Chen, C. T.; Sviripa, A.; Verma, S.; Paolucci, C.; Flaherty, D. W. Reactions of Surface Peroxides Contribute to Rates and Selectivities for C2H4 Epoxidation on Silver. *ACS Catalysis* **2025**, 1387–1398. https://doi.org/10.1021/acscatal.4c06945.
(31) Liu, C.; Wijewardena, D. P.; Sviripa, A.; Sampath, A.; Flaherty, D. W.; Paolucci, C. Computational and Experimental Insights into Reactive Forms of Oxygen Species on Dynamic Ag Surfaces under Ethylene Epoxidation Conditions. *Journal of Catalysis* **2022**, *405*, 445–461. https://doi.org/10.1016/j.jcat.2021.11.031.
(32) Campbell, T. Atomic and Molecular Oxygen Adsorption on Ag(111). *Surface Science* **1985**, *157*, 43–60.
(33) Papavassiliou, V.; Wagner, M. L.; Day, R. W. High Purity Oxygen for Ethylene Oxide Production. EP0893443A2, January 27, 1999. https://patents.google.com/patent/EP0893443A2/en (accessed 2025-06-02).

(34) Evans, W. E.; Chipman, P. I. Process for Operating the Epoxidation of Ethylene. US6717001B2, April 6, 2004. https://patents.google.com/patent/US6717001B2/en (accessed 2025-06-02).
(35) Ben Yaacov, A.; Ben David, R.; Grinter, D. C.; Held, G.; Eren, B. Identification of Adsorbed Species and Surface Chemical State on Ag(111) in the Presence of Ethylene and Oxygen Studied with Infrared and X-Ray Spectroscopies. *Physchem* **2021**, *1* (3), 259–271. https://doi.org/10.3390/physchem1030020.
(36) R. Rocha, T. C.; Oestereich, A.; V. Demidov, D.; Hävecker, M.; Zafeiratos, S.; Weinberg, G.; I. Bukhtiyarov, V.; Knop-Gericke, A.; Schlögl, R. The Silver–Oxygen System in Catalysis: New Insights by near Ambient Pressure X-Ray Photoelectron Spectroscopy. *Physical Chemistry Chemical Physics* **2012**, *14* (13), 4554–4564. https://doi.org/10.1039/C2CP22472K.
(37) Isegawa, K.; Ueda, K.; Amemiya, K.; Mase, K.; Kondoh, H. Formation and Behavior of Carbonates on Ag(110) in the Presence of Ethylene and Oxygen. *J. Phys. Chem. C* **2021**, *125* (17), 9032–9037. https://doi.org/10.1021/acs.jpcc.0c11597.
(38) Isegawa, K.; Ueda, K.; Hiwasa, S.; Amemiya, K.; Mase, K.; Kondoh, H. Formation of Carbonate on Ag(111) under Exposure to Ethylene and Oxygen Gases Evidenced by Near Ambient Pressure XPS and NEXAFS. *Chemistry Letters* **2019**, *48* (2), 159–162. https://doi.org/10.1246/cl.180891.
(39) Campbell, C. T. The Selective Epoxidation of Ethylene Catalyzed by Ag(111): A Comparison with Ag(110). *Journal of Catalysis* **1985**, *94* (2), 436–444. https://doi.org/10.1016/0021-9517(85)90208-8.
(40) Martin, N. M.; Klacar, S.; Grönbeck, H.; Knudsen, J.; Schnadt, J.; Blomberg, S.; Gustafson, J.; Lundgren, E. High-Coverage Oxygen-Induced Surface Structures on Ag(111). *J. Phys. Chem. C* **2014**, *118* (28), 15324–15331. https://doi.org/10.1021/jp504387p.
(41) Turano, M. E.; Farber, R. G.; Oskorep, E. C. N.; Rosenberg, R. A.; Killelea, D. R. Characterization of Oxygenaceous Species Formed by Exposure of Ag(111) to Atomic Oxygen. *Journal of Physical Chemistry C* **2020**, *124* (2), 1382–1389. https://doi.org/10.1021/acs.jpcc.9b09131.
(42) Knudsen, J.; Martin, N. M.; Grånäs, E.; Blomberg, S.; Gustafson, J.; Andersen, J. N.; Lundgren, E.; Klacar, S.; Hellman, A.; Grönbeck, H. Carbonate Formation on p(X4x)-O/Ag(111). *Phys. Rev. B* **2011**, *84* (11), 115430. https://doi.org/10.1103/PhysRevB.84.115430.
(43) E. Jones, T.; R. Rocha, T. C.; Knop-Gericke, A.; Stampfl, C.; Schlögl, R.; Piccinin, S. Thermodynamic and Spectroscopic Properties of Oxygen on Silver under an Oxygen Atmosphere. *Physical Chemistry Chemical Physics* **2015**, *17* (14), 9288–9312. https://doi.org/10.1039/C5CP00342C.
(44) Michaelides, A.; Bocquet, M.-L.; Sautet, P.; Alavi, A.; King, D. A. Structures and Thermodynamic Phase Transitions for Oxygen and Silver Oxide Phases on Ag{1 1 1}. *Chemical Physics Letters* **2003**, *367* (3), 344–350. https://doi.org/10.1016/S0009-2614(02)01699-8.
(45) Li, W.-X.; Stampfl, C.; Scheffler, M. Why Is a Noble Metal Catalytically Active? The Role of the O-Ag Interaction in the Function of Silver as an Oxidation Catalyst. *Phys. Rev. Lett.* **2003**, *90* (25), 256102. https://doi.org/10.1103/PhysRevLett.90.256102.

Chapter 4: Benchmarking DFT Accuracy for O 1s Binding Energies on Metal Surfaces

This chapter was modified from the following publication: Elizabeth E. Happel, E. Charles H. Sykes, and Matthew M. Montemore. Benchmarking DFT Accuracy for O 1s Binding Energies on Metal Surfaces. *Submitted JPCC* ***2025***

4.1 Abstract

X-ray photoelectron spectroscopy (XPS) is a powerful tool for probing the electronic structure and composition of materials, particularly metals and metal oxides relevant to solar cells and catalysis. Density functional theory (DFT) is often used to support XPS peak assignments, but its reliability for predicting oxygen species is not well established. Here, we compile a large dataset of experimental oxygen binding energies and evaluate corresponding DFT predictions. We find that as the binding energies of metal-bound atomic oxygen species increase, especially above ≈530 eV, there is a general decrease in accuracy of DFT predicted values. Thus, high-binding-energy atomic oxygen species, like those proposed as active for selective Ag-catalyzed epoxidation, are less well represented. The chemical nature of the oxygen species also influences accuracy, with molecularly bound species more reliably captured across the entire range of energies. These findings illustrate the limitations of DFT for interpreting XPS spectra and provide a benchmark for improving computational methods.

4.2 Introduction

X-ray photoelectron spectroscopy (XPS) is a versatile and powerful analytical technique that provides critical insights into the elemental composition, electronic structure, and chemical state of atoms within a material. Due to its high utility and generally non-destructive nature, XPS has become one of the most widely utilized tools for investigating a broad range of materials, including semiconductors, organic compounds, thin film coatings, and catalytic surfaces.[1–7] One distinguishing feature of XPS is its ability to operate under both ultra-high vacuum (UHV) and near-ambient pressure (NAP) conditions, making it ideally suited for studying surface properties under different environments.

One of the primary challenges in interpreting XPS data lies in correlating observed binding energies with specific atomic structures. Thus, while XPS yields critical insights into elemental

composition and electronic structure, interpretation often requires validation through complementary techniques.[8,9] Methods such as low-energy electron diffraction (LEED), Auger electron spectroscopy (AES), and temperature-programmed desorption (TPD) contribute valuable information on surface order, composition, and reactivity. However, each of these techniques has its own limitations; for example, LEED requires ultra-high vacuum conditions and highly ordered surfaces, restricting its use for amorphous and polycrystalline materials.[10] Furthermore, dynamic surface changes, contamination, and non-equilibrated states further complicate the interpretation of XPS spectra.[11,12]

To address these challenges, density functional theory (DFT) has emerged as an indispensable tool for linking experimental XPS results with specific structural models. By predicting core-level binding energies (BEs) based on well-defined surface structures, DFT provides a computational framework to help deconvolute the ambiguities inherent in experimental measurements.[13] However, DFT and other quantum mechanical predictions of BEs are an active area of research, and their accuracy is not always clear, particularly for oxygen.[14–20] For some classes of materials, such as polymers and molecules, there have been relatively comprehensive studies on the accuracy of binding energy predictions,[21–23] but the accuracy for O in metal systems is not clear, and some previous studies have found large errors for these systems[19,20]

Transition metal and metal oxide systems are central not only to catalytic applications, such as selective partial oxidation reactions, but also to a range of other technologies including solar cells and electronic devices. In these contexts, the synergy between experimental techniques like XPS and computational approaches such as DFT enables a more comprehensive understanding of material behavior under operational conditions. One key example of this is the investigation of oxygen species on silver surfaces for partial oxidation reactions. While extensive studies have reliably characterized nucleophilic oxygen species forming well-ordered reconstructions on Ag(111), electrophilic oxygen species remain undefined, possibly due to their more disordered nature and/or challenges in computational modeling.[24] Although silver-based systems serve as a compelling example, the insights gained from this study extend to a broader spectrum of metal/metal oxide materials.

4.3 Results and Discussion

In this work, we find a general pattern across many well-characterized surface systems: DFT performs well in predicting the binding energies of lower-energy, nucleophilic oxygen species on metals, with strong agreement between experimental and theoretical values. However, as binding energies increase, the agreement declines. The higher error, particularly above 530 eV, does not appear to be solely an artifact of binding energy, as DFT more reliably models higher binding energies of O in molecularly bound species such as CO, NO, and H_2O on metal surfaces. Understanding and addressing these limitations is essential for improving the accuracy of DFT predictions and advancing the study of catalytic surface reactions.

To test the accuracy of DFT predictions of O 1s binding energies, we first collected a dataset from previous XPS studies of adsorbed oxygen, surface oxides, and bulk oxides, all for transition metals (Table 4.1). We include 14 host metal surfaces in both BCC and FCC crystal structures. Where possible, we included references with self-consistent structural and binding energy assignments from primarily experimental techniques. Some of these structures have near-identical reported values across publications, while others show some variation, mostly within a ±0.3 eV range, depending on the X-ray source; in these circumstances the average BE of a given structure is given. A spreadsheet of these BE values is given in the Appendix, along with the DFT-relaxed structures.

Table 4.1. A summary of XPS results for well-investigated adsorbed O, surface oxide, and bulk oxide structures on transition metals

Host Metal	**Facet/Structure**	**Bulk/Surface**	**Coverage (ML)**	**Avg BE**
Au	Au_2O_3[8]	Bulk		530.1, 529.0[9,10]
	(111) 2x2	Surface	0.25	529.3[11–13]
Pt	(111) 2x2[14]	Surface	0.25	529.9[14–17]
	PtO_2[14]	Bulk		530.2[14,18,19]

Ir	(111) 2x2[20]	Surface	0.25	529.9[21–23]
	(110) 2x2[24]	Surface	~0.5	530.5[24–26]
	(100) 2x1[27]	Surface	0.5	530.6[28]
Re	ReO_2	Bulk		530.1[29]
	(0001) 2x2[30]	Surface	0.25	530.1[30–32]
	ReO_3[33]	Bulk		531.6[29,34]
Ag	(111) p(4x4)[35]	Surface	0.375	528.3[35–38]
	(111) Ag_2O[39]	Bulk		529.0[40–42]
Pd	(111) 2x2[43]	Surface	0.25	529.2[43,44]
	(110) c(2x4)[45,46]	Surface	0.5	529.3[47,48]
	Pd_5O_4[49]	Surface (over layer)		529.5[44,49–51]
	PdO[52]	Bulk		529.9[44,47,50,53]
Rh	(110) (2x1)p2mg	Surface	~0.8	530.25[54]
	(100) p(2x2)[55]	Surface	0.12-1	529.8[56]
	(100) c(2x8)[55]	Surface		528.6, 529.7[57]
Ru	(0001) 2x2[58]	Surface	0.25	529.8[59–61]
	RuO_2[62]	Bulk		529.3[63–65]
Cu	(110) 2x1[66]	Surface	0.5	530.1[66–69]
	(100) $2\sqrt{2}\times\sqrt{2}R45°$ [68]	Surface	0.5	529.9[68,70,71]
	(111) 2x2	Surface	0.25	529.7[72,73]
	(110) c(2x6)[66]	Surface	0.666	529.7[66,69]
Ni	(100) c(2x2)[74]	Surface	0.5	530.2[75–77]

Mn	Mn_2O_3	Bulk		529.9[78–80]
Ti	TiO_2[81]	Bulk		530.2[81–84]

Some of these systems listed in Table 4.1 have been very well characterized. For example, the (2×2) O structure on Pt(111) has been extensively investigated, in no small part due to its catalytic relevance. However, for some structures, like the p(4x4) O reconstruction on Ag(111), there is agreement on the general structure and binding energy, but some studies have observed multiple coexisting structures on the same sample. We have also included surfaces with more conflicting reports of saturation coverage or other structural features, like the (2x2) O structure on Cu(111). In these cases, we have assigned a coverage arbitrarily, which is needed for the DFT calculations. For further details on the data and how we chose to model the structures, see the Appendix.

There are inherent complexities that preclude complete certainty of assignments of experimental BEs in many cases. For instance, even simple assignments in the literature can be inconsistent due to factors such as sampling depth. Although XPS is considered a surface-sensitive technique, it probes multiple atomic layers, which can introduce ambiguity when distinguishing between surface and bulk species. This issue is exemplified in ReO_3, where conflicting reports suggest BEs of ≈529 and ≈531 eV, potentially reflecting contributions from both bulk and surface layers.[103,104] Such discrepancies complicate direct comparisons and necessitate careful experimental validation.

Another critical consideration in BE measurements is the spectrometer calibration method. While workfunction shifts can be corrected using valence band spectra, it is common practice to reference BEs to the well-known “adventitious carbon”. This practice, while convenient, is not always considered best practice and has been cited as a potential risk for error in reporting XPS values because carbon can exist in several forms and many compounds.[105] Consequently, minor and major differences in experimentally determined values are to be expected and systematic computational benchmarking against well-characterized reference systems can be made difficult by inconsistencies in experimental reports. Therefore, it is possible that some of the experimental

values in Table 4.1 are simply inaccurate for one of these reasons. However, by taking into account the natural variation in literature that is associated with different calibrations among other experimental inconsistencies discussed above, we expect that our data points accurately reflect accepted experimental values for these well-investigated oxygen/metal systems but should be taken with the standard cautions associated with experimental results.

We next calculated the BEs for all of the structures using DFT. We used the PBE functional and the Janak-Slater method for calculating core-level BEs, which consists of removing 0.5 electrons from the target orbital. This technique is not expected to give accurate absolute values for BEs; thus, we shifted the values based on O/Ag(111) and O/Pd(111) (see Appendix for more details). We focus on the Janak-Slater method in this work, in part because of previous work suggesting it is accurate for gas-phase species, although we compare it to other methods below.[106]

We compare the experimentally determined O 1s BEs (Table 4.1) with DFT-calculated BE values (Figure 4.1A) and observe that lower BE species (<530 eV) exhibit strong agreement between experiment and theory, with most errors less than 0.3 eV in this region. However, at higher BEs (>530 eV), the deviation between DFT and experimental values increases significantly, with many errors over 0.5 eV and several over 1 eV (Figure 4.1B). While we choose 530 eV as the cutoff for this analysis, the error in fact appears to increase relatively smoothly as the binding energy increases. This trend suggests a systematic limitation in DFT predictions for oxygen species with higher experimental BEs. Thus, DFT is not generally a reliable predictor of experimental O 1s BEs (Figure 4.1C).

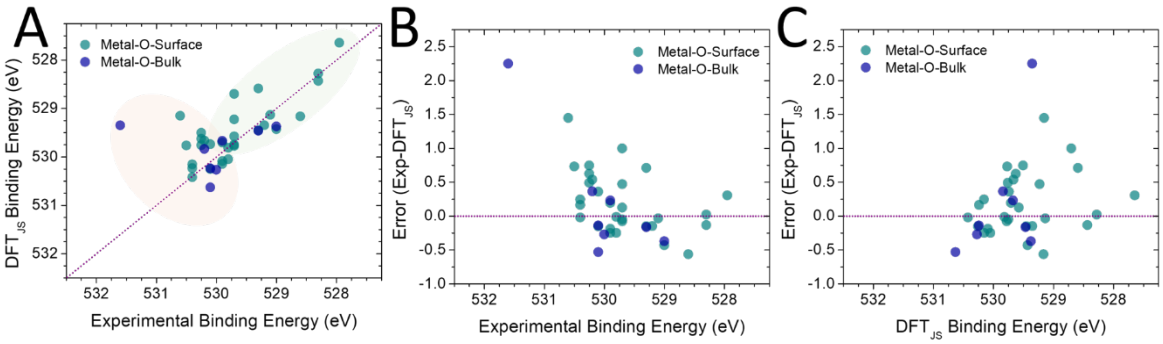

Figure 4.1. A comparison of experimental and DFT (Janak-Slater) calculated BEs for atomic oxygen systems. Plotting experimentally determined BEs against DFT predictions **(A)** reveals a decrease in accuracy as the experimental binding energy increases. The difference/error associated with these calculations **(B)** shows that the error is notably increased in the higher

binding energy range. The same error is plotted against the BEs determined by DFT **(C),** where the scatter is shifted due to the error in DFT calculated values.

Interestingly, we find that DFT accurately predicts the BEs of oxygen-containing molecular adsorbates, such as CO, even in the high-BE range (Figure 4.2). We refer to these cases as "molecularly" bound, where the O is bound to C, H, or O. This observation indicates that the discrepancies are not merely a function of BE magnitude but rather reflect fundamental differences in electronic structure

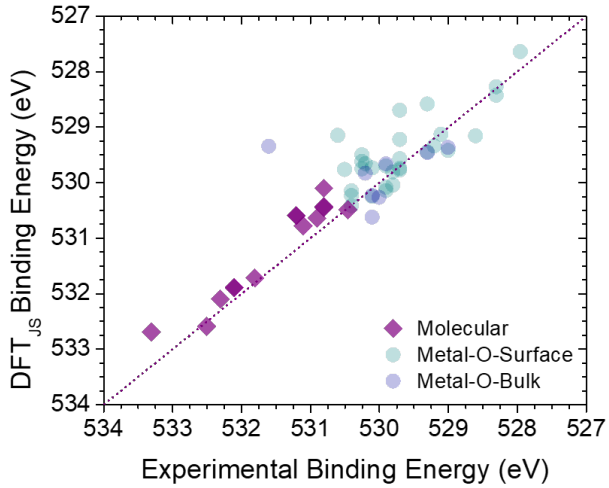

Figure 4.2. DFT predictions of BEs larger than 530 eV are more accurate for oxygen-containing molecular adsorbates on metal surfaces as compared to atomic O structures. DFT-calculated BEs vs. experimentally determined BEs for oxygen-containing molecular species (purple diamonds) and various types of atomic oxygen species (circles).

Our dataset also allows us to test the accuracy of multiple DFT BE modelling methodologies. We compared the initial state approximation, the Janak-Slate approximation, and the final-state approximation (see Supporting Information for additional details). First, it is clear that DFT predictions for molecularly bound species show consistently lower errors than for electrophilic oxygen species, as evidenced by the higher correlation (R^2) between experimental and theoretical values (Figure 4.3). This suggests that DFT's inaccuracy for high-BE species is not easily fixed by a small change to the methodology. Second, we find that the Janak-Slater approximation, which uses core-level eigenvalues after 0.5 electrons have been removed from the orbital, and the final state approximation, which uses the total energy difference between initial and final

states, give quite similar accuracies. However, the initial state approximation, which uses eigenvalues in the initial state, is less accurate. While previous studies have suggested that the initial state approximation often gives accurate trends for metal atoms' core levels, at least for a set of similar systems,[107–111] it is clearly quite inaccurate for the broad set of O 1s core levels in our dataset. We also tested two additional methodologies. The first, which we denote JS(1,0), uses the O 1s eigenvalues in the initial and final states as an alternative approximation to the Janak-Slater method.[112] The second, FS_Eigenvalue, uses the O 1s eigenvalues from the final state itself, rather than the total energy difference between initial state and final state. These are described in detail in the Methods section. Other than the initial-state approximation, all methods generally give similar R^2 values for each data subset.

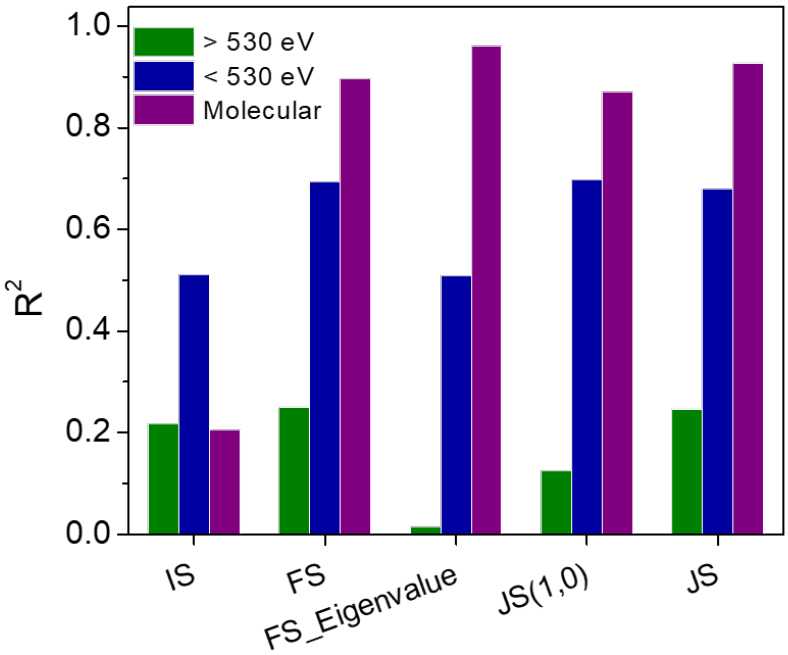

Figure 4.3. A comparison of methodologies for O1s BE calculations. R^2 values for linear fits between DFT predictions and experimental values. Across several common DFT methods the accuracy of DFT predictions for binding energies of O/metal surfaces remains similar. Apart from the initial state approximation, molecularly bound oxygen species and lower binding energy structures are more accurately predicted by these methods.

Our results raise the question of why DFT is reasonably accurate for metal-bound atomic oxygen species with BEs generally less than 530 eV and for O bound in a molecule but not for metal-

bound atomic oxygen species with increasing BEs. There are several common sources of error that are considered when addressing DFT predictions, with self-interaction error (SIE) especially of note for core-level BEs. Empirically, the SIE can be larger for O in some states than others, with O_2 and many metal oxides being cases where the SIE can lead to inaccurate total energies.[113–115] We hypothesize that SIE may also affect predicted O 1s binding energies differently for different types of systems, leading to a regime where predictions are poor. This could lead to the underestimation of experimental BEs seen in Figure 4.1, where even as experimental results yield a binding energy > 530 eV for a given species, DFT consistently predicts a lower BE. This error might have a smaller effect on reconstructed systems that tend to have lower BEs where charge may be distributed across the surface lattice, which may help mitigate some of the effects of SIE. However, there is precedent for SIE causing too much delocalization and underestimating BEs of covalent species which we do not see in our investigation.[116–118]

Therefore, development of improved functionals for predicting reaction energetics—which are based on total energies—may not necessarily improve predictions for O 1s binding energies >530 eV. This is because the core electrons are in some ways qualitatively different from the valence electrons that are the prime drivers of chemical bonding. This is in addition to the intricacy of oxygen adsorption systems, such as coverage effects and other experimental complexities.

Overall, our findings highlight the strengths and limitations of DFT in modeling core-level BEs for oxygen-metal systems. While DFT performs reasonably well for low-BE (<530 eV) oxygen and oxygen in molecular species, its accuracy decreases for high-BE (>530 eV) oxygen bound solely to metal atoms, likely due to fundamental limitations in current, commonly used exchange-correlation functionals. This could explain why previous computational studies that search for electrophilic oxygen on Ag have been unable to identify any strong candidates. This work also serves as a fundamental benchmark for future DFT investigations of the binding energies of oxygen species on metal surfaces for many research applications. Beyond this, alternative functionals or improved high-level methods should be investigated to improve the gap between experimental and computational values and optimized for better predictions going forward.

4.4 References

(1) Lee, D. W.; Yoo, B. R. Advanced Metal Oxide (Supported) Catalysts: Synthesis and Applications. *J. Ind. Eng. Chem.* **2014**, *20* (6), 3947–3959. https://doi.org/10.1016/j.jiec.2014.08.004.

(2) Huang, A.; He, Y.; Zhou, Y.; Zhou, Y.; Yang, Y.; Zhang, J.; Luo, L.; Mao, Q.; Hou, D.; Yang, J. A Review of Recent Applications of Porous Metals and Metal Oxide in Energy Storage, Sensing and Catalysis. *J. Mater. Sci.* **2019**, *54* (2), 949–973. https://doi.org/10.1007/s10853-018-2961-5.

(3) Nunes, D.; Pimentel, A.; Gonçalves, A.; Pereira, S.; Branquinho, R.; Barquinha, P.; Fortunato, E.; Martins, R. Metal Oxide Nanostructures for Sensor Applications. *Semicond. Sci. Technol.* **2019**, *34* (4), 043001. https://doi.org/10.1088/1361-6641/ab011e.

(4) Yu, X.; Marks, T. J.; Facchetti, A. Metal Oxides for Optoelectronic Applications. *Nat. Mater.* **2016**, *15* (4), 383–396. https://doi.org/10.1038/nmat4599.

(5) Danish, M. S. S.; Bhattacharya, A.; Stepanova, D.; Mikhaylov, A.; Grilli, M. L.; Khosravy, M.; Senjyu, T. A Systematic Review of Metal Oxide Applications for Energy and Environmental Sustainability. *Metals* **2020**, *10* (12), 1604. https://doi.org/10.3390/met10121604.

(6) Kumbhakar, P.; Chowde Gowda, C.; Mahapatra, P. L.; Mukherjee, M.; Malviya, K. D.; Chaker, M.; Chandra, A.; Lahiri, B.; Ajayan, P. M.; Jariwala, D.; Singh, A.; Tiwary, C. S. Emerging 2D Metal Oxides and Their Applications. *Mater. Today* **2021**, *45*, 142–168. https://doi.org/10.1016/j.mattod.2020.11.023.

(7) Chavali, M. S.; Nikolova, M. P. Metal Oxide Nanoparticles and Their Applications in Nanotechnology. *SN Appl. Sci.* **2019**, *1* (6), 607. https://doi.org/10.1007/s42452-019-0592-3.

(8) Bagus, P. S.; Ilton, E.; Nelin, C. J. Extracting Chemical Information from XPS Spectra: A Perspective. *Catal. Lett.* **2018**, *148* (7), 1785–1802. https://doi.org/10.1007/s10562-018-2417-1.

(9) A. Isaacs, M.; Davies-Jones, J.; R. Davies, P.; Guan, S.; Lee, R.; J. Morgan, D.; Palgrave, R. Advanced XPS Characterization: XPS-Based Multi-Technique Analyses for Comprehensive Understanding of Functional Materials. *Mater. Chem. Front.* **2021**, *5* (22), 7931–7963. https://doi.org/10.1039/D1QM00969A.

(10) Jagodzinski, H. Limitations of LEED-Structure Determination of Reconstructed Crystal Surfaces. *Z. Für Naturforschung A* **1982**, *37* (10), 1103–1118. https://doi.org/10.1515/zna-1982-1001.

(11) Oswald, S.; Reiche, R. Binding State Information from XPS Depth Profiling: Capabilities and Limits. *Appl. Surf. Sci.* **2001**, *179* (1), 307–315. https://doi.org/10.1016/S0169-4332(01)00299-9.

(12) Brundle, C. R.; Crist, B. V.; Bagus, P. S. Accuracy Limitations for Composition Analysis by XPS Using Relative Peak Intensities: LiF as an Example. *J. Vac. Sci. Technol. A* **2020**, *39* (1), 013202. https://doi.org/10.1116/6.0000674.

(13) Fadley, C. S. Basic Concepts of X-Ray Photoelectron Spectroscopy. In *Electron Spectroscopy: Theory, Techniques and Applications*; 1978; Vol. 2, pp 158–238.

(14) Hinsch, J. J.; Liu, J.; Wang, Y. Reinvestigating Oxygen Adsorption on Ag(111) by Using Strongly Constrained and Appropriately Normed Semi-Local Density Functional with the Revised Vydrov van Voorhis van Der Waals Force Correction. *J. Chem. Phys.* **2021**, *155* (23), 234704. https://doi.org/10.1063/5.0073407.

(15) Bajaj, A.; Kulik, H. J. Eliminating Delocalization Error to Improve Heterogeneous Catalysis Predictions with Molecular DFT + U. *J. Chem. Theory Comput.* **2022**, *18* (2), 1142–1155. https://doi.org/10.1021/acs.jctc.1c01178.

(16) Araujo, R. B.; Rodrigues, G. L. S.; dos Santos, E. C.; Pettersson, L. G. M. Adsorption Energies on Transition Metal Surfaces: Towards an Accurate and Balanced Description. *Nat. Commun.* **2022**, *13* (1), 6853. https://doi.org/10.1038/s41467-022-34507-y.

(17) Kahk, J. M.; Lischner, J. Combining the Δ-Self-Consistent-Field and GW Methods for Predicting Core Electron Binding Energies in Periodic Solids. *J. Chem. Theory Comput.* **2023**, *19* (11), 3276–3283. https://doi.org/10.1021/acs.jctc.3c00121.

(18) Li, J.; Jin, Y.; Rinke, P.; Yang, W.; Golze, D. Benchmark of GW Methods for Core-Level Binding Energies. *J. Chem. Theory Comput.* **2022**, *18* (12), 7570–7585. https://doi.org/10.1021/acs.jctc.2c00617.
(19) Zhu, T.; Chan, G. K.-L. All-Electron Gaussian-Based G0W0 for Valence and Core Excitation Energies of Periodic Systems. *J. Chem. Theory Comput.* **2021**, *17* (2), 727–741. https://doi.org/10.1021/acs.jctc.0c00704.
(20) Kahk, J. M.; Michelitsch, G. S.; Maurer, R. J.; Reuter, K.; Lischner, J. Core Electron Binding Energies in Solids from Periodic All-Electron Δ-Self-Consistent-Field Calculations. *J. Phys. Chem. Lett.* **2021**, *12* (38), 9353–9359. https://doi.org/10.1021/acs.jpclett.1c02380.
(21) Kockläuner, J.; Golze, D. GW Plus Cumulant Approach for Predicting Core-Level Shakeup Satellites in Large Molecules. *J. Chem. Theory Comput.* **2025**, *21* (6), 3101–3119. https://doi.org/10.1021/acs.jctc.4c01754.
(22) Mukatayev, I.; D'Avino, G.; Sklénard, B.; Olevano, V.; Li, J. Electronic Polarization Effects in Core-Level Spectroscopy. *Phys. Rev. B* **2024**, *109* (12), L121109. https://doi.org/10.1103/PhysRevB.109.L121109.
(23) Galleni, L.; Meulemans, A.; Sajjadian, F. S.; Singh, D. P.; Arvind, S.; Dorney, K. M.; Conard, T.; D'Avino, G.; Pourtois, G.; Escudero, D.; van Setten, M. J. Peak Broadening in Photoelectron Spectroscopy of Amorphous Polymers: The Leading Role of the Electrostatic Landscape. *J. Phys. Chem. Lett.* **2024**, *15* (3), 834–839. https://doi.org/10.1021/acs.jpclett.3c02640.
(24) Jones, T. E.; Rocha, T. C. R.; Knop-Gericke, A.; Stampfl, C.; Schlögl, R.; Piccinin, S. Insights into the Electronic Structure of the Oxygen Species Active in Alkene Epoxidation on Silver. *ACS Catal.* **2015**, *5* (10), 5846–5850. https://doi.org/10.1021/acscatal.5b01543.
(25) Shi, H.; Asahi, R.; Stampfl, C. Properties of the Gold Oxides Au 2 O 3 and Au 2 O : First-Principles Investigation. *Phys. Rev. B* **2007**, *75* (20), 205125. https://doi.org/10.1103/PhysRevB.75.205125.
(26) Min, B. K.; Alemozafar, A. R.; Pinnaduwage, D.; Deng, X.; Friend, C. M. Efficient CO Oxidation at Low Temperature on Au(111). *J. Phys. Chem. B* **2006**, *110* (40), 19833–19838. https://doi.org/10.1021/jp0616213.
(27) Stadnichenko, A. I.; Koshcheev, S. V.; Boronin, A. I. Oxidation of the Polycrystalline Gold Foil Surface and XPS Study of Oxygen States in Oxide Layers. *Mosc. Univ. Chem. Bull.* **2007**, *62* (6), 343–349. https://doi.org/10.3103/S0027131407060090.
(28) Saliba, N.; Parker, D. H.; Koel, B. E. Adsorption of Oxygen on Au(111) by Exposure to Ozone. *Surf. Sci.* **1998**, *410* (2), 270–282. https://doi.org/10.1016/S0039-6028(98)00309-4.
(29) Min, B. K.; Alemozafar, A. R.; Biener, M. M.; Biener, J.; Friend, C. M. Reaction of Au(111) with Sulfur and Oxygen: Scanning Tunneling Microscopic Study. *Top. Catal.* **2005**, *36* (1), 77–90. https://doi.org/10.1007/s11244-005-7864-4.
(30) Krozer, A.; Rodahl, M. X-Ray Photoemission Spectroscopy Study of UV/Ozone Oxidation of Au under Ultrahigh Vacuum Conditions. *J. Vac. Sci. Technol. A* **1997**, *15* (3), 1704–1709. https://doi.org/10.1116/1.580924.
(31) Miller, D. J.; Öberg, H.; Kaya, S.; Sanchez Casalongue, H.; Friebel, D.; Anniyev, T.; Ogasawara, H.; Bluhm, H.; Pettersson, L. G. M.; Nilsson, A. Oxidation of Pt(111) under Near-Ambient Conditions. *Phys. Rev. Lett.* **2011**, *107* (19), 195502. https://doi.org/10.1103/PhysRevLett.107.195502.
(32) Miller, D. J.; Öberg, H.; Näslund, L.-Å.; Anniyev, T.; Ogasawara, H.; Pettersson, L. G. M.; Nilsson, A. Low O2 Dissociation Barrier on Pt(111) Due to Adsorbate–Adsorbate Interactions. *J. Chem. Phys.* **2010**, *133* (22), 224701. https://doi.org/10.1063/1.3512618.
(33) Puglia, C.; Nilsson, A.; Hernnäs, B.; Karis, O.; Bennich, P.; Mårtensson, N. Physisorbed, Chemisorbed and Dissociated O2 on Pt(111) Studied by Different Core Level Spectroscopy Methods. *Surf. Sci.* **1995**, *342* (1), 119–133. https://doi.org/10.1016/0039-6028(95)00798-9.

(34) Parkinson, C. R.; Walker, M.; McConville, C. F. Reaction of Atomic Oxygen with a Pt(111) Surface: Chemical and Structural Determination Using XPS, CAICISS and LEED. *Surf. Sci.* **2003**, *545* (1–2), 19–33. https://doi.org/10.1016/j.susc.2003.08.029.
(35) Peuckert, M.; Bonzel, H. P. Characterization of Oxidized Platinum Surfaces by X-Ray Photoelectron Spectroscopy. *Surf. Sci.* **1984**, *145* (1), 239–259. https://doi.org/10.1016/0039-6028(84)90778-7.
(36) Vovk, E. I.; Kalinkin, A. V.; Smirnov, M. Yu.; Klembovskii, I. O.; Bukhtiyarov, V. I. XPS Study of Stability and Reactivity of Oxidized Pt Nanoparticles Supported on TiO2. *J. Phys. Chem. C* **2017**, *121* (32), 17297–17304. https://doi.org/10.1021/acs.jpcc.7b04569.
(37) Xu, Y.; Mavrikakis, M. Adsorption and Dissociation of O2 on Ir(111). *J. Chem. Phys.* **2002**, *116* (24), 10846–10853. https://doi.org/10.1063/1.1479716.
(38) Zhdan, P. A.; Boreskov, G. K.; Boronin, A. I.; Schepelin, A. P.; Withrow, S. P.; Weinberg, W. H. An XPS Investigation of CO Titration of Oxygen from an Ir(111) Surface. *Appl. Surf. Sci.* **1979**, *3* (2), 145–160. https://doi.org/10.1016/0378-5963(79)90015-1.
(39) Zhdan, P. A.; Boreskov, G. K.; Boronin, A. I.; Egelhoff, W. F.; Weinberg, W. H. An XPS Investigation of the Chemisorption of Oxygen on the Iridium (111) Surface. *Surf. Sci.* **1976**, *61* (1), 25–36. https://doi.org/10.1016/0039-6028(76)90405-2.
(40) Zhdan, P. A.; Boreskov, G. K.; Egelhoff, W. F.; Weinberg, W. H. The Application of XPS to the Determination of the Kinetics of the Co Oxidation Reaction over the Ir(111) Surface. *Surf. Sci.* **1976**, *61* (2), 377–390. https://doi.org/10.1016/0039-6028(76)90052-2.
(41) Ladas, S.; Kennou, S.; Hartmann, N.; Imbihl, R. Characterisation of the Oxygen Adsorption States on Clean and Oxidized Ir(110) Surfaces. *Surf. Sci.* **1997**, *382* (1), 49–56. https://doi.org/10.1016/S0039-6028(97)00095-2.
(42) Weststrate, C. J.; Bakker, J. W.; Rienks, E. D. L.; Martinez, J. R.; Vinod, C. P.; Lizzit, S.; Petaccia, L.; Baraldi, A.; Nieuwenhuys, B. E. Selective NH3 Oxidation on (110) and (111) Iridium Surfaces. *J. Catal.* **2005**, *235* (1), 92–102. https://doi.org/10.1016/j.jcat.2005.07.022.
(43) J. Weststrate, C.; W. Bakker, J.; L. Rienks, E. D.; P. Vinod, C.; Lizzit, S.; Petaccia, L.; Baraldi, A.; E. Nieuwenhuys, B. The Role of O Ad in the Decomposition of NH3 Adsorbed on Ir(110): A Combined TPD and High-Energy Resolution Fast XPS Study. *Phys. Chem. Chem. Phys.* **2005**, *7* (13), 2629–2634. https://doi.org/10.1039/B502350E.
(44) Ferstl, P.; Schmitt, T.; Schneider, M. A.; Hammer, L.; Michl, A.; Müller, S. Structure and Ordering of Oxygen on Unreconstructed Ir(100). *Phys. Rev. B* **2016**, *93* (23), 235406. https://doi.org/10.1103/PhysRevB.93.235406.
(45) Cao, X.; Liu, C.; Zhang, T.; Xu, Q.; Zhang, D.; Liu, X.; Jiao, H.; Wen, X.; Yang, Y.; Li, Y.; Niemantsverdriet, J. W.; Zhu, J. Revisiting Oxygen Adsorption on Ir(100). *J. Phys. Chem. C* **2022**, *126* (24), 10035–10044. https://doi.org/10.1021/acs.jpcc.2c01237.
(46) Brockawik, E.; Haber, J.; Ungier, L. Electronic Structure of Rhenium Oxides. *J. Phys. Chem. Solids* **1981**, *42* (3), 203–208. https://doi.org/10.1016/0022-3697(81)90082-2.
(47) Miniussi, E.; Hernández, E. R.; Pozzo, M.; Baraldi, A.; Vesselli, E.; Comelli, G.; Lizzit, S.; Alfé, D. Non-Local Effects on Oxygen-Induced Surface Core Level Shifts of Re(0001). *J. Phys. Chem. C* **2012**, *116* (44), 23297–23307. https://doi.org/10.1021/jp304838g.
(48) Ducros, R.; Alnot, M.; Ehrhardt, J. J.; Housley, M.; Piquard, G.; Cassuto, A. A Study of the Adsorption of Several Oxygen-Containing Molecules (O2, CO, NO, H2O) on Re(0001) by XPS, UPS and Temperature Programmed Desorption. *Surf. Sci.* **1980**, *94* (1), 154–168. https://doi.org/10.1016/0039-6028(80)90161-2.
(49) Zaera, F.; Somorjai, G. A. The Chemisorption of O2, CO, D2 and C2H4 over Epitaxially Grown Rhenium Crystalline Films. *Surf. Sci.* **1985**, *154* (1), 303–314. https://doi.org/10.1016/0039-6028(85)90367-X.
(50) Ling, S.; Mei, D.; Gutowski, M. Reactivity of Hydrogen and Methanol on (001) Surfaces of WO3, ReO3, WO3/ReO3 and ReO3/WO3. *Catal. Today* **2011**, *165* (1), 41–48. https://doi.org/10.1016/j.cattod.2011.01.017.

(51) Wei, J.; Bai, D.; Yang, L. Polymer Photovoltaic Cells with Rhenium Oxide as Anode Interlayer. *PLOS ONE* **2015**, *10* (7), e0133725. https://doi.org/10.1371/journal.pone.0133725.
(52) Michaelides, A.; Reuter, K.; Scheffler, M. When Seeing Is Not Believing: Oxygen on Ag(111), a Simple Adsorption System? *J. Vac. Sci. Technol. A* **2005**, *23* (6), 1487–1497. https://doi.org/10.1116/1.2049302.
(53) Schnadt, J.; Knudsen, J.; Hu, X. L.; Michaelides, A.; Vang, R. T.; Reuter, K.; Li, Z.; Lægsgaard, E.; Scheffler, M.; Besenbacher, F. Experimental and Theoretical Study of Oxygen Adsorption Structures on Ag(111). *Phys. Rev. B* **2009**, *80* (7), 075424. https://doi.org/10.1103/PhysRevB.80.075424.
(54) Bare, S. R.; Griffiths, K.; Lennard, W. N.; Tang, H. T. Generation of Atomic Oxygen on Ag(111) and Ag(110) Using NO2: A TPD, LEED, HREELS, XPS and NRA Study. *Surf. Sci.* **1995**, *342* (1–3), 185–198. https://doi.org/10.1016/0039-6028(95)00670-2.
(55) Bukhtiyarov, V. I.; Kaichev, V. V.; Prosvirin, I. P. Oxygen Adsorption on Ag(111): X-Ray Photoelectron Spectroscopy (XPS), Angular Dependent x-Ray Photoelectron Spectroscopy (ADXPS) and Temperature-Programmed Desorption (TPD) Studies. *J. Chem. Phys.* **1999**, *111* (5), 2169–2175. https://doi.org/10.1063/1.479488.
(56) Lan, T.; Li, C. W.; Niedziela, J. L.; Smith, H.; Abernathy, D. L.; Rossman, G. R.; Fultz, B. Anharmonic Lattice Dynamics of Ag2O Studied by Inelastic Neutron Scattering and First-Principles Molecular Dynamics Simulations. *Phys. Rev. B* **2014**, *89* (5), 054306. https://doi.org/10.1103/PhysRevB.89.054306.
(57) Hoflund, G. B.; Weaver, J. F.; Epling, W. S. Ag2O XPS Spectra. *Surf. Sci. Spectra* **1994**, *3* (2), 157–162. https://doi.org/10.1116/1.1247778.
(58) Martin, N. M.; Klacar, S.; Grönbeck, H.; Knudsen, J.; Schnadt, J.; Blomberg, S.; Gustafson, J.; Lundgren, E. High-Coverage Oxygen-Induced Surface Structures on Ag(111). *J. Phys. Chem. C* **2014**, *118* (28), 15324–15331. https://doi.org/10.1021/jp504387p.
(59) Hoflund, G. B.; Hazos, Z. F.; Salaita, G. N. Surface Characterization Study of Ag, AgO, and Ag2O Using x-Ray Photoelectron Spectroscopy and Electron Energy-Loss Spectroscopy. *Phys. Rev. B* **2000**, *62* (16), 11126–11133. https://doi.org/10.1103/PhysRevB.62.11126.
(60) Leisenberger, F. P.; Koller, G.; Sock, M.; Surnev, S.; Ramsey, M. G.; Netzer, F. P.; Klötzer, B.; Hayek, K. Surface and Subsurface Oxygen on Pd(111). *Surf. Sci.* **2000**, *445* (2–3), 380–393. https://doi.org/10.1016/S0039-6028(99)01084-5.
(61) Toyoshima, R.; Yoshida, M.; Monya, Y.; Kousa, Y.; Suzuki, K.; Abe, H.; Mun, B. S.; Mase, K.; Amemiya, K.; Kondoh, H. In Situ Ambient Pressure XPS Study of CO Oxidation Reaction on Pd(111) Surfaces. *J. Phys. Chem. C* **2012**, *116* (35), 18691–18697. https://doi.org/10.1021/jp301636u.
(62) Brena, B.; Comelli, G.; Ursella, L.; Paolucci, G. Oxygen on Pd(110): Substrate Reconstruction and Adsorbate Geometry by Tensor LEED. *Surf. Sci.* **1997**, *375* (2), 150–160. https://doi.org/10.1016/S0039-6028(96)01295-2.
(63) Tanaka, H.; Yoshinobu, J.; Kawai, M. Oxygen-Induced Reconstruction of the Pd(110) Surface: An STM Study. *Surf. Sci.* **1995**, *327* (1), L505–L509. https://doi.org/10.1016/0039-6028(95)00031-3.
(64) Titkov, A. I.; Salanov, A. N.; Koscheev, S. V.; Boronin, A. I. Mechanisms of Pd(110) Surface Reconstruction and Oxidation: XPS, LEED and TDS Study. *Surf. Sci.* **2006**, *600* (18), 4119–4125. https://doi.org/10.1016/j.susc.2006.01.131.
(65) Titkov, A. I.; Salanov, A. N.; Segrey V. Koscheev; Boronin, A. I. TDS and XPS Study of Oxygen Diffusion into Subsurface Layers of Pd(110). *React. Kinet. Catal. Lett.* **2005**, *86* (2), 371–379. https://doi.org/10.1007/s11144-005-0337-8.
(66) Lundgren, E.; Kresse, G.; Klein, C.; Borg, M.; Andersen, J. N.; De Santis, M.; Gauthier, Y.; Konvicka, C.; Schmid, M.; Varga, P. Two-Dimensional Oxide on Pd(111). *Phys. Rev. Lett.* **2002**, *88* (24), 246103. https://doi.org/10.1103/PhysRevLett.88.246103.

(67) Ketteler, G.; Ogletree, D. F.; Bluhm, H.; Liu, H.; Hebenstreit, E. L. D.; Salmeron, M. In Situ Spectroscopic Study of the Oxidation and Reduction of Pd(111). *J. Am. Chem. Soc.* **2005**, *127* (51), 18269–18273. https://doi.org/10.1021/ja055754y.
(68) Zemlyanov, D.; Aszalos-Kiss, B.; Kleimenov, E.; Teschner, D.; Zafeiratos, S.; Hävecker, M.; Knop-Gericke, A.; Schlögl, R.; Gabasch, H.; Unterberger, W.; Hayek, K.; Klötzer, B. In Situ XPS Study of Pd(111) Oxidation. Part 1: 2D Oxide Formation in 10−3mbar O2. *Surf. Sci.* **2006**, *600* (5), 983–994. https://doi.org/10.1016/j.susc.2005.12.020.
(69) Westerström, R.; Weststrate, C. J.; Gustafson, J.; Mikkelsen, A.; Schnadt, J.; Andersen, J. N.; Lundgren, E.; Seriani, N.; Mittendorfer, F.; Kresse, G.; Stierle, A. Lack of Surface Oxide Layers and Facile Bulk Oxide Formation on Pd(110). *Phys. Rev. B* **2009**, *80* (12), 125431. https://doi.org/10.1103/PhysRevB.80.125431.
(70) Peuckert, M. XPS Study on Surface and Bulk Palladium Oxide, Its Thermal Stability, and a Comparison with Other Noble Metal Oxides. *J. Phys. Chem.* **1985**, *89* (12), 2481–2486. https://doi.org/10.1021/j100258a012.
(71) Comelli, G.; Baraldi, A.; Lizzit, S.; Cocco, D.; Paolucci, G.; Rosei, R.; Kiskinova, M. Real-Time X-Ray Photoelectron Spectroscopy Study of Dissociative Oxygen Adsorption on Rh(110). *Chem. Phys. Lett.* **1996**, *261* (3), 253–260. https://doi.org/10.1016/0009-2614(96)00971-2.
(72) Gustafson, J.; Westerström, R.; Resta, A.; Mikkelsen, A.; Andersen, J. N.; Balmes, O.; Torrelles, X.; Schmid, M.; Varga, P.; Hammer, B.; Kresse, G.; Baddeley, C. J.; Lundgren, E. Structure and Catalytic Reactivity of Rh Oxides. *Catal. Today* **2009**, *145* (3), 227–235. https://doi.org/10.1016/j.cattod.2008.11.011.
(73) Fisher, G. B.; Schmieg, S. J. The Molecular and Atomic States of Oxygen Adsorbed on Rh(100): Adsorption. *J. Vac. Sci. Technol. Vac. Surf. Films* **1983**, *1* (2), 1064–1069. https://doi.org/10.1116/1.572044.
(74) Gustafson, J.; Mikkelsen, A.; Borg, M.; Andersen, J. N.; Lundgren, E.; Klein, C.; Hofer, W.; Schmid, M.; Varga, P.; Köhler, L.; Kresse, G.; Kasper, N.; Stierle, A.; Dosch, H. Structure of a Thin Oxide Film on Rh(100). *Phys. Rev. B* **2005**, *71* (11), 115442. https://doi.org/10.1103/PhysRevB.71.115442.
(75) Parrott, S. L.; Praline, G.; Koel, B. E.; White, J. M.; Taylor, T. N. Oxygen Chemisorption on a Stepped Ru (~001) Crystal. *J. Chem. Phys.* **1979**, *71* (8), 3352–3354. https://doi.org/10.1063/1.438782.
(76) Umbach, E.; Kulkarni, S.; Feulner, P.; Menzel, D. A Multimethod Study of the Adsorption of NO on Ru(001): I. XPS, UPS and XAES Measurements. *Surf. Sci.* **1979**, *88* (1), 65–94. https://doi.org/10.1016/0039-6028(79)90568-5.
(77) Shen, J. Y.; Adnot, A.; Kaliaguine, S. An ESCA Study of the Interaction of Oxygen with the Surface of Ruthenium. *Appl. Surf. Sci.* **1991**, *51* (1), 47–60. https://doi.org/10.1016/0169-4332(91)90061-N.
(78) Fuggle, J. C.; Madey, T. E.; Steinkilberg, M.; Menzel, D. Photoelectron Spectroscopic Studies of Adsorption of CO and Oxygen on Ru(001). *Surf. Sci.* **1975**, *52* (3), 521–541. https://doi.org/10.1016/0039-6028(75)90086-2.
(79) Atanasoska, Lj.; O'grady, W. E.; Atanasoski, R. T.; Pollak, F. H. The Surface Structure of RuO2: A Leed, Auger and XPS Study of the (110) and (100) Faces. *Surf. Sci.* **1988**, *202* (1), 142–166. https://doi.org/10.1016/0039-6028(88)90066-0.
(80) O'Grady, W. E.; Atanasoska, Lj.; Pollak, F. H.; Park, H. L. Single Crystal RuO2 (110): Surface Structure. *J. Electroanal. Chem. Interfacial Electrochem.* **1984**, *178* (1), 61–68. https://doi.org/10.1016/S0022-0728(84)80023-6.
(81) Madhavaram, H.; Idriss, H.; Wendt, S.; Kim, Y. D.; Knapp, M.; Over, H.; Aßmann, J.; Löffler, E.; Muhler, M. Oxidation Reactions over RuO2: A Comparative Study of the Reactivity of the (110) Single Crystal and Polycrystalline Surfaces. *J. Catal.* **2001**, *202* (2), 296–307. https://doi.org/10.1006/jcat.2001.3281.

(82) Kaga, Y.; Abe, Y.; Yanagisawa, H.; Kawamura, M.; Sasaki, K. Ru and RuO2 Thin Films by XPS. *Surf. Sci. Spectra* **1999**, *6* (1), 68–74. https://doi.org/10.1116/1.1247890.
(83) Stone, P.; Poulston, S.; Bennett, R. A.; Price, N. J.; Bowker, M. An STM, TPD and XPS Investigation of Formic Acid Adsorption on the Oxygen-Precovered c(6×2) Surface of Cu(110). *Surf. Sci.* **1998**, *418* (1), 71–83. https://doi.org/10.1016/S0039-6028(98)00683-9.
(84) Baddorf, A. P.; Wendelken, J. F. High Coverages of Oxygen on Cu(110) Investigated with XPS, LEED, and HREELS. *Surf. Sci.* **1991**, *256*, 264–271.
(85) Eren, B.; Lichtenstein, L.; Wu, C. H.; Bluhm, H.; Somorjai, G. A.; Salmeron, M. Reaction of CO with Preadsorbed Oxygen on Low-Index Copper Surfaces: An Ambient Pressure X-Ray Photoelectron Spectroscopy and Scanning Tunneling Microscopy Study. *J. Phys. Chem. C* **2015**, *119* (26), 14669–14674. https://doi.org/10.1021/jp512831f.
(86) Hashinokuchi, M.; Yoshigoe, A.; Teraoka, Y.; Okada, M. The Temperature Dependence of Cu2O Formation on a Cu(110) Surface with an Energetic O2 Molecular Beam. *J. Phys. Condens. Matter* **2012**, *24* (39), 395007. https://doi.org/10.1088/0953-8984/24/39/395007.
(87) Liu, B.-H.; Huber, M.; Van Spronsen, M. A.; Salmeron, M.; Bluhm, H. Ambient Pressure X-Ray Photoelectron Spectroscopy Study of Room-Temperature Oxygen Adsorption on Cu(1 0 0) and Cu(1 1 1). *Appl. Surf. Sci.* **2022**, *583*, 152438. https://doi.org/10.1016/j.apsusc.2022.152438.
(88) Wang, J.; Li, C.; Zhu, Y.; Boscoboinik, J. A.; Zhou, G. Insight into the Phase Transformation Pathways of Copper Oxidation: From Oxygen Chemisorption on the Clean Surface to Multilayer Bulk Oxide Growth. *J. Phys. Chem. C* **2018**, *122* (46), 26519–26527. https://doi.org/10.1021/acs.jpcc.8b09145.
(89) Shi, S.; Han, Y.; Yang, T.; Zang, Y.; Zhang, H.; Li, Y.; Liu, Z. Ambient Pressure X-ray Photoelectron Spectroscopy Study of Oxidation Phase Transitions on Cu(111) and Cu(110). *ChemPhysChem* **2023**, *24* (22), e202300543. https://doi.org/10.1002/cphc.202300543.
(90) Swallow, J. E. N.; Jones, E. S.; Head, A. R.; Gibson, J. S.; David, R. B.; Fraser, M. W.; Van Spronsen, M. A.; Xu, S.; Held, G.; Eren, B.; Weatherup, R. S. Revealing the Role of CO during CO2 Hydrogenation on Cu Surfaces with In Situ Soft X-Ray Spectroscopy. *J. Am. Chem. Soc.* **2023**, *145* (12), 6730–6740. https://doi.org/10.1021/jacs.2c12728.
(91) Fleisch, T.; Winograd, N.; Delgass, W. N. Chemisorption of Oxygen on Ni(100) by SIMS and XPS. *Surf. Sci.* **1978**, *78* (1), 141–158. https://doi.org/10.1016/0039-6028(78)90216-9.
(92) Nilsson, A.; Martensson, N. Core-Level Shake-up Spectra from Ordered C, N and O Overlayers on Ni(100). *Chem. Phys. Lett.* **1991**, *182* (2), 147–151. https://doi.org/10.1016/0009-2614(91)80119-I.
(93) Tillborg, H.; Nilsson, A.; Wiell, T.; Wassdahl, N.; Mårtensson, N.; Nordgren, J. Electronic Structure of Atomic Oxygen Adsorbed on Ni(100) and Cu(100) Studied by Soft-x-Ray Emission and Photoelectron Spectroscopies. *Phys. Rev. B* **1993**, *47* (24), 16464–16470. https://doi.org/10.1103/PhysRevB.47.16464.
(94) Benndorf, C.; Nöbl, C.; Thieme, F. Photoelectron Spectroscopic Studies of the Adsorption Geometry on Ni Single Crystals: P(2 × 2), c(2 × 2) Overlayers on Ni(100) and (2 × 1) Symmetry on Ni(110). *Surf. Sci.* **1983**, *126* (1), 265–272. https://doi.org/10.1016/0039-6028(83)90720-3.
(95) Zaki, M. I.; Hasan, M. A.; Pasupulety, L.; Kumari, K. Bulk and Surface Characteristics of Pure and Alkalized Mn2O3: TG, IR, XRD, XPS, Specific Adsorption and Redox Catalytic Studies. *New J. Chem.* **1998**, *22* (8), 875–882. https://doi.org/10.1039/A800796I.
(96) Stranick, M. A. Mn2O3 by XPS. *Surf. Sci. Spectra* **1999**, *6* (1), 39–46. https://doi.org/10.1116/1.1247889.
(97) Wagner, T.; Valbusa, D.; Bigiani, L.; Barreca, D.; Gasparotto, A.; Maccato, C. XPS Characterization of Mn2O3 Nanomaterials Functionalized with Ag and SnO2. *Surf. Sci. Spectra* **2020**, *27* (2), 024004. https://doi.org/10.1116/6.0000331.
(98) Perron, H.; Vandenborre, J.; Domain, C.; Drot, R.; Roques, J.; Simoni, E.; Ehrhardt, J.-J.; Catalette, H. Combined Investigation of Water Sorption on TiO2 Rutile (110) Single Crystal Face: XPS vs. Periodic DFT. *Surf. Sci.* **2007**, *601* (2), 518–527. https://doi.org/10.1016/j.susc.2006.10.015.

(99) Pang, C. L.; Lindsay, R.; Thornton, G. Structure of Clean and Adsorbate-Covered Single-Crystal Rutile TiO2 Surfaces. *Chem. Rev.* **2013**, *113* (6), 3887–3948. https://doi.org/10.1021/cr300409r.
(100) Ahmed, M. H. M.; Temperton, R. H.; O'Shea, J. N. An in Situ Exploration of Subsurface Defect Migration to a Liquid Water-Exposed Rutile TiO2(110) Surface by XPS. *Surf. Interface Anal.* **2021**, *53* (12), 1013–1019. https://doi.org/10.1002/sia.6906.
(101) Jones, R.; D'Acunto, G.; Shayesteh, P.; Rehman, F.; Schnadt, J. AP-XPS Study of Ethanol Adsorption on Rutile TiO2(110). *J. Phys. Chem. C* **2022**, *126* (39), 16894–16902. https://doi.org/10.1021/acs.jpcc.2c05389.
(102) Diebold, U.; Madey, T. E. TiO2 by XPS. *Surf. Sci. Spectra* **1996**, *4* (3), 227–231. https://doi.org/10.1116/1.1247794.
(103) de Simone, M.; Coreno, M.; Green, J. C.; McGrady, S.; Pritchard, H. Electronic Structure of ReO3Me by Variable Photon Energy Photoelectron Spectroscopy, Absorption Spectroscopy and Density Functional Calculations. *Inorg. Chem.* **2003**, *42* (6), 1908–1918. https://doi.org/10.1021/ic020547+.
(104) Falke, J. Electronic Structure of the Metallic Oxide ReO3. *Phys. Rev. B* **2021**, *103* (11). https://doi.org/10.1103/PhysRevB.103.115125.
(105) Greczynski, G.; Hultman, L. X-Ray Photoelectron Spectroscopy: Towards Reliable Binding Energy Referencing. *Prog. Mater. Sci.* **2020**, *107*, 100591. https://doi.org/10.1016/j.pmatsci.2019.100591.
(106) Pueyo Bellafont, N.; Viñes, F.; Hieringer, W.; Illas, F. Predicting Core Level Binding Energies Shifts: Suitability of the Projector Augmented Wave Approach as Implemented in VASP. *J. Comput. Chem.* **2017**, *38* (8), 518–522. https://doi.org/10.1002/jcc.24704.
(107) Mohrhusen, L.; Zhang, S.; Montemore, M. M.; Madix, R. J. Modifying the Reactivity of Single Pd Sites in a Trimetallic Sn-Pd-Ag Surface Alloy: Tuning CO Binding Strength. *Small* **2024**, *20* (48), 2405715. https://doi.org/10.1002/smll.202405715.
(108) Schnadt, J.; Knudsen, J.; Hu, X. L.; Michaelides, A.; Vang, R. T.; Reuter, K.; Li, Z.; Lægsgaard, E.; Scheffler, M.; Besenbacher, F. Experimental and Theoretical Study of Oxygen Adsorption Structures on Ag(111). *Phys. Rev. B* **2009**, *80* (7), 075424. https://doi.org/10.1103/PhysRevB.80.075424.
(109) Andersen, J. N.; Hennig, D.; Lundgren, E.; Methfessel, M.; Nyholm, R.; Scheffler, M. Surface Core-Level Shifts of Some 4d-Metal Single-Crystal Surfaces: Experiments and Ab Initio Calculations. *Phys. Rev. B* **1994**, *50* (23), 17525–17533. https://doi.org/10.1103/PhysRevB.50.17525.
(110) Linic, S.; Piao, H.; Adib, K.; Barteau, M. A. Ethylene Epoxidation on Ag: Identification of the Crucial Surface Intermediate by Experimental and Theoretical Investigation of Its Electronic Structure. *Angew. Chem. Int. Ed.* **2004**, *43* (22), 2918–2921. https://doi.org/10.1002/anie.200353584.
(111) Hafner, J. Ab-Initio Simulations of Materials Using VASP: Density-Functional Theory and Beyond. *J. Comput. Chem.* **2008**, *29* (13), 2044–2078. https://doi.org/10.1002/jcc.21057.
(112) Göransson, C.; Olovsson, W.; Abrikosov, I. A. Numerical Investigation of the Validity of the Slater-Janak Transition-State Model in Metallic Systems. *Phys. Rev. B* **2005**, *72* (13), 134203. https://doi.org/10.1103/PhysRevB.72.134203.
(113) Gómez, E. del V.; Burgos Paci, M. A.; Amaya-Roncancio, S.; Avalle, L. B.; Cecilia Gimenez, M. Adsorption and Diffusion of O Atoms on Metallic (1 0 0) Surfaces. Cluster and Periodic Slab Approaches. *Comput. Theor. Chem.* **2022**, *1208*, 113556. https://doi.org/10.1016/j.comptc.2021.113556.
(114) Posysaev, S.; Miroshnichenko, O.; Alatalo, M.; Le, D.; Rahman, T. S. Oxidation States of Binary Oxides from Data Analytics of the Electronic Structure. *Comput. Mater. Sci.* **2019**, *161*, 403–414. https://doi.org/10.1016/j.commatsci.2019.01.046.
(115) Ezeakunne, C.; Lamichhane, B.; Kattel, S. Integrating Density Functional Theory with Machine Learning for Enhanced Band Gap Prediction in Metal Oxides. *Phys. Chem. Chem. Phys.* **2025**, *27* (10), 5338–5358. https://doi.org/10.1039/D4CP03397C.

(116) Sharkas, K.; Wagle, K.; Santra, B.; Akter, S.; Zope, R. R.; Baruah, T.; Jackson, K. A.; Perdew, J. P.; Peralta, J. E. Self-Interaction Error Overbinds Water Clusters but Cancels in Structural Energy Differences. *Proc. Natl. Acad. Sci.* **2020**, *117* (21), 11283–11288. https://doi.org/10.1073/pnas.1921258117.
(117) Bao, J. L.; Gagliardi, L.; Truhlar, D. G. Self-Interaction Error in Density Functional Theory: An Appraisal. *J. Phys. Chem. Lett.* **2018**, *9* (9), 2353–2358. https://doi.org/10.1021/acs.jpclett.8b00242.
(118) Shukla, P. B.; Mishra, P.; Baruah, T.; Zope, R. R.; Jackson, K. A.; Johnson, J. K. How Do Self-Interaction Errors Associated with Stretched Bonds Affect Barrier Height Predictions? *J. Phys. Chem. A* **2023**, *127* (7), 1750–1759. https://doi.org/10.1021/acs.jpca.2c07894.

Chapter 5: Atomic-Scale Characterization of Oxygen Species on Ag(111): Insights into Electrophilic Oxygen and Epoxidation

Elizabeth E. Happel, Toghrul Azizli, Sarah Stratton, Matthew M. Montemore, and E. Charles H. Sykes

5.1 Abstract

A central question in the mechanism of ethylene epoxidation by Ag is the identity of the chemical intermediate responsible for selective epoxidation. There is literature evidence for an oxametallacycle comprised of ethylene coordinated to a single oxygen atom and the Ag surface but the structure of oxygen on Ag is known to be more complex. We directly visualize the binding of ethylene to electrophilic and nucleophilic p(4x4) oxygen, the two most common forms oxygen on Ag. While ethylene binds weakly to nucleophilic oxygen, we find oxametallacycle complexes are formed on electrophilic oxygen in which three ethylene molecules bind to each six-oxygen unit electrophilic structure.

5.2 Main Text

Silver-based catalysts have long played a central role in the industrial production of ethylene oxide, a $60 billion/year market, yet the precise nature of the active oxygen species responsible for selective epoxidation remains a subject of ongoing debate.[1] Despite decades of investigation, a consensus has yet to emerge on the atomic-scale structures of selective oxygen species on Ag surfaces. This uncertainty is largely due to the many types of weakly bound and dynamically interchangeable oxygen on Ag(111), which complicates both spectroscopic assignment and direct imaging.

Two main types of dissociated oxygen have been described in the literature for O/Ag systems: electrophilic oxygen ($O^{\delta+}$) and nucleophilic oxygen ($O^{\delta-}$). These species are distinguished by their XPS binding energies, ~530.4 eV and ~528.2 eV, respectively, and can be preferentially formed depending on temperature and oxygen coverage.[2–5] Electrophilic oxygen is widely associated with selective epoxidation, facilitating O insertion into the C=C bond of ethylene to form the epoxide, while nucleophilic oxygen is typically linked to total combustion via C–H bond scission.[2–4] Although these roles are generally accepted, the structural assignment of

electrophilic oxygen remains elusive, with hypotheses ranging from surface SO_4-like species to subsurface oxygen to molecular O_2 intermediates, which have more recently have gained support. [4,6–9]

The challenge of structural identification has spurred a wide range of theoretical studies, yet direct visualization remains scarce. Notably, discrepancies between DFT-predicted O 1s binding energies and experimental values have led to speculative assignments involving adventitious sulfur or complex oxygen aggregates. [2,10–16] These divergent interpretations complicate mechanistic understanding of ethylene epoxidation and hinder the rational design of more selective silver-based catalysts.

In this study, we combine controlled oxidation of Ag(111) using NO_2 with atomic-scale scanning tunneling microscopy (STM) imaging to directly investigate the nature of oxygen species formed over a range of temperatures.[17] Thermal control of oxygen speciation on Ag(111) is well established with lower temperature oxygen deposition being associated with electrophilic oxygen and higher temperatures with nucleophilic (Fig A5.1). We observe the formation of distinct surface oxygen structures: mobile ring-like assemblies at lower temperatures and reconstructed Ag/O phases at elevated temperatures. By exposing these structures to ethylene, we find that oxametallacycle (OMC) intermediates form on the low-temperature oxygen phase while ethylene appears more weakly bound and mobile on the nucleophilic p(4x4) reconstruction. Together our findings offer new atomic-scale insight into the elusive electrophilic oxygen species and its potential role in the selective oxidation chemistry of silver.

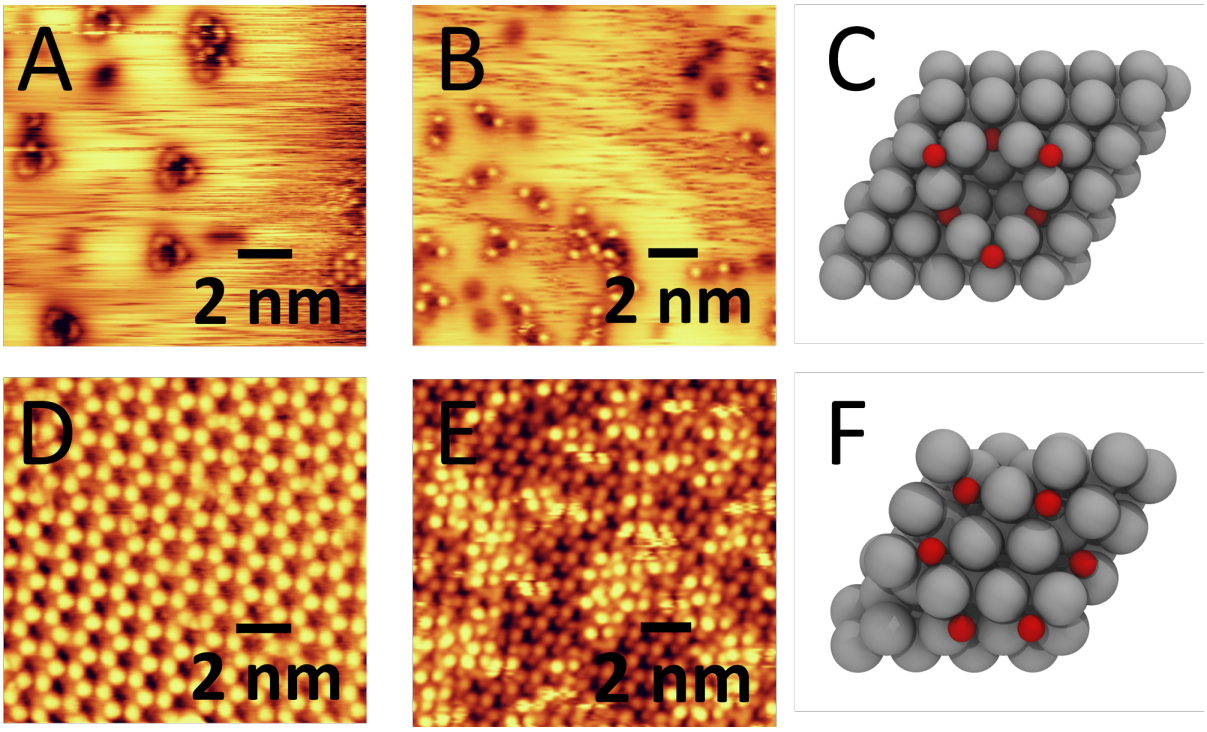

Figure 5.1. Structure of low and high temperature oxygen species on Ag(111) and their interaction with ethylene. (A) NO_2 was exposed to Ag(111) <373 K (image conditions: 0.3 nA, 50 mV) and STM images shows the formation of ring structures like what are modeled in **(C).** C_2H_4 is exposed to the same surface <23 K (0.3 nA, 50 mV) and new bright spots form on the corners of the triangular structures **(D)** Ag(111) was exposed to NO_2 between 473-523 K and a honey comb structure p(4x4) is observed (0.2 nA, 100 mV) **(E)** C_2H_4 was exposed to the same surface <23 K (0.2 nA, 100 mV) and new bright patches of ethylene molecules on top of the p(4x4) surface and observed experimentally and modeled in **(F).**

Guided by literature methods we dosed NO_2 onto Ag(111) at higher temperatures (473–523 K) and at lower temperatures (350-373 K) to attempt to distinguish these two species. Low-temperature exposure yields ordered, triangular ring-like features (Fig. 5.1A), which closely resemble the structures reported by Andryushechkin *et al*., consisting of six oxygen atoms encircling a central silver vacancy (Fig 5.1C).[18] In agreement with prior observations, three lobed features align with the close packed direction of the Ag(111) crystal. At higher temperatures, we observe the well-known *p*(4×4) reconstruction (Fig. 5.1D), commonly attributed to nucleophilic oxygen species. Notably, the triangular structures persist above NO desorption temperatures and coexist with the p(4x4), indicating that NO_2 can serve as an effective atomic oxygen precursor for both species (Fig. A5.2).

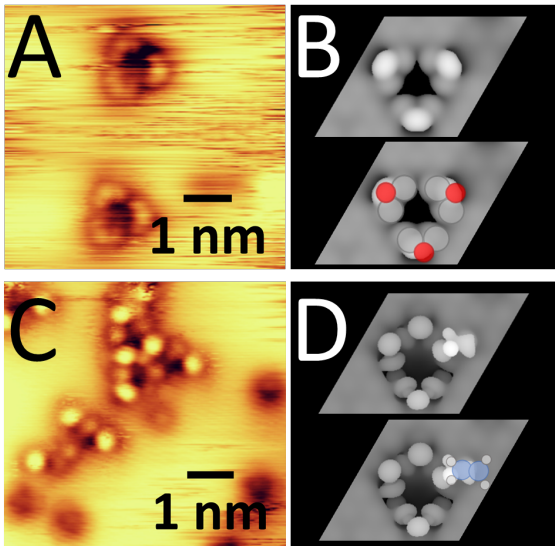

Figure 5.2. Direct STM imaging of oxametallacycle complexes formed by the adsorption of ethylene to O/Ag(111). (A) After exposure to only NO_2 at <373 K, triangular structures with three distinct bright spots that align with the close packed direction of the underlying Ag atoms. Simulated STM **(B)** reveals these bright spots are consistent with O adatoms in the surface with darker subsurface O atoms in between and a Ag atom vacancy in the middle. **(C)** After ethylene exposure at <23 K even brighter protrusions form in the same position as the three surface O atoms of the triangle **(D)** Simulated STM images help confirm this assignment as ethylene bound to O in the ring structure. All images taken 0.3 nA, 50 mV imaging conditions.

To assign these structures in STM images, we rely on their symmetry, contrast, and spatial periodicity. The triangular features consistently appear with three-lobed bright protrusions arranged in a C3 symmetry, centered around a darker depression attributed to a silver vacancy. Their orientation aligns with the close-packed direction of Ag(111) and they exhibit consistent registry with the underlying Ag lattice. In contrast, the p(4×4) structure manifests as a distinct honeycomb pattern; the brighter protrusions correspond to Ag atoms displaced by oxygen incorporation, consistent with previous assignments in the literature.

We then exposed both surfaces to ethylene at <25 K. Ethylene binds distinctly to each oxygen phase. On the triangular oxygen structures, ethylene adsorption enhances the brightness of the protrusions at the corners of the triangular oxygen structures: suggesting ethylene is bound at the corners of the rings. These molecules often organize into more linear chains linking adjacent triangular features (Fig. 5.1B). The larger oxygen trimer structure facilitates the formation of closely linked oxametallacycle (OMC) structures that differ from the isolated individual structures originally proposed by Linic and Barteau.[19] In fact, the OMC structures are not limited

to forming discrete six membered rings; we note the formation of larger complex oxygen and ethylene chains which appear after ethylene adsorption.

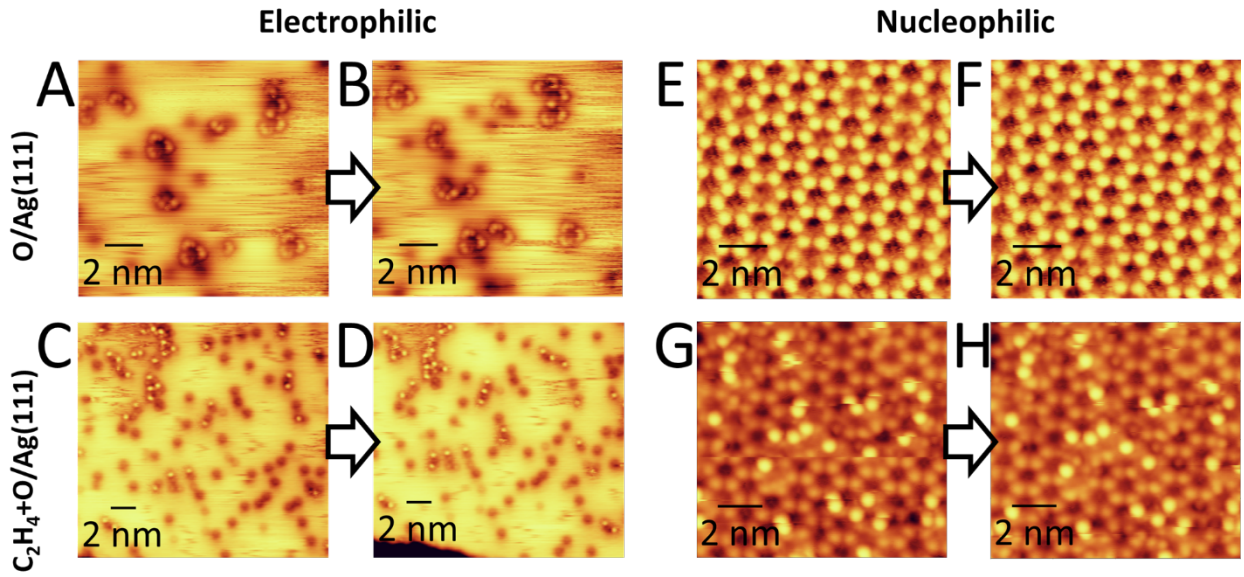

Figure 5.3. Mobility of oxygen and oxygen/ethylene structures on Ag(111). Electrophilic and nucleophilic oxygen structures before ethylene exposure (**A-B** and **E-F** respectively) and after ethylene exposure (**C-D** and **G-H** respectively). Imaging conditions for **(A-B)** and **(C-D)** 0.3 nA, 50 mV and imaging conditions for **(E-F)** and 0.2 nA, 100 mV and **(G-H)** 0.2 nA, 500 mV.

The identification of ethylene binding is based on the increased apparent height and contrast in STM after ethylene dosing, particularly at the ring corners. Before exposure to ethylene (Fig. 5.2A), triangular structures show uniform brightness; after dosing however, brighter protrusions form at the corner positions (Fig. 5.2C). Using DFT we modelled both the energetics and simulated STM images from the optimized structures. Fig. 5.2D show excellent agreement between experiment and theory.

DFT calculations of ethylene binding further indicate that ethylene preferentially binds to the "up" oxygen atoms in the 6-O ring (Fig. 5.2D), rather than occupying apparent vacancy-like regions associated with subsurface oxygen or the central Ag vacancy site. This is supported by DFT simulated STM images (Fig. 5.2B,D), which show that the enhanced contrast observed upon ethylene exposure aligns spatially with the surface O atoms of the ring.

The two oxygen structures exhibit markedly different mobility under STM imaging. The p(4×4) phase remains static over time and resists tip-induced perturbation (Fig. 5.3E–F). In contrast, the triangular features are more labile; and in Fig. 5.3A-B it can be seen that tip interactions fragment the rings into subunits that can reassemble into trefoils or smaller aggregates. This mobility may arise from weak lateral O-O interactions which would support facile restructuring under reaction.

This STM tip-induced motion was identified by comparing sequential STM frames under identical tunneling conditions. For the triangular rings, contrast changes and partial fragmentation were repeatedly observed as seen in Fig. 5.3A–B, while the p(4x4) domains remained static in analogous sequences (Fig. 5.3E–F). These differences suggest inherently weaker binding or greater structural flexibility in the low-temperature phase.

On the p(4×4) surface, ethylene remains mobile while the underlying oxygen structure remains static. Unlike the repeating structures seen in Fig. 5.3C-D, the preferred binding site of ethylene to the p(4x4) structure remains more ambiguous. Some molecules appear transiently bound within the surface vacancies, possibly interacting with oxygen atoms below the ejected Ag sites; others appear to bind centrally between bright protrusions of the p(4x4) unit cell. DFT predicts that several binding sites within the p(4x4) structure are similarly stable and this is mirrored in the more varied binding sites seen in STM images.

By combining thermal control with NO_2 dosing and STM imaging, we directly visualize two distinct oxygen phases on Ag(111): a triangular, ring-like structure formed at low temperatures and the well-known p(4×4) reconstruction at higher temperatures. The triangular phase, consistent with a six-membered oxygen ring around a silver vacancy, supports ordered ethylene adsorption and shows features reminiscent of oxametallacycle-like intermediates, in contrast to the disordered adsorption observed on the p(4×4) surface. The well characterized thermally driven formation of electrophilic and nucleophilic oxygen species on Ag surface suggest that it is reasonable to assign these species as electrophilic and nucleophilic oxygen on account of their similarly distinct thermally driven formation. These results reveal clear structural and reactive differences between the two oxygen species and provide atomic scale structures of potential intermediates in the ethylene epoxidation which will be useful in modeling the mechanism.

5.4 Materials and Methods

Sample preparation and cleaning occurred in a preparation chamber with base pressure ~ 1e-10 mbar. A Ag(111) single crystal was cleaned with a series of Ar^+ bombardment and 900 K annealing cycles. NO_2 (Aldrich >99.5%) was dosed with a precision leak valve while the sample was heated with a PBN heater in the preparation chamber. After deposition samples were cooled to room temperature and were then transferred into the scanning probe microscope (SPM) chamber (base pressure ~5e-12 mbar) where they were cooled to ~13 K to image. STM experiments were performed by a low-temperature scanning tunneling microscope (Infinty by Scienta Omicron). Ethylene was exposed to oxygen precoated samples in the SPM chamber where they were continuously cooled during deposition with maximum temperature during dosing ~ 25 K.

5.5 References

(1) Markets, R. and. Ethylene Oxide Global Industry Report 2025: Market to Reach $67.7 Billion by 2030 - Increasing Investment in Chemical Research and Development Propels Innovations in Applications. GlobeNewswire News Room. https://www.globenewswire.com/news-release/2025/03/17/3043453/28124/en/Ethylene-Oxide-Global-Industry-Report-2025-Market-to-Reach-67-7-Billion-by-2030-Increasing-Investment-in-Chemical-Research-and-Development-Propels-Innovations-in-Applications.html (accessed 2025-04-22).

(2) Jones, T. E.; Wyrwich, R.; Böcklein, S.; Carbonio, E. A.; Greiner, M. T.; Klyushin, A. Y.; Moritz, W.; Locatelli, A.; Menteş, T. O.; Niño, M. A.; Knop-Gericke, A.; Schlögl, R.; Günther, S.; Wintterlin, J.; Piccinin, S. The Selective Species in Ethylene Epoxidation on Silver. ACS Catalysis **2018**, 8 (5), 3844–3852. https://doi.org/10.1021/acscatal.8b00660.

(3) Stegelmann, C.; Schiødt, N. C.; Campbell, C. T.; Stoltze, P. Microkinetic Modeling of Ethylene Oxidation over Silver. Journal of Catalysis **2004**, 221 (2), 630–649. https://doi.org/10.1016/j.jcat.2003.10.004.

(4) Carbonio, E. A.; Rocha, T. C. R.; Klyushin, A. Y.; Píš, I.; Magnano, E.; Nappini, S.; Piccinin, S.; Knop-Gericke, A.; Schlögl, R.; Jones, T. E. Are Multiple Oxygen Species Selective in Ethylene Epoxidation on Silver? Chemical Science **2018**, 9 (4), 990–998. https://doi.org/10.1039/c7sc04728b.

(5) Bukhtiyarov, V. I.; Nizovskii, A. I.; Bluhm, H.; Hävecker, M.; Kleimenov, E.; Knop-Gericke, A.; Schlögl, R. Combined in Situ XPS and PTRMS Study of Ethylene Epoxidation over Silver. Journal of Catalysis **2006**, 238 (2), 260–269. https://doi.org/10.1016/j.jcat.2005.11.043.

(6) Liu, J.-X.; Lu, S.; Ann, S.-B.; Linic, S. Mechanisms of Ethylene Epoxidation over Silver from Machine Learning-Accelerated First-Principles Modeling and Microkinetic Simulations. ACS Catalysis **2023**, 13 (13), 8955–8962. https://doi.org/10.1021/acscatal.3c00410.

(7) Xu, Y.; Greeley, J.; Mavrikakis, M. Effect of Subsurface Oxygen on the Reactivity of the Ag(111) Surface. Journal of the American Chemical Society **2005**, 127 (37), 12823–12827. https://doi.org/10.1021/ja043727m.

(8) Pawela-Crew, J.; Madix, R. J.; Stöhr, J. The Effect of Subsurface Oxygen on the Orientation of Molecular Oxygen on Ag(110). Surface Science **1995**, 339 (1–2), 23–28. https://doi.org/10.1016/0039-6028(95)00646-X.

(9) Chen, D.; Chen, L.; Zhao, Q. C.; Yang, Z. X.; Shang, C.; Liu, Z. P. Square-Pyramidal Subsurface Oxygen [Ag4OAg] Drives Selective Ethene Epoxidation on Silver. Nature Catalysis **2024**, 7 (5), 536–545. https://doi.org/10.1038/s41929-024-01135-2.

(10) Schiller, F.; Ali, K.; Makarova, A. A.; Auras, S. V.; García-Martínez, F.; Mohammed Idris Bakhit, A.; Castrillo Bodero, R.; Villar-García, I. J.; Ortega, J. E.; Pérez-Dieste, V. Near-Ambient Pressure Oxidation of Silver in the Presence of Steps: Electrophilic Oxygen and Sulfur Impurities. ACS Catalysis **2024**, 12865–12874. https://doi.org/10.1021/acscatal.4c02985.

(11) Hinsch, J. J.; Liu, J.; Wang, Y. Reinvestigating Oxygen Adsorption on Ag(111) by Using Strongly Constrained and Appropriately Normed Semi-Local Density Functional with the Revised Vydrov van Voorhis van Der Waals Force Correction. The Journal of Chemical Physics **2021**, 155 (23), 234704. https://doi.org/10.1063/5.0073407.

(12) Bajaj, A.; Kulik, H. J. Eliminating Delocalization Error to Improve Heterogeneous Catalysis Predictions with Molecular DFT + U. J. Chem. Theory Comput. **2022**, 18 (2), 1142–1155. https://doi.org/10.1021/acs.jctc.1c01178.

(13) Araujo, R. B.; Rodrigues, G. L. S.; dos Santos, E. C.; Pettersson, L. G. M. Adsorption Energies on Transition Metal Surfaces: Towards an Accurate and Balanced Description. Nat Commun **2022**, 13 (1), 6853. https://doi.org/10.1038/s41467-022-34507-y.

(14) Kahk, J. M.; Lischner, J. Combining the Δ-Self-Consistent-Field and GW Methods for Predicting Core Electron Binding Energies in Periodic Solids. J. Chem. Theory Comput. **2023**, 19 (11), 3276–3283. https://doi.org/10.1021/acs.jctc.3c00121.

(15) Li, J.; Jin, Y.; Rinke, P.; Yang, W.; Golze, D. Benchmark of GW Methods for Core-Level Binding Energies. J. Chem. Theory Comput. **2022**, 18 (12), 7570–7585. https://doi.org/10.1021/acs.jctc.2c00617.
(16) Zhu, T.; Chan, G. K.-L. All-Electron Gaussian-Based G0W0 for Valence and Core Excitation Energies of Periodic Systems. J. Chem. Theory Comput. **2021**, 17 (2), 727–741. https://doi.org/10.1021/acs.jctc.0c00704.
(17) Bare, S. R.; Griffiths, K.; Lennard, W. N.; Tang, H. T. Generation of Atomic Oxygen on Ag(111) and Ag(110) Using NO2: A TPD, LEED, HREELS, XPS and NRA Study. Surface Science **1995**, 342 (1–3), 185–198. https://doi.org/10.1016/0039-6028(95)00670-2.
(18) Andryushechkin, B. V.; Shevlyuga, V. M.; Pavlova, T. V.; Zhidomirov, G. M.; Eltsov, K. N. Adsorption of Molecular Oxygen on the Ag(111) Surface: A Combined Temperature-Programmed Desorption and Scanning Tunneling Microscopy Study. The Journal of Chemical Physics **2018**, 148 (24), 244702. https://doi.org/10.1063/1.5037169.
(19) Linic, S.; Barteau, M. A. Formation of a Stable Surface Oxametallacycle That Produces Ethylene Oxide. J. Am. Chem. Soc. **2002**, 124 (2), 310–317. https://doi.org/10.1021/ja0118136.

Chapter 6: Nickel Promotes Selective Ethylene Epoxidation on Silver

This chapter was modified from the following publication: Elizabeth E. Happel, Anika Jalil, Laura Cramer, Adrian Hunt, Adam S. Hoffman, Iradwikanari Waluyo, Matthew M. Montemore, Phillip Christopher, and E. Charles H. Sykes. Nickel Promotes Selective Ethylene Epoxidation on Silver. *Science*. **2025,** 387, 869-873.
DFT was performed by M.M. Montemore, Nanoparticle synthesis and analysis was performed by A. Jalil, and preliminary TPD experiments were performed by L. Cramer. TPD quantification, XPS, and STM were performed by E.E. Happel.

6.1. Abstract

Over the last 80 years Cl has been the primary promoter of the ~$40B/year ethylene epoxidation reaction, providing a ~25% selectivity increase over unpromoted Ag (~55%). Promoters like Cs, Re, and Mo each add a few percent of selectivity enhancements to achieve 90% overall, but their co-dependence on Cl makes optimizing and understanding their function complex. We took a theory-guided single-atom alloy approach to identify Ni as a dopant in Ag that can facilitate selective oxidation by activating O_2 without binding O too strongly. Surface science experiments confirmed the facile adsorption/desorption of O_2 on NiAg, as well as demonstrating that Ni serves to stabilize unselective nucleophilic oxygen. Supported Ag catalyst studies revealed that a 1:200 Ni to Ag atomic ratio provides a ~25% selectivity increase without the need for Cl co-flow, and acts cooperatively with Cl resulting in a further 10% initial increase in selectivity.

6.2 Introduction

Ethylene oxide (EO, C_2H_4O) is a platform chemical in the production of many consumer goods including plastics and antifreeze, with a growing global market currently valued at ~40 billion USD per year. [1] It is produced from ethylene (C_2H_4) and molecular oxygen (O_2) by using Ag/α-Al_2O_3 heterogeneous catalysts. Because of the instability of EO, industrial reactors are operated at only ~10 to 15% per pass ethylene conversion to minimize combustion of EO into CO_2 and H_2O.[2]

The low per-pass conversion, low reactant partial pressures (> 50% of the feed is inert to mitigate thermal runaway), and high production volumes all necessitate large-volume recycle streams. These energy-intensive separation processes add to the 10% CO_2 emitted as a by-

product of the 90% selective EO production process, so EO has the highest CO_2 emission among high-value chemicals on a per volume basis.[3] Thus, even small improvements in EO selectivity could lead to large decreases in associated CO_2 emissions and energy costs, making the design of selective EO production catalysts of continued interest.[4,5]

Achieving high EO selectivity requires minimizing both the direct combustion of ethylene and the secondary combustion of EO to CO_2. The relatively high fraction of EO produced over silver (Ag) catalysts has been widely attributed to its oxygen adsorption properties.[6–8] Ag/α-Al_2O_3 catalysts exhibit ~50 to 60% EO selectivity at <10% ethylene conversion, although selectivity decreases with increasing ethylene conversion through EO combustion.

Despite the safety and environmental impacts as well as its corrosive nature, chlorine (Cl) is ubiquitously used to promote the selectivity of industrial EO catalysts which consist of large (50 nm-1μm diameter) Ag particles supported on low surface area (< 1 m^2/g) α-alumina (α-Al_2O_3). Chlorine is co-fed as an alkyl chloride and increases EO selectivity by ~25% at low ethylene conversion compared to pure Ag/α-Al_2O_3 and enables EO selectivity to be retained at higher conversion, which suggests that Cl promotes EO formation by depressing the rates of both the primary and secondary combustion reactions.[9–11]

Other promoters of industrial EO catalysts include alkali metals such as cesium (Cs) and lithium (Li), and oxyanions of transition metals such as molybdenum (Mo) and rhenium (Re), which each offer modest ~1 to 5% increases in EO selectivity but require the presence of Cl to be effective. Furthermore, promoters can be co-dependent on one another. For example, Re only increases selectivity in the presence of Cs, which itself requires Cl. These requirements make the system complex, as the addition of parts per million (ppm) levels of alkyl chloride and other promoters (promoter:Ag molar ratios of 10^{-4}-10^{-2}) required for ~90% EO selectivity at 10 to 15% ethylene conversion results in crowded, multi-component catalytic surfaces.[12–16]

Promoters are thought to influence the amount, accessibility and reactivity of oxygen species.[9,14,17–22] The ubiquity of Cl as a promoter in most catalyst formulations has limited research into the identification of new promoters that act independently of Cl. A few reports exist of modest (5-10%) selectivity increases by using unconventional (not currently used in industrial formulations)

promoters, but high EO selectivity at reasonable ethylene conversion remains a challenge without Cl.[23–25]

Herein, we report that the addition of ppm amounts of Ni to supported Ag catalysts substantially enhanced EO selectivity by ~25%, rivaled only by the ubiquitously used Cl promoter. Our theoretical and experimental surface science studies demonstrate that dispersed Ni in Ag(111) simultaneously influenced the quantity and reactivity of adsorbed oxygen species. Further, catalytic studies revealed that dilute Ni promoters (at 200:1 Ag:Ni ratio) on supported Ag/α-Al_2O_3 catalysts function synergistically with Cl feeds to enable 90% EO selectivity at 10% ethylene conversion, indicating that Ni offers a new avenue for catalyst and process optimization in EO production.

6.3 Theory-guided catalyst discovery

We initially searched for promoters for Ag-based EO producing catalysts using our single-atom alloy (SAA) approach that has identified new selective (de)hydrogenation catalysts, including RhCu, PtCu and PdCu SAAs.[26–29] These catalysts derive their function from the facile dissociation of strong bonds and weak binding of intermediates enabled by the SAA geometry that can decouple transition and final state energies. We applied this concept to selective oxidations using density functional theory (DFT) calculations to identify single-atom dopants in Ag surfaces with a low dissociative oxygen chemisorption activation barrier ($E_{a,diss}$) and weak atomic oxygen binding energy when bound in hollow sites on each side of the dopant site ($E_{ads,2O}$; Fig. S5.2) as shown in Fig. 5.1A. [6] Among the screened dopants, Ni stood out as breaking the scaling relationship (Fig. S5.1) between $E_{a,diss}$ and $E_{ads,2O}$, with DFT predicting near barrierless dissociation of O_2 (<0.05 eV) while maintaining moderate atomic oxygen atom binding (-2.2 eV).[30]

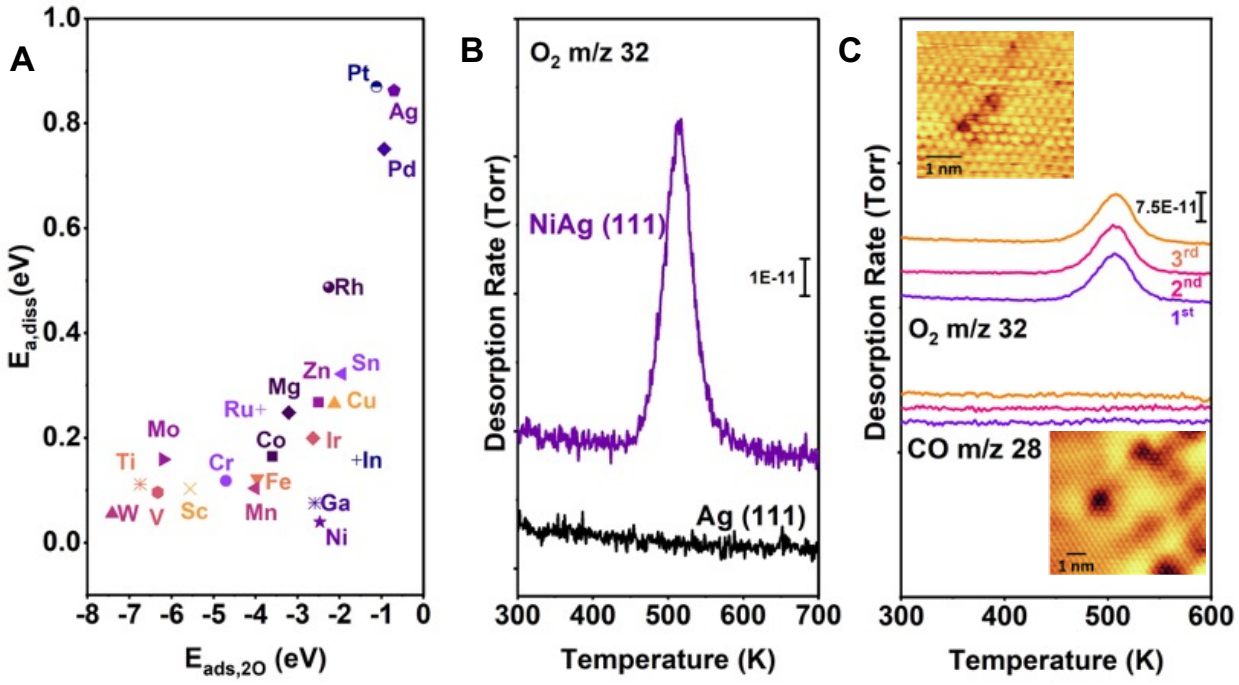

Figure 6.1. Theory-guided identification of Ni dopant that enables facile O_2 dissociation and spillover of oxygen to Ag. (A) DFT calculations of the O_2 dissociation barrier $E_{a,diss}$ as a function of the adsorption energy of the resulting dissociated O atoms ($E_{ads,2O}$) for various single-atom dopants in Ag(111). **(B)** O_2 temperature-programmed desorption (TPD) traces for Ag(111) and ~1% NiAg(111) after 500 Langmuirs (L) of oxygen dosed at 350 K, cooling to room temperature, and recording the TPD with a 1 K/s heating rate. **(C)** Sequential TPD traces involving a 500 L exposure of O_2 at 350 K and TPD, followed by 0.5 L CO exposure at 90 K and TPD, insets show 13 K STM images of subsurface Ni in Ag(111) immediately after Ni deposition (upper image, image conditions 0.2 nA, 100 mV) and Ni at the surface of Ag(111) cooling from 473 K after in O_2 (lower image, 0.3 nA, 50 mV).

6.4 Surface adsorption experiments

To test this prediction, we conducted surface-science studies of O_2 activation on 1% Ni-doped Ag(111) single-crystal surfaces. In these experiments, 1% monolayer (ML) of Ni was alloyed into the Ag(111) surface to obtain dispersed Ni in the surface and subsurface (Fig. 6.1C and S6.5). The dissociative sticking probability of O_2 on Ag(111) is ~10^{-6} which requires high O_2 pressures in the Torr range, or a more reactive oxidant such as NO_2, to saturate the surface with atomic oxygen.[31,32] However, Fig. 6.1B shows that the addition of 1% monolayer (ML) Ni to Ag(111) enabled uptake of oxygen on Ag at 10^{-6} Torr pressure of O_2.

The NiAg(111) sample was then exposed to 500 L (1 L = 1x10^{-6} Torr.sec) of O_2 at 350 K. Temperature-programmed desorption (TPD) of adsorbed oxygen demonstrates facile uptake and spillover of the dissociated oxygen atoms to sites on Ag(111). Calibration of the trace in Fig. 6.1B

indicated that 1% ML Ni enabled the uptake of ~4% ML O. Furthermore, O_2 desorbed from NiAg at 520 K. This temperature is ~70 K lower than typically from pure Ag (Fig. 6.1B) and consistent with our DFT prediction (Fig. 6.1A and Table S6.1) of promoted O_2 uptake and release by Ni dopants.[31,33]

Consecutive CO and O_2 adsorption TPDs demonstrated that the Ni atoms were mobile within the Ag sample. The Ni atoms were in the Ag(111) surface under oxidizing conditions but moved to the subsurface under vacuum conditions (Fig. 6.1C). Specifically, we used CO as a probe molecule to measure the surface concentration of Ni. Although CO does not bind to Ag(111) above ~50 K, the introduction of Ni to Ag(111) led to observation of a CO desorption peak at ~350 K (Fig. S6.6) [34]. This CO desorption temperature is ~80 K lower than that observed for Ni(111) and is further evidence of the high dispersion of Ni in Ag(111).[35]

After O_2 exposure and subsequent TPD, we exposed the NiAg surface to 0.5 L of CO, but no CO desorption was observed in TPD. This result indicated that Ni moved to the subsurface by the end of the O_2 desorption TPD ramp to 700 K. Subsequent exposure to O_2 brought Ni back to the surface. This preference is expected based on the more oxophilic nature of Ni, and the reversibility of Ni surface segregation over three full cycles is shown in Fig. 6.1C.

6.5 Nanoparticle catalysts for epoxidation

To determine if the surface-science and theoretical studies could be translated to supported catalysts, we synthesized highly dilute NiAg nanoparticle alloys and compared their performance in ethylene epoxidation to pure Ag/α-Al_2O_3 catalysts (Fig. 6.2). Ag nanoparticles of ~70 nm diameter were synthesized (Fig. A6.4, A6.7, and A6.8) with varying Ni content through a colloidal approach. This particle size was chosen because smaller (5 to 50 nm) and larger (>250 nm) diameter Ag particles exhibit lower reaction rates, and smaller Ag particles are prone to rapid sintering.[11,36–38] The Ag nanoparticles were post-synthetically doped with Ni to ensure a constant Ag particle size distribution.[39,40]

Our TPD results showing Ni mobility and segregation to the surface after O_2 exposure emphasized that under ethylene epoxidation reaction conditions, the oxophilicity of Ni should provide a thermodynamic driving force for Ni to move to the Ag nanoparticle surface. Further, the reaction temperature (473-523 K) is high enough to kinetically enable Ni to segregate to the surface as

observed in TPD when Ni diffusion to the surface occurred at 350 K. Therefore, in order to calculate nominal Ni surface coverages we made the simplifying assumption that all the Ni in a nanoparticle resided at the Ag surface when O_2 is present. This allowed us to calculate a range of target Ni:Ag ratios for the synthesis, assuming spherical nanoparticles (Fig. A6.7). We then synthesized catalysts with Ni loadings ranging from 1:500 (0.2 mol %) to 1:50 (2 mol%) which corresponded to 10% and 80% estimated Ni surface coverage, respectively. It should be noted that this is an upper limit as the thermodynamics of Ni partitioning between the bulk and surface is dependent on particle size and environmental conditions.

Catalysts were characterized with a variety of techniques (Figs. A6.8-S6.11, A6.14-S6.17, Tables S6.2-S6.4). Inductively coupled plasma (ICP) measurements showed that the desired Ni loadings were achieved (Table A6.4). Ni K-edge high-energy resolution fluorescence detection–x-ray absorption near-edge structure (HERFD-XANES) spectroscopy measurements were collected for an as prepared 9 wt% $NiAg_{200}/\alpha$-Al_2O_3 catalyst and for ~5 nm NiO particles on α-Al_2O_3 (Figs. S6.14-S6.16) during a temperature programmed reduction (TPR). Linear-combination fitting of the NiO TPR produced negligible residuals, demonstrating that the spectra were fit well using NiO and reduced Ni nanoparticle basis sets (Fig. A6.15, A6.16A). The spectrum of the as-prepared $NiAg_{200}$ samples was poorly fit by the same basis set. The different electronic structure and local coordination environment of Ni in $NiAg_{200}$ compared to pure Ni on α-Al_2O_3 evidenced by the HERFD-XANES indicated that the synthetic procedure effectively incorporated Ni in Ag and is different from pure dispersed Ni on α-Al_2O_3.

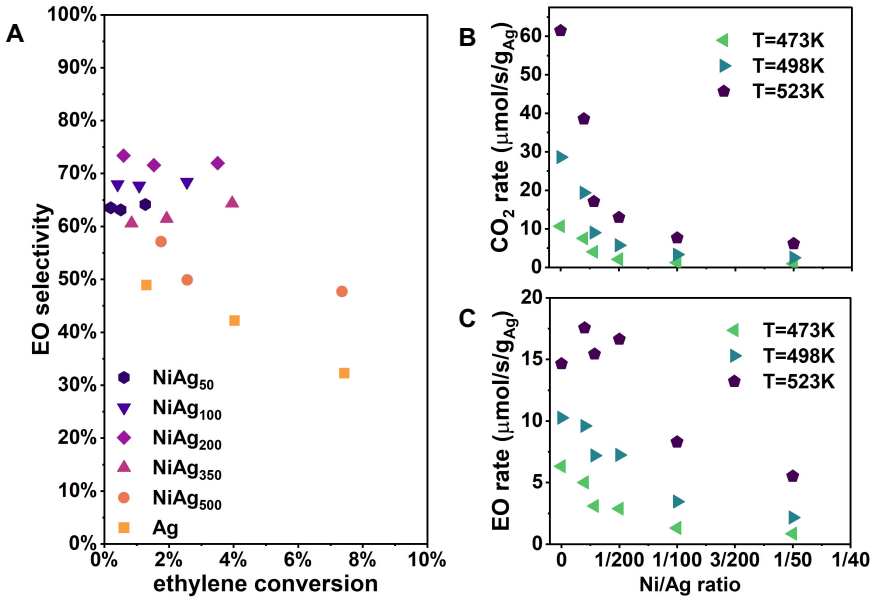

Figure 6.2. Ni doping of Ag nanoparticles at a molar ratio of 1:200 Ni:Ag increases EO selectivity by ~25% compared to pure Ag. Influence of Ni loading on 5 wt% Ag/α-Al_2O_3 catalyst reactivity in 10% C_2H_4, 10% O_2, balance He inlet with 100-150 mg catalyst. The Ni:Ag molar ratio was varied from 0:100 (pure Ag) to 1:50 (2% Ni). **(A)** EO selectivity as a function of steady-state ethylene conversion. The ethylene conversion was varied by changing the temperature between 473, 498 and 523 K and holding for 2 hours to allow the system to reach a new steady state. **(B)** CO_2 and **(C)** EO formation rates at different temperatures as a function of Ni:Ag molar ratio.

Steady-state reactivity experiments were performed with a feed of 10% ethylene and 10% molecular oxygen (at 1 bar in 80% inert) at 473, 498, and 523 K. Ni-doped 5 wt% Ag/α-Al_2O_3 ($NiAg_x$/α-Al_2O_3) catalysts with stoichiometries ranging from $NiAg_{500}$ to $NiAg_{50}$ were all prepared from the same parent batch of Ag colloids (see Fig. A6.18, A6.20 and Table A6.5 for details on the reactivity protocols). Steady-state ethylene conversion for Ag/α-Al_2O_3 was varied from 2 to 8% with 100 to 150 mg of catalyst in the reactor by varying the reaction temperature (Fig. 6.2A).

The EO selectivity for Ag/α-Al_2O_3, calculated as $\frac{N_{EO}}{N_{EO}+0.5N_{CO_2}}$, where N_i is the molar flow rate of each species, decreased from 50% to 30% as conversion increased, consistent with previous reports (Table S6.6) [36,41–43]. The addition of just 1:350 Ni:Ag (0.3 atom % of Ni) to Ag resulted in an increase in EO selectivity by 5 to 10% at all conversions. Increasing the Ni loading further increased EO selectivity and decreased ethylene conversion. $NiAg_{200}$ appeared to be the optimum Ni content for this batch of Ag particles, which exhibited a 25 to 30% increase in selectivity over Ag, comparable to the known behavior of Cl promoters. Fig. A6.12 shows the effect of increasing

Ni loading on selectivity at 2% ethylene conversion revealing a maximum selectivity at a 1:200 Ni:Ag molar ratio which improves EO selectivity by ~25% over pure Ag. The selectivity at low conversion (< 2%) can be considered the primary selectivity (at the limit of low EO combustion rate), and at higher ethylene conversions the rate of secondary EO combustion is relevant. Thus, the results in Fig. 6.2A demonstrate that 1:200 Ni:Ag (0.5% Ni) mitigated both primary ethylene and secondary EO combustion. At Ni loadings higher than $NiAg_{200}$ both selectivity and conversion decreased, suggesting that extended NiO_x domains may block reactive sites on Ag and further facilitate EO combustion (see Fig. A6.19).

Increasing the Ni loading led to a decrease in CO_2 production rate while the EO production rate decreased to a lesser degree, resulting in overall increased EO selectivity (Fig. 6.2, B and C). The ethylene conversion at 473 K was < 2% and thus the CO_2 and EO production in Fig. 6.2, B and C, demonstrates the influence of Ni on the primary reaction pathways (conversion of ethylene to CO_2 or EO). At 523 K, where ethylene conversion was higher and the secondary reaction of EO combustion was likely more prevalent, the depression in CO_2 production rates with Ni addition was clearly observed with no change (or even a small increase) in EO production rates. The larger influence of Ni incorporation on selectivity at higher temperatures supported the conclusion that Ni suppressed secondary EO combustion while also promoting primary selectivity. Interestingly, the trends in selectivity and rates of product formation as a function of Ni concentration were similar to how Cl performs as a promoter (Fig. A6.13).

The $NiAg_{200}$ formulation offered consistent performance improvement over Ag catalyst samples across multiple catalyst syntheses. The magnitude and statistical significance of the optimal Ni loading was quantified by comparing the reactivity of seven independently prepared batches of $Ag/\alpha\text{-}Al_2O_3$ and $NiAg_{200}/\alpha\text{-}Al_2O_3$ at an ~8% wt. Ag loading. The temperature, catalyst loading, and total flow rate were varied to compare EO selectivity at a broad range of ethylene conversions. Fig. 6.3A shows that even with batch-to-batch performance variation, $NiAg_{200}$ repeatedly improved EO selectivity by at least 20% over a broad range of ethylene conversions up to 10%.

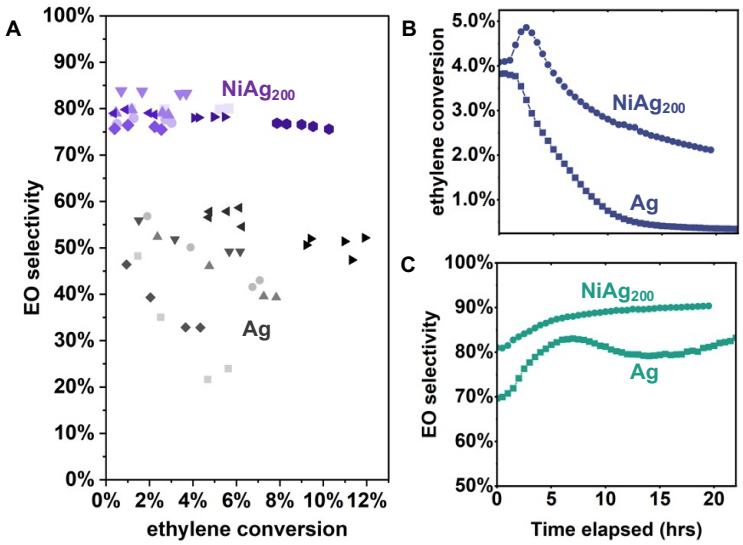

Figure 6.3. $NiAg_{200}$ catalysts show a consistent ~25% selectivity enhancement over Ag and additive influence of Cl co-promoter. (A) EO selectivity as a function of ethylene conversion for seven batches of ~8 wt% Ag and $NiAg_{200}$ on α-Al_2O_3 at 10% C_2H_4, 10% O_2, balance He. The reactivity of separate batches is shown by using various shades of purple ($NiAg_{200}$) and gray (Ag). See Table S5 for details on all samples. **(B and C)** Effect of Cl co-flow at 25% C_2H_4, 10% O_2, 0.5% CO_2 and 0.5 ppm EtCl, balance He (total flow rate 40 standard cubic centimeters per minute) at 523 K: **(B)** $NiAg_{200}$ and Ag ethylene conversion (see Fig. A6.21 for product formation rates over time) and corresponding **(C)** $NiAg_{200}$ and Ag selectivity.

To explore the promoting influence of Ni at more industrially relevant reaction conditions, a feed composition containing 25% C_2H_4, 10% O_2, 0.5% CO_2 and 0.5 ppm ethyl chloride (EtCl) was used [44]. Although the conversion of Ag/α-Al_2O_3 declined substantially with time upon Cl introduction, decreasing from 3.8% to 0.3% in 18 hours (Fig. 6.3B and A6.21A), the selectivity increased from 68% to 82% (Fig. 6.3C). $NiAg_{200}$ had a comparatively lower decrease in rates (~2x as compared to > 10x for Ag) after an initial increase in reactivity, with selectivity increasing to just > 90%. The initial increase in EO formation rate for $NiAg_{200}$ and lower decrease in rate due to Cl introduction (Fig. A6.21B) suggested that Ni and Cl were interacting on the Ag surface to modify the epoxidation pathways, which further supports the hypothesis that Ni is incorporated directly into the Ag nanoparticles rather than being located on the support. We note that optimized performance of Cl with other promoters is known to require co-optimization as a function of reaction conditions, suggesting that further improvements in performance are possible.

6.6 Ambient-pressure surface spectroscopy

Ambient-pressure x-ray photoelectron spectroscopy (AP-XPS) experiments demonstrated that the addition of Ni stabilized nucleophilic oxygen, which is generally believed to be responsible for non-selective primary and secondary combustion reactions on the Ag surface.[45] Specifically, exposure of both Ag(111) and NiAg(111) surfaces to 1 Torr O_2 at 325 K led primarily to the formation of electrophilic (~530.2 eV) and nucleophilic (~528.5 eV) oxygen species (Fig. 6.4). The NiAg sample exhibited an additional O 1s peak at 529.3 eV (blue trace, Fig. 6.4B), consistent with a Ni-O species (labeled as "Ni-philic"; Table S6.7).[46] Apart from the presence of the Ni-philic oxygen species on the NiAg(111) sample, both the Ag(111) and NiAg(111) surfaces behave similarly from 325 to 550 K: as the surface temperature is raised, the electrophilic oxygen is seen converting to nucleophilic oxygen on both surfaces. However, it is clear from Fig. 6.4B that on the NiAg surface nucleophilic oxygen persists up to 700 K vs. 550 K on Ag(111). We hypothesize that this increased thermal stability of the nucleophilic oxygen induced by Ni incorporation should decrease its reactivity, lowering the non-selective primary and secondary combustion rates thereby enhancing EO selectivity compared to the Ni-free system, as seen in the catalytic measurements. Our DFT calculations show that Ni stabilizes nucleophilic O on Ag (Fig. A6.3), rendering the nucleophilic oxygen which typically drives combustion more "spectator-like," and less reactive to ethylene combustion.[47]

Our reactivity data in Fig. 6.3 also support this hypothesis in that the addition of Ni to Ag decreased the combustion rate more than the EO formation rate, providing a coherent picture of the proposed mechanism whereby Ni decreases unselective reactions of ethylene and EO with nucleophilic oxygen by stabilizing the O atoms in the structure. Further studies are aimed at developing scalable synthetic protocols on low surface area supports that further increase EO selectivity by minimizing secondary combustion sites for operation at higher reactor pressures.

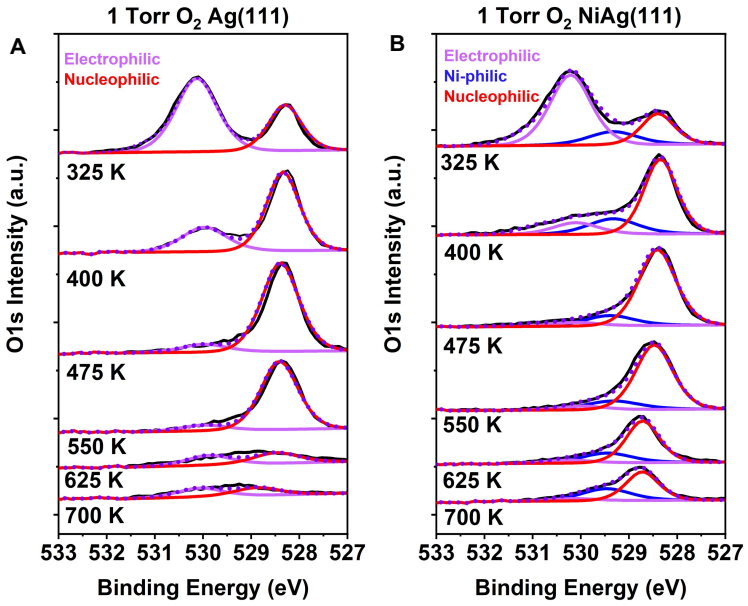

Figure 6.4. Electronic structure of oxygen on Ag(111) and NiAg(111) as a function of temperature in 1 Torr O_2. AP-XP spectra showing a change in oxygen species from primarily electrophilic oxygen (pink, ~530.2 eV) to more nucleophilic oxygen (red, ~528.5 eV) as the temperature was increased on **(A)** Ag(111) and **(B)** ~5% NiAg(111). The Ni-philic O species (529.3 eV) is shown in blue and was only observed for the NiAg sample. O 1s spectra taken at 760 eV from 325 to 700 K in 1 Torr O_2. The dotted traces represent the combined fits of the oxygen species overlaid with the solid black raw spectra.

6.7 Conclusion

Guided by theory and experimental surface science results, we synthesized and tested dilute Ni-doped Ag nanoparticles and found an EO selectivity increase of ~25% compared to pure Ag, a promotion magnitude previously only achievable with a co-flow of Cl. Our study identified dilute (~1:200) Ni:Ag alloys as an optimal concentration for promoting selective ethylene oxide formation on ~75 nm Ag nanoparticles, and the addition of Cl was found to further promote the selectivity of NiAg to ~90% without the need for promoters like Cs and Re that are normally required to reach this selectivity. Our AP-XPS results suggest that the ~25% selectivity enhancement results from Ni-induced stabilization of nucleophilic oxygen on the Ag surface, thereby decreasing the rates of ethylene and EO combustion. Overall, this study highlights the potential of theory-led exploration in dilute alloy materials space and the utility of our single-atom alloy approach for the design of selective oxidation catalysts.

6.8 References

(1) *Ethylene Oxide and Ethylene Glycol Market | Size, Share, Growth, Trends | Industry Analysis | Forecast 2025 | Technavio*. https://www.technavio.com/report/ethylene-oxide-and-ethylene-glycol-market-industry-analysis (accessed 2022-04-12).

(2) Miller, J. H.; Joshi, A.; Li, X.; Bhan, A. Catalytic Degradation of Ethylene Oxide over Ag/α-Al2O3. *Journal of Catalysis* **2020**, *389*, 714–720. https://doi.org/10.1016/J.JCAT.2020.07.008.

(3) Iea. Technology Roadmap Energy and GHG Reductions in the Chemical Industry via Catalytic Processes. **2013**.

(4) *Ethylene Oxide (EO) Catalysts | Shell Catalysts & Technologies | Shell Global*. https://www.shell.com/business-customers/catalysts-technologies/catalysts/petrochemical-catalysts/ethylene-oxide-catalysts.html (accessed 2022-06-08).

(5) Stegelmann, C.; Schiødt, N. C.; Campbell, C. T.; Stoltze, P. Microkinetic Modeling of Ethylene Oxidation over Silver. *Journal of Catalysis* **2004**, *221* (2), 630–649. https://doi.org/10.1016/j.jcat.2003.10.004.

(6) Li, H.; Cao, A.; Nørskov, J. K. Understanding Trends in Ethylene Epoxidation on Group IB Metals. *ACS Catalysis* **2021**, *11* (19), 12052–12057. https://doi.org/10.1021/acscatal.1c03094.

(7) Ozbek, M. O.; Onal, I.; Van Santen, R. A. Why Silver Is the Unique Catalyst for Ethylene Epoxidation. *Journal of Catalysis* **2011**, *284* (2), 230–235. https://doi.org/10.1016/J.JCAT.2011.08.004.

(8) Kokalj, A.; Gava, P.; de Gironcoli, S.; Baroni, S. What Determines the Catalyst's Selectivity in the Ethylene Epoxidation Reaction. *Journal of Catalysis* **2008**, *254* (2), 304–309. https://doi.org/10.1016/j.jcat.2008.01.008.

(9) Campbell, C. T. Chlorine Promoters in Selective Ethylene Epoxidation over Ag(111): A Comparison with Ag(110). *Journal of Catalysis* **1986**, *99* (1), 28–38. https://doi.org/10.1016/0021-9517(86)90195-8.

(10) Chen, C. J.; Harris, J. W.; Bhan, A. Kinetics of Ethylene Epoxidation on a Promoted Ag/α-Al2O3 Catalyst—The Effects of Product and Chloride Co-Feeds on Rates and Selectivity. *Chemistry - A European Journal* **2018**, *24* (47), 12405–12415. https://doi.org/10.1002/chem.201801356.

(11) Van Hoof, A. J. F.; Hermans, E. A. R.; Van Bavel, A. P.; Friedrich, H.; Hensen, E. J. M. Structure Sensitivity of Silver-Catalyzed Ethylene Epoxidation. *ACS Catalysis* **2019**, *9* (11), 9829–9839. https://doi.org/10.1021/acscatal.9b02720.

(12) Jankowiak, J. T.; Barteau, M. A. Ethylene Epoxidation over Silver and Copper–Silver Bimetallic Catalysts: II. Cs and Cl Promotion. *Journal of Catalysis* **2005**, *236* (2), 379–386. https://doi.org/10.1016/J.JCAT.2005.10.017.

(13) Huš, M.; Hellman, A. Dipole Effect on Ethylene Epoxidation: Influence of Alkali Metals and Chlorine. https://doi.org/10.1016/j.jcat.2018.04.008.

(14) Hwang, A.; Klaucke, J.; Lizandara-Pueyo, C.; Karpov, A.; Iglesia, E. Roles of Re and Cs Promoters and Organochlorine Moderators in the Synthesis of Ethylene Oxide on Ag-Based Catalysts. *ChemCatChem* **2023**. https://doi.org/10.1002/cctc.202301369.

(15) Diao, W.; Digiulio, C. D.; Schaal, M. T.; Ma, S.; Monnier, J. R. An Investigation on the Role of Re as a Promoter in Ag-Cs-Re/α-Al2O3 High-Selectivity, Ethylene Epoxidation Catalysts. *Journal of Catalysis* **2015**, *322*, 14–23. https://doi.org/10.1016/j.jcat.2014.11.007.

(16) Pu, T.; Tian, H.; Ford, M. E.; Rangarajan, S.; Wachs, I. E. Overview of Selective Oxidation of Ethylene to Ethylene Oxide by Ag Catalysts. *ACS Catalysis* **2019**, 10727–10750. https://doi.org/10.1021/acscatal.9b03443.
(17) Linic, S.; Barteau, M. A. Formation of a Stable Surface Oxametallacycle That Produces Ethylene Oxide. *Journal of the American Chemical Society* **2002**, *124* (2), 310–317. https://doi.org/10.1021/ja0118136.
(18) Wu, S.; Tatarchuk, B. J.; Adamczyk, A. J. Ethylene Oxidation on Unpromoted Silver Catalysts: Reaction Pathway and Selectivity Analysis Using DFT Calculations. *Surface Science* **2021**, *708*, 121834. https://doi.org/10.1016/J.SUSC.2021.121834.
(19) Dhalewadikar, S. V.; Martinez, E. N.; Varma, A. Complex Dynamic Behaviour during Ethylene Oxidation on a Supported Silver Catalyst. *Chemical Engineering Science* **1986**, *41* (7), 1743–1746. https://doi.org/10.1016/0009-2509(86)87052-X.
(20) Carbonio, E. A.; Rocha, T. C. R.; Klyushin, A. Y.; Píš, I.; Magnano, E.; Nappini, S.; Piccinin, S.; Knop-Gericke, A.; Schlögl, R.; Jones, T. E. Are Multiple Oxygen Species Selective in Ethylene Epoxidation on Silver? *Chemical Science* **2018**, *9* (4), 990–998. https://doi.org/10.1039/C7SC04728B.
(21) Linic, S.; Barteau, M. A. Construction of a Reaction Coordinate and a Microkinetic Model for Ethylene Epoxidation on Silver from DFT Calculations and Surface Science Experiments. *Journal of Catalysis* **2003**, *214* (2), 200–212. https://doi.org/10.1016/S0021-9517(02)00156-2.
(22) Jingfa, D.; Jun, Y.; Shi, Z.; Xiaohong, Y. Promoting Effects of Re and Cs on Silver Catalyst in Ethylene Epoxidation. *Journal of Catalysis; (United States)* **1992**, *138:1* (1), 395–399. https://doi.org/10.1016/0021-9517(92)90033-E.
(23) Dellamorte, J. C.; Lauterbach, J.; Barteau, M. A. Palladium-Silver Bimetallic Catalysts with Improved Activity and Selectivity for Ethylene Epoxidation. *Applied Catalysis A: General* **2011**, *391*, 281–288. https://doi.org/10.1016/j.apcata.2010.06.023.
(24) Linic, S.; Jankowiak, J.; Barteau, M. A. Selectivity Driven Design of Bimetallic Ethylene Epoxidation Catalysts from First Principles. *Journal of Catalysis* **2004**, *224* (2), 489–493. https://doi.org/10.1016/J.JCAT.2004.03.007.
(25) Huš, M.; Grilc, M.; Teržan, J.; Gyergyek, S.; Likozar, B.; Hellman, A. Going Beyond Silver in Ethylene Epoxidation with First-Principles Catalyst Screening. *Angewandte Chemie - International Edition* **2023**, *62* (31). https://doi.org/10.1002/anie.202305804.
(26) Marcinkowski, M. D.; Liu, J.; Murphy, C. J.; Liriano, M. L.; Wasio, N. A.; Lucci, F. R.; Flytzani-Stephanopoulos, M.; Sykes, E. C. H. Selective Formic Acid Dehydrogenation on Pt-Cu Single-Atom Alloys. *ACS Catalysis* **2017**, *7* (1), 413–420. https://doi.org/10.1021/acscatal.6b02772.
(27) Giannakakis, G.; Kress, P.; Duanmu, K.; Ngan, H. T.; Yan, G.; Hoffman, A. S.; Qi, Z.; Trimpalis, A.; Annamalai, L.; Ouyang, M.; Liu, J.; Eagan, N.; Biener, J.; Sokaras, D.; Flytzani-Stephanopoulos, M.; Bare, S. R.; Sautet, P.; Sykes, E. C. H. Mechanistic and Electronic Insights into a Working NiAu Single-Atom Alloy Ethanol Dehydrogenation Catalyst. *Journal of the American Chemical Society* **2021**, *143* (51), 21567–21579. https://doi.org/10.1021/JACS.1C09274/SUPPL_FILE/JA1C09274_SI_001.PDF.
(28) Kyriakou, G.; Boucher, M. B.; Jewell, A. D.; Lewis, E. a; Lawton, T. J.; Baber, A. E.; Tierney, H. L.; Flytzani-stephanopoulos, M.; Sykes, E. C. H. Isolated Metal Atom Geometries as a Strategy for Selective Heterogeneous Hydrogenations. *Science (New York,*

N.Y.) **2012**, *335* (March), 1209–1212. https://doi.org/10.1016/B978-0-12-557160-9.50008-3.
(29) Hannagan, R. T.; Giannakakis, G.; Réocreux, R.; Schumann, J.; Finzel, J.; Wang, Y.; Michaelides, A.; Deshlahra, P.; Christopher, P.; Flytzani-Stephanopoulos, M.; Stamatakis, M.; Sykes, E. C. H. First-Principles Design of a Single-Atom-Alloy Propane Dehydrogenation Catalyst. *Science* **2021**, *372* (6549), 1444–1447. https://doi.org/10.1126/SCIENCE.ABG8389.
(30) Montemore, M. M.; Van Spronsen, M. A.; Madix, R. J.; Friend, C. M. O2 Activation by Metal Surfaces: Implications for Bonding and Reactivity on Heterogeneous Catalysts. *Chemical Reviews* **2018**, *118* (5), 2816–2862. https://doi.org/10.1021/acs.chemrev.7b00217.
(31) Bare, S. R.; Griffiths, K.; Lennard, W. N.; Tang, H. T. Generation of Atomic Oxygen on Ag(111) and Ag(110) Using NO2: A TPD, LEED, HREELS, XPS and NRA Study. *Surface Science* **1995**, *342* (1–3), 185–198. https://doi.org/10.1016/0039-6028(95)00670-2.
(32) Campbell, C. T. The Selective Epoxidation of Ethylene Catalyzed by Ag(111): A Comparison with Ag(110). *Journal of Catalysis* **1985**, *94* (2), 436–444. https://doi.org/10.1016/0021-9517(85)90208-8.
(33) Klust, A.; Madix, R. J. Partial Oxidation of Higher Olefins on Ag(1 1 1): Conversion of Styrene to Styrene Oxide, Benzene, and Benzoic Acid. *Surface Science* **2006**, *600* (23), 5025–5040. https://doi.org/10.1016/J.SUSC.2006.08.049.
(34) Hansen, W.; Bertolo, M.; Jacobi, K. Physisorption of CO on Ag(111): Investigation of the Monolayer and the Multilayer through HREELS, ARUPS, and TDS. *Surface Science* **1991**, *253* (1–3), 1–12. https://doi.org/10.1016/0039-6028(91)90576-E.
(35) Netzer, F. P.; Madey, T. E. The Structure of CO on Ni(111). *The Journal of Chemical Physics* **1982**, *76* (1), 710–715. https://doi.org/10.1063/1.442674.
(36) Van Den Reijen, J. E.; Kanungo, S.; Welling, T. A. J.; Versluijs-Helder, M.; Nijhuis, T. A.; De Jong, K. P.; De Jongh, P. E. Preparation and Particle Size Effects of Ag/a-Al 2 O 3 Catalysts for Ethylene Epoxidation. **2017**. https://doi.org/10.1016/j.jcat.2017.10.001.
(37) Iyer, K. R.; Bhan, A. Particle Size Dependence of Ethylene Epoxidation Rates on Ag/α-Al2O3 Catalysts: Why Particle Size Distributions Matter. *Journal of Catalysis* **2023**, *420*, 99–109. https://doi.org/10.1016/J.JCAT.2023.02.008.
(38) Egelske, B. T.; Xiong, W.; Zhou, H.; Monnier, J. R. Effects of the Method of Active Site Characterization for Determining Structure-Sensitivity in Ag-Catalyzed Ethylene Epoxidation. *Journal of Catalysis* **2022**. https://doi.org/10.1016/j.jcat.2022.03.021.
(39) Liu, J.; Shan, J.; Lucci, F. R.; Cao, S.; Sykes, E. C. H.; Flytzani-Stephanopoulos, M. Palladium-Gold Single Atom Alloy Catalysts for Liquid Phase Selective Hydrogenation of 1-Hexyne. *Catalysis Science and Technology* **2017**, *7* (19), 4276–4284. https://doi.org/10.1039/c7cy00794a.
(40) Gao, X.; Du, X.; Liu, D.; Gao, H.; Wang, P.; Yang, J. Core-Shell Gold-Nickel Nanostructures as Highly Selective and Stable Nonenzymatic Glucose Sensor for Fermentation Process. *Scientific Reports 2020 10:1* **2020**, *10* (1), 1–10. https://doi.org/10.1038/s41598-020-58403-x.
(41) Christopher, P.; Linic, S. Shape- and Size-Specific Chemistry of Ag Nanostructures in Catalytic Ethylene Epoxidation. *ChemCatChem* **2010**, *2* (1), 78–83. https://doi.org/10.1002/cctc.200900231.

(42) Keijzer, P. H.; van den Reijen, J. E.; Keijzer, C. J.; de Jong, K. P.; de Jongh, P. E. Influence of Atmosphere, Interparticle Distance and Support on the Stability of Silver on α-Alumina for Ethylene Epoxidation. *Journal of Catalysis* **2022**, *405*, 534–544. https://doi.org/10.1016/j.jcat.2021.11.016.
(43) Keijzer, C. J.; Smulders, L. C. J.; Wezendonk, D.; de Rijk, J. W.; de Jongh, P. E. Influence of Ag Particle Size and Ag : Al2O3 Surface Ratio in Catalysts for the Chloride-Promoted Ethylene Epoxidation. *Catalysis Today* **2024**, *428*, 114447. https://doi.org/10.1016/J.CATTOD.2023.114447.
(44) Lockemeyer, J. R.; Lohr, T. L. Ethylene Oxide Catalysis Under Commercial Conditions – A Guide for Researchers. *ChemCatChem* **2023**, *15* (13), 1–6. https://doi.org/10.1002/cctc.202201511.
(45) Bukhtiyarov, V. I.; Prosvirin, I. P.; Kvon, R. I. Study of Reactivity of Oxygen States Adsorbed at a Silver Surface towards C2H4 by XPS, TPD and TPR. *Surface Science* **1994**, *320* (1–2), 2–5. https://doi.org/10.1016/0039-6028(94)00562-1.
(46) Peck, M. A.; Langell, M. A. Comparison of Nanoscaled and Bulk NiO Structural and Environmental Characteristics by XRD, XAFS, and XPS. *Chemistry of Materials* **2012**, *24* (23), 4483–4490. https://doi.org/10.1021/cm300739y.
(47) Dostert, K.-H.; O' Brien, C. P.; Ivars-Barceló,Barceló, F.; Schauermann, S.; Freund, H.-J. Spectators Control Selectivity in Surface Chemistry: Acrolein Partial Hydrogenation Over Pd. *J. Am. Chem. Soc* **2015**, *137*, 13496–13502. https://doi.org/10.1021/jacs.5b04363.

Chapter 7: The Effect of Ni on Oxygen Activation and Oxygen-Induced Reconstruction on Ag(111)

Elizabeth E. Happel, Laura Cramer, Avery S. Daniels, Cole Easton, Adrian Hunt, Matthew M. Montemore, Iradwikanari Waluyo, and E. Charles H. Sykes

7.1 Abstract

Ni-doped Ag catalysts have recently been shown to enhance selectivity in ethylene epoxidation, motivating a deeper investigation into how Ni modifies surface oxygen behavior. Here, we use temperature-programmed desorption (TPD) and X-ray photoelectron spectroscopy (XPS) to study oxygen activation and binding on NiAg(111) under ultra-high vacuum (UHV) and ambient pressure (AP) conditions. Even at 1% surface concentration, Ni enables O_2 activation and spillover onto Ag, producing Ni-bound, electrophilic, subsurface, and nucleophilic oxygen species. Unlike on pure Ag, nucleophilic oxygen forms at low coverages and without surface sputtering. Thermal evolution experiments reveal distinct desorption sequences depending on oxygen coverage, with Ni-bound oxygen remaining the most persistent. These results demonstrate that Ni not only lowers the kinetic barrier for O_2 dissociation on Ag but also broadens the range of accessible surface oxygen species. By providing mechanistic insight under controlled conditions, this work helps rationalize the enhanced performance of NiAg catalysts and informs strategies for designing further selective oxidation systems.

7.2 Introduction

Nickel-doped silver (NiAg) has recently emerged as a promising new catalyst for ethylene epoxidation, demonstrating an increase in selectivity comparable to that achieved with the ubiquitous chlorine promoter.[1] This discovery presents an opportunity to deepen our mechanistic understanding of ethylene epoxidation by enabling the study of oxygen spillover on Ag(111) even under ultra-high vacuum (UHV) conditions without the need for sources of atomic oxygen like NO_2 or O_3. Industrially, heavily promoted silver catalysts achieve up to ~90% selectivity, but this still results in substantial CO_2 byproduct formation.[3–5] Achieving high selectivity remains

challenging due to both the difficulty of activating molecular oxygen on Ag and the thermodynamic preference for total combustion pathways that compete with the desired epoxidation reaction. [3,6,7]

While oxygen activation on bare Ag is widely recognized a potentially rate-limiting step in ethylene epoxidation, the nature of the oxygen species that form also plays a critical role in determining catalytic selectivity.[8,9] Two dominant surface oxygen species are typically observed on Ag: electrophilic oxygen, which forms at lower temperatures and pressures and is generally associated with selective epoxidation, and nucleophilic oxygen, which is thought to correspond to an oxygen-induced surface reconstruction that forms under higher pressures and temperatures and promotes total oxidation.[10–17] Interestingly, early results suggest that Ni stabilizes this nucleophilic oxygen species.

Despite the observed improvement in selectivity upon Ni addition, the mechanism by which Ni promotes catalytic performance remains unclear. Prior theoretical work predicted that Ni would lower the activation barrier for O_2 dissociation on Ag(111) which was then experimentally confirmed. However, this increased activation alone does not fully explain the enhanced selectivity observed for NiAg catalysts relative to pure Ag.

In this study, we investigate the spillover of oxygen onto NiAg(111), focusing on both the thermal desorption behavior (temperature programmed desorption (TPD)) in comparison to Ag(111) and the distribution of surface oxygen species using synchrotron-based X-ray photoelectron spectroscopy (XPS). We find that Ni not only facilitates the activation and spillover of oxygen onto Ag(111) but also enables the formation of a broader range of oxygen species, even at low surface coverages. Our results reveal a relationship between NiAg and nucleophilic oxygen formation that may offer insight into the origin of the enhanced selectivity previously reported for this system.

7.3 Results and Discussion

The incorporation of as little as 1% Ni into Ag(111) significantly alters the surface chemistry of silver toward oxygen. As shown in Figure 7.1A, TPD measurements reveal that Ni enables the activation of O_2 under UHV conditions, overcoming the inherently low sticking probability of

oxygen on Ag(111) (~1 × 10^{-6}). The resulting oxygen uptake on NiAg(111) reaches ~6% of a monolayer (ML) (Figure 7.1B), despite the Ni surface concentration being only ~1%. This disparity suggests that oxygen activation occurs at Ni sites, followed by spillover onto adjacent Ag sites. Suggesting NiAg behaves similarly to other well-established behavior in single atom alloy systems wherein a more reactive dopant facilitates activation while the host metal accommodates diffusing intermediates.

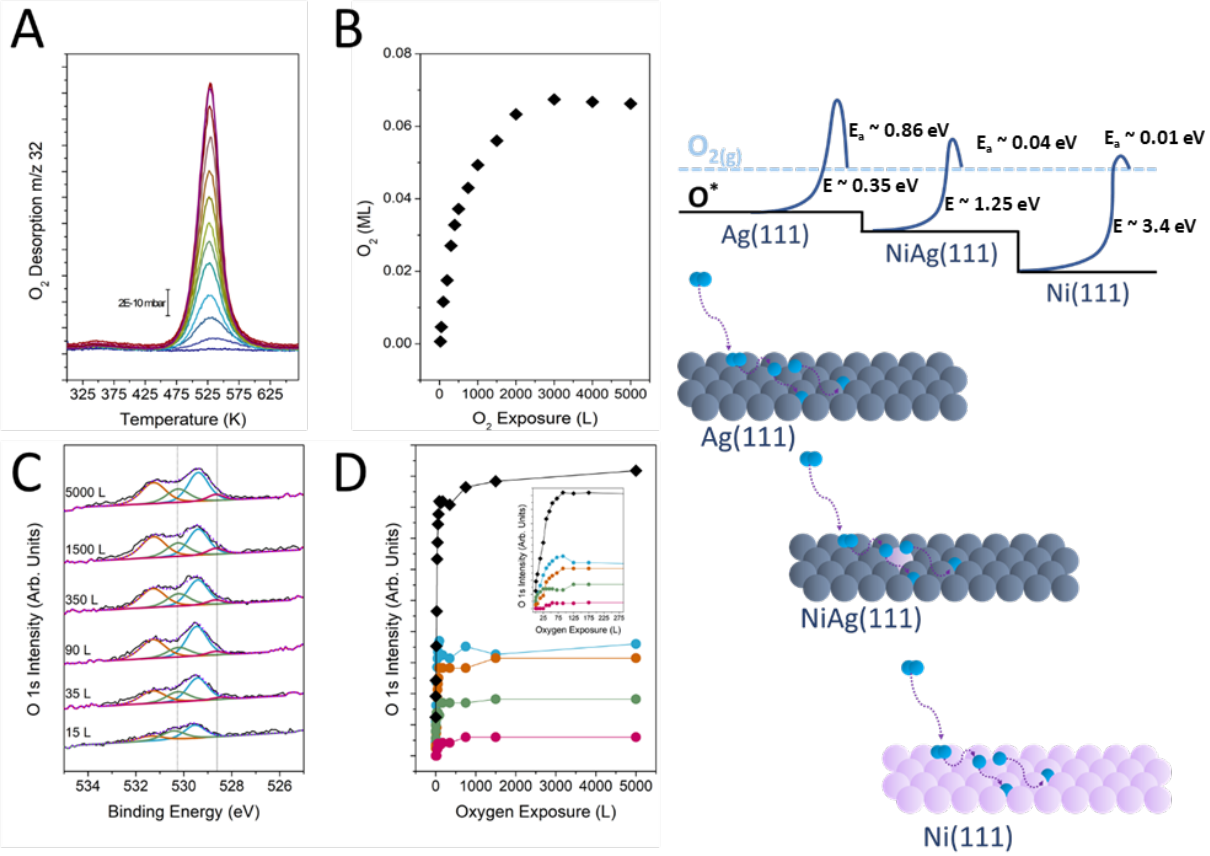

Figure 7.1: The uptake and spillover of oxygen onto NiAg(111). (A) TPD spectra of oxygen desorption from 1% NiAg show uptake under UHV conditions, consistent with spillover onto Ag**. (B)** Integrated uptake reaches ~6% ML, well above the Ni surface concentration, confirming spillover. **(C)** O 1s XPS spectra show sequential formation of Ni-philic (blue), electrophilic (green), subsurface (orange), and nucleophilic (pink) oxygen. **(D)** Peak areas reveal early saturation of Ni-philic oxygen and growth of Ag-associated species, indicating spillover-driven speciation.

XPS provides further insight into the nature and evolution of surface oxygen species on NiAg(111) (Figure 7.1C). Sequential exposures of NiAg(111) to increasing O_2 doses reveal the mechanism of oxygen spillover from Ni to Ag. The initial oxygen species observed is Ni-bound

oxygen (~529.4 eV), consistent with NiO and a Ni(II) oxidation state (Fig A7.1). Upon further exposure, higher-binding-energy species emerge: ~530.4 eV (electrophilic oxygen), ~531.2 eV (subsurface oxygen), followed by nucleophilic oxygen formation (~528.5 eV). These changes coincide with saturation of the Ni-philic oxygen feature, indicating that excess oxygen spills over to Ag, forming both electrophilic and nucleophilic oxygen species known to reside on Ag(111) (Figure 7.1D). The binding energies of these species are consistent with those on pure Ag, further supporting their assignment to Ag-bound oxygen rather than mixed-metal or interfacial species.

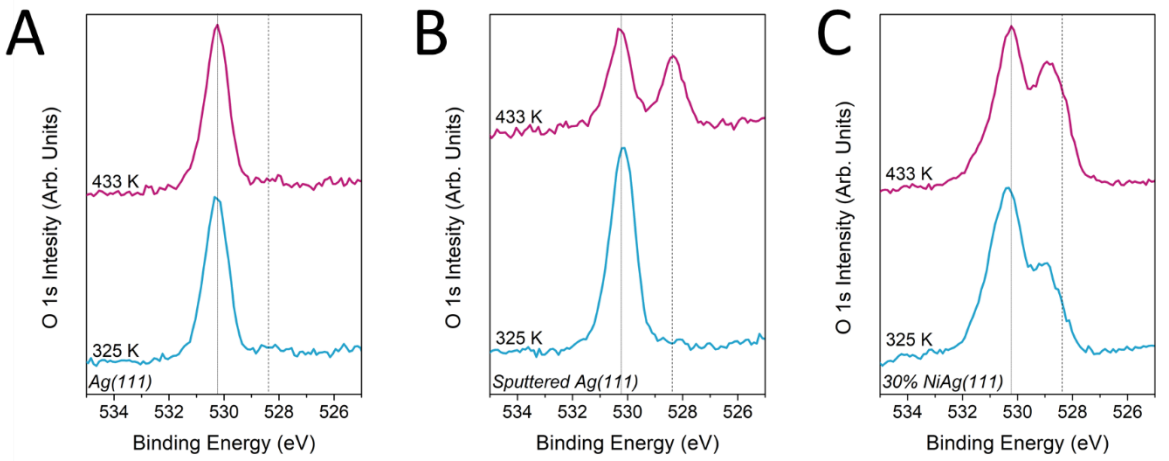

Figure 7.2. Temperature induced conversion of oxygen species on Ag(111) and NiAg(111). In 200 mTorr O_2 at 325 K Ag(111) forms primarily electrophilic oxygen (~530.4 eV) and when annealed to 433 K a pristine Ag(111) surface **(A)** shows no shift in surface species while a surface sputtered for 3 minutes **(B)** there is significant conversion to form nucleophilic oxygen (~528.3 eV). A 30% NiAg surface **(C)** has primarily electrophilic, Ni-philic (529.5 eV) and even some nucleophilic at 325 K when heated to 433 K there is a notable increase in nucleophilic oxygen at the surface.

Beyond enabling oxygen activation, Ni also modifies the energetics of oxygen adsorption. Oxygen desorption from NiAg(111) begins at ~525 K, approximately 60 K lower than on pure Ag(111), indicating both a reduced dissociation barrier and a moderate binding energy for surface oxygen.[1] This intermediate binding strength is characteristic of Ag's capacity for selective oxidations, such as in ethylene epoxidation. However, Ni's role extends beyond facilitating activation; it also alters the distribution of oxygen species on the surface. Notably, nucleophilic oxygen appears on NiAg even at low coverages and moderate temperatures:

conditions under which this species does not typically form on Ag(111). As shown in Figure 7.2A, a clean, annealed Ag surface fails to form nucleophilic oxygen even under ambient pressures (200 mTorr O_2), whereas a lightly sputtered surface enables its formation (Figure 7.2B). These findings are consistent with previous studies by King and co-workers, who describe the necessity of defect sites for nucleophilic oxygen formation on Ag.[2]

In contrast, NiAg forms nucleophilic oxygen under the same temperature and pressure conditions without requiring additional sputtering (Figure 7.2C). While annealing similarly shifts the electrophilic-to-nucleophilic ratio on both Ag and NiAg, the emergence of nucleophilic oxygen even after low-pressure UHV exposures (Figure 7.1) suggests that Ni could serves as an intrinsic nucleation center or reduce the formation barrier. Thus, Ni not only overcomes the initial hurdle of oxygen activation but also enables a more diverse coverage of oxygen species than what forms on bare Ag(111).

Importantly, nucleophilic oxygen is not selective for ethylene oxide formation and instead promotes total oxidation. Prior work has shown that Ni stabilizes this unselective species, reducing its reactivity and thereby improving ethylene oxide selectivity on NiAg. While the formation of nucleophilic oxygen is typically associated with unselective total oxidation, it is important to note that Ni doping, which promotes its formation, also improves selectivity. This apparent contradiction may point to a more nuanced relationship between oxygen speciation and reactivity. In particular, the behavior of nucleophilic oxygen on NiAg surfaces appears to depend on its coverage and local environment. At lower concentrations, this species may be present in a more stable or less reactive form, while higher coverages lead to greater surface restructuring and persistence.

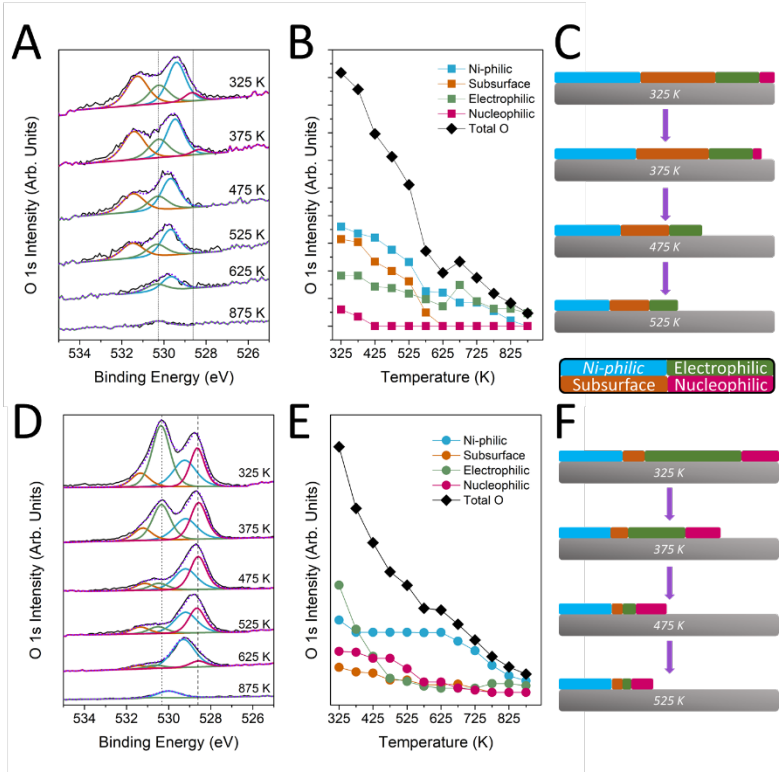

Figure 7.3. Thermal evolution and reversibility of oxygen species on NiAg(111). O 1s spectra of NiAg(111) following saturation with 5000 L O_2 **(A)** show the progressive loss of oxygen species with annealing. Integrated peak areas **(B)** indicate nucleophilic oxygen (pink) desorbs first, followed by electrophilic (green), subsurface (orange), and Ni-philic (blue) species. After exposure to 10 mTorr O_2 at 325 K, all four species are present in different relative intensities **(D)**, and stepwise annealing of this surface **(E)** shows a desorption sequence in which electrophilic oxygen decreases first, followed by subsurface, nucleophilic, and Ni-philic species. Schematic representations of the relative surface coverages at 325 K are shown for the UHV-dosed **(C)** and ambient-exposed **(F)** surfaces, normalized to their respective saturation levels.

The transition of oxygen species as a function of temperature provides key insight into their relative stabilities and the reversibility of their formation. Following oxygen saturation through sequential UHV exposures, stepwise annealing (Figures 7.3A and 7.3B) reveals a clear desorption sequence: nucleophilic oxygen desorbs first, followed by electrophilic and subsurface species, while Ni-philic oxygen persists to the highest temperatures. Although early desorption of nucleophilic oxygen might seem inconsistent with its association with the thermally stable p(4×4) reconstruction on Ag(111), this behavior occurs only under low-coverage conditions. XPS data (Fig A7.2) show minimal changes to the Ag 3d region, indicating that the Ag lattice remains largely metallic, and thus the spillover process follows near-reversible kinetics.

Following more oxidizing conditions (e.g., 10 mTorr O_2), the desorption order notably changes. Figures 7.3D and 7.3E show that electrophilic oxygen now desorbs first, while nucleophilic and subsurface oxygen persist; this reflects a more significantly reconstructed surface that is less reversibly formed compared to lower coverages. Still, Ni-philic oxygen remains the most thermally stable species, with significant coverage persisting at 625 K. This strong binding highlights Ni's enduring influence on the oxygen environment even at elevated temperatures.

7.4 Conclusions

This study demonstrates that incorporating as little as 1% Ni into Ag(111) fundamentally alters the surface chemistry of oxygen adsorption and activation. Ni acts as an efficient site for O_2 dissociation, enabling oxygen spillover onto Ag and overcoming the intrinsically low sticking probability oxygen on pure Ag(111). NiAg not only enhances oxygen uptake but also diversifies the oxygen species that populate the surface under both UHV and AP conditions.

The formation of nucleophilic oxygen on Ag(111) typically requires high pressures, elevated temperatures, or defect sites, Ni doping promotes its formation even under more moderate conditions. Despite this, the behavior of surface oxygen remains dynamic, as evidenced by the thermally induced evolution toward nucleophilic oxygen which parallels trends observed on sputtered Ag. This suggests that while Ni facilitates oxygen activation and spillover, the resulting oxygen species remain sensitive to temperature and local environment.

Importantly, although nucleophilic oxygen is generally associated with unselective total oxidation, its stabilization at low coverages and temperatures on NiAg may reconcile its presence with the enhanced ethylene oxide selectivity reported for Ni-doped catalysts. This provides a mechanistic basis for prior observations that NiAg nanoparticles produce less CO_2 compared to Ag, despite our measured higher levels of nucleophilic oxygen.

Beyond spillover and speciation, Ni introduces a highly stable Ni–O species that persists even after extensive annealing, outlasting both electrophilic and nucleophilic oxygen on Ag. This strongly bound oxygen may serve as a reservoir or anchor, potentially supporting oxygen availability under reaction conditions. Moreover, Ni facilitates the appearance of subsurface

oxygen, a species that has been theorized to play an important role in maintaining the long-term activity of Ag-based catalysts under oxidizing environments.

Overall, these findings offer insight into how Ni enhances both the activity and selectivity of Ag in ethylene epoxidation: by enabling oxygen activation, broadening surface speciation, and stabilizing less reactive forms of unselective oxygen. This mechanistic clarity helps resolve prior ambiguities about the role of nucleophilic oxygen on NiAg and provides a framework for further tuning of oxygen-metal interactions in selective oxidation catalysis.

7.5 References

(1) Jalil, A.; Happel, E. E.; Cramer, L.; Hunt, A.; Hoffman, A. S.; Waluyo, I.; Montemore, M. M.; Christopher, P.; Sykes, E. C. H. Nickel Promotes Selective Ethylene Epoxidation on Silver. *Science* **2025**, *387* (6736), 869–873. https://doi.org/10.1126/science.adt1213.

(2) Carlisle, C. I.; Fujimoto, T.; Sim, W. S.; King, D. A. Atomic Imaging of the Transition between Oxygen Chemisorption and Oxide Film Growth on Ag{1 1 1}. *Surface Science* **2000**, *470* (1), 15–31. https://doi.org/10.1016/S0039-6028(00)00831-1.

(3) Pu, T.; Tian, H.; Ford, M. E.; Rangarajan, S.; Wachs, I. E. Overview of Selective Oxidation of Ethylene to Ethylene Oxide by Ag Catalysts. *ACS Catalysis* **2019**, 10727–10750. https://doi.org/10.1021/acscatal.9b03443.

(4) Hwang, A.; Klaucke, J.; Lizandara-Pueyo, C.; Karpov, A.; Iglesia, E. Roles of Re and Cs Promoters and Organochlorine Moderators in the Synthesis of Ethylene Oxide on Ag-Based Catalysts. *ChemCatChem* **2023**. https://doi.org/10.1002/cctc.202301369.

(5) Diao, W.; Digiulio, C. D.; Schaal, M. T.; Ma, S.; Monnier, J. R. An Investigation on the Role of Re as a Promoter in Ag-Cs-Re/α-Al2O3 High-Selectivity, Ethylene Epoxidation Catalysts. *Journal of Catalysis* **2015**, *322*, 14–23. https://doi.org/10.1016/j.jcat.2014.11.007.

(6) Michaelides, A.; Reuter, K.; Scheffler, M. When Seeing Is Not Believing: Oxygen on Ag(111), a Simple Adsorption System? *Journal of Vacuum Science & Technology A: Vacuum, Surfaces, and Films* **2005**, *23* (6), 1487–1497. https://doi.org/10.1116/1.2049302.

(7) Grant, R. B.; Lambert, R. M. A Single Crystal Study of the Silver-Catalysed Selective Oxidation and Total Oxidation of Ethylene. *Journal of Catalysis* **1985**, *92* (2), 364–375. https://doi.org/10.1016/0021-9517(85)90270-2.

(8) Setiawan, A.; Pu, T.; Wachs, I. E.; Rangarajan, S. Expanding the Reaction Network of Ethylene Epoxidation on Partially Oxidized Silver Catalysts. *ACS Catal* **2024**, *14* (23), 17880–17892. https://doi.org/10.1021/acscatal.4c04521.

(9) Özbek, M. O.; Van Santen, R. A. The Mechanism of Ethylene Epoxidation Catalysis. *Catal Lett* **2013**, *143* (2), 131–141. https://doi.org/10.1007/s10562-012-0957-3.

(10) Bukhtiyarov, V. I.; Hävecker, M.; Kaichev, V. V.; Knop-Gericke, A.; Mayer, R. W.; Schlögl, R. Atomic Oxygen Species on Silver: Photoelectron Spectroscopy and x-Ray Absorption Studies. *Physical Review B - Condensed Matter and Materials Physics* **2003**, *67* (23), 2354221–23542212. https://doi.org/10.1103/PhysRevB.67.235422.

(11) Campbell, C. T.; Koel, B. E. Chlorine Promotion of Selective Ethylene Oxidation over Ag(110): Kinetics and Mechanism. *Journal of Catalysis* **1985**, *92* (2), 272–283. https://doi.org/10.1016/0021-9517(85)90261-1.

(12) Force, E. L.; Bell, A. T. The Relationship of Adsorbed Species Observed by Infrared Spectroscopy to the Mechanism of Ethylene Oxidation over Silver. *Journal of Catalysis* **1975**, *40* (3), 356–371. https://doi.org/10.1016/0021-9517(75)90267-5.

(13) Kaichev, V. V.; Bukhtiyarov, V. I.; Hävecker, M.; Knop-Gercke, A.; Mayer, R. W.; Schlögl, R. The Nature of Electrophilic and Nucleophilic Oxygen Adsorbed on Silver. *Kinetics and Catalysis* **2003**, *44* (3), 432–440. https://doi.org/10.1023/A:1024459305551.

(14) Bukhtiyarov, V. I.; Nizovskii, A. I.; Bluhm, H.; Hävecker, M.; Kleimenov, E.; Knop-Gericke, A.; Schlögl, R. Combined in Situ XPS and PTRMS Study of Ethylene Epoxidation over Silver. *Journal of Catalysis* **2006**, *238* (2), 260–269. https://doi.org/10.1016/j.jcat.2005.11.043.

(15) Jones, T. E.; Wyrwich, R.; Böcklein, S.; Carbonio, E. A.; Greiner, M. T.; Klyushin, A. Y.; Moritz, W.; Locatelli, A.; Menteş, T. O.; Niño, M. A.; Knop-Gericke, A.; Schlögl, R.; Günther, S.; Wintterlin, J.; Piccinin, S. The Selective Species in Ethylene Epoxidation on Silver. *ACS Catalysis* **2018**, *8* (5), 3844–3852. https://doi.org/10.1021/acscatal.8b00660.
(16) Carbonio, E. A.; Rocha, T. C. R.; Klyushin, A. Y.; Píš, I.; Magnano, E.; Nappini, S.; Piccinin, S.; Knop-Gericke, A.; Schlögl, R.; Jones, T. E. Are Multiple Oxygen Species Selective in Ethylene Epoxidation on Silver? *Chemical Science* **2018**, *9* (4), 990–998. https://doi.org/10.1039/c7sc04728b.
(17) Stegelmann, C.; Schiødt, N. C.; Campbell, C. T.; Stoltze, P. Microkinetic Modeling of Ethylene Oxidation over Silver. *Journal of Catalysis* **2004**, *221* (2), 630–649. https://doi.org/10.1016/j.jcat.2003.10.004.

Chapter 8: Redox-Driven Mobility of Ni in Ag(111) in Oxidizing and Reducing Environments

Elizabeth E. Happel, Avery S. Daniels, Cole Easton, Adrian Hunt, Matthew M. Montemore, Iradwikanari Waluyo, and E. Charles H. Sykes

8.1 Abstract

Nickel-doped silver (NiAg) catalysts exhibit enhanced activity and selectivity for ethylene epoxidation, yet the complete mechanistic role of Ni remains incompletely understood. In this work, we examine how redox conditions modulate the spatial distribution and chemical state of Ni in NiAg(111) using synchrotron X-ray photoelectron spectroscopy (XPS). We identify a distinct temperature window (475–550 K) in which oxygen promotes Ni segregation to the surface, coinciding with the formation of nucleophilic oxygen species known as the selective species for combustion pathways. At higher temperatures (>700 K), Ni diffuses irreversibly into the Ag bulk, eliminating its surface availability. The Ni 2p spectral features evolve continuously with temperature and O_2 exposure, indicating that Ni remains electronically and structurally dynamic under operando conditions. These findings demonstrate that Ni surface accessibility is governed by a dynamic relationship between redox potential and thermal energy, establishing design principles for redox-responsive alloy catalysts in epoxidation and beyond.

8.2 Introduction

The partial oxidation of hydrocarbons is one of the most important classes of industrial heterogeneous catalysis. [1–4] Among the most prominent examples are formaldehyde synthesis and ethylene epoxidation, both catalyzed by silver and used to produce primary chemicals for a wide range of downstream products.[4,5] In both reactions, the identity of the surface oxygen species present under reaction conditions has a significant effect on catalytic performance.[6–8] Silver is reported to host two primary oxygen species with distinct O 1s binding energies: electrophilic oxygen (~530.4 eV) and nucleophilic oxygen (~528.3 eV).[7,9–11] Its ability to bind oxygen with intermediate strength has been cited as a key reason for its effectiveness in partial oxidation reactions.[12] In ethylene epoxidation specifically, the electrophilic oxygen species is widely associated with the selective epoxidation pathway, and extensive efforts have been made

to promote its formation and improve reaction selectivity. The nucleophilic oxygen species, by contrast, is more strongly bound and is typically linked to total combustion.

To enhance selectivity, a variety of promoters have been developed and applied in industrial formulations, which are thought to influence surface charge, oxygen binding, and reaction energetics.[7,13–18] However, the overall catalyst system remains complex and poorly understood. Achieving high selectivity often requires multiple promoters—most notably chlorine, but also Cs, Mo, and Re—which leads to a crowded surface that complicates mechanistic interpretation.[13,19–21] Even the role of Cl, the most ubiquitous promoter, remains unclear. Other promoters often function only in tandem with Cl or in the presence of multiple co-promoters, further complicating surface chemistry. As a result, the surface structures formed by these promoters, and how they are affected by reaction conditions, remain poorly understood.

In addition to promoters, other surface species such as carbonates have also been implicated in ethylene epoxidation. Carbonates are often considered a component of catalyst deactivation, possibly forming through the reaction of nucleophilic oxygen with hydrocarbon intermediates or combustion products. These site-blocking species are generally thought to poison the catalyst surface, but there is no comprehensive understanding of how they interact with promoters or active oxygen species.[22–25]

With the recent discovery that Ni can act as a promoter for ethylene epoxidation on Ag, it has become important to understand how this material behaves under different environmental conditions.[26] Given the established relationship between Ni, Ag, and the activation of oxygen species on Ag(111), we aim to investigate the stability of Ni in this surface to help determine the optimal working conditions for this new catalyst formulation. It has been established that Ni is mobile in Ag(111), with early studies showing that deposited Ni is capped by Ag or resides in the subsurface until oxygen is introduced.[26]

Additionally, given the well-studied deactivation pathways in supported metal catalysts—such as sintering and coking—it is important to understand the behavior of this catalyst under redox cycling. To this end, we use synchrotron-based ambient pressure XPS (AP-XPS) to track the physical and electronic state of Ni in NiAg(111) under oxidizing and reducing conditions. Our

results identify a temperature window in which surface-accessible Ni is stabilized by oxygen exposure, and a redox-dependent threshold above which Ni irreversibly diffuses into the bulk. These findings provide mechanistic insight into how environmental conditions affect promoter stability, with implications for the design of redox-responsive alloy catalysts in ethylene epoxidation and related oxidation reactions.

8.3 Materials and Methods

Ambient pressure XPS was performed at beamline 23-ID-2 (IOS) of the National Synchrotron Light Source II (NSLS- II) at Brookhaven National Laboratory.[27] All experiments were performed on a Ag(111) crystal cleaned with Ar^+ ion sputtering and annealing to 900 K until XPS spectra were free from impurities. High purity O_2 (Matheson, 99.994%) was introduced to the chamber via precision leak valve while the sample was heated with a pyrolytic boron nitride heater. Temperature was measured with a K-type thermocouple mounted between the Ag(111) crystal and the heater. NiAg(111) alloys were prepared similarly by evaporating a Ni rod (Goodfellow, 99.99%) with a SPECS EBE-4 e-beam evaporator.

Photon energies of 1090 and 760 eV were used to generate photoelectrons with kinetic energies of ~200 eV for the Ni 2p and O 1s core levels, respectively, to maintain similar probing depths. Reference Ag 3d spectra were taken at each photon energy. Spectra were corrected with respect to the Fermi edge and metallic Ag $3d_{5/2}$ binding energy. We observed four oxygen species with discrete binding energies; one attributed to nucleophilic oxygen with binding energy ~ 528.4 eV, [7,9,10,28,29] one associated with a Ni bound oxygen species ~529.3 eV, [30,31] one associated with electrophilic oxygen ~530.1 eV,[11,32–34]and one associated with subsurface oxygen ~531.1 eV.[35,36] XPS data was analyzed with CasaXPS and fit with a linear background; each species was assigned and fit according to literature values for the different types of oxygen.

All spectra were corrected with a relative sensitivity factor (RSF) for each photon energy used. Where necessary, peak intensity was corrected for the decreased electron inelastic mean free path

(IMFP) resulting from increased chamber pressure. Monolayer coverages were calculated with respect to a monolayer of Ag(111). To do this the $Ag3d_{5/2}$ spectra were first corrected for spin orbit splitting and RSF as well as IMFP as the Ag 3d reference spectra were taken at photon energies more surface sensitive to Ni 2p and O 1s species. The fraction of the total Ag 3d intensity attributed to the surface layer of Ag, 0.19 and 0.23 was calculated using the electron escape depth for each photon energy, 1090 and 760 eV, respectively; and these values were used to extract a monolayer reference for coverage calculations.

8.4 Results and Discussion

To examine how local oxygen environments influence the distribution and chemical state of Ni in NiAg(111), we tracked the evolution of the Ni $2p_3/_2$ XPS signal during stepwise thermal annealing under three different conditions: continuous exposure to 10 mTorr O_2, annealing in UHV following an O_2 exposure, and annealing in UHV with no prior O_2 exposure. These conditions enable us to isolate the roles of environmental oxygen and thermal energy in governing Ni segregation, oxidation, and dissolution into the Ag(111) bulk.

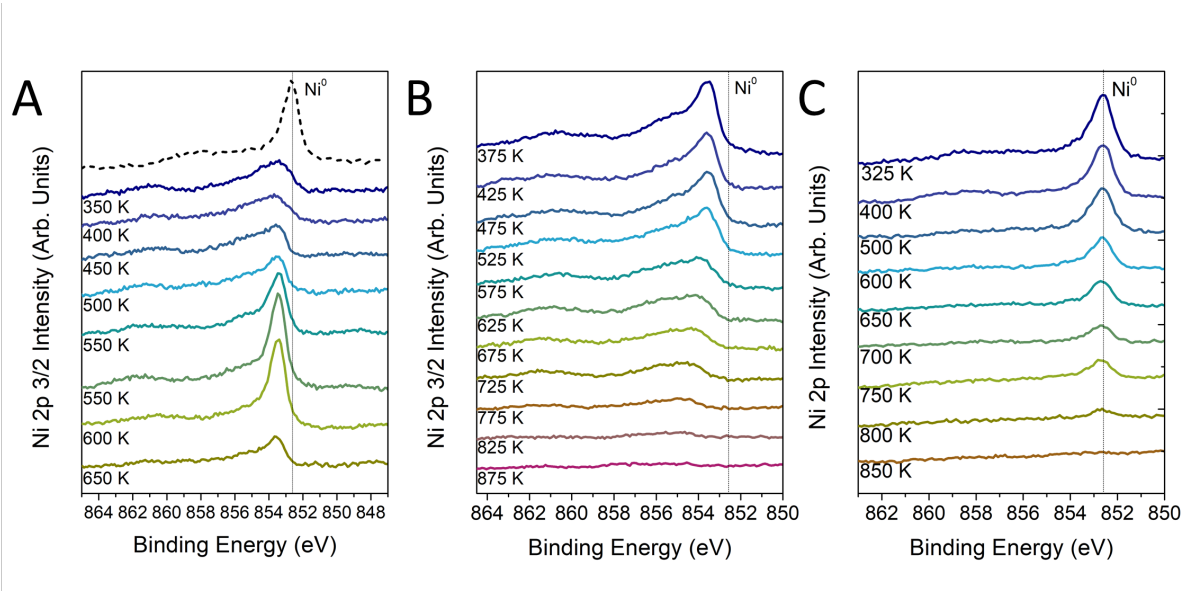

Fig 8.1. Dissolution of Ni into Ag(111) as a function of temperature. In 10mTorr O_2 **(A)** heating NiAg results in an increase of oxidized surface Ni before bulk segregation occurs. While heating NiAg after 10mTorr O_2 exposure **(B)** results in a consistent decrease in surface Ni until out of XPS detection range. Similarly, heating NiAg in UHV without any prior oxygen exposure

(C) leaves no shift in oxidation state of Ni during the consistent loss of intensity during bulk dissolution.

When annealed in UHV without any prior exposure to oxygen, the NiAg(111) surface exhibits no evidence of Ni oxidation (Fig. 8.1C). The Ni $2p_3/_2$ peak maintains the narrow linewidth and binding energy characteristic of metallic Ni (~852.7 eV), and no satellite or multiplet features emerge across the temperature range studied. Beginning at 325 K, the Ni signal progressively decreases in intensity as the sample is heated, consistent with Ni migrating below the XPS sampling depth. By ~800–850 K, the Ni signal is nearly undetectable, indicating complete dissolution into the Ag(111) host. The absence of any spectral evolution aside from intensity loss confirms that in the absence of oxygen, Ni remains metallic and undergoes bulk diffusion in a linear, thermally activated manner.

In contrast, samples pre-exposed to 10 mTorr O_2 and then transferred to UHV for annealing (Fig. 8.1B) display distinctly oxidized Ni features at the initial measurement temperature. The Ni $2p_3/_2$ peak shifts to higher binding energy (~853 eV) and is accompanied by both multiplet splitting and a satellite feature near ~860 eV which are both hallmarks of Ni(II) species. Despite returning to UHV conditions, the Ni remains oxidized throughout the annealing sequence. Notably, the binding energy and spectral shape remain essentially unchanged with temperature, even as the Ni signal steadily decreases in intensity. This suggests that once oxidized, Ni retains its +2 oxidation state in vacuum and is gradually lost to the bulk without undergoing reduction. The disappearance of the satellite and multiplet structure near ~800 K marks the point at which surface Ni is no longer detectable. Importantly, the thermal stability of oxidized Ni in this case is nearly identical to that of metallic Ni under UHV, indicating that oxidation alone does not substantially alter the ultimate segregation depth or thermal mobility of Ni in the absence of additional oxygen.

However, a markedly different behavior emerges when the NiAg(111) sample is annealed in the continuous presence of 10 mTorr O_2 (Fig. 8.1A). At low temperature, the Ni $2p_3/_2$ spectra again show features consistent with Ni^{2+}, including a broadened main peak and a well-defined satellite. As the sample is heated, the spectra evolve in a non-linear manner. Between 500–600 K, the main Ni peak narrows significantly, and the satellite intensity diminishes, even as the overall Ni

signal increases. This simultaneous sharpening of the peak and rise in intensity suggest a redistribution of Ni to the surface, likely driven by a temperature window in which Ni becomes mobile and is stabilized by surface oxygen species. Importantly, the binding energy remains consistent with Ni^{2+} throughout this regime, indicating that the Ni remains oxidized but undergoes a change in coordination environment or surface binding configuration. Only upon further heating beyond 600 K does the Ni signal begin to diminish.

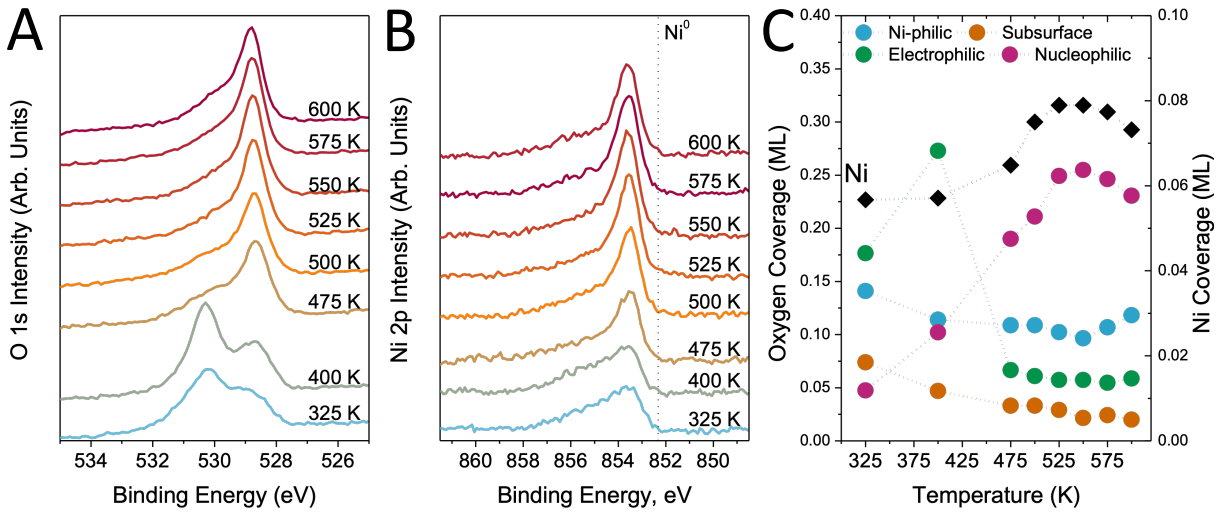

Figure 8.2. The shift in surface composition of NiAg(111) as a function of temperature in an O_2 environment. XPS spectra of NiAg(111) being annealed in 10 mTorr O_2 shows the shift in O 1s spectra **(A)** from higher to lower binding energies as the Ni $2p_{3/2}$ spectra **(B)** narrows but remains at a constant binding energy. Integrated areas of (A) and (B) show the relative increase in both total Ni coverage and shift in oxygen species formation as temperatures rise in **(C).**

To more precisely resolve the temperature window in which Ni segregates to the surface of Ag(111), we conducted a fine-stepped thermal annealing experiment on a ~7% NiAg(111) sample in the presence of 10 mTorr O_2. The Ni $2p_3/_2$ XPS spectra reveal a modest increase in surface Ni coverage between 325 and 475 K, followed by a pronounced rise between 475 and 500 K (Fig. 8.2C). The intensity continues to increase slightly up to 525 K, at which point the surface coverage plateaus, maintaining a near-maximum until ~550 K. Beyond this temperature, the Ni signal begins to decline, consistent with thermal diffusion of Ni into the bulk.

The spectral shape of the Ni $2p_3/_2$ region evolves with temperature. At lower coverages (325–450 K), the peak is broad, characteristic of low-coverage Ni(II) species in a heterogeneous environment. As Ni segregates to the surface and coverage increases, the peak narrows significantly: indicating a more uniform local chemical environment. This evolution in peak morphology suggests that the increasing Ni population is not forming large clusters, but rather remains atomically dispersed, minimizing Ni–Ni interactions that may otherwise give rise to multiplet splitting or pronounced satellite features.

Simultaneous collection of O 1s spectra provides further insight into the surface chemistry governing Ni segregation. Four distinct oxygen species are known to form on NiAg(111): nucleophilic oxygen (~528.4 eV), electrophilic oxygen (~530.5 eV), subsurface oxygen (~531.1 eV), and Ni-bound "ni-philic" oxygen (~529.4 eV). At low temperature, the dominant species are electrophilic and ni-philic oxygen. As the sample is heated through the segregation window, the oxygen speciation shifts markedly: nucleophilic oxygen becomes the dominant component above ~500 K, consistent with prior studies showing that nucleophilic O forms preferentially at elevated temperatures under oxidizing conditions.

Interestingly, despite the concurrent increase in surface Ni, there is no significant rise in the ni-philic oxygen signal. Instead, the increase in surface Ni correlates more directly with the formation of nucleophilic oxygen. This observation challenges the notion that surface Ni always forms discrete Ni–O complexes in a 1:1 stoichiometry. Instead, it suggests that Ni may associate more loosely with the oxygenated Ag surface—perhaps residing at the periphery of nucleophilic O domains or within an extended, reconstructed O/Ag matrix. In this configuration, Ni could still interact strongly with oxygen, but in a manner that does not produce the spectral fingerprint of traditional ni-philic oxygen.

This model is further supported by the narrowing of the Ni $2p_3/_2$ peaks as the sample is heated. Rather than forming clusters or NiO-like domains, the surface Ni appears to remain highly dispersed, likely coordinated by the surrounding oxygen environment in a manner that suppresses electronic features such as satellites. The lack of satellite intensity and the absence of multiplet structure are consistent with isolated Ni(II) species, suggesting that Ni–O interactions dominate over Ni–Ni coordination during segregation.

These results reinforce the view that Ni's role in promoting ethylene epoxidation may stem not from forming distinct Ni–O active sites, but rather from stabilizing the nucleophilic oxygen environment that supports selective epoxide formation. By enhancing nucleophilic oxygen coverage while remaining electronically dynamic and spatially dispersed, Ni may contribute to both catalytic selectivity and structural resilience under redox cycling.

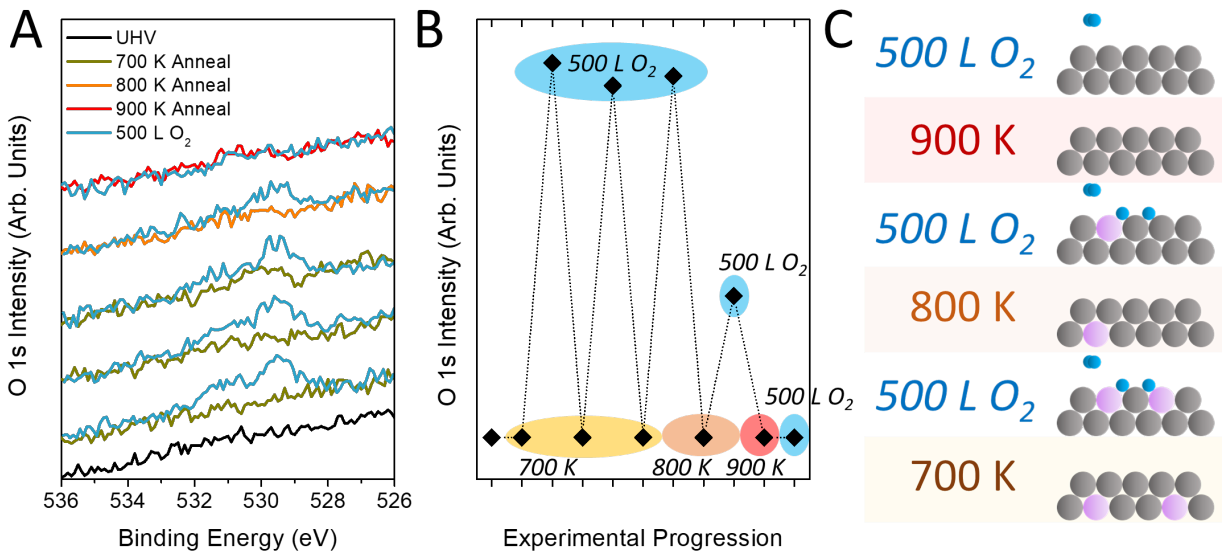

Figure 8.3 Redox cycling of 2% NiAg(111). (A) O 1s spectra of NiAg(111) after exposure to 500 L O_2 at 350 K followed by annealing to 700 K (yellow), 800 K (orange), and 900 K (red). **(B)** Integrated areas of XPS spectra from **(A)** and **(C)** cartoon description of Ni dissolution into bulk Ag(111) with increased anneal temperatures.

Given the demonstrated mobility of Ni in oxidizing environments, a key question is whether surface Ni enrichment is reversible after high-temperature annealing. Previous temperature-programmed desorption (TPD) studies have shown that subsurface Ni in NiAg(111) can reappear at the surface with oxygen exposure after repeated heating cycles up to ~700 K, suggesting a degree of reversibility in Ni segregation. To investigate this behavior more systematically and explore its upper thermal limits, we employed XPS to track both Ni surface coverage and oxygen speciation over multiple annealing and reoxidation cycles on a 2% NiAg(111) sample.

Upon initial exposure to 500 L O_2 at 350 K, the NiAg(111) surface exhibits a low but consistent O 1s signal composed primarily of Ni-bound oxygen (~529.4 eV), accompanied by a smaller feature corresponding to electrophilic oxygen on adjacent Ag sites (~530.4 eV) (Fig. 8.3A). This distribution indicates limited oxygen spillover from Ni to Ag at low coverage, but nonetheless confirms that even submonolayer doses of O_2 are sufficient to activate some degree of spillover from Ni sites.

Following a thermal anneal to 700 K, the sample was re-exposed to 500 L O_2. XPS reveals that the oxygen signal recovers to near-identical levels, and the Ni 2p signal remains clearly detectable, indicating that Ni segregation is reversible under these conditions. These observations are consistent with prior TPD results.

However, when the surface is flash-annealed to 800 K and re-exposed to O_2, the oxygen signal is significantly diminished (Fig 8.3B). The remaining O 1s intensity is almost entirely attributed to the Ni-philic component, with little to no evidence of spillover to Ag. Simultaneously, the Ni $2p_3/_2$ signal drops considerably, indicating that a substantial fraction of Ni has migrated below the XPS probing depth. The reduction in spillover following high-temperature annealing implies that the density of accessible Ni sites at the surface has declined to a point where oxygen activation is no longer sufficient to drive oxygen migration across the alloy interface.

To further probe the limits of Ni reversibility, the sample was subjected to an additional flash to 900 K, followed by a final 500 L O_2 exposure. At this stage, no oxygen signal is detected on the surface, and the Ni 2p signal remains absent. This result suggests that Ni has diffused irreversibly into the Ag bulk and is no longer available to participate in surface oxidation or spillover chemistry. The lack of any oxygen adsorption implies that the catalytic surface is now functionally equivalent to pure Ag(111), with negligible contributions from Ni.

8.5 Conclusions

These results collectively demonstrate that the spatial distribution and chemical state of Ni in NiAg(111) are governed by a relationship between redox environment and thermal treatment. Under reducing conditions (UHV), Ni irreversibly diffuses into the Ag bulk upon annealing, regardless of prior oxidation, limiting its surface availability. In contrast, when annealed in an

oxidizing atmosphere, surface Ni coverage increases substantially between 475–550 K, indicating that oxygen promotes Ni segregation to the surface. This surface enrichment occurs within a defined thermal window; beyond ~650 K, oxygen desorbs and Ni begins to dissolve into the bulk. Annealing above 700 K results in irreversible loss of Ni from the surface, with diminished ability to support spillover or oxygen activation.

The correlation between Ni surface enrichment and the formation of nucleophilic oxygen species suggests that Ni does not simply form discrete Ni–O complexes but may stabilize oxygen within extended O/Ag domains. This dispersed configuration likely facilitates oxygen activation while limiting Ni–Ni interactions, consistent with the absence of satellite features in the Ni 2p XPS spectra.

Overall, these findings reveal that surface-accessible Ni is not static, but rather dynamically modulated by redox environment and temperature. While O_2 exposure enables re-segregation of subsurface Ni and sustains active site populations, high-temperature operation poses a risk of irreversible Ni loss. Designing redox-responsive alloy catalysts therefore requires careful control over both the chemical potential of the environment and the thermal conditions of operation—factors that are critical to ensuring long-term activity, selectivity, and structural resilience under working conditions.

8.6 References

(1) Pinaeva, L. G.; Noskov, A. S. Prospects for the Development of Ethylene Oxide Production Catalysts and Processes (Review). *Pet. Chem.* **2020**, *60* (11), 1191–1206. https://doi.org/10.1134/S096554412011016X.

(2) Markets, R. and. *Ethylene Oxide Global Industry Report 2025: Market to Reach $67.7 Billion by 2030 - Increasing Investment in Chemical Research and Development Propels Innovations in Applications*. GlobeNewswire News Room. https://www.globenewswire.com/news-release/2025/03/17/3043453/28124/en/Ethylene-Oxide-Global-Industry-Report-2025-Market-to-Reach-67-7-Billion-by-2030-Increasing-Investment-in-Chemical-Research-and-Development-Propels-Innovations-in-Applications.html (accessed 2025-04-22).

(3) Vodyankina, O. V. Silver Catalysts for the Partial Oxidation of Alcohols. *Catal. Ind.* **2022**, *14* (3), 314–326. https://doi.org/10.1134/S2070050422030059.

(4) Nagy, A.; Mestl, G. High Temperature Partial Oxidation Reactions over Silver Catalysts. *Applied Catalysis A: General* **1999**, *188* (1), 337–353. https://doi.org/10.1016/S0926-860X(99)00246-X.

(5) Qian, M.; Liauw, M. A.; Emig, G. Formaldehyde Synthesis from Methanol over Silver Catalysts. *Applied Catalysis A: General* **2003**, *238* (2), 211–222. https://doi.org/10.1016/S0926-860X(02)00340-X.

(6) Karatok, M.; Sensoy, M. G.; Vovk, E. I.; Ustunel, H.; Toffoli, D.; Ozensoy, E. Formaldehyde Selectivity in Methanol Partial Oxidation on Silver: Effect of Reactive Oxygen Species, Surface Reconstruction, and Stability of Intermediates. *ACS Catal.* **2021**, *11* (10), 6200–6209. https://doi.org/10.1021/acscatal.1c00344.

(7) Carbonio, E. A.; Rocha, T. C. R.; Klyushin, A. Y.; Píš, I.; Magnano, E.; Nappini, S.; Piccinin, S.; Knop-Gericke, A.; Schlögl, R.; Jones, T. E. Are Multiple Oxygen Species Selective in Ethylene Epoxidation on Silver? *Chemical Science* **2018**, *9* (4), 990–998. https://doi.org/10.1039/c7sc04728b.

(8) Aljama, H.; Yoo, J. S.; Nørskov, J. K.; Abild-Pedersen, F.; Studt, F. Methanol Partial Oxidation on Ag(1 1 1) from First Principles. *ChemCatChem* **2016**, *8* (23), 3621–3625. https://doi.org/10.1002/cctc.201601053.

(9) Jones, T. E.; Wyrwich, R.; Böcklein, S.; Carbonio, E. A.; Greiner, M. T.; Klyushin, A. Y.; Moritz, W.; Locatelli, A.; Menteş, T. O.; Niño, M. A.; Knop-Gericke, A.; Schlögl, R.; Günther, S.; Wintterlin, J.; Piccinin, S. The Selective Species in Ethylene Epoxidation on Silver. *ACS Catalysis* **2018**, *8* (5), 3844–3852. https://doi.org/10.1021/acscatal.8b00660.

(10) Stegelmann, C.; Schiødt, N. C.; Campbell, C. T.; Stoltze, P. Microkinetic Modeling of Ethylene Oxidation over Silver. *Journal of Catalysis* **2004**, *221* (2), 630–649. https://doi.org/10.1016/j.jcat.2003.10.004.

(11) Bukhtiyarov, V. I.; Nizovskii, A. I.; Bluhm, H.; Hävecker, M.; Kleimenov, E.; Knop-Gericke, A.; Schlögl, R. Combined in Situ XPS and PTRMS Study of Ethylene Epoxidation over Silver. *Journal of Catalysis* **2006**, *238* (2), 260–269. https://doi.org/10.1016/j.jcat.2005.11.043.

(12) Li, H.; Cao, A.; Nørskov, J. K. Understanding Trends in Ethylene Epoxidation on Group IB Metals. *ACS Catal.* **2021**, *11* (19), 12052–12057. https://doi.org/10.1021/acscatal.1c03094.

(13) Hwang, A.; Klaucke, J.; Lizandara-Pueyo, C.; Karpov, A.; Iglesia, E. Roles of Re and Cs Promoters and Organochlorine Moderators in the Synthesis of Ethylene Oxide on Ag-Based Catalysts. *ChemCatChem* **2023**. https://doi.org/10.1002/cctc.202301369.

(14) Campbell, C. T. Chlorine Promoters in Selective Ethylene Epoxidation over Ag(111): A Comparison with Ag(110). *Journal of Catalysis* **1986**, *99* (1), 28–38. https://doi.org/10.1016/0021-9517(86)90195-8.
(15) Chen, C. J.; Harris, J. W.; Bhan, A. Kinetics of Ethylene Epoxidation on a Promoted Ag/α-Al2O3 Catalyst—The Effects of Product and Chloride Co-Feeds on Rates and Selectivity. *Chemistry - A European Journal* **2018**, *24* (47), 12405–12415. https://doi.org/10.1002/chem.201801356.
(16) Van Hoof, A. J. F.; Hermans, E. A. R.; Van Bavel, A. P.; Friedrich, H.; Hensen, E. J. M. Structure Sensitivity of Silver-Catalyzed Ethylene Epoxidation. *ACS Catalysis* **2019**, *9* (11), 9829–9839. https://doi.org/10.1021/acscatal.9b02720.
(17) Linic, S.; Barteau, M. A. Formation of a Stable Surface Oxametallacycle That Produces Ethylene Oxide. *Journal of the American Chemical Society* **2002**, *124* (2), 310–317. https://doi.org/10.1021/ja0118136.
(18) Linic, S.; Barteau, M. A. Construction of a Reaction Coordinate and a Microkinetic Model for Ethylene Epoxidation on Silver from DFT Calculations and Surface Science Experiments. *Journal of Catalysis* **2003**, *214* (2), 200–212. https://doi.org/10.1016/S0021-9517(02)00156-2.
(19) Jankowiak, J. T.; Barteau, M. A. Ethylene Epoxidation over Silver and Copper-Silver Bimetallic Catalysts: I. Kinetics and Selectivity. *Journal of Catalysis* **2005**, *236* (2), 366–378. https://doi.org/10.1016/j.jcat.2005.10.018.
(20) Huš, M.; Hellman, A. Dipole Effect on Ethylene Epoxidation: Influence of Alkali Metals and Chlorine. *Journal of Catalysis* **2018**, *363*, 18–25. https://doi.org/10.1016/j.jcat.2018.04.008.
(21) Diao, W.; Digiulio, C. D.; Schaal, M. T.; Ma, S.; Monnier, J. R. An Investigation on the Role of Re as a Promoter in Ag-Cs-Re/α-Al2O3 High-Selectivity, Ethylene Epoxidation Catalysts. *Journal of Catalysis* **2015**, *322*, 14–23. https://doi.org/10.1016/j.jcat.2014.11.007.
(22) Pu, T.; Tian, H.; Ford, M. E.; Rangarajan, S.; Wachs, I. E. Overview of Selective Oxidation of Ethylene to Ethylene Oxide by Ag Catalysts. *ACS Catalysis* **2019**, *9* (12), 10727–10750. https://doi.org/10.1021/acscatal.9b03443.
(23) Isegawa, K.; Ueda, K.; Amemiya, K.; Mase, K.; Kondoh, H. Formation and Behavior of Carbonates on Ag(110) in the Presence of Ethylene and Oxygen. *J. Phys. Chem. C* **2021**, *125* (17), 9032–9037. https://doi.org/10.1021/acs.jpcc.0c11597.
(24) Serafin, J. G.; Liu, A. C.; Seyedmonir, S. R. Surface Science and the Silver-Catalyzed Epoxidation of Ethylene: An Industrial Perspective. *Journal of Molecular Catalysis A: Chemical* **1998**, *131* (1), 157–168. https://doi.org/10.1016/S1381-1169(97)00263-X.
(25) Lu, X.; Zhang, P.; Deng, Z.; He, C.; Zhang, R. Reaction Gas Induced Activity Enhancement for Silver Catalyst in Ethylene Epoxidation. *Fuel* **2025**, *381*, 133346. https://doi.org/10.1016/j.fuel.2024.133346.
(26) Jalil, A.; Happel, E. E.; Cramer, L.; Hunt, A.; Hoffman, A. S.; Waluyo, I.; Montemore, M. M.; Christopher, P.; Sykes, E. C. H. Nickel Promotes Selective Ethylene Epoxidation on Silver. *Science* **2025**, *387* (6736), 869–873. https://doi.org/10.1126/science.adt1213.
(27) Waluyo, I.; Hunt, A. Ambient Pressure X-Ray Photoelectron Spectroscopy at the IOS (23-ID-2) Beamline at the National Synchrotron Light Source II. *Synchrotron Radiation News* **2022**, *35* (3), 31–38. https://doi.org/10.1080/08940886.2022.2082180/ASSET/BDB66E5A-0587-4FF9-8A92-46D92E6F9330/ASSETS/IMAGES/GSRN_A_2082180_F0005_C.JPG.

(28) Turano, M. E.; Farber, R. G.; Oskorep, E. C. N.; Rosenberg, R. A.; Killelea, D. R. Characterization of Oxygenaceous Species Formed by Exposure of Ag(111) to Atomic Oxygen. *Journal of Physical Chemistry C* **2020**, *124* (2), 1382–1389. https://doi.org/10.1021/acs.jpcc.9b09131.
(29) Martin, N. M.; Klacar, S.; Grönbeck, H.; Knudsen, J.; Schnadt, J.; Blomberg, S.; Gustafson, J.; Lundgren, E. High-Coverage Oxygen-Induced Surface Structures on Ag(111). *J. Phys. Chem. C* **2014**, *118* (28), 15324–15331. https://doi.org/10.1021/jp504387p.
(30) Uhlenbrock, S.; Scharfschwerdt, C.; Neumann, M.; Illing, G.; Freund, H. J. The Influence of Defects on the Ni 2p and O 1s XPS of NiO. *Journal of Physics: Condensed Matter* **1992**, *4* (40), 7973–7978. https://doi.org/10.1088/0953-8984/4/40/009.
(31) Mcintyre, N. S.; Cook, M. G. X-Ray Photoelectron Studies on Some Oxides and Hydroxides of Cobalt, Nickel, and Copper. *Analytical Chemistry* **1975**, *47* (13), 2208–2213. https://doi.org/10.1021/ac60363a034.
(32) Campbell, C. T.; Koel, B. E. Chlorine Promotion of Selective Ethylene Oxidation over Ag(110): Kinetics and Mechanism. *Journal of Catalysis* **1985**, *92* (2), 272–283. https://doi.org/10.1016/0021-9517(85)90261-1.
(33) Force, E. L.; Bell, A. T. The Relationship of Adsorbed Species Observed by Infrared Spectroscopy to the Mechanism of Ethylene Oxidation over Silver. *Journal of Catalysis* **1975**, *40* (3), 356–371. https://doi.org/10.1016/0021-9517(75)90267-5.
(34) Kaichev, V. V.; Bukhtiyarov, V. I.; Hävecker, M.; Knop-Gercke, A.; Mayer, R. W.; Schlögl, R. The Nature of Electrophilic and Nucleophilic Oxygen Adsorbed on Silver. *Kinetics and Catalysis* **2003**, *44* (3), 432–440. https://doi.org/10.1023/A:1024459305551.
(35) Rocca, M.; Savio, L.; Vattuone, L.; Burghaus, U.; Palomba, V.; Novelli, N.; Buatier de Mongeot, F.; Valbusa, U.; Gunnella, R.; Comelli, G.; Baraldi, A.; Lizzit, S.; Paolucci, G. Phase Transition of Dissociatively Adsorbed Oxygen on Ag(001). *Phys. Rev. B* **2000**, *61* (1), 213–227. https://doi.org/10.1103/PhysRevB.61.213.
(36) Johansson, F. O. L.; Leitner, T.; Bidermane, I.; Born, A.; Föhlisch, A.; Svensson, S.; Mårtensson, N.; Lindblad, A. Auger- and Photoelectron Coincidences of Molecular O2 Adsorbed on Ag(111). *Journal of Electron Spectroscopy and Related Phenomena* **2022**, *256*, 147174. https://doi.org/10.1016/j.elspec.2022.147174.

Chapter 9: The Effect of Ni Surface Oxygen Speciation on Ag(111) under Conditions Relevant to Ethylene Epoxidation

Elizabeth E. Happel, Avery S. Daniels, Cole Easton, Adrian Hunt, Matthew M. Montemore, Iradwikanari Waluyo, and E. Charles H. Sykes

9.1 Abstract:

Very recent research has identified that trace amounts of Ni promote the selectivity of ethylene epoxidation to the same degree as the ubiquitous industrial promotor Cl. Given that the selective epoxidation of ethylene over supported silver catalysts is strongly influenced by the species and distribution of oxygen at the surface it is imperative to understand the influence of Ni. Using ambient pressure X-ray photoelectron spectroscopy (AP-XPS), we compare Ag(111) and Ni-doped Ag(111) (NiAg) surfaces under varying O_2:C_2H_4 ratios and temperatures relevant to industrial operation. Both surfaces form comparable coverages of nucleophilic oxygen (~0.3 monolayers) in oxygen-only environments, but NiAg additionally stabilizes Ni–O, subsurface oxygen, and trace electrophilic oxygen, resulting in nearly twice the total oxygen coverage under the same conditions. Upon ethylene introduction, both surfaces generate surface carbonates, yet NiAg uniquely supports dual-site carbonate formation with distinct Ag and Ni associated contributions. Across all conditions, NiAg maintains higher surface oxygen coverage and greater speciation than Ag alone. Temperature cycling reveals that NiAg responds more rapidly to thermal changes, recovering nucleophilic oxygen and reversing hydrocarbon buildup at lower temperatures, whereas Ag remains largely unchanged under the same perturbations and more prone to persistent surface carbon. In addition to subsurface oxygen and carbonate on Ag and several addition species on NiAg a low-coverage O_2^- species is observed on both surfaces at low temperature and disappears with heating, potentially linking to transient intermediates relevant to epoxidation. These findings demonstrate that Ni alters both the composition and dynamic response of the Ag surface under realistic conditions, offering new insight into how promoters enhance catalytic selectivity and durability in ethylene epoxidation.

9.2 Introduction

Ethylene oxide (EO) is an important precursor chemical used in the production of coolants, pharmaceuticals, and certain plastic resins. Demand for EO is projected to grow at a rate of approximately 5% annually, largely due to the increasing use of polyester fibers.[1,2] However, the massive reach of this reaction comes at a significant environmental cost, with an estimated 3.4 million tons of CO_2 produced annually as a byproduct.[3]

To catalyze this reaction, heavily promoted, supported silver nanoparticles are currently employed, achieving selectivities around ~90% toward EO formation.[4–6] Despite this success, the catalyst system remains complex and not well understood. Achieving such high selectivity requires the addition of multiple promoters, most notably chlorine, but also cesium, molybdenum, and rhenium, which contribute to a crowded surface and complicate mechanistic interpretation. [4–6] Furthermore, these materials, particularly chlorine, are toxic and environmentally harmful, highlighting the need for more sustainable alternatives.

One of the core challenges in designing improved catalysts for EO production is the lack of mechanistic understanding of the reaction. While some key features have been identified, many uncertainties remain. For example, two major types of oxygen species are known to form on Ag surfaces under reaction conditions: electrophilic oxygen (binding energy ~530.4 eV), which is commonly associated with EO selectivity, and nucleophilic oxygen (binding energy ~528.4 eV), which is often linked to the combustion or total oxidation pathway. [7–10] These species play critical roles in determining selectivity, yet their precise interactions with promoters and ethylene remain elusive.

Other species like hydroxy groups and subsurface oxygen are also thought to play a role in reactivity of the surface. [11–16] However, the crowded and heterogeneous nature of industrial catalyst surfaces makes it difficult to isolate their contributions. In fact, it is commonly accepted that surface crowding and having a complex, densely packed surface is one of the most important effects of promoters in Ag systems.[17–20]

Beyond oxygen species, there is growing interest in the role of carbonate adsorbates on the catalyst surface. Initially, carbonate was thought to form as a byproduct of unselective CO_2 formation and to act as a poison that deactivates the catalyst. [21] More recent studies, however,

suggest that carbonate may instead stabilize subsurface oxygen, thus increasing the reservoir of reactive oxygen species available to replenish surface sites.[22] Despite these insights, no consensus has been reached regarding the mechanistic function of carbonate, and its role remains actively debated. [6,23]

In this context, NiAg has recently emerged as a promising alternative catalyst. NiAg can achieve selectivity levels comparable to chlorine-promoted Ag surfaces, but without the associated environmental hazards. Prior studies have shown that, under oxidizing conditions, Ni incorporation into Ag surfaces stabilizes reactive oxygen species involved in the total oxidation pathway. This stabilization is posited to reduce the reactivity of unselective oxygen, thereby improving EO selectivity. However, while these findings are promising, the surface of NiAg has not yet been investigated under the industrial conditions of ethylene epoxidation, where both ethylene and oxygen are present.

Although it is known that Ni promotes the formation of diverse oxygen species and stabilizes nucleophilic oxygen on Ag(111) under oxidizing conditions, its behavior under the more reducing, hydrocarbon-rich environments typical of EO production remains unexplored. In this study, we address this gap by using synchrotron-based ambient pressure X-ray photoelectron spectroscopy (AP-XPS) to compare the surface chemistry of Ag(111) and NiAg(111) under various gas environments and temperatures. This approach allows us to examine the dynamic restructuring and evolution of surface species on NiAg relative to Ag under industrially relevant ethylene epoxidation conditions.

9.3 Results and Discussion

Understanding the transformation of both Ag(111) and NiAg(111) in different environments of oxygen and ethylene provides insight into the similarities and differences between each surface as a catalyst for ethylene epoxidation. It is known that Ni facilitates the facile activation of O_2 onto Ag(111) surfaces, and this effect is evident upon exposing both Ag(111) and 30% NiAg(111) to 0.2 Torr of O_2 at 433 K, where XPS spectra were collected continuously until oxygen saturation. From the O 1s spectra (Figure 9.1A), while similar binding energy (BE) species are observed on both surfaces, NiAg(111) displays both a higher overall oxygen coverage and a broader distribution of BE species, as evidenced by the wider light blue traces.

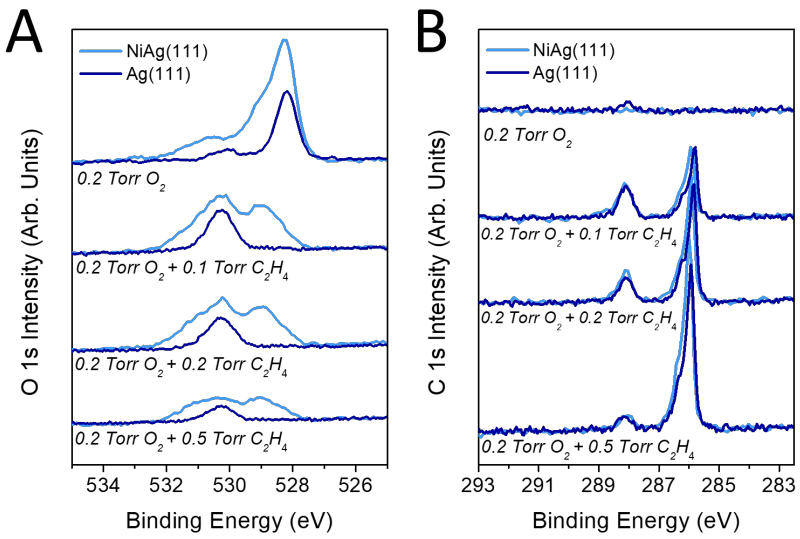

Figure 9.1. A comparison of XPS Spectra for Ag(111) and NiAg(111) under different ratios of ethylene and oxygen. (A) O 1s and **(B)** C 1s spectra of Ag(111) (dark blue) and 30% NiAg(111) (light blue) first under 0.2 Torr O_2 followed by the stepwise addition of ethylene at 433 K. Alternating carbon and oxygen spectra were taken under each condition until no further changes were detectible with XPS.

Upon introduction of ethylene, both surfaces undergo a rapid transformation in the O 1s spectra: low-BE oxygen species decrease in intensity and overall oxygen coverage declines over time. Ethylene dosing is clearly seen in the C 1s spectra through the emergence of a sharp gas-phase peak centered in Figure 9.1B. In addition to this gas-phase feature, a distinct surface-bound carbon species appears on both Ag and NiAg surfaces. Notably, the evolution of the C 1s spectra is more closely mirrored between the two surfaces compared to the O 1s spectra, suggesting more comparable carbon-related behavior under reaction conditions.

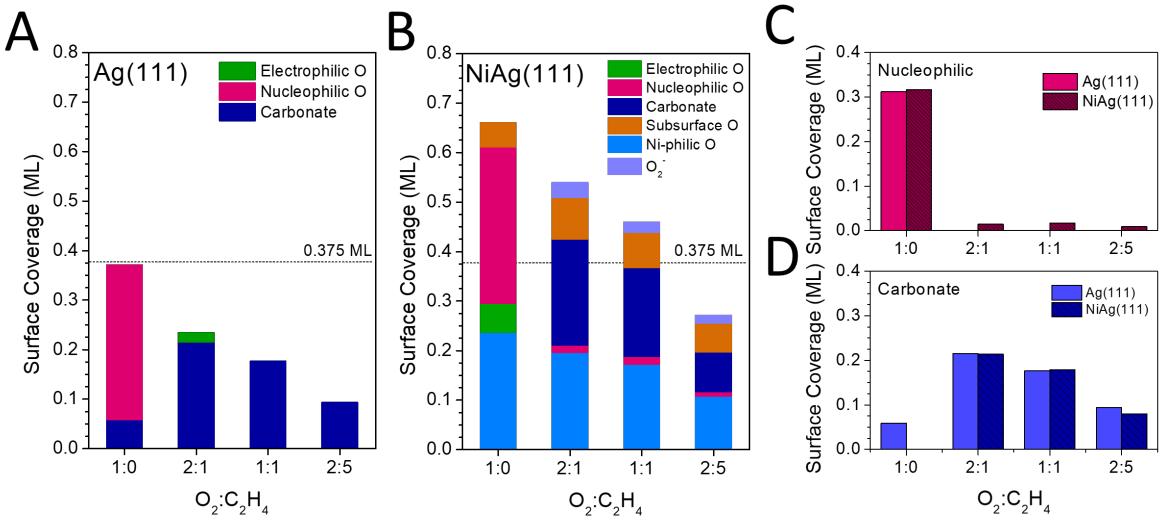

Figure 9.2. Quantification of oxygen containing surface species on Ag(111) and NiAg(111) different ratios of ethylene and oxygen. The surface coverage in monolayers with respect to the Ag(111) surface of **(A)** Ag(111) and **(B)** NiAg(111) under purely oxidizing conditions followed by the stepwise addition of ethylene to the oxygen environment. While NiAg(111) consistently has a higher total coverage of oxygen species both surface exhibit similar coverages of **(C)** nucleophilic oxygen and **(D)** carbonates under the same conditions.

Under oxidizing conditions, the dominant oxygen species on both surfaces has a BE of ~528.4 eV, which aligns with the well-known nucleophilic oxygen associated with the p(4×4) reconstruction. At saturation, both surfaces reach a coverage of ~0.3 ML of this species (Figure 9.2), in agreement with literature values for nucleophilic oxygen saturation (~0.375 ML).[24–27] This finding indicates that the surfaces are fully covered in this state. Additionally, due to the elevated background pressure of oxygen in the chamber, the Ag(111) sample also accumulates some carbonate which is a known phenomenon in ambient pressure XPS setups. [28–30]

In addition to nucleophilic oxygen, NiAg(111) forms several other oxygen species when saturated under 0.2 Torr O_2. The second most prevalent is a species referred to as "Ni-philic" oxygen, with a BE around ~529.2 eV depending on the Ni content, consistent with oxygen bound to Ni sites in the surface alloy. This assignment is supported by the simultaneous presence of Ni(II) peaks in the Ni 2p spectra (Fig A9.1), suggesting partial formation of NiO-like structures. Two additional species are present in lower concentrations under oxidizing conditions: electrophilic oxygen (~530.4 eV) and subsurface oxygen (~531.5 eV). Electrophilic oxygen is

distinguished from is distinguished from carbonate by the absence of a corresponding carbonate feature in the C 1s spectrum, justifying its assignment despite their overlapping BEs ~530.4 eV.[10,31–33]

The coexistence of selective (electrophilic) and unselective (nucleophilic) oxygen species on NiAg(111) is notable and must be considered when evaluating the increased selectivity of this alloy for ethylene epoxidation. While NiAg(111) uniquely supports formation of selective electrophilic oxygen, it also stabilizes nucleophilic oxygen similarly to Ag under oxidizing conditions. Interestingly, upon ethylene introduction, the nucleophilic oxygen species decreases on both surfaces, but trace amounts persist on NiAg(111) even under the most reducing 2:5 O_2:C_2H_4 environment, suggesting greater thermal or chemical stability.

Carbonate formation exhibits similar qualitative trends on both surfaces. On Ag(111), carbonate becomes the dominant oxygen-containing species under oxidizing conditions (0.2 Torr O_2 : 0.1 Torr C_2H_4), reaching a surface coverage of ~0.2 ML, only slightly above the DFT-predicted saturation of ~0.16 ML, indicating near-complete surface saturation. This coverage remains consistent under near-equimolar oxygen and ethylene conditions but is reduced to ~0.1 ML under industrially relevant 2:5 O_2:C_2H_4 conditions, at which point a significant portion of the Ag surface becomes bare (see Chapter 3).

Similarly, carbonate coverage on NiAg(111) follows a comparable trend: decreasing from ~0.2 ML under oxidizing conditions to ~0.1 ML under more ethylene-rich environments. Despite this, the total oxygen coverage on NiAg(111) remains higher than on Ag(111) across all conditions. Ni-philic and subsurface oxygen species are retained during ethylene exposure, while carbonate decreases and a new peak at ~533 eV emerges, which we assign to water formation.[34,35] Water formation begins on Ag(111) after more significant temperature cycling (Figure 9.4).

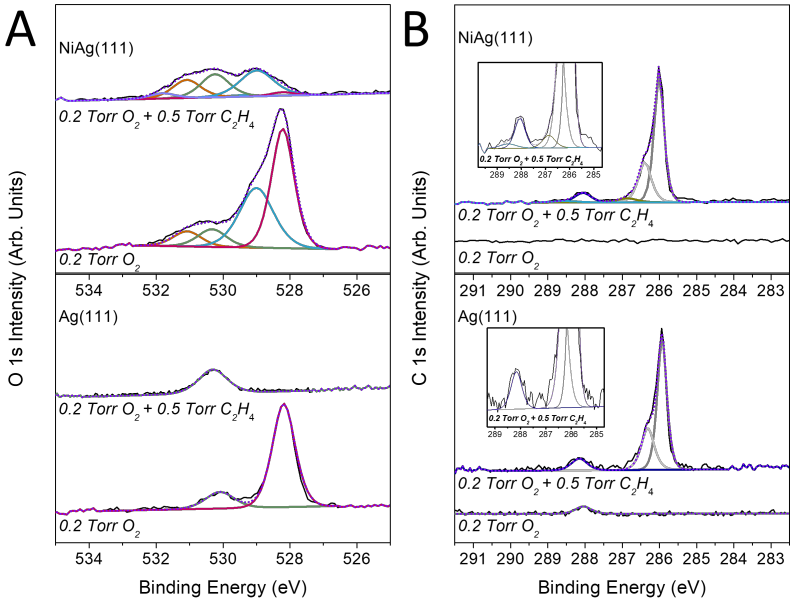

Figure 9.3. A comparison of surface species on Ag(111) and NiAg(111) under oxidizing and reducing conditions. Direct comparison of Ag(111) and NiAg(111) under first 0.2 Torr O_2 followed by 0.2 Torr O_2 and 0.5 Torr C_2H_4 reveals significant difference in the **(A)** O 1s spectra and **(B)** C 1s spectra. In addition to electrophilic (green) and nucleophilic (pink) oxygen species on both surfaces, NiAg(111) hosts other oxygen species including ni-philic (light blue) and subsurface (orange) species. The C 1s spectra both have distinct gas phase ethylene features (grey) as well as Ag bound carbonate (dark blue). NiAg(111) additionally hosts a Ni associated carbonate species also fit with a light blue trace. Sum of fit traces are displayed as purple dashed lines over original black traces.

However, differences in carbonate speciation between Ag and NiAg surfaces are revealed in the C 1s spectra (Figure 9.3B). Both samples exhibit a carbonate peak at ~288.1 eV, characteristic of carbonate bound to Ag.[25,28] However, NiAg additionally shows a distinct second peak at ~288.5 eV, attributed to carbonate bound to Ni, consistent with literature assignments.[36,37] At a 2:1 O_2:C_2H_4 ratio, the Ag:Ni carbonate peak ratio is ~70:30, shifting to ~80:20 as ethylene content increases. This difference in carbonate coordination may significantly affect carbonate reactivity and could influence selectivity.

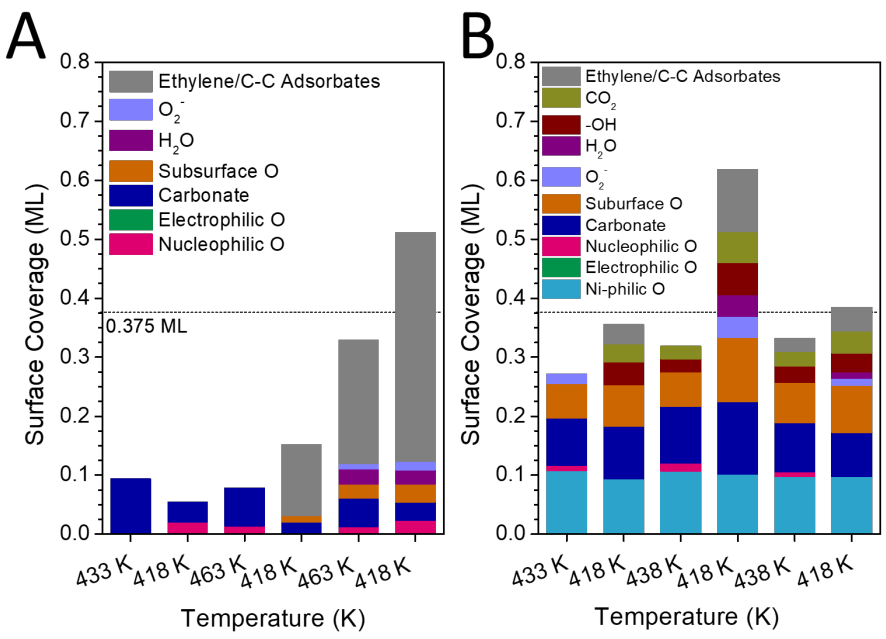

Figure 9.4. The effect of thermal cycling on Ag(111) and NiAg(111) under ethylene epoxidation conditions. Both Ag(111) **(A)** and NiAg(111) **(B)** show increases in carbonaceous species (grey) after lowering the surface temperature to 418 K. Cycling from cooler to hotter temperatures reveals the formation of an O_2^- species (dark purple) on both surfaces. The NiAg(111) surface also shows a build up of new species including CO_2 (yellow) and hydroxy groups (maroon).

To further explore the thermal behavior of the system, both samples were held in 0.2 Torr O_2 and 0.5 Torr C_2H_4 and subjected to heating and cooling cycles. At lower temperatures (418 K), both surfaces accumulate long-chain surface-bound carbon species, including ethylene-derived fragments and other low-BE carbonaceous species (Fig A9.2). NiAg accumulates these species more readily at this temperature but also responds more quickly to annealing. Heating to 438 K significantly reduces the carbonaceous coverage on NiAg(111) while concurrently increasing nucleophilic oxygen intensity (Figure 9.4). Ag(111), by contrast, shows neither a significant formation of nucleophilic oxygen nor the same rate of carbon species removal, even when heated to 463 K.

After thermal cycling, both samples were held at 418 K for extended periods. Under these conditions, a new O 1s peak emerges at ~532 eV on Ag(111) that had earlier grown on NiAg(111). Although its coverage remains low, this feature behaves reversibly with temperature and is reminiscent of the species assigned as O_2^- by Campbell and coworkers.[38] The appearance

of this feature only under high surface coverage at low temperatures suggests that it may require crowding to form. Given the consistently higher oxygen coverage on NiAg(111), this surface may be more conducive to O_2^- formation, though further investigation is warranted to confirm its identity and role in ethylene epoxidation.

9.4 Conclusions

The comparative analysis of surface species and coverages on Ag(111) and NiAg(111) surfaces highlights key mechanistic insights that help explain the recently discovered differences in selectivity observed in reactor studies of ethylene epoxidation. Most notably, the NiAg alloy consistently exhibits a higher surface coverage of oxygen-containing species than pure Ag under identical, industrially relevant conditions. The incorporation of Ni facilitates the formation and stabilization of additional oxygen species—including a Ni-philic species and subsurface oxygen—that persist across a range of temperatures and reaction conditions. Of particular significance is the behavior of nucleophilic oxygen: while this species saturates at similar coverage on both surfaces, it is reversibly formed and retained on NiAg(111) as a function of temperature, in contrast to its depletion on Ag(111). This persistence suggests that the nucleophilic oxygen species are more stable and less reactive toward total combustion on NiAg, providing further support for the observed increased thermal stability of nucleophilic oxygen reported in our previous work (see Chapter 6).

Interestingly, while the total carbonate coverage remains similar on both Ag(111) and NiAg(111), two distinct carbonate species are observed on the bimetallic surface. One binds to Ag sites, as on the pure Ag surface, while the other appears to bind at or near Ni. Although we cannot definitively say the Ni-bound carbonate is more stable, its presence under conditions where the Ag-bound species alone would typically dominate suggests that Ni may influence carbonate binding in a way that alters surface reactivity. This difference could affect selectivity by blocking reactive sites or limiting the further oxidation of intermediates into CO_2.

Finally, Ni promotes the formation and spillover of a wider variety of oxygen species, including even subsurface oxygen, which is often thought to play a role in replenishing reactive sites at the surface. This oxygen-rich, crowded surface mirrors one of the commonly proposed mechanisms for industrial promoters: disrupting pools of reactive, unselective oxygen through site blocking

and surface crowding. In this way, the behavior of NiAg aligns with established concepts in catalyst design while offering new insight into the microscopic origins of selectivity. Together, these findings provide mechanistic insight into the distinct behaviors of Ag and NiAg surfaces under reaction conditions and offer a foundation for future investigations. These results can serve as a useful reference for theoretical and experimental studies aimed at understanding and improving selectivity in ethylene epoxidation.

9.5 References

(1) Pinaeva, L. G.; Noskov, A. S. Prospects for the Development of Ethylene Oxide Production Catalysts and Processes (Review). *Pet. Chem.* **2020**, *60* (11), 1191–1206. https://doi.org/10.1134/S096554412011016X.

(2) Markets, R. and. *Ethylene Oxide Global Industry Report 2025: Market to Reach $67.7 Billion by 2030 - Increasing Investment in Chemical Research and Development Propels Innovations in Applications*. GlobeNewswire News Room. https://www.globenewswire.com/news-release/2025/03/17/3043453/28124/en/Ethylene-Oxide-Global-Industry-Report-2025-Market-to-Reach-67-7-Billion-by-2030-Increasing-Investment-in-Chemical-Research-and-Development-Propels-Innovations-in-Applications.html (accessed 2025-04-22).

(3) Ghanta, M.; Ruddy, T.; Fahey, D.; Busch, D.; Subramaniam, B. Is the Liquid-Phase H2O2-Based Ethylene Oxide Process More Economical and Greener Than the Gas-Phase O2-Based Silver-Catalyzed Process? *Ind. Eng. Chem. Res.* **2013**, *52* (1), 18–29. https://doi.org/10.1021/ie301601y.

(4) Hwang, A.; Klaucke, J.; Lizandara-Pueyo, C.; Karpov, A.; Iglesia, E. Roles of Re and Cs Promoters and Organochlorine Moderators in the Synthesis of Ethylene Oxide on Ag-Based Catalysts. *ChemCatChem* **2023**. https://doi.org/10.1002/cctc.202301369.

(5) Diao, W.; Digiulio, C. D.; Schaal, M. T.; Ma, S.; Monnier, J. R. An Investigation on the Role of Re as a Promoter in Ag-Cs-Re/α-Al2O3 High-Selectivity, Ethylene Epoxidation Catalysts. *J. Catal.* **2015**, *322*, 14–23. https://doi.org/10.1016/j.jcat.2014.11.007.

(6) Pu, T.; Tian, H.; Ford, M. E.; Rangarajan, S.; Wachs, I. E. Overview of Selective Oxidation of Ethylene to Ethylene Oxide by Ag Catalysts. *ACS Catal.* **2019**, *9* (12), 10727–10750. https://doi.org/10.1021/acscatal.9b03443.

(7) Jones, T. E.; Wyrwich, R.; Böcklein, S.; Carbonio, E. A.; Greiner, M. T.; Klyushin, A. Y.; Moritz, W.; Locatelli, A.; Menteş, T. O.; Niño, M. A.; Knop-Gericke, A.; Schlögl, R.; Günther, S.; Wintterlin, J.; Piccinin, S. The Selective Species in Ethylene Epoxidation on Silver. *ACS Catal.* **2018**, *8* (5), 3844–3852. https://doi.org/10.1021/acscatal.8b00660.

(8) Stegelmann, C.; Schiødt, N. C.; Campbell, C. T.; Stoltze, P. Microkinetic Modeling of Ethylene Oxidation over Silver. *J. Catal.* **2004**, *221* (2), 630–649. https://doi.org/10.1016/j.jcat.2003.10.004.

(9) Carbonio, E. A.; Rocha, T. C. R.; Klyushin, A. Y.; Píš, I.; Magnano, E.; Nappini, S.; Piccinin, S.; Knop-Gericke, A.; Schlögl, R.; Jones, T. E. Are Multiple Oxygen Species Selective in Ethylene Epoxidation on Silver? *Chem. Sci.* **2018**, *9* (4), 990–998. https://doi.org/10.1039/c7sc04728b.

(10) Bukhtiyarov, V. I.; Nizovskii, A. I.; Bluhm, H.; Hävecker, M.; Kleimenov, E.; Knop-Gericke, A.; Schlögl, R. Combined in Situ XPS and PTRMS Study of Ethylene Epoxidation over Silver. *J. Catal.* **2006**, *238* (2), 260–269. https://doi.org/10.1016/j.jcat.2005.11.043.

(11) Guo, M.; Dongfang, N.; Iannuzzi, M.; van Bokhoven, J. A.; Artiglia, L. Structure and Reactivity of Active Oxygen Species on Silver Surfaces for Ethylene Epoxidation. *ACS Catal.* **2024**, 10234–10244. https://doi.org/10.1021/acscatal.4c01566.

(12) Mize, C. J.; Crosby, L. D.; Isbill, S. B.; Roy, S. Insight into Subsurface Adsorption Derived from a Lattice-Gas Model and Monte Carlo Simulations. *J. Phys. Chem. C* **2022**, *126* (11), 5343–5353. https://doi.org/10.1021/acs.jpcc.2c00342.

(13) Xu, Y.; Greeley, J.; Mavrikakis, M. Effect of Subsurface Oxygen on the Reactivity of the Ag(111) Surface. *J. Am. Chem. Soc.* **2005**, *127* (37), 12823–12827. https://doi.org/10.1021/ja043727m.
(14) Pawela-Crew, J.; Madix, R. J.; Stöhr, J. The Effect of Subsurface Oxygen on the Orientation of Molecular Oxygen on Ag(110). *Surf. Sci.* **1995**, *339* (1–2), 23–28. https://doi.org/10.1016/0039-6028(95)00646-X.
(15) Chen, D.; Chen, L.; Zhao, Q. C.; Yang, Z. X.; Shang, C.; Liu, Z. P. Square-Pyramidal Subsurface Oxygen [Ag4OAg] Drives Selective Ethene Epoxidation on Silver. *Nat. Catal.* **2024**, *7* (5), 536–545. https://doi.org/10.1038/s41929-024-01135-2.
(16) van den Reijen, J. E.; Versluis, W. C.; Kanungo, S.; d'Angelo, M. F.; de Jong, K. P.; de Jongh, P. E. From Qualitative to Quantitative Understanding of Support Effects on the Selectivity in Silver Catalyzed Ethylene Epoxidation. *Catal. Today* **2019**, *338*, 31–39. https://doi.org/10.1016/j.cattod.2019.04.049.
(17) Linic, S.; Barteau, M. A. Formation of a Stable Surface Oxametallacycle That Produces Ethylene Oxide. *J. Am. Chem. Soc.* **2002**, *124* (2), 310–317. https://doi.org/10.1021/ja0118136.
(18) Campbell, C. T. Chlorine Promoters in Selective Ethylene Epoxidation over Ag(111): A Comparison with Ag(L110). *J. Catal.* **1986**, *99*, 28–38.
(19) Iyer, K. R.; Bhan, A. The Role of Chlorine Promoters in Mediating Particle Size Effects in Silver-Catalyzed Ethylene Epoxidation. *J. Catal.* **2024**, *436*, 115583. https://doi.org/10.1016/j.jcat.2024.115583.
(20) Jones, T. E.; Wyrwich, R.; Böcklein, S.; Rocha, T. C. R.; Carbonio, E. A.; Knop-Gericke, A.; Schlögl, R.; Günther, S.; Wintterlin, J.; Piccinin, S. Oxidation of Ethylene on Oxygen Reconstructed Silver Surfaces. *J. Phys. Chem. C* **2016**, *120* (50), 28630–28638. https://doi.org/10.1021/acs.jpcc.6b10074.
(21) Serafin, J. G.; Liu, A. C.; Seyedmonir, S. R. Surface Science and the Silver-Catalyzed Epoxidation of Ethylene: An Industrial Perspective. *J. Mol. Catal. Chem.* **1998**, *131* (1), 157–168. https://doi.org/10.1016/S1381-1169(97)00263-X.
(22) Lu, X.; Zhang, P.; Deng, Z.; He, C.; Zhang, R. Reaction Gas Induced Activity Enhancement for Silver Catalyst in Ethylene Epoxidation. *Fuel* **2025**, *381*, 133346. https://doi.org/10.1016/j.fuel.2024.133346.
(23) Isegawa, K.; Ueda, K.; Amemiya, K.; Mase, K.; Kondoh, H. Formation and Behavior of Carbonates on Ag(110) in the Presence of Ethylene and Oxygen. *J. Phys. Chem. C* **2021**, *125* (17), 9032–9037. https://doi.org/10.1021/acs.jpcc.0c11597.
(24) Knudsen, J.; Martin, N. M.; Grånäs, E.; Blomberg, S.; Gustafson, J.; Andersen, J. N.; Lundgren, E.; Klacar, S.; Hellman, A.; Grönbeck, H. Carbonate Formation on p(X4x)-O/Ag(111). *Phys. Rev. B* **2011**, *84* (11), 115430. https://doi.org/10.1103/PhysRevB.84.115430.
(25) Isegawa, K.; Ueda, K.; Hiwasa, S.; Amemiya, K.; Mase, K.; Kondoh, H. Formation of Carbonate on Ag(111) under Exposure to Ethylene and Oxygen Gases Evidenced by Near Ambient Pressure XPS and NEXAFS. *Chem. Lett.* **2019**, *48* (2), 159–162. https://doi.org/10.1246/cl.180891.
(26) Turano, M. E.; Farber, R. G.; Oskorep, E. C. N.; Rosenberg, R. A.; Killelea, D. R. Characterization of Oxygenaceous Species Formed by Exposure of Ag(111) to Atomic Oxygen. *J. Phys. Chem. C* **2020**, *124* (2), 1382–1389. https://doi.org/10.1021/acs.jpcc.9b09131.

(27) Michaelides, A.; Reuter, K.; Scheffler, M. When Seeing Is Not Believing: Oxygen on Ag(111), a Simple Adsorption System? *J. Vac. Sci. Technol. A* **2005**, *23* (6), 1487–1497. https://doi.org/10.1116/1.2049302.
(28) Ben Yaacov, A.; Ben David, R.; Grinter, D. C.; Held, G.; Eren, B. Identification of Adsorbed Species and Surface Chemical State on Ag(111) in the Presence of Ethylene and Oxygen Studied with Infrared and X-Ray Spectroscopies. *Physchem* **2021**, *1* (3), 259–271. https://doi.org/10.3390/physchem1030020.
(29) R. Rocha, T. C.; Oestereich, A.; V. Demidov, D.; Hävecker, M.; Zafeiratos, S.; Weinberg, G.; I. Bukhtiyarov, V.; Knop-Gericke, A.; Schlögl, R. The Silver–Oxygen System in Catalysis: New Insights by near Ambient Pressure X-Ray Photoelectron Spectroscopy. *Phys. Chem. Chem. Phys.* **2012**, *14* (13), 4554–4564. https://doi.org/10.1039/C2CP22472K.
(30) Isegawa, K.; Ueda, K.; Amemiya, K.; Mase, K.; Kondoh, H. Formation and Behavior of Carbonates on Ag(110) in the Presence of Ethylene and Oxygen. *J. Phys. Chem. C* **2021**, *125* (17), 9032–9037. https://doi.org/10.1021/acs.jpcc.0c11597.
(31) Campbell, C. T.; Koel, B. E. Chlorine Promotion of Selective Ethylene Oxidation over Ag(110): Kinetics and Mechanism. *J. Catal.* **1985**, *92* (2), 272–283. https://doi.org/10.1016/0021-9517(85)90261-1.
(32) Force, E. L.; Bell, A. T. The Relationship of Adsorbed Species Observed by Infrared Spectroscopy to the Mechanism of Ethylene Oxidation over Silver. *J. Catal.* **1975**, *40* (3), 356–371. https://doi.org/10.1016/0021-9517(75)90267-5.
(33) Kaichev, V. V.; Bukhtiyarov, V. I.; Hävecker, M.; Knop-Gercke, A.; Mayer, R. W.; Schlögl, R. The Nature of Electrophilic and Nucleophilic Oxygen Adsorbed on Silver. *Kinet. Catal.* **2003**, *44* (3), 432–440. https://doi.org/10.1023/A:1024459305551.
(34) Schwaner, A. L.; White, J. M. Electron-Induced Chemistry of Methanol on Ag(111). *J. Phys. Chem. B* **1997**, *101* (49), 10414–10422. https://doi.org/10.1021/jp972136y.
(35) Felter, T. E.; Weinberg, W. H.; Lastushkina, G. Ya.; Zhdan, P. A.; Boreskov, G. K.; Hrbek, J. The Adsorption of Methanol on Ag(111) and Its Reaction with Preadsorbed Oxygen. *Appl. Surf. Sci.* **1983**, *16* (3), 351–364. https://doi.org/10.1016/0378-5963(83)90079-X.
(36) Knudsen, J.; Merte, L. R.; Peng, G.; Vang, R. T.; Resta, A.; Lægsgaard, E.; Andersen, J. N.; Mavrikakis, M.; Besenbacher, F. Low-Temperature CO Oxidation on Ni(111) and on a Au/Ni(111) Surface Alloy. *ACS Nano* **2010**, *4* (8), 4380–4387. https://doi.org/10.1021/nn101241c.
(37) Heine, C.; Lechner, B. A. J.; Bluhm, H.; Salmeron, M. Recycling of CO2: Probing the Chemical State of the Ni(111) Surface during the Methanation Reaction with Ambient-Pressure X-Ray Photoelectron Spectroscopy. *J. Am. Chem. Soc.* **2016**, *138* (40), 13246–13252. https://doi.org/10.1021/jacs.6b06939.
(38) T. Campbell, C. An XPS Study of Molecularly Chemisorbed Oxygen on Ag(111). *Surf. Sci.* **1986**, *173* (2), L641–L646. https://doi.org/10.1016/0039-6028(86)90191-3.

Chapter 10: Preliminary STM Investigation of the Effects of Ni on Oxygen Structures on Ag(111)

Elizabeth E. Happel, and E. Charles H. Sykes

10.1 Introduction

The presence of transition metal dopants in noble metal surfaces has emerged as a powerful strategy for tuning surface reactivity, particularly in catalytic processes. Previous studies have shown that even highly dilute concentrations of nickel in silver, specifically on Ag(111) surfaces, can substantially alter the chemical behavior of adsorbed species especially those revenant to ethylene epoxidation. In ultra-high vacuum (UHV) environments, the incorporation of Ni atoms into Ag(111) has been found to dramatically modify the adsorption, activation, and desorption properties of oxygen species. These changes have primarily been characterized using temperature-programmed desorption (TPD) and x-ray photoelectron spectroscopy (XPS), which together provide a detailed picture of surface reactivity and the associated electronic structure. Through these methods, shifts in the binding energy and changes in the oxidation states of both Ag and Ni have been observed, offering important insights into the electronic modifications induced by Ni doping.

However, while these spectroscopic techniques are effective in probing electronic and chemical environments, they lack the spatial resolution needed to directly visualize the atomic-scale structural rearrangements that accompany such electronic changes. In particular, it remains unclear how Ni atoms are structurally incorporated into the Ag(111) lattice and how their presence perturbs the adsorption geometry, distribution, and local bonding environment of oxygen species. A more detailed understanding of these structural effects is critical, as they can strongly influence surface reactivity and catalytic behavior.

In this study, we employ low-temperature scanning tunneling microscopy (LT-STM) to obtain an atomically resolved view of the Ni-doped Ag(111) surface. This technique enables us to directly visualize both the distribution of Ni atoms in the silver surface and any structural changes to adsorbed oxygen species as they relate to Ni. In addition to unique oxidation at step edges in the

NiAg(111) sample, we also find similarities in the oxygen species on terraces compared to those found on Ag(111).

10.2 Methods

STM experiments were performed in a low-temperature scanning tunneling microscope (Infinity by Scienta Omicron) under UHV. Sample cleaning, annealing, and Ni deposition were performed in the preparation chamber with a base pressure ~1×10^{-10} mbar. High resolution imaging was performed in the STM chamber with a base pressure <1×10^{-11} mbar at ~13 K with an etched W tip. These experiments utilized a Ag(111) crystal that was cleaned with cycles of Ar^+ ion sputtering (1.0 keV, 8μA) followed by annealing to 900 K. Ag(111) samples were exposed to NO_2 (Aldrich >99.5%) with a precision leak valve while the sample was heated to ~373 K with a PBN heater in the preparation chamber. NiAg(111) surface alloys were prepared by deposition of Ni (Goodfellow, 99.99%) via electron beam evaporation (Omicron, EFM 3) onto a Ag(111) crystal held at 373 K. NiAg samples were exposed to O_2 (Middlesex, 99.999%) via precision leak valve while cooling from 473 K in the preparation chamber and moved to the STM chamber where they were cooled from room temperature to ~13 K before imaging.

10.3 Results and Discussion

Deposition of Ni onto Ag(111) induces notable restructuring at step edges relative to the clean surface (Fig. 10.1). Bright protrusions ranging from 0.2 to 0.5 nm in apparent height emerge along the step edges and are attributed to Ni atoms capped by Ag. This capping behavior is common with Ag based alloys on account of the low surface free energy of Ag(111). [1–5] In addition to these features, certain regions exhibit fewer protrusions and instead display clustered, shallow depressions near step brims. These depressions are assigned to subsurface Ni that is mobile in the lattice of the Ag(111). Time-lapse imaging reveals lateral mobility of these depressions toward step edges, suggesting dynamic incorporation and redistribution within the near-surface region.. The subsurface nature of these Ni species is unsurprising in part due to the negative segregation energy of Ni in Ag(111) which suggests Ni is more stable in the bulk of the host.[6]

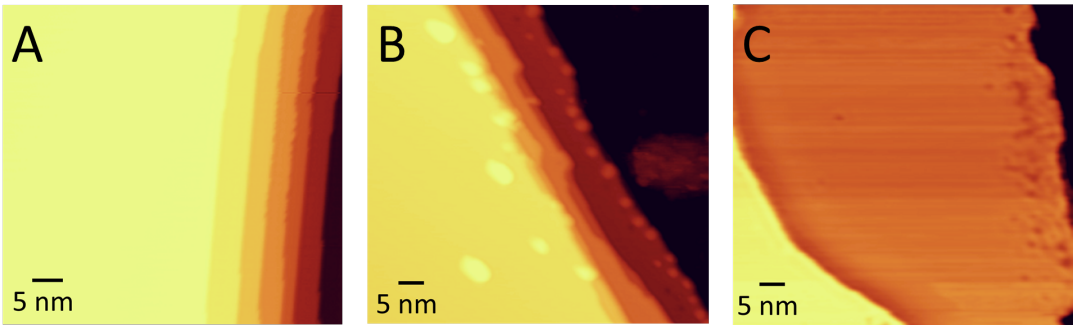

Figure 10.1. Changes in step edges of Ag(111) with deposition of Ni. The straight and smooth step edges of a clean Ag(111) surface **(A)** are transformed into slightly more jagged edges with either bright protrusions assigned to Ag capped Ni sites **(B)** or with patches of shallow depressions clustered at the edges assigned to subsurface Ni sites **(C)**. Imaging conditions for **(A)** 0.5 nA, 100 mV, **(B)** 0.3 nA, 300 mV and **(C)** 0.2 nA, 150 mV.

The presence of shallow depressions in STM images is indicative of subsurface perturbations to the Ag(111) lattice. Given the thermodynamic favorability of Ni incorporation into the Ag bulk and the elevated deposition temperature, it is expected that Ni resides beneath the surface. Notably, the characteristic hexagonal symmetry of the Ag(111) surface is preserved, even within darker regions of the lattice, implying that these features arise from subsurface Ni as compared to an apparent vacancy which more typically assigned as a surface alloy or adsorbate. The persistence of long-range order despite local contrast changes suggests that subsurface Ni modifies the electronic structure at the surface without disrupting the atomic registry.

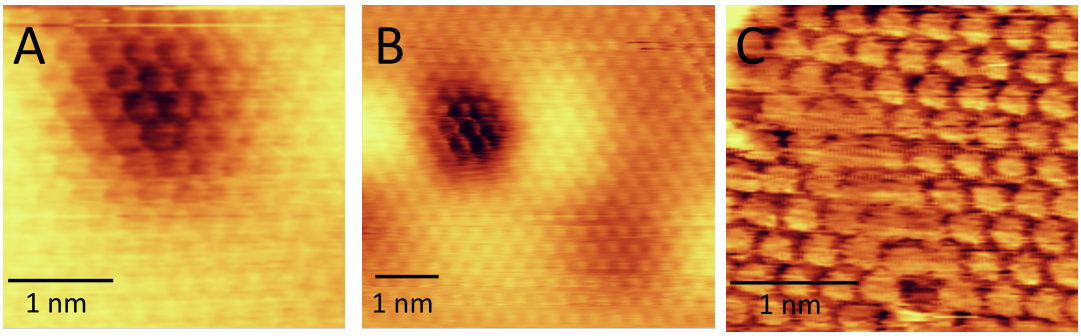

Figure 10.2. The apparent shift in Ag(111) lattice when Ni segregates to the surface. The distinct shift in the surface lattice indicates the different depths of subsurface Ni sites with **(A)** likely representing a single Ag layer depth compared to **(B)** which is likely 2-3 layers subsurface. These Ni atoms remain in the subsurface region after being deposited at ~373 K the intact surface lattice contrasts the appearance of a surface vacancy that appears when O_2 is introduced and Ni is temporarily held at the Ag surface **(C).** Imaging conditions for **(A)** 0.1 nA, 100 mV, **(B)** 0.2 nA, 100 mV and **(C)** 0.2 nA, 100 mV.

The specific surface perturbation depends on the depth of the embedded Ni species, as evidenced by the varying contrast and apparent depression depths observed in Fig. 10.2.[7] These features are consistent with prior studies on NiAg(111), which demonstrate that mild annealing of the surface promotes reversible Ni segregation into the subsurface region (Chapter 8). Thus, deposition at modestly elevated temperatures likely results in the formation of near-surface Ni species that is neither fully bulk nor exposed, that remain catalytically active. This is in line with our previous observations that such species are able to participate in oxygen spillover, even when embedded beneath the topmost Ag layer.

Upon exposure to 5000 L (1^{-6} Torr*s) of O_2 at ~373 K, a transient vacancy-like feature appears in some images, attributed to Ni temporarily stabilized at the surface by adsorbed oxygen (Fig. 10.2C). These features are difficult to image consistently, as the oxygen is prone to displacement under the influence of the STM tip. Tip-induced motion is evident in the form of streaking and local disruption of the close-packed lattice direction. Subsequent imaging of the same region often reveals restoration of the undisturbed Ag(111) lattice, suggesting resegregation of the Ni atom into the subsurface following oxygen desorption. This behavior mirrors that observed in previous studies, where surface-bound Ni reversibly returns to the subsurface in the absence of adsorbates (Chapter 8).

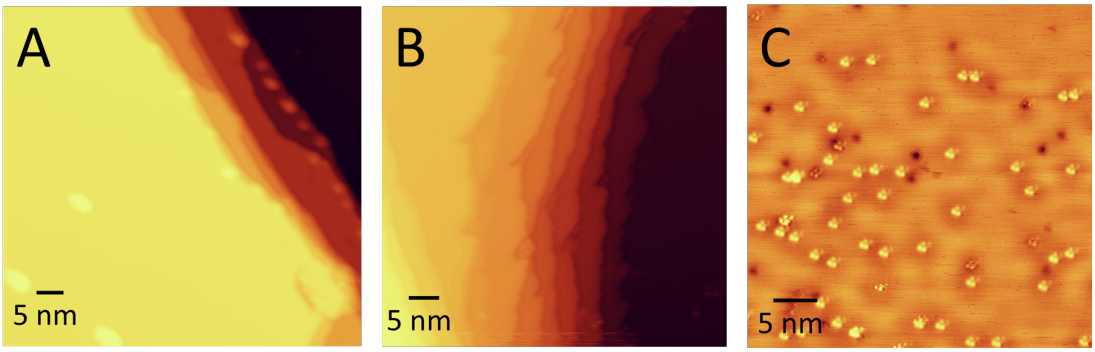

Figure 10.3. The effects of oxygen exposure on NiAg(111). (A) Shows a representative image of NiAg(111) after Ni deposition. **(B)** Shows the shift in shape of step edges to a more jagged and oxidized looking shape with distinct triangular defects at stepedges when 5000 L O_2 is introduced to the surface. **(C)** Shows a patch of oxygen on a terrace of NiAg(111) after the same oxygen exposure. Imaging conditions for **(A)** 0.3 nA, -300 mV, **(B)** 0.3 nA, -150 mV and **(C)** 0.1 nA, -50 mV.

In addition to promoting surface segregation of Ni, exposure of NiAg(111) to oxygen induces significant changes in surface morphology, particularly at step edges (Fig. 10.3A–B). The previously smooth and well-defined step edges adopt a jagged, etched structure characteristic of other moderately oxidized metal surfaces. Notably, the bright protrusions and shallow subsurface depressions observed prior to O_2 exposure are no longer present, suggesting oxygen-induced restructuring and possible redistribution of Ni.

The most prominent oxygen-induced features are triangular defect structures that localize almost exclusively along step edges. These difficult to resolve patches are notably absent from terrace regions, which remain largely bare or exhibit sparse oxygen coverage (Fig. 10.3C). Given the enrichment of Ni at step edges and the known affinity of oxygen for Ni sites, we tentatively assign these triangular features to chemisorbed oxygen bound to surface-exposed Ni atoms.

This assignment is consistent with prior XPS uptake studies of O_2 on Ni/Ag(111), which indicate the initial formation of a Ni-philic oxygen species with a binding energy characteristic of NiO. Furthermore, in agreement with earlier findings, we observe isolated regions of oxygen on Ag(111) terraces, consistent with the formation of a secondary, electrophilic oxygen species associated with Ag-bound O.

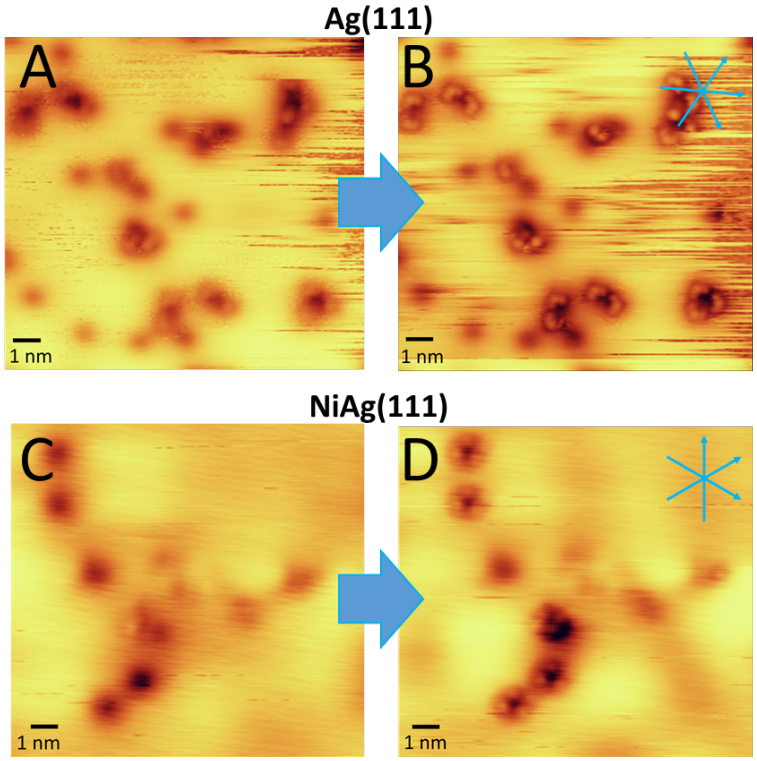

Figure 10.4. The effect of tip state on resolving oxygen on Ni/Ag(111). Chemisorbed oxygen species on both Ag(111) and NiAg(111) require specific stability of the tip to resolve the finer features of oxygen structures on the surface. Changing imaging conditions to get closer to the surface of a O coated Ag(111) from **(A)** 0.3 nA, 100 mV to **(B)** 0.3 nA, 50 mV results in improved clarity and increased structural definition. Similarly, on NiAg(111) going from **(C)** 6 nA, -50 mV to **(D)** 7 nA, -5 mV reveals a similar oxygen structure to the Ag(111) surface. Blue arrows demonstrate the close packed direction of the Ag(111) host lattice.

Accurate resolution of chemisorbed oxygen on Ag(111) and NiAg(111) surfaces is highly sensitive to the electronic state and stability of the STM tip. This is particularly important for oxygen species on Ag,

where weak binding leads to high mobility and poor contrast under standard imaging conditions. As shown in Fig. 10.4A, oxygen typically appears as a diffuse depression on Ag(111). However, reducing the bias voltage to 50 mV while maintaining tunneling current improves image contrast, revealing a triangular feature composed of three distinct lobes aligned with the close-packed direction of the crystal surface (Fig. 10.4B).

A similar tip-dependent resolution behavior is observed on NiAg(111). Under initial imaging conditions (6 nA, –50 mV), oxygen appears as a shallow, poorly resolved depression (Fig. 10.4C). Upon further optimization of tip conditions (7 nA, –5 mV), we observe the emergence of triangular oxygen structures with lobe orientation and spacing nearly identical to those on Ag(111) (Fig. 10.4D). The alignment of these features with the Ag lattice confirms their registry with the substrate.

The observation of identical triangular structures on both Ag(111) and Ni/Ag(111) provides strong evidence for the spillover of oxygen from Ni-rich step edges to Ag terrace sites. This is consistent with prior work (Chapter 7), which indicates a sequential oxygen uptake mechanism: initial binding of oxygen to Ni sites (Ni-philic oxygen), followed by migration to Ag sites where oxygen adopts an electrophilic character. The ability to resolve this spillover product confirms not only the migration pathway but also supports its assignment as electrophilic oxygen.

10.4 Conclusion

In summary, deposited Ni atoms are either capped by Ag or incorporated within the subsurface lattice of Ag(111). Upon exposure to oxygen, significant morphological changes occur at the Ag step edges, accompanied by the emergence of small domains which we tentatively assign as Ni–O species. Additionally, oxygen spillover from Ni sites onto adjacent Ag regions is observed, mirroring prior findings. Notably, the spillover oxygen adopts a triangular configuration, previously identified (see Chapter 5) as electrophilic on Ag(111). This observation aligns with earlier data indicating that, at ultra-low oxygen coverages, Ni-philic oxygen species form initially, followed by the migration of electrophilic oxygen onto silver sites (Chapter 7).

The structural changes made apparent on a very mildly oxidized NiAg surface compared to a Ag surface more strongly oxidized with NO_2 may have significant impactions in the reactivity of the catalyst surface. For instance, Ni-philic oxygen defects at step edges may serve as nucleation sites for oxygen-induced surface reconstructions on Ag(111), which may explain the facile formation of nucleophilic oxygen on

NiAg(111) without the necessity for sputtering (Chapter 7). The resulting structures even bear resemblance to initial stages of the p(4×4) and "inverted p(4×4)" nucleation reported by Killelea and colleagues.[8] Further investigations, particularly at higher oxygen exposures, are warranted to elucidate these structural assignments and to explore the genesis of additional oxygen species, notably nucleophilic oxygen.

10.5 References

(1) Patel, D. A.; Kress, P. L.; Cramer, L. A.; Larson, A. M.; Sykes, E. C. H. Elucidating the Composition of PtAg Surface Alloys with Atomic-Scale Imaging and Spectroscopy. *Journal of Chemical Physics* **2019**, *151* (16). https://doi.org/10.1063/1.5124687.

(2) Darby, M. T.; Sykes, E. C. H.; Michaelides, A.; Stamatakis, M. Carbon Monoxide Poisoning Resistance and Structural Stability of Single Atom Alloys. *Topics in Catalysis* **2018**, *61* (5–6), 428–438. https://doi.org/10.1007/s11244-017-0882-1.

(3) Tyson W.R.; W.A., M. Surface Free Energies of Solid Metals Estimation from Liquid Surface Tension Measurements. *Surface Science* **1977**, *62*, 267–276.

(4) O'Connor, C. R.; Duanmu, K.; Patel, D. A.; Muramoto, E.; van Spronsen, M. A.; Stacchiola, D.; Sykes, E. C.; Sautet, P.; Madix, R. J.; Friend, C. M. Facilitating Hydrogen Atom Migration via a Dense Phase on Palladium Islands to a Surrounding Silver Surface. *Proceedings of the National Academy of Sciences of the United States of America* **2020**, *117* (37), 22657–22664. https://doi.org/10.1073/pnas.2010413117.

(5) Patel, D. A.; Kress, P. L.; Cramer, L. A.; Larson, A. M.; Sykes, E. C. H. Elucidating the Composition of PtAg Surface Alloys with Atomic-Scale Imaging and Spectroscopy. *Journal of Chemical Physics* **2019**, *151* (16). https://doi.org/10.1063/1.5124687.

(6) Darby, M. T.; Sykes, E. C. H.; Michaelides, A.; Stamatakis, M. Carbon Monoxide Poisoning Resistance and Structural Stability of Single Atom Alloys. *Top Catal* **2018**, *61* (5), 428–438. https://doi.org/10.1007/s11244-017-0882-1.

(7) Knudsen, J.; Nilekar, A. U.; Vang, R. T.; Schnadt, J.; Kunkes, E. L.; Dumesic, J. A.; Mavrikakis, M.; Besenbacher, F. A Cu/Pt Near-Surface Alloy for Water–Gas Shift Catalysis. *J. Am. Chem. Soc.* **2007**, *129* (20), 6485–6490. https://doi.org/10.1021/ja0700855.

(8) Turano, M. E.; Juurlink, L. B. F.; Gillum, M. Z.; Jamka, E. A.; Hildebrandt, G.; Lewis, F.; Killelea, D. R. Oxygen-Induced Surface Reconstructions on Curved Ag(111). *Journal of Vacuum Science & Technology A* **2021**, *39* (5), 053201. https://doi.org/10.1116/6.0001167.

Chapter 11: A Preliminary Investigation on the Effects of Ni on the Partial Oxidation of Methanol on Ag(111)

11.1 Abstract:

NiAg has been established as an effective catalyst for the partial oxidation of ethylene to ethylene oxide. We have identified that while Ni lowers the barrier for oxygen activation it also facilities the formation of a greater diversity of oxygen species under reaction conditions, namely subsurface oxygen, which is often considered to play an important role in the partial oxidation of methanol to formaldehyde. This reaction, which is also catalyzed by silver, was investigated with synchrotron based ambient pressure X-ray photoelectron spectroscopy (XPS), where significant difference in surface adsorbates are noted under different partial pressure of oxygen:methanol on Ag(111) and NiAg(111). These preliminary results suggest the need for further investigation with both follow up XPS and temperature programmed desorption studies.

11.2 Introduction

NiAg has proven to be a highly effective catalyst for the selective partial oxidation of ethylene to ethylene oxide. This enhancement has been attributed to Ni's ability to promote oxygen activation without significantly altering the favorable binding characteristics of Ag. Given this success, it is compelling to consider the extension of NiAg catalysts to other industrially relevant partial oxidation reactions.

In this work, we investigate the role of Ni in the partial oxidation of methanol to formaldehyde for two main reasons. First, Ag is already used commercially for this transformation, yet its catalytic efficiency is limited by the formation of active oxygen species [1] And second, subsurface oxygen has been proposed as a key intermediate or co-reactant in the selective pathway toward formaldehyde, and Ni doping may favor its formation.[2,3]

Therefore, NiAg emerges as a promising candidate for methanol oxidation, as it has already been shown to lower the activation barrier for oxygen dissociation while retaining Ag's moderate oxygen binding energy, as discussed in previous chapters. Moreover, Ni is known to stabilize oxygen species in the subsurface more readily than pure Ag, which may directly support the

formation of reactive oxygen intermediates critical for formaldehyde selectivity.[2–4] By probing the evolution of oxygen species under methanol and oxygen co-dosing on NiAg(111) compared to Ag(111), we aim to establish a mechanistic foundation for the role of Ni in tuning surface speciation and reactivity.

11.3 Methods

Ambient pressure XPS was performed at beamline 23-ID-2 (IOS) of the National Synchrotron Light Source II (NSLS- II) at Brookhaven National Laboratory.[5] All experiments were performed on a Ag(111) crystal cleaned with Ar^+ ion sputtering and annealing to 900 K until XPS spectra were free from impurities. High purity O_2 and CH_3OH were introduced to the chamber via precision leak valve while the sample was heated with a pyrolytic boron nitride heater. Temperature was measured with a K-type thermocouple mounted between the Ag(111) crystal and the heater. NiAg(111) alloys were prepared similarly by evaporating a Ni rod (Goodfellow, 99.99%) with a SPECS EBE-4 e-beam evaporator. Photon energies of 1090, 760, and 500 eV were used to generate photoelectrons with kinetic energies of ~200 eV for the Ni 2p, O 1s, and C 1s core levels, respectively, to maintain similar probing depths. Reference Ag 3d spectra were taken at each photon energy. Spectra were corrected with respect to the Fermi edge and metallic Ag 3d binding energy. XPS data was analyzed with CasaXPS and fit with a linear background; each species was assigned and fit according to literature values for the different types of oxygen as described in previous chapters. All spectra were corrected with a relative sensitivity factor (RSF) for each photon energy used.

11.4 Results and Discussion

Distinct differences emerge in the C 1s and O 1s XPS spectra of Ag(111) and NiAg(111) surfaces upon exposure to varying oxygen:methanol mixtures. These variations highlight how Ni doping alters the oxygen speciation and surface reactivity of Ag.

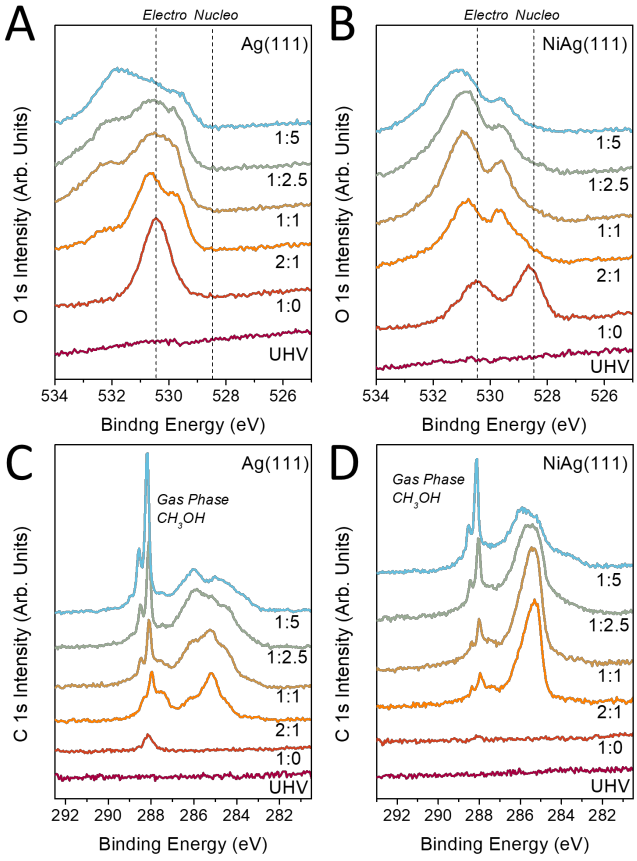

Figure 11.1. A comparison of carbon and oxygen species formed on Ag and NiAg(111) during methanol oxidation. The O 1s **(A/B)** and C 1s **(C/D)** spectra for Ag(111) and NiAg(111) respectively shift as a function of increasing ratios of oxygen:methanol as both samples are held at 325 K.

Under a pure oxygen atmosphere (0.1 Torr), Ag(111) primarily supports the formation of electrophilic oxygen, characterized by a sharp O 1s peak at ~530.4 eV. Introduction of methanol to this environment results in a rapid restructuring of the surface species. New features appear in both the O 1s and C 1s regions, indicating the formation of additional oxygenated species. Notably, while the electrophilic oxygen signal decreases, it remains the dominant surface species. Methoxy groups (O 1s ~531.2 eV; C 1s ~285.2 eV) and carbonate-like species (O 1s ~529.7 eV; C 1s ~287.2 eV) emerge as secondary products. Lower-intensity features also develop at ~533 eV and ~532 eV, corresponding to chemisorbed O_2-like species and hydroxyl groups, respectively.

As methanol partial pressure increases under constant 0.1 Torr O_2, the coverages of methoxy and carbonate species stabilize, while signals associated with molecular oxygen and water continue to grow. This trend could indicate increasing formation of hydrogen-bonded surface species and/or condensed-phase water. A sharp decline in electrophilic oxygen coverage is observed only when the methanol content reaches a 1:5 O_2:CH_3OH ratio, suggesting a threshold beyond which oxygen consumption by methanol dominates.

The speciation trends on NiAg(111) are more complex due to the presence of additional oxygen species and overlapping binding energies. Even under oxygen alone, NiAg(111) supports three extra oxygen features not observed on pure Ag: Ni-philic oxygen (~529.4 eV), nucleophilic oxygen (528.4 eV), and subsurface oxygen (531.1 eV). Subsurface oxygen appears at binding energies that overlap with methoxy (~531 eV), complicating direct deconvolution. Despite spectral overlap, the C 1s signal at ~285.2 eV provides a useful fingerprint for methoxy species. The strong 1:1 correlation between this carbon feature and the overlapping O 1s peak suggests that subsurface oxygen is largely converted to surface-bound methoxy upon methanol exposure. Upon methanol exposure, both electrophilic and nucleophilic oxygen species diminish rapidly, as does the subsurface oxygen signal. However, the Ni-philic oxygen component remains relatively stable across all methanol concentrations.

Interestingly, both surfaces exhibit the formation of a carbonate-like species with a C 1s binding energy at ~287.2 eV and a corresponding O 1s feature at ~529.7 eV. While slightly shifted from typical carbonate assignments, the consistent 3:1 oxygen-to-carbon ratio supports the assignment of this species as a surface-bound tridentate carbonate or a related C–O complex. The ability of both Ag and NiAg(111) to support this structure implies that its formation does not require Ni but may be stabilized or made more reactive in the presence of Ni dopants.

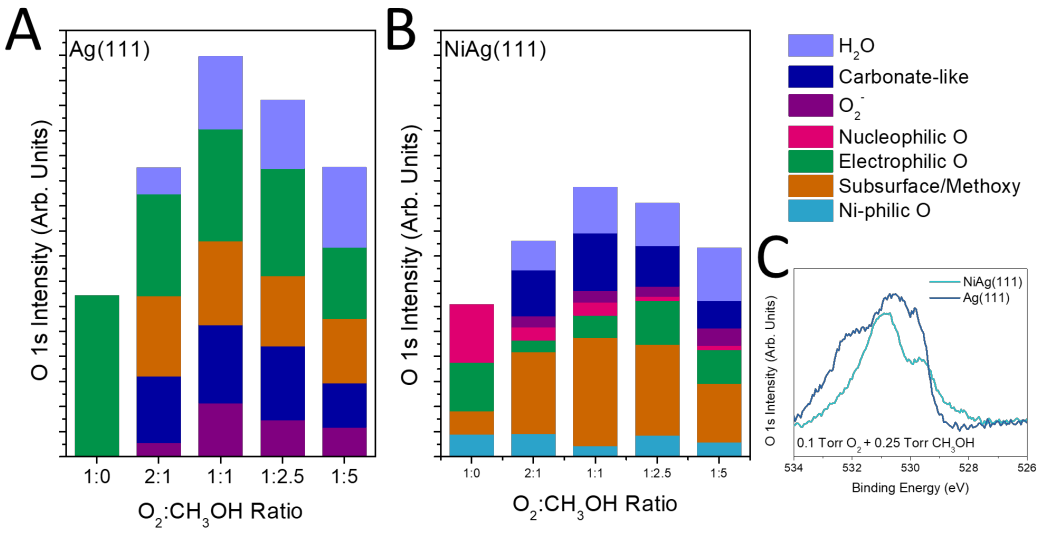

Figure 11.2. Coverage of oxygen containing species on Ag(111) and NiAg(111) as a function of methanol partial pressure. (A) Ag(111) forms only four species throughout different reaction environments with minimal changes to the ratios of adsorbates **(B)** NiAg(111) forms more oxygen species and sees more dynamic shifts in oxygen species a function of methanol partial pressure. **(C)** A comparison of O1s traces for Ag and NiAg(111) under 0.1 Torr O_2 and 0.25 Torr CH_3OH.

Given the importance of methanol activation via surface-bound methoxy intermediates, the formation of methoxy groups on both Ag(111) and NiAg(111) provides valuable insight into how each catalyst facilitates the early steps of partial oxidation. Methoxy species are widely considered key intermediates in the pathway to formaldehyde, particularly under low-temperature and low-conversion conditions where overoxidation to CO or CO_2 can be minimized.[6–8]

A consistently higher fraction of the total oxygen coverage being present as methoxy on NiAg(111) across multiple oxygen-to-methanol dosing ratios could suggest that Ni facilitates more efficient methanol activation at the surface. This enhanced activation is consistent with Ni's role in promoting both oxygen dissociation and the stabilization of reactive oxygen species, which in turn enables rapid reaction with methanol to form methoxy.

In addition to this effect, a lower relative coverage of electrophilic oxygen is observed on NiAg(111) compared to Ag(111) under otherwise identical conditions. This may reflect a higher turnover rate of electrophilic oxygen into downstream products such as water or formaldehyde,

rather than a deficiency in its formation. Notably, previous studies have shown that NiAg(111) is capable of sustaining oxygen activation even under mildly reducing environments (Chapter 9), suggesting that the surface can replenish reactive oxygen species during continuous turnover. This observation is also consistent with a Mars–van Krevelen-type mechanism, in which lattice or subsurface oxygen participates directly in oxidation reactions and is subsequently replenished by molecular oxygen from the gas phase.[9] In this framework, the reduced steady-state coverage of electrophilic oxygen on NiAg(111) could reflect a catalytically active cycle wherein adsorbed oxygen species are rapidly consumed to generate oxidation products, including water and formaldehyde, rather than accumulating on the surface.

11.5 Conclusions

While preliminary, these results clearly demonstrate that Ag(111) and NiAg(111) exhibit markedly different surface adsorbate distributions under conditions relevant to formaldehyde synthesis. Prior studies have suggested that both electrophilic and subsurface oxygen species contribute to methanol partial oxidation, and both are readily formed on NiAg(111). A key distinction between the two surfaces lies in their response to increasing methanol partial pressure: NiAg(111) shows more dynamic shifts in surface coverage, particularly a suppression of high-binding-energy O 1s features such as molecular oxygen and water.

This behavior may reflect an altered adsorption/desorption equilibrium or enhanced surface reactivity toward hydrogen-containing species enabled by the presence of Ni, which modifies the local electronic structure of Ag. Such effects could facilitate more efficient oxygen utilization or promote the formation of reactive intermediates that are not stabilized on pure Ag(111).

These findings could point to a more efficient consumption or transformation of reactive oxygen species on Ni-doped surfaces. Additionally, the formation of a carbonate-like species on both surfaces with a consistent 3:1 O:C ratio suggests a common intermediate that may serve as a marker for selective oxidation pathways. Understanding how Ni influences the formation, stabilization, or reactivity of this intermediate may help guide rational catalyst design.

Further quantitative analysis is necessary to resolve overlapping species and establish precise coverage trends. Complementary TPD measurements would provide valuable kinetic insight and,

together with the current electronic structure data, help clarify the mechanistic role of specific oxygen species in methanol activation and formaldehyde formation. In particular, correlating desorption profiles with binding energy assignments may allow us to directly link specific oxygen species to reactive intermediates or products, providing a more comprehensive mechanistic framework.

11.6 References

(1) Aljama, H.; Yoo, J. S.; Nørskov, J. K.; Abild-Pedersen, F.; Studt, F. Methanol Partial Oxidation on Ag(1 1 1) from First Principles. *ChemCatChem* **2016**, *8* (23), 3621–3625. https://doi.org/10.1002/cctc.201601053.

(2) Karatok, M.; Sensoy, M. G.; Vovk, E. I.; Ustunel, H.; Toffoli, D.; Ozensoy, E. Formaldehyde Selectivity in Methanol Partial Oxidation on Silver: Effect of Reactive Oxygen Species, Surface Reconstruction, and Stability of Intermediates. *ACS Catal.* **2021**, *11* (10), 6200–6209. https://doi.org/10.1021/acscatal.1c00344.

(3) Qian, M.; Liauw, M. A.; Emig, G. Formaldehyde Synthesis from Methanol over Silver Catalysts. *Applied Catalysis A: General* **2003**, *238* (2), 211–222. https://doi.org/10.1016/S0926-860X(02)00340-X.

(4) Felter, T. E.; Weinberg, W. H.; Lastushkina, G. Ya.; Zhdan, P. A.; Boreskov, G. K.; Hrbek, J. The Adsorption of Methanol on Ag(111) and Its Reaction with Preadsorbed Oxygen. *Applications of Surface Science* **1983**, *16* (3), 351–364. https://doi.org/10.1016/0378-5963(83)90079-X.

(5) Waluyo, I.; Hunt, A. Ambient Pressure X-Ray Photoelectron Spectroscopy at the IOS (23-ID-2) Beamline at the National Synchrotron Light Source II. *Synchrotron Radiation News* **2022**, *35* (3), 31–38. https://doi.org/10.1080/08940886.2022.2082180/ASSET/BDB66E5A-0587-4FF9-8A92-46D92E6F9330/ASSETS/IMAGES/GSRN_A_2082180_F0005_C.JPG.

(6) Malik, M. I.; Abatzoglou, N.; Achouri, I. E. Methanol to Formaldehyde: An Overview of Surface Studies and Performance of an Iron Molybdate Catalyst. *Catalysts* **2021**, *11* (8), 893. https://doi.org/10.3390/catal11080893.

(7) Lafyatis, D. S.; Creten, G.; Froment, G. F. TAP Reactor Study of the Partial Oxidation of Methanol to Formaldehyde Using an Industrial Fe-Cr-Mo Oxide Catalyst. *Applied Catalysis A: General* **1994**, *120* (1), 85–103. https://doi.org/10.1016/0926-860X(94)80335-8.

(8) Lervold, S.; Lødeng, R.; Yang, J.; Skjelstad, J.; Bingen, K.; Venvik, H. J. Partial Oxidation of Methanol to Formaldehyde in an Annular Reactor. *Chemical Engineering Journal* **2021**, *423*, 130141. https://doi.org/10.1016/j.cej.2021.130141.

(9) Bhattacharyya, S. K.; Nag, N. K.; Ganguly, N. D. Kinetics of Vapor-Phase Oxidation of Methanol on Reduced Silver Catalyst. *Journal of Catalysis* **1971**, *23* (2), 158–167. https://doi.org/10.1016/0021-9517(71)90037-6.

Chapter 12: Conclusions and Future Directions

Silver-based partial oxidation catalysis remains one of the most well-studied classes of heterogeneous catalysis, yet many open questions persist regarding the nature of active sites, specifically the role of oxygen species and their structures. Even the interaction of oxygen with clean Ag surfaces, prior to the introduction of any additional reactants, continues to challenge structural characterization and mechanistic interpretation. Oxygen species formed on Ag are known to play a central role in determining product selectivity, especially in the partial oxidation of ethylene to ethylene oxide (EO).

In Chapter 3, I employed ambient-pressure X-ray photoelectron spectroscopy (AP-XPS) to study the chemical state of Ag under ethylene epoxidation conditions relevant to industrial processes. By quantifying surface coverages of oxygen and carbon species, I demonstrated that Ag(111) remains largely metallic, with only sub-monolayer carbonate coverage under these conditions. These findings provide essential surface coverage benchmarks that can guide realistic modeling of catalytic intermediates.

In Chapter 4, I examined the long-standing discrepancy between experimental and theoretical descriptions of electrophilic oxygen on Ag. By benchmarking density functional theory (DFT) predictions of O 1s binding energies across a range of metal surfaces, we identified a broader limitation of DFT: it systematically underestimates the binding energies of weakly bound oxygen species, particularly those with binding energies >530 eV. This insight helps explain why electrophilic oxygen remains difficult to model and underscores the need for improved theoretical treatments of such species and cooperative experimental support.

Without reliable DFT predictions, Chapter 5 turned to scanning tunneling microscopy (STM) to directly visualize oxygen structures formed via NO_2 exposure on Ag(111). I identified two distinct surface oxygen configurations on Ag(111): a lower-temperature ring-like structure, tentatively assigned to electrophilic oxygen, and a higher-temperature reconstruction consistent with nucleophilic oxygen. When exposed to ethylene, the lower-temperature phase promoted formation of a surface-bound intermediate consistent with the oxametallacycle (OMC), whereas the nucleophilic surface showed only transient ethylene adsorption. These results provide the

first direct imaging of a potential OMC precursor on Ag(111) and support the selective role of electrophilic oxygen.

In Chapter 6, I collaborated on the design and evaluation of a new catalyst, NiAg, for EO production. Guided by theory, this work showed that Ni facilitates O_2 activation on Ag(111) while maintaining moderate oxygen binding strength. I found that Ni preferentially stabilizes nucleophilic oxygen species, limiting its combustion and therefore enhances EO selectivity to levels comparable with Cl-promoted catalysts, but without the associated toxicity and environmental drawbacks.

Building on this, Chapters 7 and 8 explored the dynamic behavior of Ni in the Ag lattice and the effect of oxidation on NiAg(111). I showed that Ni is mobile on Ag(111), enabling spillover of activated oxygen and the formation of a wider variety of surface oxygen species, including a newly identified class I term "Ni-philic" oxygen. These findings highlight the multifunctional role of Ni in both oxygen activation and oxygen speciation.

In Chapter 9, I directly compared Ag(111) and NiAg(111) with operando XPS studies which further demonstrated that Ni continues to stabilize nucleophilic oxygen even under reducing conditions (specifically, in the simultaneous presence of ethylene and oxygen). I also identified two distinct carbonate species on NiAg that form under industrially relevant epoxidation conditions and observed enhanced formation of subsurface oxygen, a species thought to participate in replenishing reactive surface sites. Together, these results provide mechanistic insight into how Ni influences both the kinetics and thermodynamics of EO catalysis.

Finally, in Chapter 10, I began characterizing the structure of Ni-philic oxygen species using STM. These preliminary results suggest that Ni incorporation dramatically alters the structure of Ag step edges, potentially explaining why nucleophilic oxygen forms more readily on NiAg surfaces under milder conditions.

12.1 Broader Impacts and Future Directions

This dissertation contributes a multifaceted understanding of oxygen speciation and promoter effects in ethylene epoxidation. I have characterized the reactive state of Ag under realistic conditions, visualized distinct surface oxygen species, and provided the first STM evidence of a

possible OMC precursor on Ag(111). I have also helped to explain persistent gaps between experimental and theoretical descriptions of electrophilic oxygen by identifying broader limitations in DFT predictions.

Beyond fundamental insights, this work lays the foundation for a new class of chlorine-free, selective oxidation catalysts. The NiAg system introduced here achieves selectivity comparable to conventional promoters but with improved environmental and safety profiles. Characterizing the mechanistic role of Ni not only advances our understanding of this specific system but may also guide the design of other bifunctional oxidation catalysts in the future.

Continued exploration of Ni-philic oxygen structures and their dynamics, particularly under operando conditions, will be essential for unraveling the precise roles these species play in catalytic cycles. Promising preliminary results suggest that NiAg may continue to be a useful catalyst for other partial oxidations including formaldehyde synthesis and beyond.

Appendices

Appendix to Chapter 3:

This appendix was modified from the supplementary materials from the following publication: Elizabeth E. Happel, Toghrul Azizli, Avery S. Daniels, Cole Easton, Adrian Hunt, Phillip Christopher, Iradwikanari Waluyo, Matthew M. Montemore, and E. Charles H. Sykes. Ag(111) Remains Significantly Reduced In Situ Under Simulated Ethylene Epoxidation Conditions. *Submitted JPCL* ***2025***

Experimental Methods

Ambient pressure X-ray photoelectron spectroscopy (AP-XPS) data were collected at beamline 23-ID-2 of the National Synchrotron Light Source II (NSLS-II) at Brookhaven National Laboratory.[1] The Ag(111) sample was mounted on a pyrolytic boron nitride (PBN) heater and temperature was measured with a K type thermocouple located between the back of the sample and heater. The crystal was cleaned by repeating cycles of Ar^+ sputtering and annealing to 900 K until XPS spectra showed no impurities. High purity O_2 (Matheson, 99.994%) and C_2H_4 (Matheson, 99.95%) were introduced to the chamber using precision leak valves. Photon energies of 760 and 500 eV were used to generate photoelectrons with the same kinetic energies of ~200 eV for O 1s and C 1s spectra respectively. Reference Ag 3d spectra were taken at both photon energies and, in addition to the Fermi edge, were used to calibrate binding energy shifts. The XPS spectra were analyzed with CasaXPS, linear backgrounds were used, and peaks fit as described in detail in Table A3.1.

Computational Methods

DFT Calculations

DFT calculations were performed using the Vienna Ab initio Simulation Package (VASP).[2,3] For the exchange-correlation potential, the Perdew–Burke–Ernzerhof (GGA-PBE)[4] functional was used, coupled with Tkatchenko-Scheffler (TS) dispersion corrections.[5] The projector-augmented wave method was utilized to treat the electron-ion interactions, and the plane wave cutoff energy was 400 eV. The relaxation of each geometry was done with 10^{-5} eV electronic energy and 0.03 eV/Å force tolerances. The Table S1 below shows the cell sizes and the corresponding k points sampled.

Table A3.1. Cell sized and corresponding k points sampled for calculated structures.

Species	Surface Cell Sizes	K-point grid
Bare Silver	3 × 3 × 4	7 × 7 × 1
Oxide Ring	5 × 5 × 4	5 × 5 × 1
p-(4x4)	4 × 4 × 5	5 × 5 × 1
1/9 O ML	3 × 3 × 4	7 × 7 × 1
1/4 CO_3 ML	2 × 2 × 4	10 × 10 × 1
1/6 CO_3 ML	2 × 3 × 4	10 × 7 × 1
1/9 CO_3 ML	3 × 3 × 4	7 × 7 × 1

Vibrational Calculations

Harmonic vibrational energy calculations were carried out for the surfaces with 1/9 O ML, oxide ring, p-(4×4) reconstruction, and CO_3 with different coverages. Only adsorbates on the surface were displaced while all metal atoms were fixed. The calculations were performed with 0.005 Å displacements and 2×10^{-6} eV electronic energy criterion.

Phase Diagram

All thermodynamic parameters were computed using the thermochemistry module of the Atomic Simulation Environment (ASE)[6], with harmonic vibrational frequencies and DFT electronic energies as calculated input. The surface free energy as a function of temperature and partial pressures is given by:

$$\gamma(T) = \frac{1}{A_{surf}}\left(F_{system}(T) + 2N_c\mu_{H_2O}(T, P_{H_2O}) - \frac{N_O}{2}\mu_{O_2}(T, P_{O_2}) - \frac{N_C}{2}\mu_{C_2H_4}(T, P_{C_2H_4})\right)$$

where N_C and N_O denote the number of carbon and oxygen atoms, respectively, in the system, and A_{surf} is the surface area of the unit cell. F_{system} represents the Helmholtz free energy of the system, while μ_{H_2O}, μ_{O_2} and $\mu_{C_2H_4}$ correspond to the chemical potentials of gaseous water, oxygen, and ethylene, respectively.

The Helmholtz free $F_{system}(T)$ energy was computed within the harmonic approximation using ASE's HarmonicThermo class. For gaseous water and ethylene, chemical potentials were calculated in the ideal gas limit using ASE's IdealGasThermo class.

Due to the inaccuracy of DFT-GGA in describing the ground state energy of O_2, an alternative approach was employed to determine its bond strength and thus chemical potential.[7] The DFT energy of O_2 was derived indirectly via:

$$E_{O_2,gas} = 2 * (E_{H_2O,gas} - E_{O_2,gas} + \Delta ZPE + \Delta_f H^{\circ}_{0,H_2O})$$

where ΔZPE is the zero-point energy correction and $\Delta_f H^{\circ}_{0,H_2O}$ is the standard formation enthalpy of water at 0 K, both taken from tabulated values.[7] The chemical potential of O_2 was then computed as:

$$\mu_{O_2}(T, P_{O_2}) = E_{O_2,gas} + k_B T ln\left(\frac{P}{P^0}\right) + h_{int}(T) - h(0) - T\big(s_{int}(T) - s(0)\big)$$

Here, h_{int} and s_{int} are the molar enthalpy and entropy, respectively, interpolated from the NIST thermochemical tables for O_2.[8]

XPS Spectral Analysis

Table A3.2. Description of components of XPS spectra

C 1s Component	Binding Energy	FWHM	Line Shape (L:G)
Carbonate	288.0-288.2	0.5	50:50
Gas Phase Ethylene	285.9	0.3	70:30
Gas Phase Ethylene	286.3	0.4	70:30

O 1s Component	Binding Energy	FWHM	Line Shape (L:G)
Electrophilic	530.1-4	1	50:50
Nucleophilic	528.1-2	0.8	50:50

Ag 3d 5/2 Component	Binding Energy	FWHM	Line Shape (L:G)
Metallic Ag	368.2-3	0.4	100:0
Reconstructed Ag	368.7-8	0.7	50:50
Carbonate on Ag	368.0-1	0.6	70:30

All spectra were corrected with a relative sensitivity factor (RSF) for each photon energy used. Where necessary, peak intensity was corrected for the decreased electron inelastic mean free path (IMFP) resulting from increased chamber pressure. Monolayer coverages were calculated with respect to a monolayer of Ag(111). To do this the $Ag3d_{5/2}$ spectra were first corrected for spin orbit splitting and RSF as well as IMFP as the Ag 3d reference spectra were taken at photon energies more surface sensitive to C 1s and O 1s species. The fraction of the total Ag 3d intensity attributed to the surface layer of Ag, 0.23 and 0.35, was calculated using the electron escape depth for each photon energy, 760 and 500 eV, respectively; and these values were used to extract a monolayer reference for coverage calculations.

Additional confirmation of saturation coverage was performed by measuring the $Ag3d_{5/2}$ spectra with 500 eV photon energy (KE ~150 eV). At this surface sensitivity, the apparent formation and saturation of a surface reconstruction like the p(4x4) results in the growth of a lower binding energy shoulder in the Ag 3d spectra (Fig 2). The ratio of the reconstructed Ag3d shoulder to the total Ag monolayer results in saturation of ~0.7 a complete monolayer (1:1 with Ag atoms at the surface). This coverage aligns well with the saturation of nucleophilic oxygen measured in the O 1s spectra at ~0.288 ML (1:1 with Ag atoms at the surface). Given the known saturation coverage of p(4x4) on Ag(111) as 0.375 ML this makes good agreement between the fraction of the Ag surface that should be reconstructed by 0.288 ML of nucleophilic oxygen (i.e. 0.288/0.375 = ~0.77 of saturated p(4x4) surface).[9–12] We note that the fractional oxygen and reconstructed Ag coverages of the surface align well further confirming the surface calibration. In order to present a more realistic surface coverage of oxygen species, a saturation of the p(4x4) reconstruction (0.375 ML O atoms to surface Ag atoms on Ag(111)) was used as a reference for % monolayer calculations throughout the text.

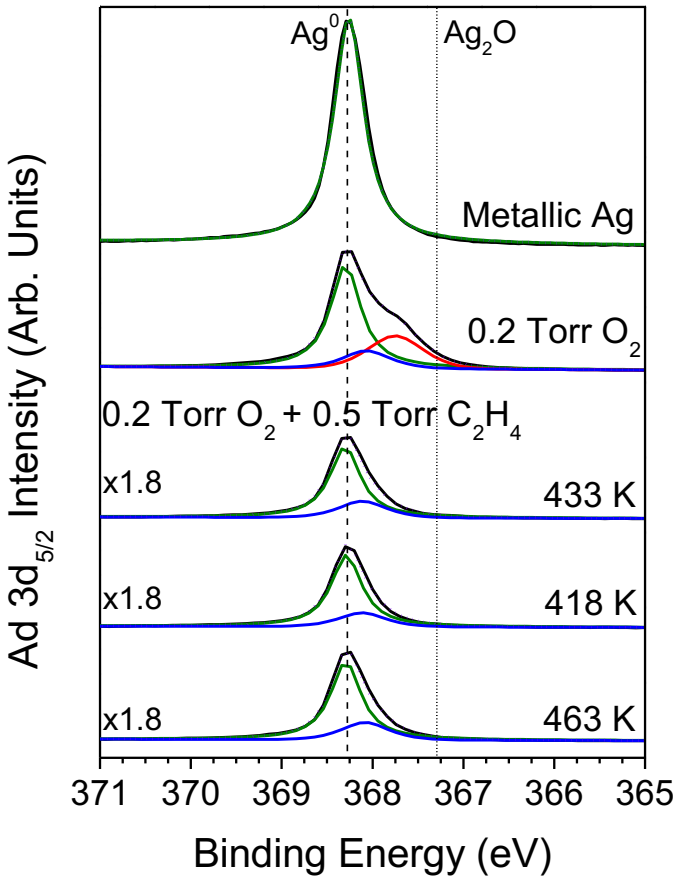

Figure A3.1. The formation and loss of a shoulder on Ag $3d_{5/2}$ spectra of Ag(111) consistent with Ag restructuring under oxidizing and reducing conditions. There is a shift in oxidation state of Ag from metallic (green trace) under UHV conditions, to saturated with a reconstructed atomic oxygen layer (red trace) under 0.2 Torr O_2 followed by a return to predominately metallic under more reducing conditions (0.2 Torr O_2 and 0.5 Torr C_2H_4). While the red trace is typically associated with an oxygen-induced surface reconstruction, is not present under more reducing conditions. A small feature with a slight offset (~0.2 eV) from the metallic BE appears is seen and remains in oxidizing and reducing conditions. This feature (blue trace) is often assigned to Ag in the furrows below O atoms or is associated with oxygen containing surface species present at higher coverages of e.g. carbonate.[9–11]

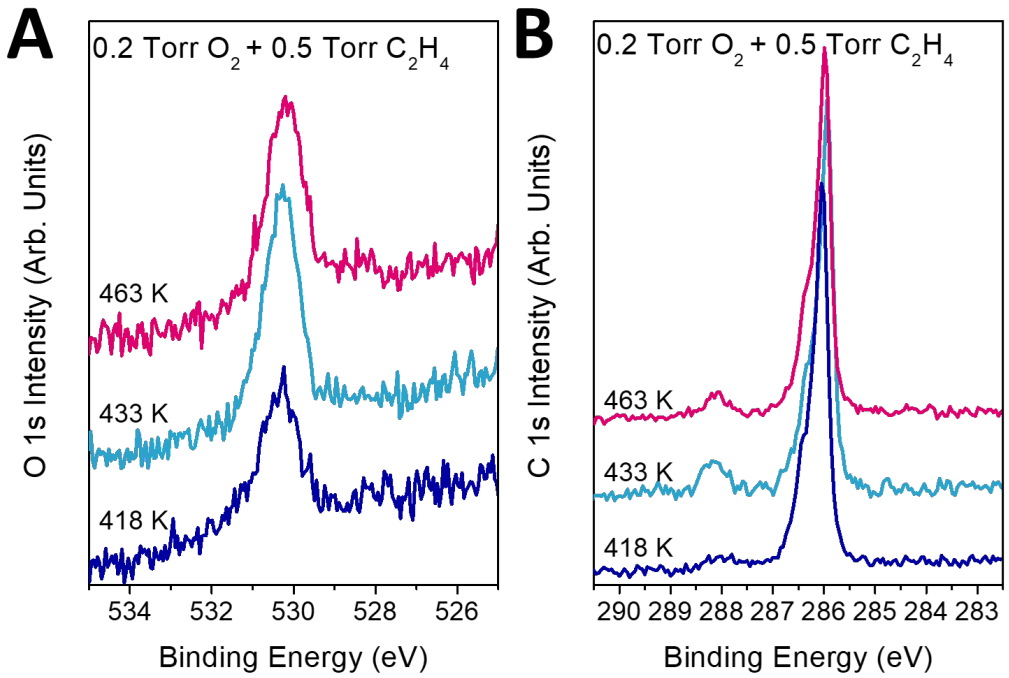

Figure A3.2. The effect of temperature on the surface coverage on Ag(111) under epoxidation conditions. Increasing the temperature of a Ag(111) sample under 0.2 Torr O_2 and 0.5 Torr C_2H_4 from 418 K to 463 K reveals an increase in carbonate in the O 1s (A) and C 1s (B) spectra at intermediate (teal) temperatures and a reduction at higher (pink) and lower (dark blue) temperatures.

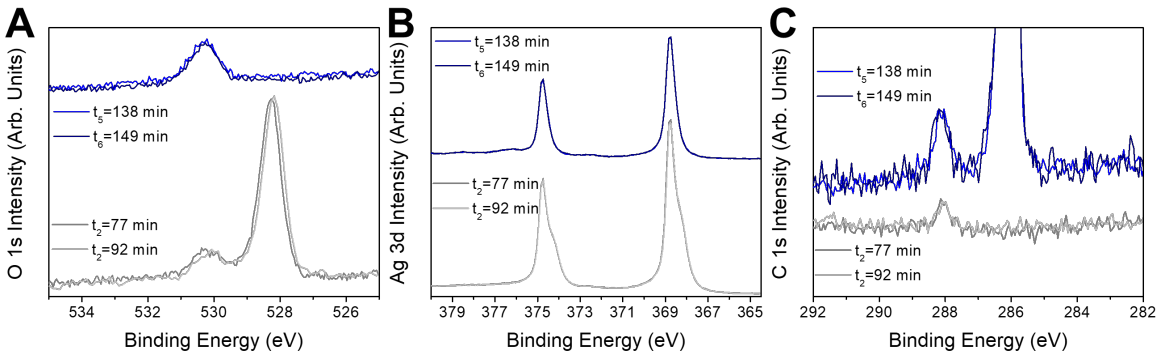

Figure A3.3. Equilibration of XPS spectra under oxidizing and reducing conditions. XPS spectra were continuously collected at 0.2 Torr O_2 at 433 K (grey) until no further changes in line shape were observed in any of the (A) O 1s, (B) Ag 3d, or (C) C 1s spectra before introducing 0.5 Torr C_2H_4 where spectra (blue) continued to be collected again until no changes were observed.

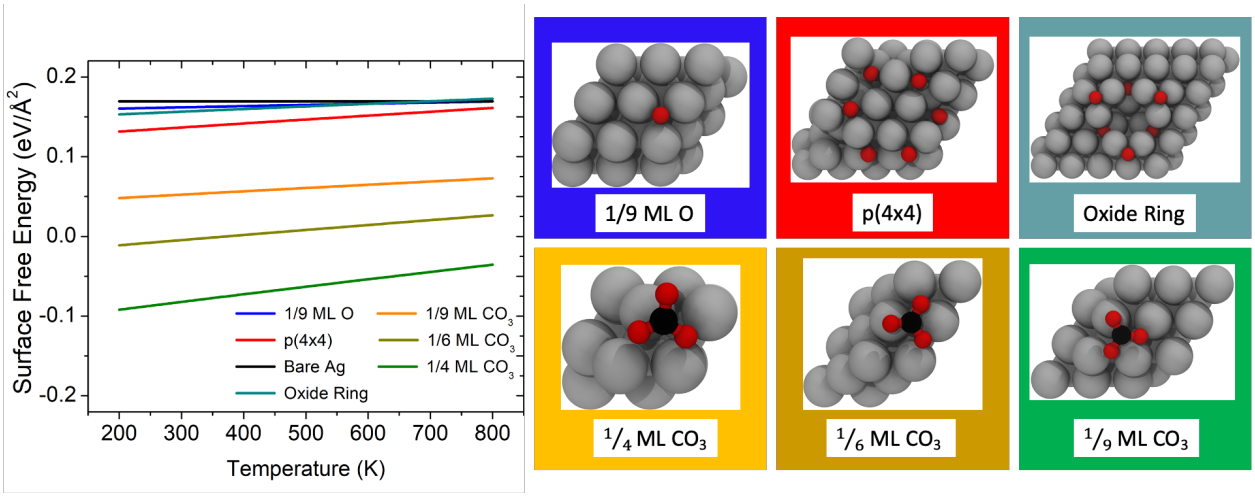

Fig. A3.4 DFT-calculated phase diagram showing the stability of a metallic, carbonate-covered Ag surface under simulated reaction conditions. Surface free energies for bare Ag(111), O/Ag(111) at 1/9 ML, the p(4x4) reconstruction, and CO_3/Ag(111) at three different coverages. Conditions: pO_2 = 0.1 Bar, pC_2H_4 = 0.1 Bar, pH_2O = 0.01 Bar.

References

(1) Waluyo, I.; Hunt, A. Ambient Pressure X-Ray Photoelectron Spectroscopy at the IOS (23-ID-2) Beamline at the National Synchrotron Light Source II. *Synchrotron Radiation News* **2022**, *35* (3), 31–38. https://doi.org/10.1080/08940886.2022.2082180.

(2) Kresse, G.; Furthmüller, J. Efficiency of Ab-Initio Total Energy Calculations for Metals and Semiconductors Using a Plane-Wave Basis Set. *Computational Materials Science* **1996**, *6* (1), 15–50. https://doi.org/10.1016/0927-0256(96)00008-0.

(3) Kresse, G.; Hafner, J. Ab Initio Molecular Dynamics for Liquid Metals. *Phys. Rev. B* **1993**, *47* (1), 558–561. https://doi.org/10.1103/PhysRevB.47.558.

(4) Perdew, J. P.; Burke, K.; Ernzerhof, M. Generalized Gradient Approximation Made Simple [Phys. Rev. Lett. 77, 3865 (1996)]. *Phys. Rev. Lett.* **1997**, *78* (7), 1396–1396. https://doi.org/10.1103/PhysRevLett.78.1396.

(5) Tkatchenko, A.; Scheffler, M. Accurate Molecular Van Der Waals Interactions from Ground-State Electron Density and Free-Atom Reference Data. *Phys. Rev. Lett.* **2009**, *102* (7), 073005. https://doi.org/10.1103/PhysRevLett.102.073005.

(6) Hjorth Larsen, A.; Jørgen Mortensen, J.; Blomqvist, J.; Castelli, I. E.; Christensen, R.; Dułak, M.; Friis, J.; Groves, M. N.; Hammer, B.; Hargus, C.; Hermes, E. D.; Jennings, P. C.; Bjerre Jensen, P.; Kermode, J.; Kitchin, J. R.; Leonhard Kolsbjerg, E.; Kubal, J.; Kaasbjerg, K.; Lysgaard, S.; Bergmann Maronsson, J.; Maxson, T.; Olsen, T.; Pastewka, L.; Peterson, A.; Rostgaard, C.; Schiøtz, J.; Schütt, O.; Strange, M.; Thygesen, K. S.; Vegge, T.; Vilhelmsen, L.; Walter, M.; Zeng, Z.; Jacobsen, K. W. The Atomic Simulation Environment—a Python Library for Working with Atoms. *J. Phys.: Condens. Matter* **2017**, *29* (27), 273002. https://doi.org/10.1088/1361-648X/aa680e.

(7) *Chemisorbed Oxygen on the Au(321) Surface Alloyed with Silver: A First-Principles Investigation | The Journal of Physical Chemistry C*. https://pubs.acs.org/doi/10.1021/jp511884k (accessed 2025-08-12).

(8) NIST Office of Data and. *NIST Chemistry WebBook, O_2*. https://webbook.nist.gov/cgi/cbook.cgi?ID=C7782447 (accessed 2025-08-12).

(9) Knudsen, J.; Martin, N. M.; Grånäs, E.; Blomberg, S.; Gustafson, J.; Andersen, J. N.; Lundgren, E.; Klacar, S.; Hellman, A.; Grönbeck, H. Carbonate Formation on p(X4x)-O/Ag(111). *Phys. Rev. B* **2011**, *84* (11), 115430. https://doi.org/10.1103/PhysRevB.84.115430.

(10) Isegawa, K.; Ueda, K.; Hiwasa, S.; Amemiya, K.; Mase, K.; Kondoh, H. Formation of Carbonate on Ag(111) under Exposure to Ethylene and Oxygen Gases Evidenced by Near Ambient Pressure XPS and NEXAFS. *Chemistry Letters* **2019**, *48* (2), 159–162. https://doi.org/10.1246/cl.180891.

(11) Turano, M. E.; Farber, R. G.; Oskorep, E. C. N.; Rosenberg, R. A.; Killelea, D. R. Characterization of Oxygenaceous Species Formed by Exposure of Ag(111) to Atomic Oxygen. *J. Phys. Chem. C* **2020**, *124* (2), 1382–1389. https://doi.org/10.1021/acs.jpcc.9b09131.

(12) Michaelides, A.; Reuter, K.; Scheffler, M. When Seeing Is Not Believing: Oxygen on Ag(111), a Simple Adsorption System? *Journal of Vacuum Science & Technology A* **2005**, *23* (6), 1487–1497. https://doi.org/10.1116/1.2049302.

Appendix to Chapter 4

This chapter was modified from the supplemental materials from the following publication: Elizabeth E. Happel, E. Charles H. Sykes, and Matthew M. Montemore. Benchmarking DFT Accuracy for O 1s Binding Energies on Metal Surfaces. *Submitted JPCL* ***2025***

Computational Details

Density functional theory (DFT) calculations were performed using the plane-wave VASP code[1,2] with the projector-augmented wave method[3] for core electrons. The PBE functional was used with the Tkatchenko-Scheffler method for dispersion corrections.[4,5] The energy cut-off was set to 400 eV. An energy convergence tolerance of 10^{-5} was used in all cases, and for relaxations the geometric convergence tolerance was 0.03 eV/Å. For 3×3 surface cells, we used a 7×7×1 k-point grid, and for other cases we calculated the number of k-points n in each non-vacuum direction as $n = 62\ \text{Å} / |\vec{a}|$, where $|\vec{a}|$ is the length of the corresponding lattice vector. We performed a few test calculations that suggested our calculated BE values do not change significantly (<0.04 eV) upon significantly increasing the k-point sampling density or energy cutoff, changing the O pseudopotential, or including spin-orbit coupling. For surface calculations, four layers were typically used, with the bottom two fixed at their bulk positions. To ensure that BE calculations were not overly influenced by small unit cells, supercells were created for BE calculations such that lattice vectors were typically larger than 8 to 10 Å. The relaxed structure for each case is provided separately in VASP POSCAR format.

The Janak-Slater method was the primary focus of this work, which uses core-level eigenvalues after 0.5 electrons have been removed from the orbital. We also tested the JS(0,1) method[6], which uses the equation $\epsilon(1) + \frac{1}{2}[\epsilon(0) - \epsilon(1)]$ where $\epsilon(0)$ is the eigenvalue in the initial state and $\epsilon(1)$ is the eigenvalue in the final state (i.e., with 1 electron removed from the orbital). This method has previously been shown to give similar values to the Janak-Slater method for many metal systems, with non-negligible deviations observed in some systems.[6] The final state method uses the total energy difference between the initial state and final state. The initial-state method employs Janak's theorem and uses the eigenvalue in the initial state.[7] Finally, we tested the use of the eigenvalues in the final state, which we denote FS_Eigenvalue. All eigenvalues were referenced to the Fermi energy.

For Figures 4.1, 4.2, A4.1, and A4.2, we shifted the DFT predictions from their raw values, as the raw values are not expected to be quantitatively accurate. Similar shifts have been performed in previous work,[8] and this gives similar BEs for the systems we have in common with this previous work. An alternative approach would be to shift based on a linear fit to all of the data.[9,10] In our case, this would use systems with large errors as part of the shift and decrease the accuracy for systems that seem to be well represented. Furthermore, this approach would require future studies testing advanced methodologies to perform a large number of calculations to directly compare with our work. Thus, we used the average of the O/Ag(111) and O/Pd(111) structures to shift the DFT predictions to the experimental values. This avoids relying on a single system but also focuses on the BE region where we find DFT to be more accurate while requiring only a small number of calculations to test other methodologies. For the Janak-Slater method, this corresponds to shifting all BEs down by 10.56 eV. Note that this shift has no effect on Figure 3, as that involves R^2 values of linear fits.

Data Collection and Processing

Where possible, references where surface structure and binding energy were determined concurrently were prioritized. For surfaces where XPS measurements were consistently taken independently of specific structural measurements without any instances of self-contained structural and binding energy data, supplemental structure-only references are included and are then solely referenced in the *Structure/Facet* columns of each table. Most species have been validated structurally with explicit structural references; however, some were described only through standard naming practices (e.g. (2×2) structure on Au(111)). Priority was given to samples with explicit characterization in addition to BE measurements and we therefore report that in many cases experimental results are not based on pristine samples of only one species and as such there is an expectation for some variety in resolution and FWHM.

For some cases, we chose a coverage for the DFT model even though the coverage was somewhat unclear or varied in the experimental work; specifically: Ir(110) (2×2), Rh(100) c(2×8), and Rh(110) (2×1)p2mg. These cases typically did not give large errors, suggesting our choices were reasonable.

The structures for two bulk materials were collected solely from the Materials Project rather than direct experimental references: ReO_2 and Mn_2O_3.[11] We relaxed these structures prior to calculating the BEs. Both materials have been well characterized by XPS and have good agreement between DFT-calculated and experimental binding energies.

Finally, we have taken into account the change in assignments of specific binding energy features in literature over time, specifically with the Ir(100) (2×1) surface. There are some disagreements about the assignment of two features in the O 1s spectra for this surface: originally, investigations assigned a peak at ≈529.5 eV to oxygen in a twofold coordinated bridge site[12], while more recent investigations reassign this lower BE species to oxygen in hollow sites and a higher BE feature ≈530.6 eV as oxygen at bridge sites[13,14]. We use the more updated assignment for our experimental averages. Although there is a high error for DFT-calculated BEs for this species, it does not appear that the older assignment would entirely resolve this discrepancy because no DFT study has identified a ≈530.6 species.

Table A4.1. A summary of XPS results for surface structures of oxygen-containing molecular species on transition metals.

Host Metal	Facet/Structure	Bonded Species and Site	Coverage (ML)	Avg BE
Pt	(111) (2x2)[15]	NO *Hollows*	0.25[15]	530.5[15,16]
Ir	(111) √3x√3[17]	CO *Atop*	0.33[17]	532.1[18–20]
Ag	(111)	H_2O		533.3[21,22]
Pd	(111) c(2x4)[23]	CO *Hollows*	0.5[23]	531.2[24,25]
Rh	(111) 2x2[26]	CO *Atop*	~0.5[26]	532.1[27,28]
	(111) c(2x4)	CO *Hollows*		530.8[20,28,29]
	(111) c(2x4)[30]	NO *Hollows*	0.5[30]	530.9[30,31]
	(110) 2x2[32]	CO *Atop*	>0.5[32]	531.8[32–34]
Cu	(110) (2x1) [35]	CO	<0.5[35]	532.5[36–38]
Ni	(111) 2x2 [39]	CO *Atop*	~0.5[39]	532.3[39,40]
	(111) 2x2 [39]	CO *Hollows*	~0.5[39]	530.8[39]
	(111) 2x2 [39]	CO *Bridge*	~0.5[39]	531.1[39,40]

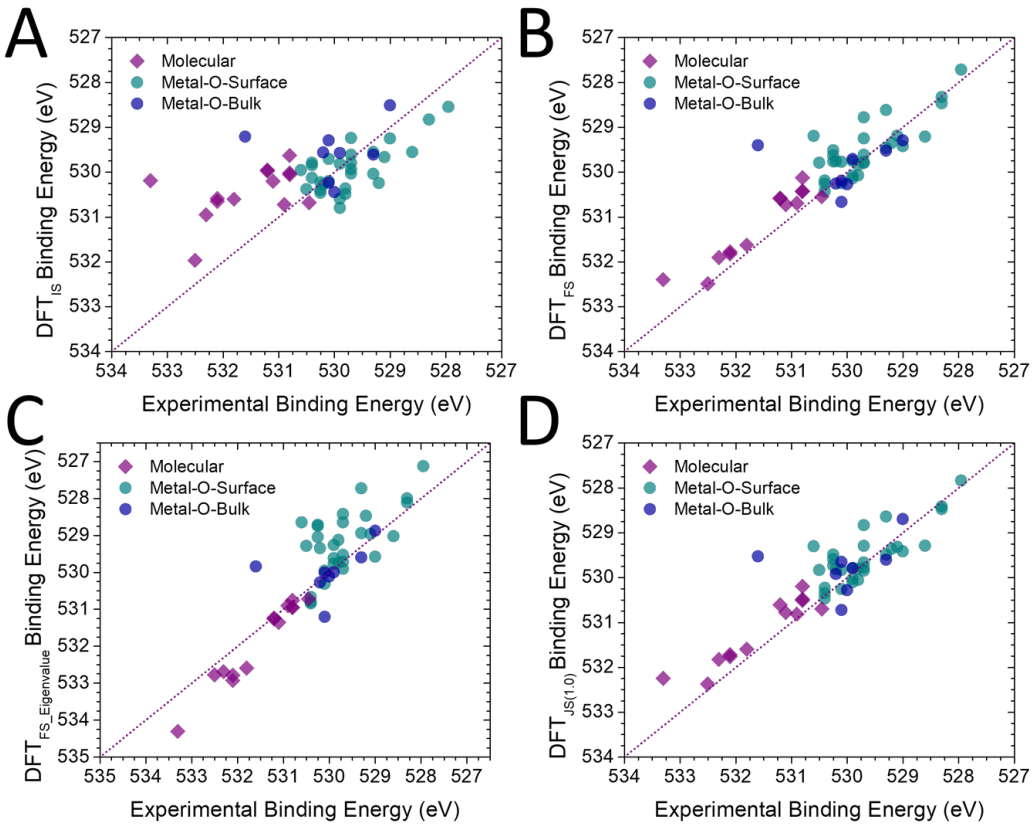

Figure A4.1. The accuracy of different DFT approximations in predicting the binding energies of molecular and atomic oxygen species. Experimentally determined BE values compared to DFT values using (A) initial state (B) final state (C) final state eigenvalues and (D) JS(1,0) approximations all reveal similar inconsistencies between predicted BEs for atomic oxygen species (circles) and more accurate predictions for molecular species (diamonds).

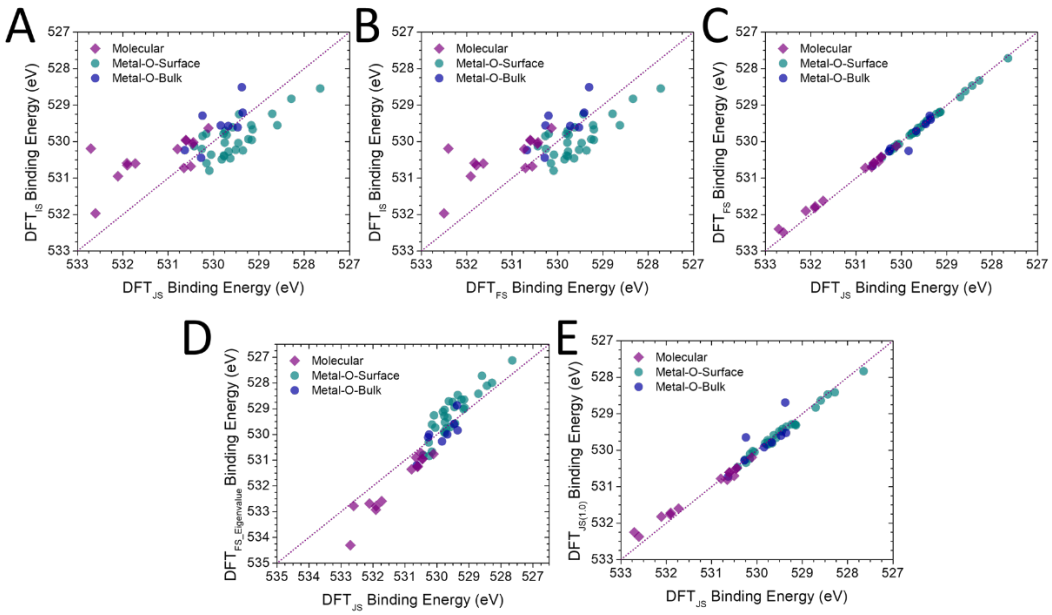

Figure A4.2. A comparison of binding energy predictions between Janak-Slater and other DFT approximations. Alternative approximations (A) initial state, (C) final state, (D) final state eigenvalues and (E) JS(1,0) compared to Janak-Slater tend to reveal minimal differences calculated BEs, with initial state approximations having the most varied results compared to both Janak-Slater and final state approximations (B).

References

(1) Kresse, G.; Hafner, J. Ab Initio Molecular Dynamics for Liquid Metals. *Phys. Rev. B* **1993**, *47* (1), 558–561. https://doi.org/10.1103/PhysRevB.47.558.

(2) Kresse, G.; Furthmüller, J. Efficiency of Ab-Initio Total Energy Calculations for Metals and Semiconductors Using a Plane-Wave Basis Set. *Comput. Mater. Sci.* **1996**, *6* (1), 15–50. https://doi.org/10.1016/0927-0256(96)00008-0.

(3) Blöchl, P. E. Projector Augmented-Wave Method. *Phys. Rev. B* **1994**, *50* (24), 17953–17979. https://doi.org/10.1103/PhysRevB.50.17953.

(4) Perdew, J. P.; Burke, K.; Ernzerhof, M. Generalized Gradient Approximation Made Simple. *Phys. Rev. Lett.* **1996**, *77* (18), 3865–3868. https://doi.org/10.1103/PhysRevLett.77.3865.

(5) Tkatchenko, A.; Scheffler, M. Accurate Molecular Van Der Waals Interactions from Ground-State Electron Density and Free-Atom Reference Data. *Phys. Rev. Lett.* **2009**, *102* (7), 073005. https://doi.org/10.1103/PhysRevLett.102.073005.

(6) Göransson, C.; Olovsson, W.; Abrikosov, I. A. Numerical Investigation of the Validity of the Slater-Janak Transition-State Model in Metallic Systems. *Phys. Rev. B* **2005**, *72* (13), 134203. https://doi.org/10.1103/PhysRevB.72.134203.

(7) Janak, J. F. Proof That dE/Dni = Ei in Density-Functional Theory. *Phys. Rev. B* **1978**, *18* (12), 7165–7168. https://doi.org/10.1103/PhysRevB.18.7165.

(8) Jones, T. E.; Rocha, T. C. R.; Knop-Gericke, A.; Stampfl, C.; Schlögl, R.; Piccinin, S. Insights into the Electronic Structure of the Oxygen Species Active in Alkene Epoxidation on Silver. *ACS Catal.* **2015**, *5* (10), 5846–5850. https://doi.org/10.1021/acscatal.5b01543.

(9) Leftwich, T. R.; Teplyakov, A. V. Calibration of Computationally Predicted N *1s* Binding Energies by Comparison with X-Ray Photoelectron Spectroscopy Measurements. *J. Electron Spectrosc. Relat. Phenom.* **2009**, *175* (1), 31–40. https://doi.org/10.1016/j.elspec.2009.07.002.

(10) Zhao, J.; Gao, F.; Pujari, S. P.; Zuilhof, H.; Teplyakov, A. V. Universal Calibration of Computationally Predicted N 1s Binding Energies for Interpretation of XPS Experimental Measurements. *Langmuir* **2017**, *33* (41), 10792–10799. https://doi.org/10.1021/acs.langmuir.7b02301.

(11) Jain, A.; Ong, S. P.; Hautier, G.; Chen, W.; Richards, W. D.; Dacek, S.; Cholia, S.; Gunter, D.; Skinner, D.; Ceder, G.; Persson, K. A. Commentary: The Materials Project: A Materials Genome Approach to Accelerating Materials Innovation. *APL Mater.* **2013**, *1* (1), 011002. https://doi.org/10.1063/1.4812323.

(12) Novotny, Z.; Tobler, B.; Artiglia, L.; Fischer, M.; Schreck, M.; Raabe, J.; Osterwalder, J. Kinetics of the Thermal Oxidation of Ir(100) toward IrO2 Studied by Ambient-Pressure X-Ray Photoelectron Spectroscopy. *J. Phys. Chem. Lett.* **2020**, *11* (9), 3601–3607. https://doi.org/10.1021/acs.jpclett.0c00914.

(13) Cao, X.; Liu, C.; Zhang, T.; Xu, Q.; Zhang, D.; Liu, X.; Jiao, H.; Wen, X.; Yang, Y.; Li, Y.; Niemantsverdriet, J. W.; Zhu, J. Revisiting Oxygen Adsorption on Ir(100). *J. Phys. Chem. C* **2022**, *126* (24), 10035–10044. https://doi.org/10.1021/acs.jpcc.2c01237.

(14) Martin, R.; Kim, M.; Lee, C. J.; Mehar, V.; Albertin, S.; Hejral, U.; Merte, L. R.; Lundgren, E.; Asthagiri, A.; Weaver, J. F. High-Resolution X-Ray Photoelectron Spectroscopy of an IrO2(110) Film on Ir(100). *J. Phys. Chem. Lett.* **2020**, *11* (17), 7184–7189. https://doi.org/10.1021/acs.jpclett.0c01805.

(15) Zhu, J. F.; Kinne, M.; Fuhrmann, T.; Denecke, R.; Steinrück, H.-P. In Situ High-Resolution XPS Studies on Adsorption of NO on Pt(111). *Surf. Sci.* **2003**, *529* (3), 384–396. https://doi.org/10.1016/S0039-6028(03)00298-X.

(16) Shimada, T.; Mun, B. S.; Nakai, I. F.; Banno, A.; Abe, H.; Iwasawa, Y.; Ohta, T.; Kondoh, H. Irreversible Change in the NO Adsorption State on Pt(111) under High Pressure Studied by AP-XPS, NEXAFS, and STM. *J. Phys. Chem. C* **2010**, *114* (40), 17030–17035. https://doi.org/10.1021/jp102777j.

(17) Lauterbach, J.; Boyle, R. W.; Schick, M.; Mitchell, W. J.; Meng, B.; Weinberg, W. H. The Adsorption of CO on Ir(111) Investigated with FT-IRAS. *Surf. Sci.* **1996**, *350* (1), 32–44. https://doi.org/10.1016/0039-6028(95)01114-5.
(18) Zhdan, P. A.; Boreskov, G. K.; Boronin, A. I.; Schepelin, A. P.; Withrow, S. P.; Weinberg, W. H. An XPS Investigation of CO Titration of Oxygen from an Ir(111) Surface. *Appl. Surf. Sci.* **1979**, *3* (2), 145–160. https://doi.org/10.1016/0378-5963(79)90015-1.
(19) Zhdan, P. A.; Boreskov, G. K.; Egelhoff, W. F.; Weinberg, W. H. The Application of XPS to the Determination of the Kinetics of the Co Oxidation Reaction over the Ir(111) Surface. *Surf. Sci.* **1976**, *61* (2), 377–390. https://doi.org/10.1016/0039-6028(76)90052-2.
(20) Ueda, K.; Isegawa, K.; Amemiya, K.; Mase, K.; Kondoh, H. Operando NAP-XPS Observation and Kinetics Analysis of NO Reduction over Rh(111) Surface: Characterization of Active Surface and Reactive Species. *ACS Catal.* **2018**, *8* (12), 11663–11670. https://doi.org/10.1021/acscatal.8b03180.
(21) Felter, T. E.; Weinberg, W. H.; Lastushkina, G. Ya.; Zhdan, P. A.; Boreskov, G. K.; Hrbek, J. The Adsorption of Methanol on Ag(111) and Its Reaction with Preadsorbed Oxygen. *Appl. Surf. Sci.* **1983**, *16* (3), 351–364. https://doi.org/10.1016/0378-5963(83)90079-X.
(22) Schwaner, A. L.; White, J. M. Electron-Induced Chemistry of Methanol on Ag(111). *J. Phys. Chem. B* **1997**, *101* (49), 10414–10422. https://doi.org/10.1021/jp972136y.
(23) Surnev, S.; Sock, M.; Ramsey, M. G.; Netzer, F. P.; Wiklund, M.; Borg, M.; Andersen, J. N. CO Adsorption on Pd(111): A High-Resolution Core Level Photoemission and Electron Energy Loss Spectroscopy Study. *Surf. Sci.* **2000**, *470* (1–2), 171–185. https://doi.org/10.1016/S0039-6028(00)00853-0.
(24) Toyoshima, R.; Yoshida, M.; Monya, Y.; Kousa, Y.; Suzuki, K.; Abe, H.; Mun, B. S.; Mase, K.; Amemiya, K.; Kondoh, H. In Situ Ambient Pressure XPS Study of CO Oxidation Reaction on Pd(111) Surfaces. *J. Phys. Chem. C* **2012**, *116* (35), 18691–18697. https://doi.org/10.1021/jp301636u.
(25) Martin, N. M.; Van den Bossche, M.; Grönbeck, H.; Hakanoglu, C.; Zhang, F.; Li, T.; Gustafson, J.; Weaver, J. F.; Lundgren, E. CO Adsorption on Clean and Oxidized Pd(111). *J. Phys. Chem. C* **2014**, *118* (2), 1118–1128. https://doi.org/10.1021/jp410895c.
(26) Schwegmann, S.; Over, H.; De Renzi, V.; Ertl, G. The Atomic Geometry of the O and CO + O Phases on Rh(111). *Surf. Sci.* **1997**, *375* (1), 91–106. https://doi.org/10.1016/S0039-6028(97)01249-1.
(27) Wagner, F. T.; Moylan, T. E.; Schmieg, S. J. Hydrophilic versus Hydrophobic Coadsorption: Carbon Monoxide and Water on Rh(111) versus Pt(111). *Surf. Sci.* **1988**, *195* (3), 403–428. https://doi.org/10.1016/0039-6028(88)90350-0.
(28) DeLOUISE, L. A.; White, E. J.; Winugrad, N. Characterization of CO Binding Sites on Rh(111) and Rh(331) Surfaces by XPS and LEED: Comparison to EELS Results.
(29) DeLouise, L. A.; Winograd, N. Carbon Monoxide Adsorption and Desorption on Rh{111} and Rh{331} Surfaces. *Surf. Sci.* **1984**, *138* (2), 417–431. https://doi.org/10.1016/0039-6028(84)90256-5.
(30) Toyoshima, R.; Yoshida, M.; Monya, Y.; Suzuki, K.; Amemiya, K.; Mase, K.; Mun, B. S.; Kondoh, H. High-Pressure NO-Induced Mixed Phase on Rh(111): Chemically Driven Replacement. *J. Phys. Chem. C* **2015**, *119* (6), 3033–3039. https://doi.org/10.1021/jp507542h.
(31) DeLouise, L. A.; Winograd, N. Adsorption and Dessorption of NO from Rh(111) and Rh(331) Surfaces. *Surf. Sci.* **1985**, *159*, 199–213.
(32) Dhanak, V. R.; Baraldi, A.; Comelli, G.; Paolucci, G.; Kiskinova, M.; Rosei, R. CO Adsorption on Unreconstructed and Reconstructed Rh(110) Surfaces: LEED and XPS Studies. *Surf. Sci.* **1993**, *295* (3), 287–294. https://doi.org/10.1016/0039-6028(93)90275-O.
(33) Nguyen, L.; Liu, L.; Assefa, S.; Wolverton, C.; Schneider, W. F.; Tao, F. F. Atomic-Scale Structural Evolution of Rh(110) during Catalysis. *ACS Catal.* **2017**, *7* (1), 664–674. https://doi.org/10.1021/acscatal.6b02006.

(34) Baird, R. J.; Ku, R. C.; Wynblatt, P. The Chemisorption of CO and NO on Rh(110). *Surf. Sci.* **1980**, *97* (2), 346–362. https://doi.org/10.1016/0039-6028(80)90672-X.
(35) Hofmann, Ph.; Schindler, K.-M.; Bao, S.; Fritzsche, V.; Bradshaw, A. M.; Woodruff, D. P. A Photoelectron Diffraction Study of the Structure of the Cu{110}(2 × 1)-CO System. *Surf. Sci.* **1995**, *337* (3), 169–176. https://doi.org/10.1016/0039-6028(95)00612-5.
(36) Eren, B.; Lichtenstein, L.; Wu, C. H.; Bluhm, H.; Somorjai, G. A.; Salmeron, M. Reaction of CO with Preadsorbed Oxygen on Low-Index Copper Surfaces: An Ambient Pressure X-Ray Photoelectron Spectroscopy and Scanning Tunneling Microscopy Study. *J. Phys. Chem. C* **2015**, *119* (26), 14669–14674. https://doi.org/10.1021/jp512831f.
(37) Christiansen, M.; Thomsen, E. V.; Onsgaard, J. Coadsorption of K and CO on Cu(110). *Surf. Sci.* **1992**, *261* (1), 179–190. https://doi.org/10.1016/0039-6028(92)90230-4.
(38) Gruzalski, G. R.; Zehner, D. M.; Wendelken, J. F. An XPS Study of Oxygen Adsorption on Cu(110). *Surf. Sci.* **1985**, *159* (2), 353–368. https://doi.org/10.1016/0039-6028(85)90433-9.
(39) Held, G.; Schuler, J.; Sklarek, W.; Steinrück, H.-P. Determination of Adsorption Sites of Pure and Coadsorbed CO on Ni(111) by High Resolution X-Ray Photoelectron Spectroscopy. *Surf. Sci.* **1998**, *398* (1), 154–171. https://doi.org/10.1016/S0039-6028(98)80020-4.
(40) Degerman, D.; Lömker, P.; Goodwin, C. M.; Shipilin, M.; García-Martínez, F.; Schlueter, C.; Nilsson, A.; Amann, P. State of the Surface During CO Hydrogenation over Ni(111) and Ni(211) Probed by Operando X-Ray Photoelectron Spectroscopy. *J. Phys. Chem. C* **2023**, *127* (8), 4021–4032. https://doi.org/10.1021/acs.jpcc.2c07650.

Appendix to Chapter 5

Materials and Methods

Sample preparation and cleaning occurred in a preparation chamber with base pressure ~ $1e^{-10}$ mbar. A Ag(111) single crystal was cleaned with a series of Ar^+ bombardment and 900 K annealing cycles. NO_2 (Aldrich >99.5%) was dosed with a precision leak valve while the sample was heated with a PBN heater in the preparation chamber. After deposition, samples were cooled to room temperature and were then transferred into the scanning probe microscope (SPM) chamber (base pressure ~$5e^{-11}$ mbar) where they were cooled to ~13 K to image. STM experiments were performed by a low-temperature scanning tunneling microscope (Infinty by Scienta Omicron). Ethylene was exposed to oxygen precoated samples in the SPM chamber with maximum temperature during dosing ~ 25 K.

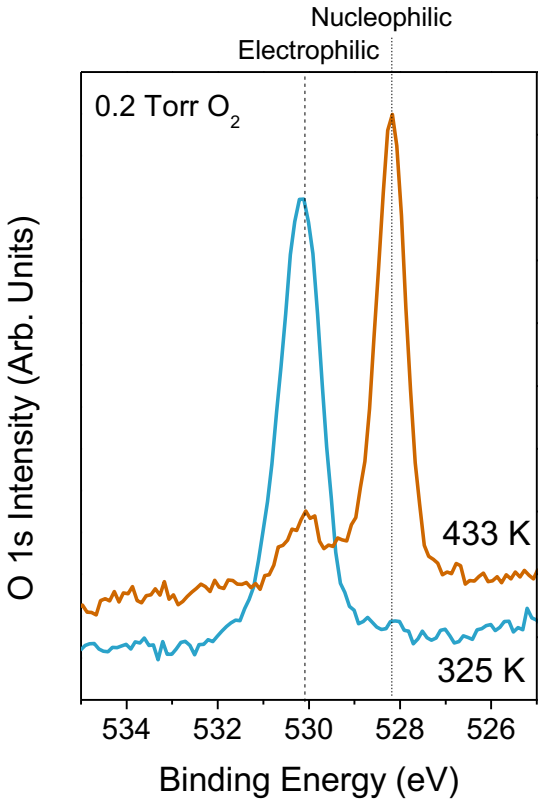

Figure A5.1. The effect of annealing on oxygen species on Ag(111). O 1s XPS spectra of Ag(111) in 0.2 Torr O_2 first at 325 K (blue) where higher binding energy electrophilic is the only oxygen species present. Followed by heating the sample to 433 K where the oxygen species shifts to predominately nucleophilic oxygen with some remaining electrophilic species.

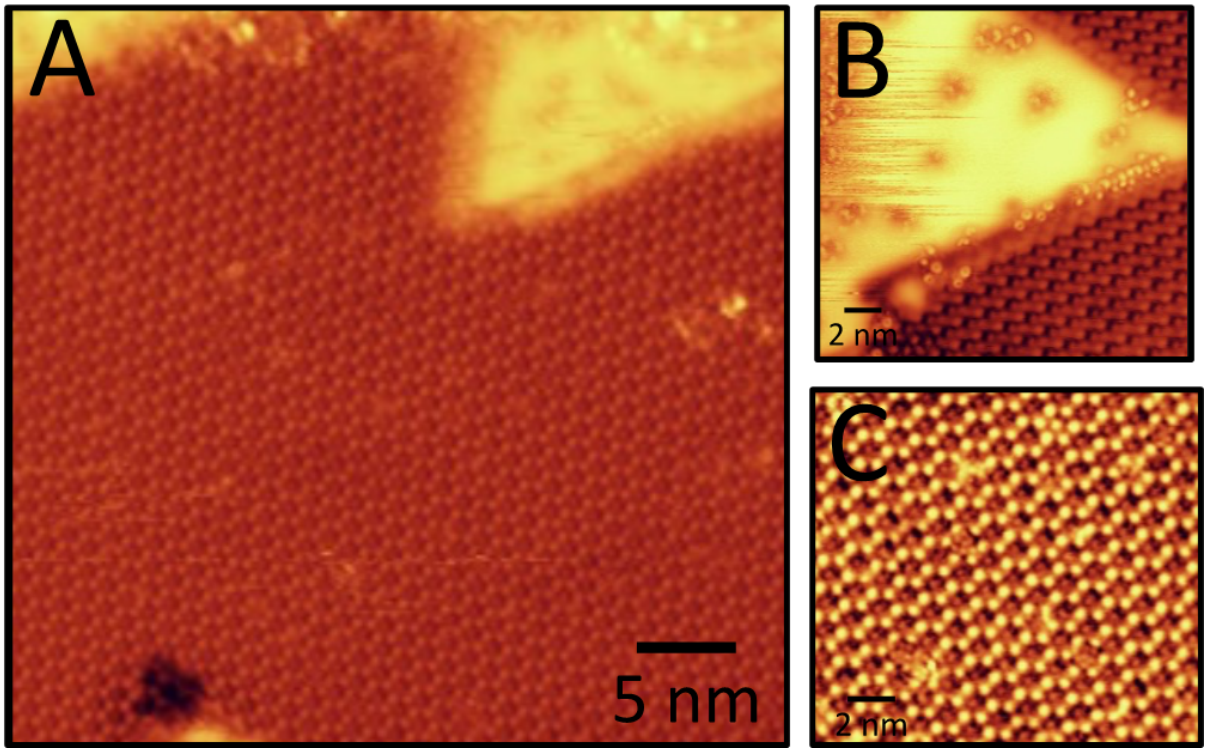

Figure A5.2. Ag(111) exposed to NO_2 between 220-250°C. (A) Large scale image of O/Ag(111) after high temperature exposure to NO_2 showing that the p(4x4) phase **(C)** dominates surface coverage at this deposition temperature. However, some remainder coverage of the triangular oxygen species are still seen at higher temperatures **(B)**. Image conditions A: 0.2 nA, 300 mV, B: 0.3 nA, -50 mV, and C: 0.2 nA, 300 mV.

Appendix to Chapter 6:

This chapter was modified from the supplemental materials from the following publication: Elizabeth E. Happel, Anika Jalil, Laura Cramer, Adrian Hunt, Adam S. Hoffman, Iradwikanari Waluyo, Matthew M. Montemore, Phillip Christopher, and E. Charles H. Sykes. Nickel Promotes Selective Ethylene Epoxidation on Silver. *Science*. **2025,** 387, 869-873.
DFT was performed by M.M. Montemore, Nanoparticle synthesis and analysis was performed by A. Jalil, and preliminary TPD experiments were performed by L. Cramer. TPD quantification, XPS, and STM were performed by E.E. Happel.

Materials and Methods

Density functional theory (DFT)

The VASP plane-wave DFT code was used to perform DFT calculations [1,2]. The PBE exchange-correlation functional was used with the Tkatchenko-Scheffler dispersion correction method [3,4]. The projector-augmented wave method was used for the core electrons. The plane-wave energy cutoff was 400 eV, and the k-point sampling was 7 × 7 × 1 for a 3 × 3 surface cell with four layers. The bottom two layers were fixed at their bulk positions. The dimer method was used for transition state calculations [5]. Spin polarization was used in all calculations unless previous calculations had indicated it was unnecessary for a specific case.

One Ag(111) surface atom was replaced with the dopant. Adsorption energies were calculated relative to gas-phase O_2 such that a negative value corresponds to favorable adsorption. O_2 was placed on top of the dopant and relaxed to determine the initial state and associated energy for O_2 activation. For the dissociated 2O* state, the two O atoms were placed in hollow sites on either side of the dopant atom in all cases, even for cases where it is more favorable for one O atom to move away from the other, which is the case for pure Ag. In contrast to Ag, the two O atoms in hollow sites on either side of the dopant site is the most stable configuration for NiAg. This means that for O_2 to desorb from Ag(111) the two O atoms must first move back together, which is energetically 0.4 eV uphill, before overcoming the desorption barrier. The O_2 transition state on NiAg was confirmed with a frequency calculation, as only one imaginary frequency was observed and corresponded to O-O bond cleavage.

DFT was then used to calculate O_2 desorption barriers on Ag and NiAg, revealing that O_2 desorption is kinetically more favorable on NiAg than Ag (Table S1), in agreement with our TPD results. Specifically, we calculated the O_2 desorption barrier originating from both the 2O/NiAg and 3O/NiAg states. For these states, the initial configuration has all the O atoms at the Ni site, as that is the most stable state. As mentioned for pure Ag, the initial state consists of the two O atoms in separate unit cells, as that is the most stable state. Together, these calculations indicate that the O_2 desorption barrier is at least 0.23 eV lower for NiAg than Ag(111), consistent with the TPD results. Note that Figure 1a in the main text is calculated for two O atoms on either side of the dopant atom on all surfaces, including pure Ag, to enable direct comparison.

Surface	Reaction	Barrier (eV)
NiAg	$2O/Ni_1Ag \rightarrow O_2(g) + Ni_1Ag$	1.51
NiAg	$3O/Ni_1Ag \rightarrow O_2(g) + 1O/Ni_1Ag$	1.03
Ag	$2O/Ag \rightarrow O_2(g) + Ag$	1.74

Table A6.1.O_2 desorption barriers from NiAg and Ag. For Ag, the initial state consists of two O atoms in separate unit cells.

Our DFT calculations predict that 2 O atoms adsorbed at the NiAg site are more stable than 1 O at the NiAg site and 1 O on an Ag site. This may seem contradictory to our experimental finding of O spillover onto Ag sites. However, under conditions where O is more stable on Ag than in the gas phase as $1/2O_2(g)$ there is a thermodynamic driving force for oxygen to move from the gas phase to Ag surface sites via the Ni atom, making O spillover to Ag energetically favorable. Furthermore, a spillover pathway was calculated for NiAg starting with two O atoms at the Ni site. One O atom then diffuses away from the Ni site which has a barrier of 0.96 eV and an O_2 molecule dissociates at the 1O/NiAg site which has a barrier of 0.13 eV. Both barriers should be surmountable at 350 K or above, demonstrating that there is at least one mechanism by which O atom spillover from Ni to Ag can occur.

To understand why these systems deviate from typical scaling relations, we examined a number of potential correlations. First, we plotted the O_2 dissociation barrier (relative to adsorbed O_2) against the 2O adsorption energy (the same as Fig. 1a), the O_2 adsorption energy, and the O_2 transition state energy, all relative to gas-phase O_2. All three plots show a similar trend: a rough, non-linear correlation with significant scatter. Ni appears promising, with a relatively low dissociation barrier in all three plots. We next plotted the adsorption energy of all three states—2O, adsorbed O_2, and the O_2 transition state—against each other. In all cases, there is a linear correlation with only a small amount of scatter. Overall, all the individual states correlate reasonably well with each other, but the dissociation barrier does not correlate well with any of the states. This is because the barrier calculation involves subtracting two similar energies, which amplifies the small deviations from linearity.

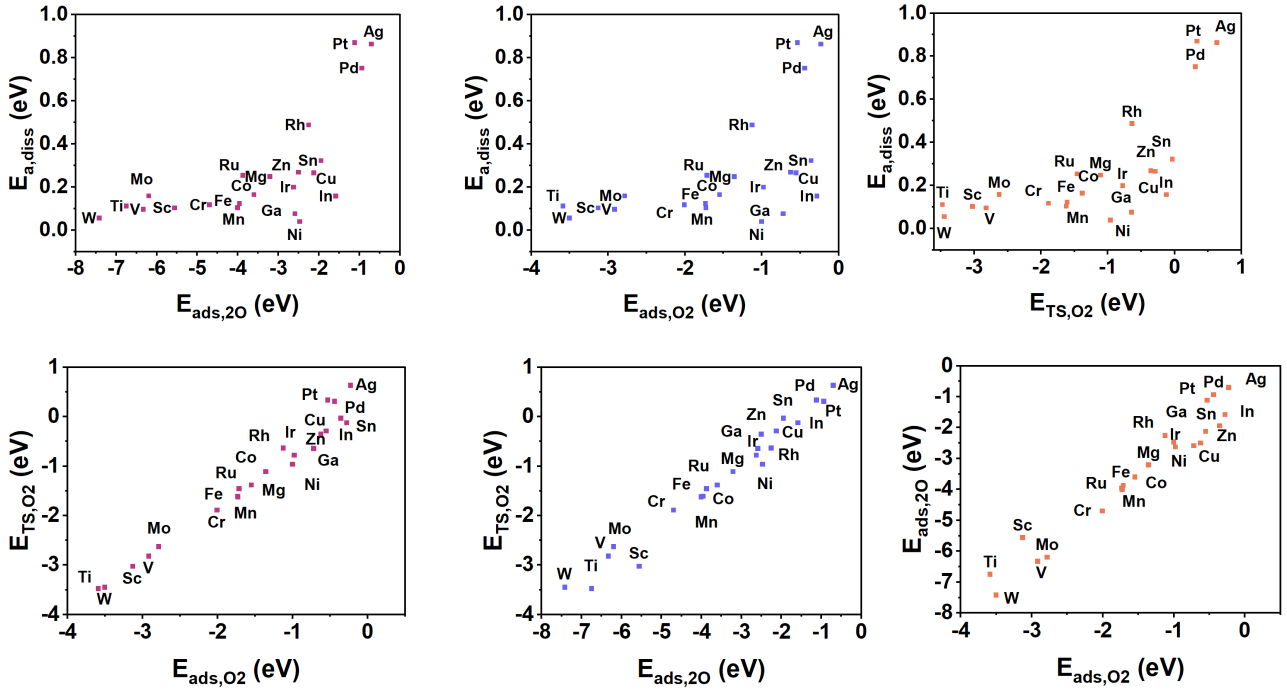

Figure A6.1. Correlations between the O_2 dissociation barrier (relative to adsorbed O_2) and the adsorption energies of 2O, O_2, and the O_2 transition state (all relative to gas-phase O_2).

Therefore, the mechanism for breaking linear scaling relations for O_2 dissociation on Ag-based single-atom alloys may be different than the mechanisms elucidated previously for e.g. C-H and H_2 activation. For H_2, the transition state can deviate from scaling relations because it is small and mostly interacts with the dopant atom, while the final state interacts mostly with host atoms [6]. For hydrocarbons, scaling relations are often broken for a similar reason: different states (i.e., different adsorbates and transition states) often occupy different sites where they interact with different elements in the surface [6–8]. For early transition metals, agostic C-H-M interactions can also play a role [7,8]. In contrast, our results suggest that the O_2 dissociation barrier on Ag-based single-atom alloys deviates from linear scaling due mostly to the relatively strongly adsorbed O_2 state, as the difference between the TS and O_2* is sensitive to small fluctuations from the scaling line.

Atomic graphics of the O_2 adsorbed state, O_2 transition state, and 2O state on NiAg are shown in Fig A6.2.

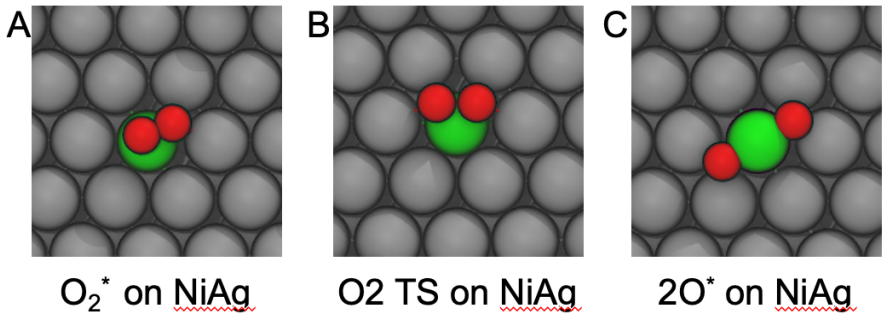

Figure A6.2. Structures for the O_2 dissociation pathway on NiAg.

We performed DFT calculations of the thermodynamics of ethylene reacting with O in the Ag(111) p-(4x4) reconstruction, which is widely considered to be nucleophilic and non-selective in epoxidation [9,10]. Specifically, we computed the energy for formation of acetaldehyde, the product when ethylene reacts with nucleophilic O, as described in the literature [10]. We then performed the same calculation with a Ni atom doped into the Ag(111) p-(4x4) reconstruction wherein ethylene reacts with one of the O atoms that is bound to Ni. As shown in Fig. S3, the reaction becomes significantly less favorable in the presence of Ni which binds the nucleophilic oxygen more strongly, making it more "spectator like". This thermodynamic effect, and the fact that Ni also increases the activation barrier for the unselective combustion reaction, decreases the rate of reaction of nucleophilic O with ethylene significantly. This will directly stabilize O atoms bound to Ni, and because of favorable O-Ag-O interactions this stabilizing effect is expected to extend beyond the O atoms directly bound to Ni. In support of this, as described in the catalysis section, the surface coverage of Ni on supported catalysts is estimated to be > 10% ML and thus it is expected that Ni stabilizes the majority of the O on the surface at the optimum coverage. Together, this is consistent with the catalysis data showing that Ni reduces the rate of CO_2 production to a greater degree than EO which is reported to be formed from electrophilic oxygen [11–13].

It is important to note that the quantitative value of stabilization shown here cannot be directly used to predict the change in rate of ethylene (or EO) combustion caused by Ni incorporation. These calculations focus only on O local to Ni, and thus the influence on O species sitting one or two lattice sites away from Ni is likely smaller. A quantitative comparison of the theoretical prediction and the measured decrease in CO_2 formation kinetics requires a complete description of the AgNi surface under reaction conditions, which is outside the scope of these studies. However, the results certainly support the hypothesis that Ni serves to stabilize nucleophilic O species on Ag and thus decrease the rates of primary and secondary combustion.

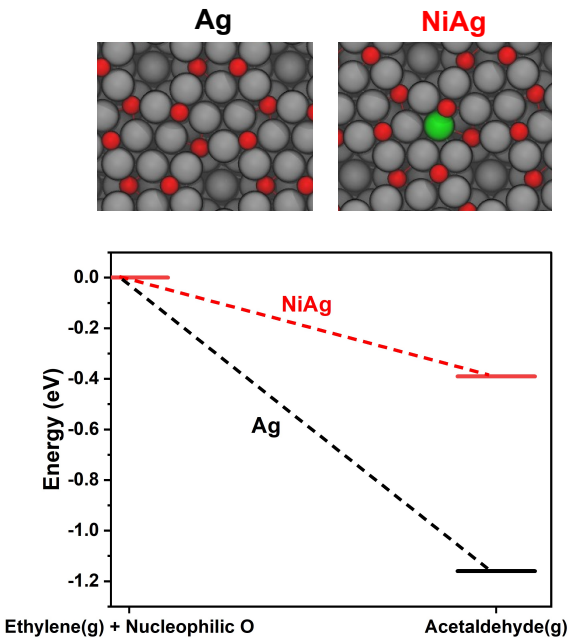

Figure A6.3. Energetics of ethylene reacting with nucleophilic O on Ag and NiAg(111).

Temperature programmed desorption (TPD)

TPD experiments were conducted in an ultra-high vacuum (UHV) chamber with a base pressure $>1\times10^{-10}$ mbar equipped with a Hidden Hal RC 201 mass spectrometer capable of advancing to within 1 mm of the Ag(111) crystal surface. The crystal was cleaned with cycles of Ar^+ ion sputtering (~2 μA drain current, 1.0 keV beam energy) and annealing to 725 K. Temperatures were measured with a K-type thermocouple welded to the back of a crystal. The crystal was heated resistively via its support wires, and cooled with liquid nitrogen. NiAg(111) surface alloys were prepared by deposition of Ni (Goodfellow, 99.99%) via electron beam evaporation (Omicron, EFM 3) onto a Ag(111) crystal held at 473 K. Exposures of O_2 (Middlesex, 99.999%) were performed with a precision leak valve.

Scanning tunneling microscopy (STM)

STM experiments were performed in a low-temperature scanning tunneling microscope (Infinity by Scienta Omicron) under UHV. Sample cleaning, annealing, and Ni deposition were performed in the preparation chamber with a base pressure $\sim1\times10^{-10}$ mbar. High resolution imaging was performed in the STM chamber with a base pressure $<1\times10^{-11}$ mbar at ~13 K with an etched W tip. These experiments utilized a Ag(111) crystal that was cleaned with cycles of Ar^+ ion sputtering (1.0 keV, 8μA) followed by annealing to 900 K. NiAg(111) surface alloys were prepared via electron beam evaporation as described above. Samples were exposed to O_2 (Middlesex, 99.999%)

via precision leak valve while cooling from 473 K in the preparation chamber and moved to the STM chamber where they were cooled from room temperature to ~13 K before imaging.

X-ray photoemission spectroscopy (XPS)

Ambient pressure XPS was performed at beamline 23-ID-2 (IOS) of the National Synchrotron Light Source II (NSLS- II) at Brookhaven National Laboratory [14]. All experiments were performed on a Ag(111) crystal cleaned with Ar^+ ion sputtering and annealing to 900 K until XPS spectra were free from impurities. High purity O_2 (Matheson, 99.994%) was introduced to the chamber via precision leak valve while the sample was heated with a pyrolytic boron nitride heater. Temperature was measured with a K-type thermocouple mounted between the Ag(111) crystal and the heater. NiAg(111) alloys were prepared similarly by evaporating a Ni rod (Goodfellow, 99.99%) with a SPECS EBE-4 e-beam evaporator. Ni coverage was calculated by using the corrected Ni 2p peak area referenced to a saturated oxygen surface. For the XPS data in Fig. 4 the sample was exposed to 1 Torr O_2 at 325 K, heated at a rate of 40 K/min, then held at each temperature for ~20 min while the XPS spectra were collected, all under 1 Torr O_2. Photon energies of 1090, 760, and 500 eV were used to generate photoelectrons with kinetic energies of ~200 eV for the Ni 2p, O 1s, and C 1s core levels, respectively, to maintain similar probing depths. Reference Ag 3d spectra were taken at each photon energy. Spectra were corrected with respect to the Fermi edge and metallic Ag 3d binding energy. We observed three oxygen species with discrete binding energies; one attributed to nucleophilic oxygen with binding energy ~ 528.4 eV, one associated with a Ni bound oxygen species ~529.3 eV, and one associated with electrophilic oxygen ~530.1 eV. XPS data was analyzed with CasaXPS and fit with a linear background; each species was assigned and fit according to literature values for the different types of oxygen as described in Table S7.

Synthesis of Ag and NiAg catalysts

Ag colloids

Colloidal Ag nanoparticles were synthesized through a polyol process [15]. 100 mg of $AgNO_3$ (Sigma-Aldrich CAS: 7761-88-8) was dissolved in 3 mL of ethylene glycol (VWR Chemicals BDH CAS: 107-21-1, lot: C23A3001). Separately, in a 20 mL vial, 7 mL of ethylene glycol was added to 1 g (for ~60-70 nm particles) or 250 mg (for ~90-100 nm particles) of polyvinylpyrrolidone (PVP, MW ~58,000 Sigma-Aldrich CAS: 9003-39-8, lot: 50002401) and placed in a 160°C silicone oil bath stirring at 300 rpm with the cap open for 3-4 minutes until a clear, colorless solution was formed. This step enabled the dissolution of PVP, evaporation of residual water in ethylene glycol and the initial formation of glycolaldehyde which is the primary reducing agent [16]. The $AgNO_3$ solution was then pipetted into the PVP mixture while the vials were in the bath, and the caps were quickly screwed on. Upon addition of $AgNO_3$ the solution changed color to a light amber, which deepened to brown over the course of the reaction. The growth to larger nanoparticles was marked by a color change to opaque gray. For 60-70 nm particles, the

reaction was stopped after 1 hour of mixing by removing from the heat. For 90-100 nm particles— after 1 hour of mixing, the vial caps were opened to add in 750 mg more of PVP and the cap reattached. The mixture was stirred at temperature for a further 30 minutes before taking the vials out to cool to room temperature. The second PVP addition is crucial for the effective incorporation of Ni in subsequent steps into the larger nanoparticle sizes. We found that the shape, size and final NiAg alloy stability were all sensitive to the supplier and lot number of ethylene glycol used. The batch of ethylene glycol used in this study had <100 ppb of trace impurities including Ca, Fe and Na. Higher concentrations of such impurities can preferentially bind to one facet of Ag leading to unequal facet growth rates which results in a range of nanoparticle shapes and sizes [17,18]. Such impurities may also affect the binding of PVP to the surface of the Ag nanoparticles which ultimately affects particle growth and Ni incorporation [19]. The presence of such impurities and the highly hygroscopic nature of ethylene glycol can therefore lead to variability in the synthesis of Ag nanoparticles when different suppliers and lot numbers of ethylene glycol are involved.

NiAg colloids and Ag control

For the synthesis of NiAg, a stoichiometric volume of a mixture of $Ni(NO_3)_2.6H_2O$ (Sigma-Aldrich, CAS: 13478-00-7, lot: 0000017640) in ethylene glycol (5 mg/mL) was pipetted into the synthesized Ag nanoparticle vials at room temperature. Sodium hydroxide (50 wt%, Sigma-Aldrich, lot: STBK1331) and hydrazine (35 wt%, Sigma-Aldrich, lot: MKCN1602) were added in molar ratios NaOH:Ni 200:1 and hydrazine:Ni 115:1 respectively. Sodium hydroxide and hydrazine solutions in excess act cooperatively to ensure the kinetic reduction and incorporation of Ni into Ag [20]. The vial was then placed in a 120°C oil bath stirring at 300 rpm to facilitate the reduction (Ni^{2+} to Ni^0) process. The reaction was quenched after 30 minutes by removing the vial and adding 10 mL of 97 proof ethanol (Sigma-Aldrich). The color of the unwashed AgNi colloids were similar to pure Ag— opaque gray. After cooling completely to room temperature, the particles were cleaned by adding up to 60 mL (total 80 mL of the mixture) more of ethanol and centrifuging the mixture at 10,000 rpm for 40 minutes. Most of the supernatant was decanted and the mixture was made up to 80 mL with more ethanol and centrifuged again at 10,000 rpm for 20 minutes before decanting again. The centrifuge contained a dark plug of concentrated NiAg nanoparticles at the bottom, and a clear, pale-yellow supernatant. For NiAg, the pellet was especially prone to agitation, making it so that the decantation process could redisperse the pellet. To avoid the loss of NiAg, some supernatant solution was left behind during decanting for NiAg.

Ag control samples were made identically to NiAg, just without the Ni addition step. Interestingly, the Ag control pellet was a deep amber color while the NiAg was purple-brown. The color of the Ag colloids is dictated by the nature of the localized surface plasmon resonance supported by the nanoparticles, which is a function of the particle size and is sensitive to the composition of the nanoparticle itself which can change the dielectric function. The incorporation of Ni will modify the local dielectric function of the metal at the surface, resulting in a change in color [21]. The colloids

were then redispersed in a total volume of 20 mL ethanol (resulting in 2-3 mg/mL solution of Ag nanoparticles) and sonicated for 1 hr before use; after sonication both the solutions returned an opaque gray color that looked amber on the sides when the container was gently swirled.

Figure A6.4. Configuration of typical Ag and AgNi colloidal synthesis— the frame ensured that the vials had enough support to be continuously stirred and heated throughout the synthesis period. Design of the frame adapted from Ref [18].

Ag and NiAg supported catalysts

The sonicated nanoparticles in ethanol were mixed with α-Al_2O_3 powder (5-6 m^2/g, 20-50 micron APS, Alfa-Aesar, CAS:1344-28-1, lot: T12C026) in an evaporating dish. ICP analytics of the support are shown in Table S2. The volume of nanoparticles and mass of powder depended on the desired weight loading. To evaporate the ethanol, the dish was placed in a 110°C oven for 4-6 hours with a piece of foil with holes covering the top of the dish. For 5-10 wt% by Ag, the resulting powder was mixed thoroughly with a spatula, resulting in a homogenous gray powder. To analyze whether PVP was removed from the supported NiAg catalysts, the C 1s and N 1s features were analyzed between dried and calcined NiAg on α-Al_2O_3 catalysts with XPS measurements (ThermoFisher Escalab Xi+). The catalyst powders were sprinkled onto double sided tape for measurements.

5 nm Ni nanoparticles and Ni/α-Al_2O_3

Ni nanoparticles were synthesized as described in a previous procedure [22]. Briefly, 514 mg of $Ni(acac)_2$ was dissolved in 30 mL of oleylamine and 0.64 mL of oleic acid and degassed with Ar. Separately, 885 mg of borane tert-butyl amine borane (BTB) and 4 mL oleylamine were dissolved and degassed. After heating the $Ni(acac)_2$ mixture at 110°C (oil bath) at 300 rpm to give a teal solution for 30 minutes, the temperature was decreased to 90°C. When cooled to 90°C, the BTB mixture was quickly injected into the flask. This created a color change instantly to black, signaling Ni reduction. The reaction was continued for 1 hour before quenching with acetone. The entire reaction was carried out under Ar. The particles were then centrifuged at 5000 rpm for 10 minutes

with a mixture of acetone and toluene which caused Ni nanoparticle crystals to precipitate out. The centrifuge process was repeated three times before collecting the Ni crystals and storing them dry.

The Ni crystals were weighed out and dispersed in toluene while stirring in a flask. α-Al_2O_3 powder was then added to the solution and stirred overnight with a stopper to prevent the evaporation of excess toluene. The powder was then separated by centrifugation and calcined via a rapid thermal calcination process at 500°C for 2 minutes. For 1 wt% Ni/α-Al_2O_3 the result was a homogenous, light gray powder.

Inductively coupled plasma-optical emission spectroscopy (ICP-OES)

For analysis of Ag weight loading, the samples were digested in room temperature, concentrated (70 v/v%) nitric acid overnight, diluted down to a 5 wt% acid solution and filtered to remove the support particles. For Ni quantification, inverse aqua regia—a mixture of 1:3 hydrochloric acid (37 v/v%): nitric acid (70 v/v%)—was used instead of nitric acid, to precipitate out Ag as AgCl that might otherwise occlude the relatively small Ni signal. Ni can be difficult to solubilize since exposure to concentrated acid can passivate the Ni surface by forming NiO [23]. A known standard of 1 wt% Ni/α-Al_2O_3 was digested with the same protocol to measure the offset between actual Ni loading and measured Ni digested by the process described; this offset was applied to measured Ni concentrations to determine the real Ni loading in NiAg samples. The digested solutions were run alongside Ag and Ni standard solutions on a Thermo iCAP 6300 ICP-OES.

Electron microscopy

Scanning electron microscopy (SEM)

SEM was performed on Ag and NiAg nanoparticle catalysts because of the greater field of view, offering more statistically significant particle counting. The colloidal samples were dispersed on p-doped Si wafers and dried in vacuum at room temperature; powder samples were sprinkled onto C tape for direct imaging. Measurements were performed on Thermo Scientific Apreo C LoVac FEG SEM. For powder catalysts, the T1 detector was used that enables high Z-contrast between heavier Ag nanoparticles and the support and the beam voltage and current were kept low at 2 kV and 25 pA to minimize material charging. Particle size counting was automated using Fiji software and multiple images from different parts of the stub were imaged for analysis.

Transmission electron microscopy (TEM)

High angle annular dark field (HAADF)- scanning TEM (STEM) was performed with a Thermo Scientific Spectra 200 with probe aberration correction and a cold field emission gun. Samples were prepared by drop casting IPA sonicated sample onto a 200 mesh Cu grid with lacey C (Electron Microscopy Sciences). For quantification of average Ni nanoparticle size on Ni/α-Al_2O_3,

automated particle analysis was conducted that implements artificial intelligence algorithms for particle identification and segmentation [24]. This algorithm overcomes the poor contrast between Ni and the support seen in the STEM image (Fig. S17).

High energy resolution fluorescence detection- X-ray absorption near edge structure (HERFD-XANES)

HERFD-XANES measurements were performed at the Stanford Synchrotron Radiation Light Source (SSRL) at beamline 15-2. M1 KB mirrors were used for vertical and horizontal beam focusing with an 18 keV cutoff at 3 mrad. The incident beam was measured in He at atmospheric pressure within a ~15 cm long I_0 at 200 V. A liquid-nitrogen cooled double-crystal Si(311) monochromator was equipped to select the energy of the incident beam with a flux of ~3.5×10^{12} photons per second [25]. A Rowland circle spectrometer (radius 1 m) equipped with six spherically bent Si(620) analyzers and a silicon drift detector was used to select the Ni $K_{\alpha 1}$ (7480.3 eV) emission line with a measured resolution of 1.1 eV and beam spot size of 130×720 μm^2. Approximately 25 mg of powder samples were pressed and sieved between an 80 and 120 size mesh, then loaded into a 1 mm thick-walled capillary tube [26]. 20 sccm of He (UHP Airgas) was flowed through the catalyst bed to collect spectra in the as-prepared state. A temperature programmed reduction (TPR) in 20 sccm of 10% H_2/He from room temperature to 500°C at a ramp rate of 10° C/min was conducted on the pure Ni/α-Al_2O_3 sample to obtain standards for the oxidized and reduced Ni states in the supported catalyst (Fig. S15).

To normalize and remove background for a dataset, Athena from the Demeter package was used [27]. Four consecutive scans of the as-prepared sample were merged in Fig. S14 for Ni and NiAg samples. The parameters from Athena were then used to normalize TPR data sets composed of 35 spectra using the xraylarch package on Python. Linear combination fitting (LCF) was consequently carried out by modifying the "LCF of XANES data iPython notebook" available on GitHub [28]. The initial and final states of the pure Ni sample—nickel oxide (NiO) and reduced Ni—were used as basis sets to fit the spectra taken over the course of the Ni TPR (Fig. S15) as well as the as prepared $NiAg_{200}$ sample shown in Fig. S16B.

Catalytic reactivity

The catalytic activity of the catalysts was tested in a fixed-bed quartz reactor operating at atmospheric pressure. Generally, 100-650 mg of the catalyst was vortexed with 5-10 times the amount of SiO_2 or SiC as dilutant and loaded in between two plugs of quartz wool. For the reactivity studies at higher conversion in Figs. 3A and B, the catalyst was pressed and sieved between 35 and 40 size mesh. Gas flow rates were controlled using mass flow controllers from Teledyne Hastings. The reactor temperature was monitored using a K-type thermocouple in the center of the quartz reactor and controlled using an Omega Engineering temperature controller. The catalysts were calcined in-situ before epoxidation treatments and consisted of heating in 60 sccm 10% O_2 (UHP, Airgas), balance He (UHP, Airgas) for 4 hours at 400°C. In Fig. 2, the samples were all cooled in the reactor after the in-situ calcination, purged in He and exposed to a

pretreatment of 10 sccm H_2 at 450°C for 1 hour before cooling to 250°C and purging with He. The H_2 pretreatment procedure was removed during the optimization process so all data in Fig. 3 are collected post calcination (see reactivity protocol in Fig. S18). He was used as the inert gas for all measurements.

Before varying conversion by changing the residence time or temperature, the catalysts were "soaked" at 250°C for 8 hours in a feed consisting of 60 sccm, 10% ethylene (UHP, Airgas) and 10% oxygen. The soaking step allowed the particles to reach a steady state such that we can disentangle the effect of particle sintering from the effect of Ni when varying conversion. Experiments were performed between 200-250°C at a total gas flow rate of 40-60 sccm. The inlet feed to the reactor was generally 10% O_2, 10% C_2H_4 (UHP, Airgas) and the inert He (UHP, Airgas). Ethylene conversion was varied by changing the temperature or inlet flow rate or mass of catalyst loaded. The reactor effluent was then analyzed using gas chromatography (GC, SRI 8610C) where O_2 and C_2H_4 partial pressures were monitored using the thermal conductivity detector (TCD) and EO formation was monitored using the flame ionization detector (FID) equipped with a methanizer for the detection of CO_2. To introduce CO_2 and Cl into the feed, 10% CO_2/Ar (Airgas) and 100 ppm EtCl/He (Airgas) were used.

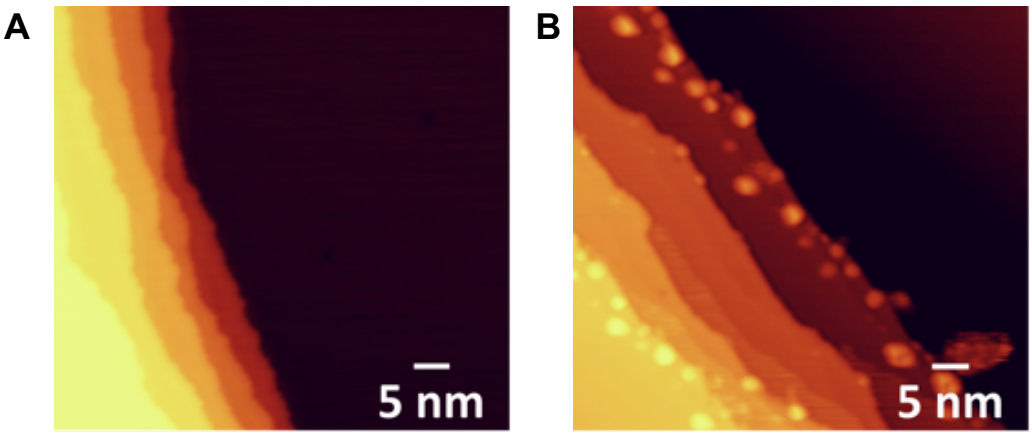

Figure A6.5.
STM images comparing Ag(111) and NiAg(111). Panel A shows an STM image of the clean Ag(111) surface (recorded at 0.5 nA and 150 mV). Panel B shows the Ag(111) sample after Ni deposition in which protrusions appear near the step edges. These protrusions, ranging in height from 0.2-0.5 nm, are likely due to Ag capping of the Ni incorporated into the surface (0.3 nA, 300 mV) [29]. The low surface free energy of Ag and the elevated deposition temperature of Ni likely led to this Ag capping which is seen in other Ag alloys.

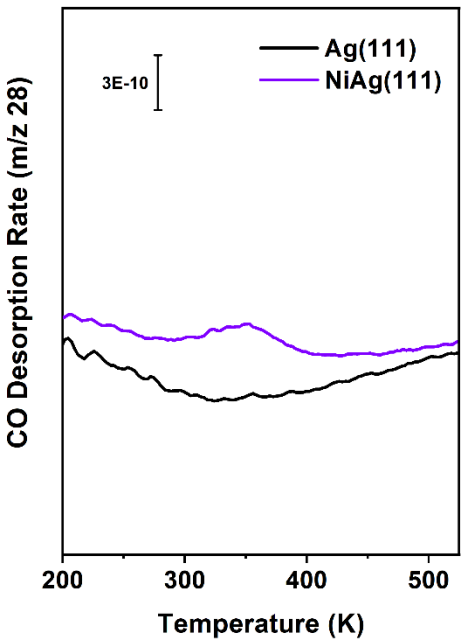

Figure A6.6.
TPD showing no CO desorption from Ag(111) compared to CO desorption from as-deposited NiAg(111) at 350 K. Both Ag(111) and ~1% NiAg(111) samples were exposed to 0.5 L CO at 90 K and TPD was performed. Ni coverage was calculated by using the CO trace area referenced to a known ethanol monolayer coverage [30,31].

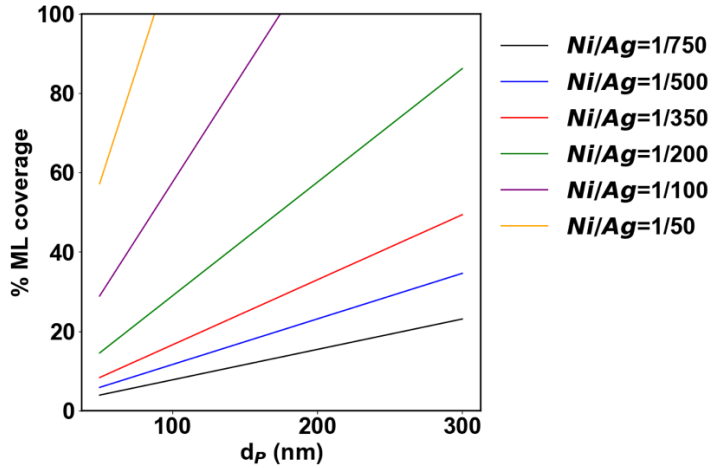

Figure A6.7.

Maximum surface coverage of Ni varies as a function of particle diameter (d_p) and loading, assuming all Ni dopant atoms move to the surface. Since Ni:Ag molar ratios are on a volume basis, increasing the particle size results in a near linear increase in the monolayer (% ML) coverage of Ni since volume ($\sim r^3$) increases more than surface area ($\sim r^2$) at larger r values.

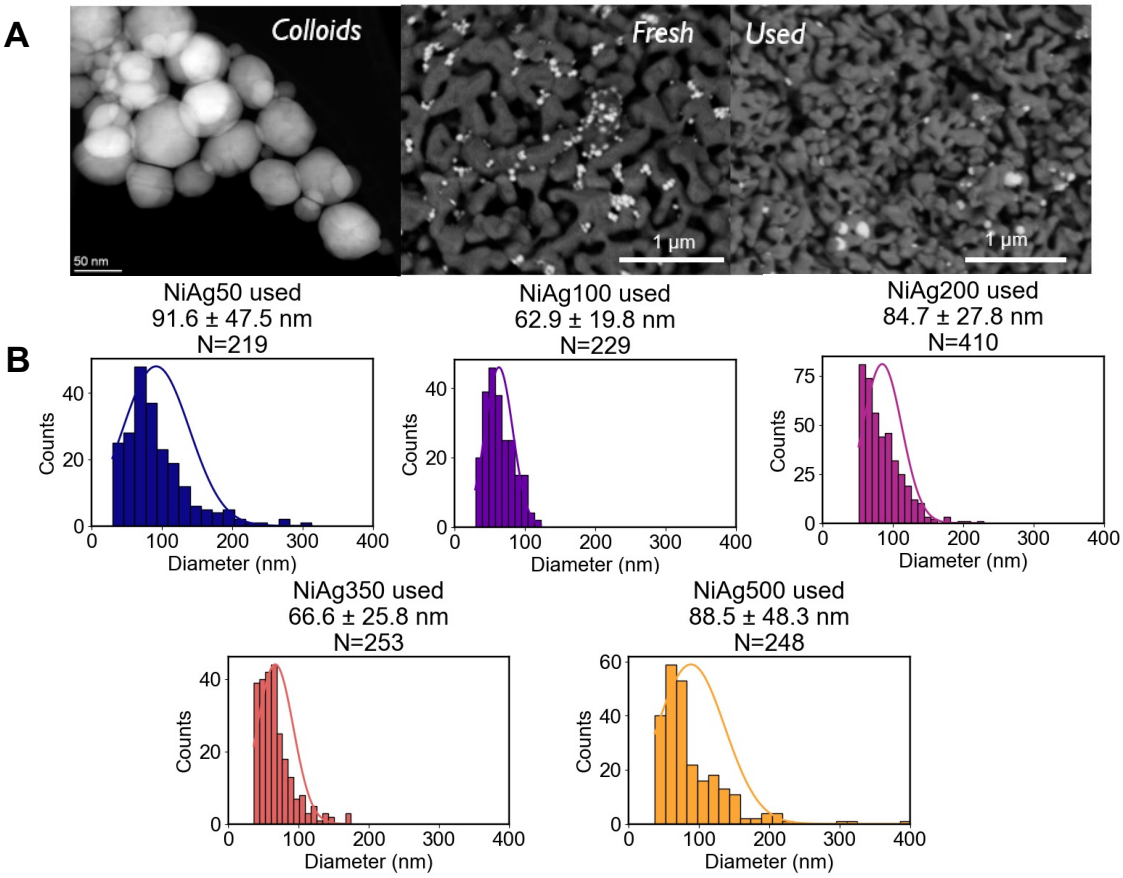

Figure A6.8.

A. Representative images of $NiAg_{50}$ (used to collect reactivity data in Fig 2A) as synthesized, unsupported colloidal particles (TEM), freshly supported particles on Al_2O_3 after drying (SEM) and post reaction (SEM). In the SEM images, the bright white particles are the Ag nanoparticles. B. Post reaction particle size distributions across all the samples used for reactivity data in Fig. 2A and B. Post reaction SEMs are most representative of the final state of particle distribution and thus most useful in disentangling particle size effects. Although some variations exist across the mean and standard deviation of the particle size, these differences in this particle size regime and weight loading (5 wt% Ag) are insufficient to create the stark differences in rates and selectivity observed in Fig. 6.2 [32,33].

Element	Weight %
Na	0.11
Si	0.33
Mg	0.077
Zn	0.028

Table A6.2: Analytical ICP data of the α-Al_2O_3 support.

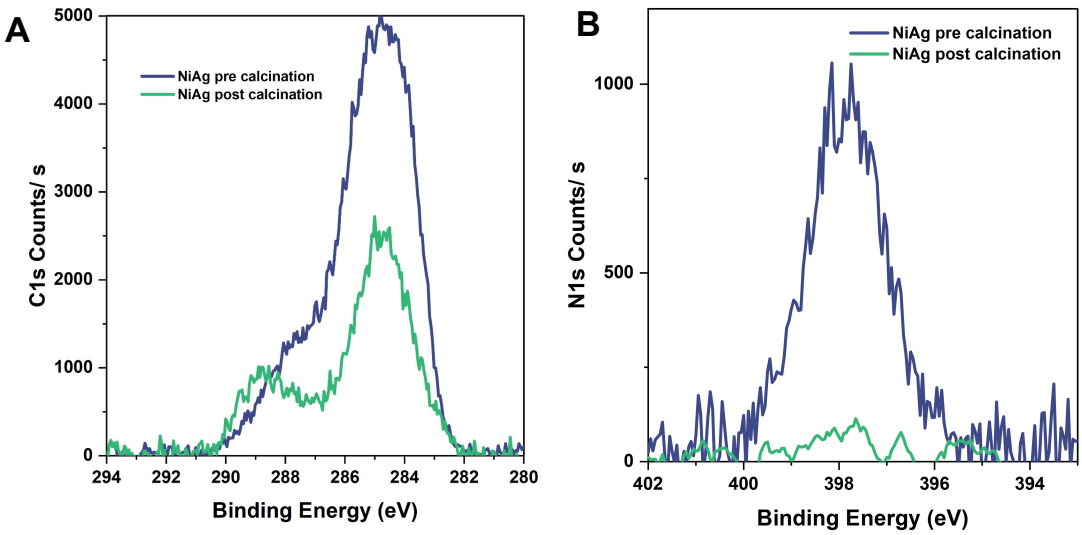

Figure A6.9: Comparison of XPS features of NiAg samples in the A) C 1s region and B) N 1s region before and after calcination. After calcination the peak intensity of the C 1s has decreased significantly and the N 1s peak is absent. Quantification of the C and N peaks are shown in Table S3.

Sample	Atomic % C (C/(C+N+O+Al))	Atomic % N (N/(C+N+O+Al))
Pre calcination	48.9	3.4
Post calcination	10.6	0

Table A6.3. Quantification of the C and N from the C 1s and N 1s XPS peaks. The atomic percentages were calculated using the peak area of C 1s or N 1s divided by the total area of C 1s, N 1s, O 1s and Al 2p peaks.

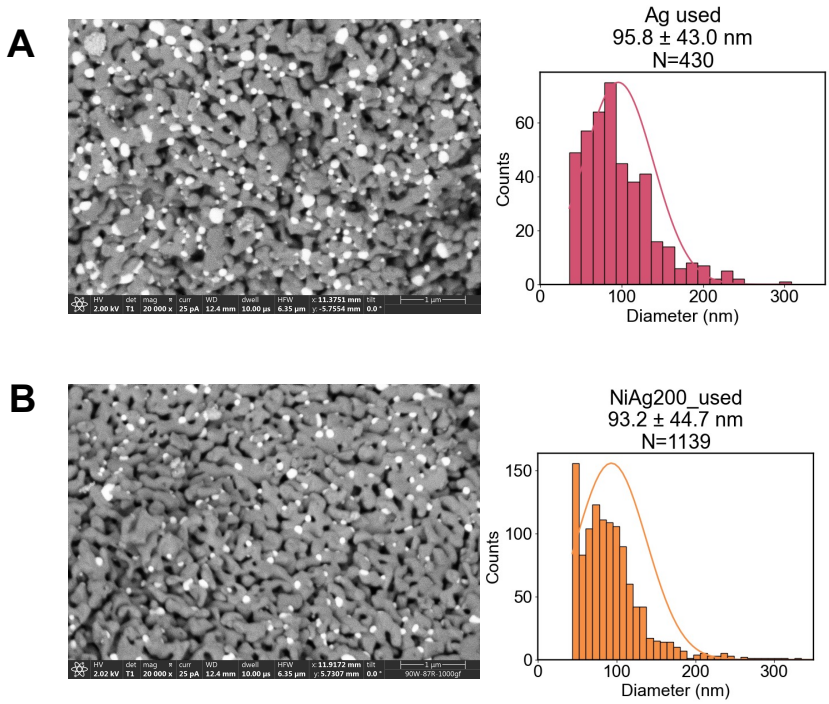

Figure A6.10.

Representative SEM images before and after reaction (from Fig. 3A) of A. 8 wt% Ag and B. 8 wt% $NiAg_{200}$. Samples were imaged post reaction, after being on stream for ~24 hours (including the in-situ pretreatment, catalyst soaking and consequent conversion dependent reactivity measurements).

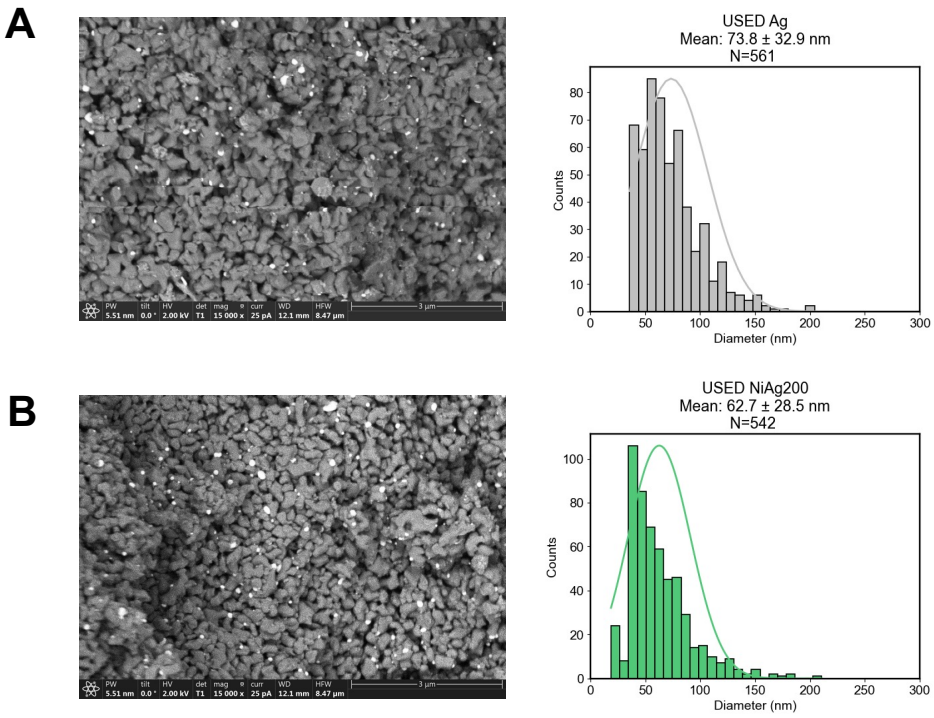

Figure A6.11.

SEM images after EtCl and CO_2 coflow (from samples used to generate reactivity data in Fig. 3B). The samples were imaged post reaction after being on-stream for ~48 hrs, A. 11 wt% Ag control sample and B. 9 wt% $NiAg_{200}$, both supported on α-Al_2O_3.

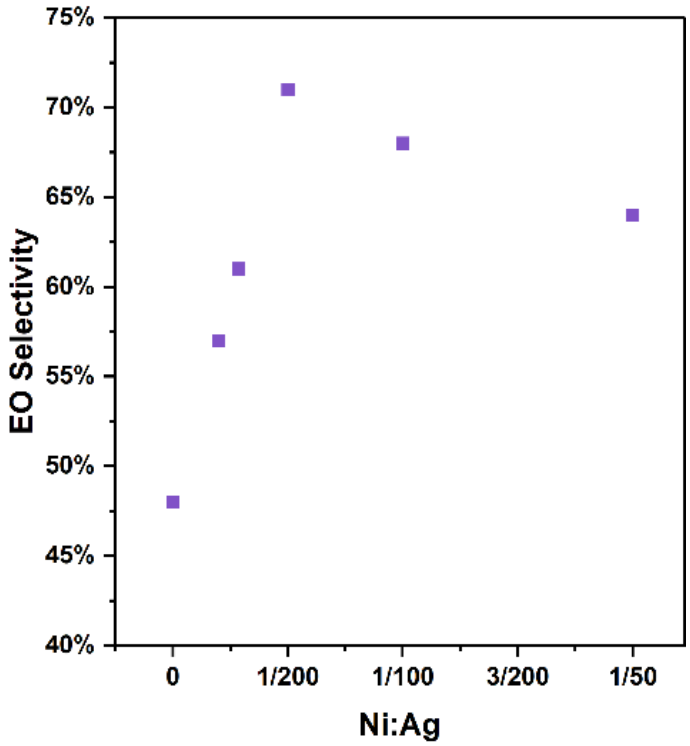

Figure A6.12.

Effect of increasing Ni:Ag molar ratio on EO selectivity corresponding to 2% ethylene conversion for each datapoint from Fig. 62A.

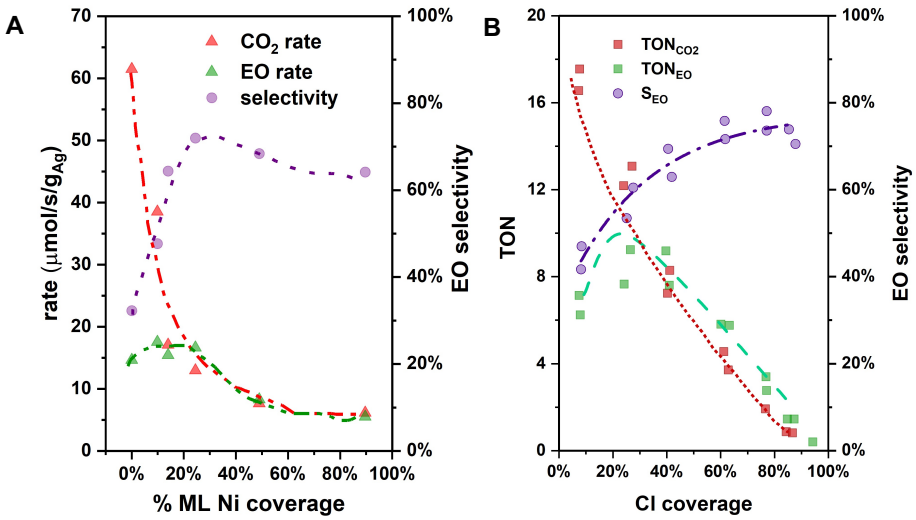

Figure A6.13.

Comparison of NiAg reactivity with Campbell's Cl study, A. Dependence of rate and selectivity on Ni coverage (assumed to be nominal based on wt% and complete surface segregation) and B. Dependence of rate and selectivity as a function of the surface Cl coverage, adapted from Ref. [34] on Ag(111) at 563 K, 20 Torr C_2H_4 and 150 Torr O_2. Similar to Cl, there appears to be an optimum Ni coverage at which the CO_2 rate has dropped significantly more than the EO rate thereby maximizing EO selectivity. One critical difference between the Cl- and Ni-based Ag systems is that at higher coverages Ni will form extended NiO_x islands while Cl continues to poison Ag sites thought to be responsible for combustion. This optimal Ni coverage is likely to be dependent on reaction conditions and the addition of co-promoters. (TON = turnover number)

Sample	Ag (wt%)	Ni (wt%)	Ag:Ni atomic ratio
$NiAg_{200}$ 2	9.5	0.028	185:1
$NiAg_{200}$ 5	9.1	0.022	230:1
$NiAg_{200}$ 6,7,8 (also used for Cl coflow experiment)	8.8	0.022	220:1
Ag 2	6.0	0	n/a
Ag 6 and Ag 7	10.5	0	n/a
Ag 5	7.8	0	n/a

Table A6.4.

ICP measurements of supported $Ag/\alpha\text{-}Al_2O_3$ and $NiAg/\alpha\text{-}Al_2O_3$ catalysts. Weight loadings of representative samples from the data shown in Fig. 6.3.

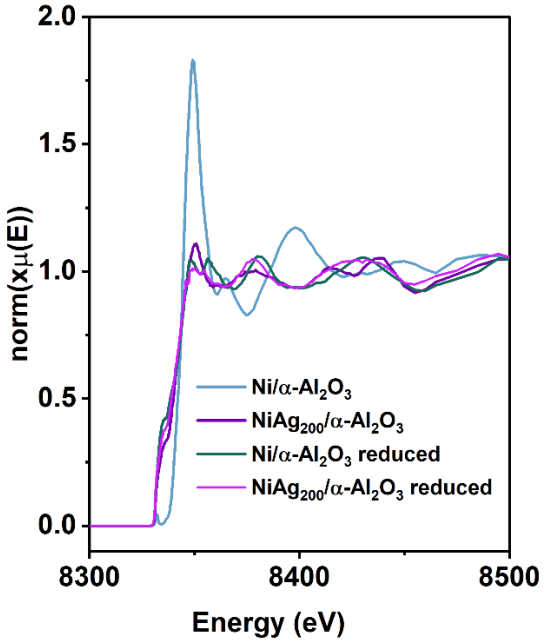

Figure A6.14.

HERFD-XANES of 0.5 wt% 5 nm Ni/α-Al_2O_3 in the as prepared (blue) and reduced (teal) states and 9.1 wt% (0.022 wt% Ni) 90 nm $NiAg_{200}$/α-Al_2O_3 in the as prepared (purple) and reduced (pink) states. Both samples were calcined before the measurement. Each spectrum is a merge of 4 scans taken in 20 sccm He at room temperature. In the as-prepared state for Ni/α-Al_2O_3, there is a pre-edge peak near 8330 eV as well as strong white line intensity indicating the presence of oxidized Ni [35,36]. After the TPR, Ni becomes reduced (teal) as seen with the shift in absorption edge towards lower energy, decrease in white line intensity and emergence of a shoulder on the edge. In comparison to the as-prepared Ni sample, $NiAg_{200}$ appears to have lower white line intensity even in the as-prepared (calcined) state. The pre-edge shoulder is not as intense as in the reduced Ni/α-Al_2O_3 sample and there is a lack of the doublet feature associated with reduced Ni. Compared to the reduced Ni/α-Al_2O_3 sample, the as-prepared $NiAg_{200}$ has greater white line intensity but a less intense shoulder on the edge.

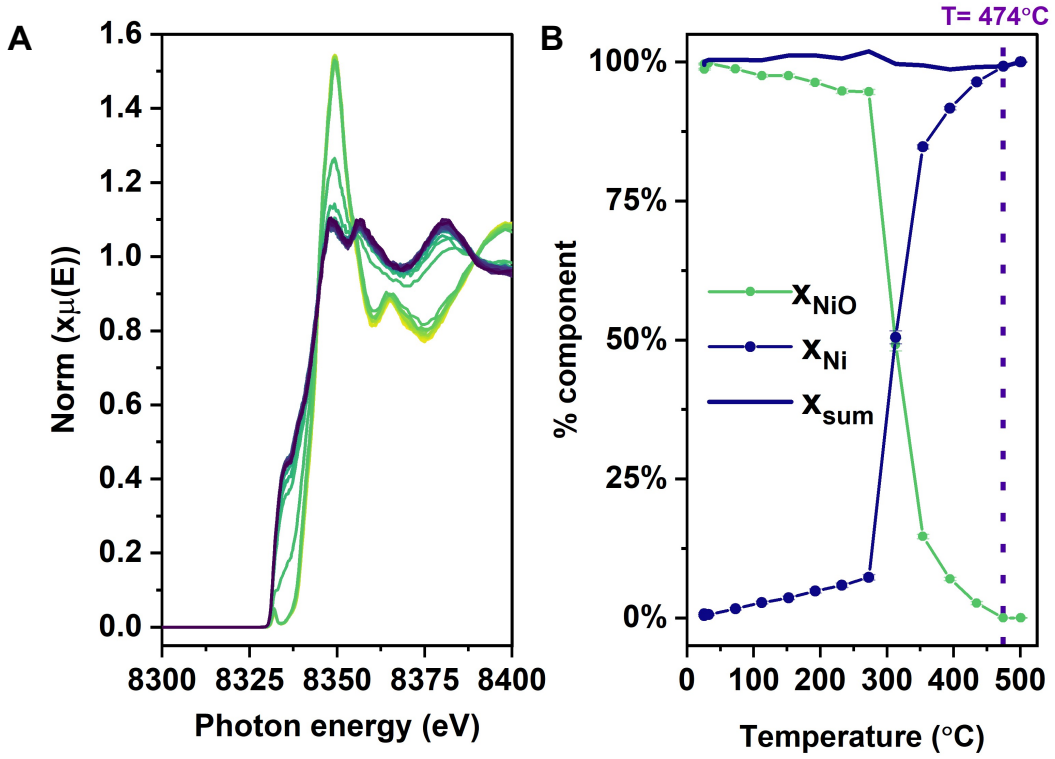

Figure A6.15.

A. HERFD-XANES spectra taken during a temperature programmed reduction (TPR) of the Ni/α-Al_2O_3 sample in 10% H_2/He from room temperature to 500°C at 10°C/min. Spectrum colors from light green to deep blue represent increasing temperature with time (or TPR progression). B. Results from linear combination fitting performed on the dataset considering the initial state (as-prepared Ni/α-Al_2O_3, called NiO for simplicity) and final state (reduced Ni/α-Al_2O_3, called Ni for simplicity) to be the basis sets of the fitting. Each fit was constrained to fractions between 0 and 1 but the total sum of the component fractions was not constrained to 1. The excellent fit across the entire temperature range suggests that data is reasonably fit by a simple combination of reduced Ni and oxidized Ni/α-Al_2O_3. Thus, nanoparticles of NiO_x have characteristic HERFD-XANES spectra that are well modelled by a combination of the spectra of Ni and NiO nanoparticles.

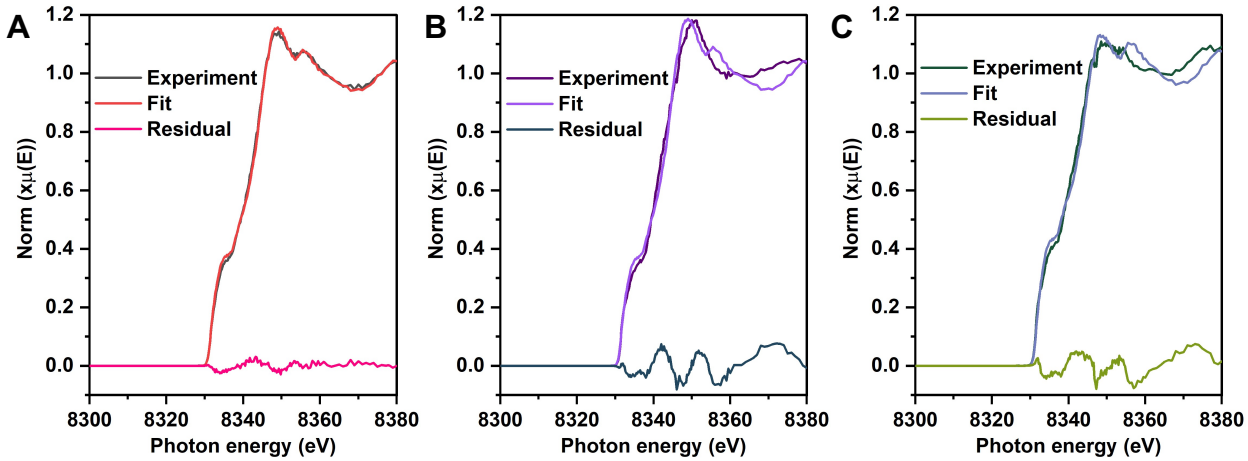

Figure A6.16.

HERFD-XANES fits generated using the spectra of the as-prepared and post TPR Ni/Al_2O_3 sample as the basis set compared to experimental data. Panel A shows an example spectrum of the Ni/α-Al_2O_3 during the TPR (at 354°C) and the fit to the spectrum using the described basis set. The LCF fit (red) reconstructs the features in the experimental data (black) well, with a reduced χ^2 value of 1.5×10^{-4}. This shows that the as-prepared Ni/α-Al_2O_3 and reduced Ni/α-Al_2O_3 basis is capable of capturing features in an intermediate TPR state from the Ni/α-Al_2O_3 sample and there is no statistically significant intermediate species. Panel B shows the HERFD-XANES spectrum of the as prepared $NiAg_{200}$/α-Al_2O_3 sample (dark purple) and the attempted LCF fit (light purple) using the same basis set used to fit spectra from the Ni/α-Al_2O_3 sample. There are notable misfits in the shape of the edge, and the fit is unable to produce a white line that is only a single peak; the reduced χ^2 for this fit is 1.4×10^{-3}. Panel C shows the spectrum of reduced $NiAg_{200}$/α-Al_2O_3 (dark green) and the attempted LCF fit (gray) using the same basis set as panel A and B; the reduced χ^2 for this fit is 1.1×10^{-3}, similarly, showing misfits in the shape. Thus, the Ni in the $NiAg_{200}$ sample cannot be represented by the characteristics of supported Ni alone. This is a strong indication that Ni in NiAg is not the same as bulk Ni in the supported Ni catalyst, and further supports the assertion that Ni is located in the Ag nanoparticles.

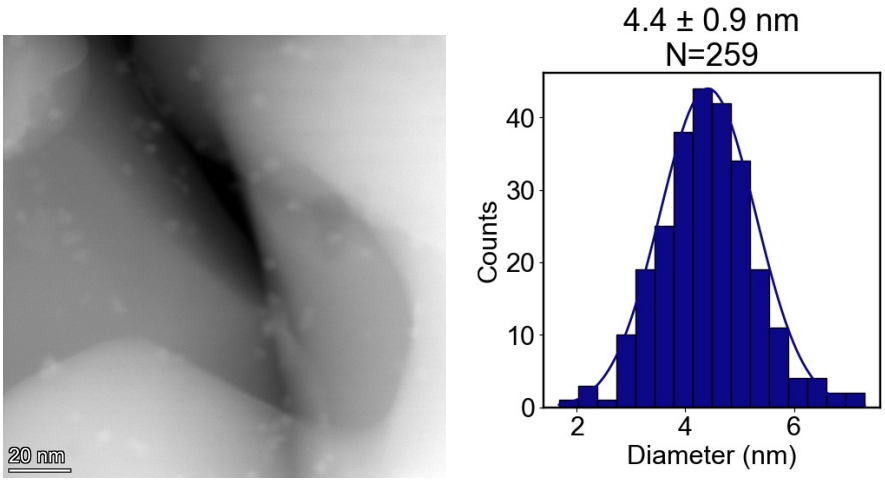

Figure A6.17.

HAADF-STEM image on Ni/α-Al_2O_3 measured in XANES (Figs. S14-16). The YOLOv8 object detection model overcomes the low contrast between particles and support seen on the image, and enables accurate particle size quantification [24].

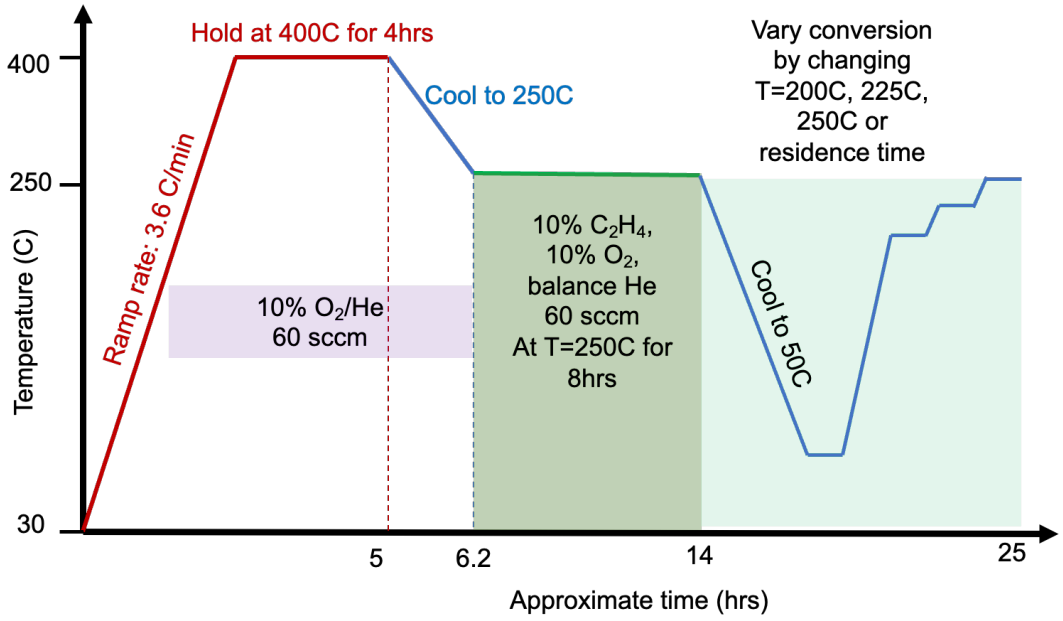

Figure A6.18.

Reactivity testing protocol. For samples in Fig. 6.2, there was an additional reduction step of heating to 450°C at H_2 for 1 hour after the in-situ calcination treatment. The conversion can alternatively be varied by changing the residence time instead of temperature. When changing conversion (by varying temperature or total flow rate), the system is left to achieve steady state for 2 hours. The 8 hour soaking step ensures that particles grow to a stable size such that the effect of inevitable particle growth can be disentangled from the effect of Ni between the various samples.

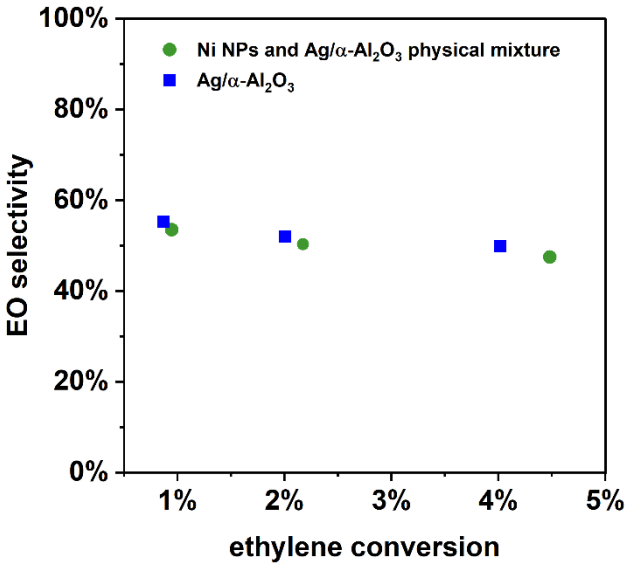

Figure A6.19.

Comparison of 11 wt% Ag/α-Al_2O_3 (synthesized identically to $NiAg_{200}$ without Ni) and a physical mixture of 0.022 wt% Ni NPs with the same 11 wt% Ag/α-Al_2O_3 sample; reaction conditions: 100 mg of catalyst diluted in 1 g of SiC, following the reactivity protocol shown in Fig. A6.18 at 10% ethylene, 10% oxygen feed where conversion is varied by changing temperature. The selectivity vs. conversion profiles for both the materials are very similar, with slightly lower selectivity on the Ni-Ag mixture suggesting secondary combustion of EO on NiO [37]. This control experiment demonstrates that Ni and Ag must be alloyed together to change the selectivity of the catalyst and that Ni on the support has a minimal effect. Extended NiO_x domains in Ag may react similarly to NiO_x on the support.

Sample	Mass of catalyst (mg)	Mass of diluent (g)/type	Flow rate (sccm)	Pretreatment after in-situ calcination	Pressed and sieved?	Notes on synthesis/reactivity
5 wt% $Ag/\alpha\text{-}Al_2O_3$	133	1.2/SiO_2	60	450C, UHP H_2 1 hr then cool to R.T	N	
5 wt% $NiAg_{500}/\alpha\text{-}Al_2O_3$	168	1.2/SiO_2	60	450C, UHP H_2 1 hr then cool to R.T	N	
5 wt% $NiAg_{350}/\alpha\text{-}Al_2O_3$	134	1/2/SiO_2	60	450C, UHP H_2 1 hr then cool to R.T	N	
5 wt% $NiAg_{200}/\alpha\text{-}Al_2O_3$	120	1.2/SiO_2	60	450C, UHP H_2 1 hr then cool to R.T	N	
5 wt% $NiAg_{100}/\alpha\text{-}Al_2O_3$	170	1.0/SiO_2	60	450C, UHP H_2 1 hr then cool to R.T	N	
5 wt% $NiAg_{50}/\alpha\text{-}Al_2O_3$	116	1.0/SiO_2	60	450C, UHP H_2 1 hr then cool to R.T	N	
Ag 1 (6 wt% $Ag//\alpha\text{-}Al_2O_3$)	205	1.8/SiC	60	none	N	Synthesis protocol for $NiAg_{200}$ used without Ni
Ag 2 (8 wt% $Ag/\alpha\text{-}Al_2O_3$)	100	1.2/SiC	60	none	Y	Synthesis protocol for $NiAg_{200}$ used without Ni
Ag 3 (8 wt% $Ag/\alpha\text{-}Al_2O_3$)	210	2.0/SiC	60	none	N	Pure Ag synthesis protocol
Ag 4 (8 wt% $Ag/\alpha\text{-}Al_2O_3$)	207	2.0/SiC	60	none	N	Pure Ag synthesis protocol
Ag 5 (8 wt% $Ag/\alpha\text{-}Al_2O_3$)	208	2.1/SiC	60	none	N	Synthesis protocol for $NiAg_{200}$ used without Ni
Ag 6 (11 wt% $Ag/\alpha\text{-}Al_2O_3$)	149	0.8/SiC	40-60	none	Y	Synthesis protocol for $NiAg_{200}$ used without Ni
Ag 7 (11 wt% $Ag/\alpha\text{-}Al_2O_3$)	325	1.4/SiC	40-60	none	Y	Synthesis protocol for $NiAg_{200}$ used without Ni ***Used for Cl coflow experiment***
$NiAg_{200}$ 1 (9 wt% $Ag/\alpha\text{-}Al_2O_3$)	200	2.0/SiC	60	none	N	
$NiAg_{200}$ 2 (10 wt% $Ag/\alpha\text{-}Al_2O_3$)	203	1.9/SiC	60	none	N	

▲ $NiAg_{200}$ 3 (9 wt% Ag/α-Al_2O_3)	152	1.9/SiC	60	none	N	
$NiAg_{200}$ 4 (9 wt% Ag/α-Al_2O_3)	197	1.9/SiC	60	none	N	
◆ $NiAg_{200}$ 5 (9 wt% Ag/α-Al_2O_3)	197	1.9/SiC	60	none	N	
◀ $NiAg_{200}$ 6 (9 wt% Ag/α-Al_2O_3)	103	1.0/SiC	40-60	none	Y	
▶ $NiAg_{200}$ 7 (9 wt% Ag/α-Al_2O_3)	301	1.2/SiC	40-60	none	Y	
⬢ $NiAg_{200}$ 8 (9 wt% Ag/α-Al_2O_3)	652	1.8/SiC	40-60	none	Y	***Used for Cl coflow experiment***

Table A6.5.

All details of reactivity, including masses of catalyst added, pretreatment conditions, soaking period, flow rate in Fig. 6.2 and 6.3.

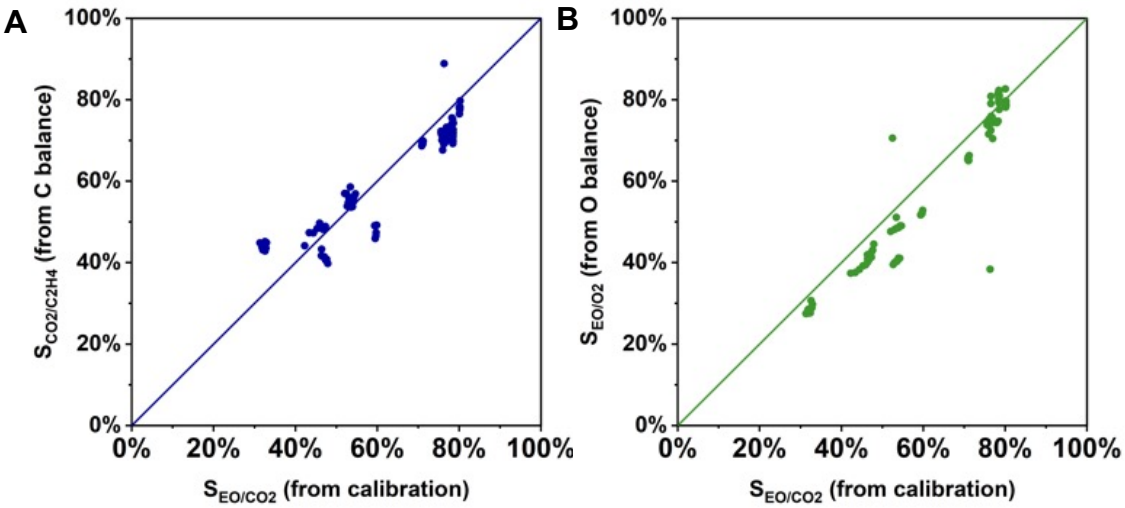

Figure A6.20.

Parity plot of mass balances (from data in Fig. 6.3A) plotted against selectivity from product calibration where $S_{EO/CO2} = \frac{\Delta n_{EO}}{\Delta n_{EO}+0.5\Delta n_{CO2}}$ with A showing the C balance selectivity, where $S_{CO2/C2H4} = \frac{\Delta n_{C2H4}-0.5\Delta n_{CO2}}{\Delta n_{C2H4}}$, and B showing O balance selectivity, where $S_{EO/O2} = \frac{\Delta n_{EO}}{\Delta n_{C2H4}} = \frac{\Delta n_{EO}}{\frac{5}{6}\Delta n_{EO}+\frac{1}{3}\Delta n_{O2}}$. From all three approaches—direct calibration, C and O mass balances—the selectivities are in good agreement with each other.

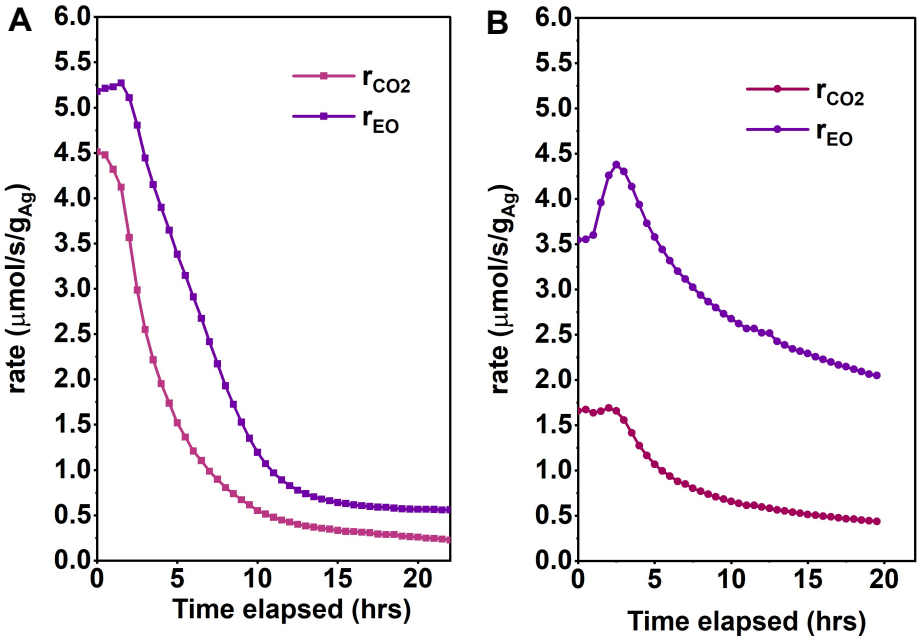

Figure A6.21.

Progression of EO and CO_2 production rates after the introduction of 0.5ppm EtCl in a feed composed of 25% C_2H_4, 10% O_2, 0.5% CO_2, balance He, 40sccm at T=250°C for A. Ag and B. $NiAg_{200}$ (from Fig. 6.3B). Cl is known to influence epoxidation chemistry on Ag, rather than on the support (for example by blocking acidic sites), and thus the increase in rate seen for $NiAg_{200}$ upon Cl introduction is strong evidence that Ni and Cl are working together on the Ag surface to promote epoxidation. This is again evidence that Ni is located on (or in) Ag rather than on the support.

Material	Citation	Surface area (m^2/g)	Feed composition	Cl (Y/N)?	Temperature (°C)	Total Pressure (atm)	Ethylene conversion (%)	Ethylene oxide selectivity (%)
unsupported Ag foil	[38]	0.02	23.8% C_2H_4, 7.19% O_2	N	237	1	2.1	80
supported Ag nanowires/α-Al_2O_3 175nm	[17]	0.3	60% C_2H_4, 10% O_2	N	237	1	3	62
supported Ag nanocubes/α-Al_2O_3 350nm	[17]	0.3	20% C_2H_4, 10% O_2	N	237	1	3	75
Ag(0.6wt%, 200nm)/ α-Al_2O_3	[39]	7	2% C_2H_4, 7% O_2	N	237	1		23
Ag (3.7wt%, 400nm)/ α-Al_2O_3	[39]	7	2% C_2H_4, 7% O_2	N	237	1		64
Ag (18.4wt%, 400nm)/ SiO2	[39]	200	2% C_2H_4, 7% O_2	N	237	1		43
Ag (11-13wt%)/α-Al_2O_3	[40]	0.3	10% C_2H_4, 10% O_2	N	267	1.36	6.2	26
Ag (11-13wt%)/aα-Al_2O_3	[40]	0.3	10% C_2H_4, 10% O_2, 1ppm EtCl	Y	267	1.36	1.5	47
Ag (11-13wt%)/α-Al_2O_3	[40]	0.3	10% C_2H_4, 60% O_2	N	267	1.36		43
Ag (11-13wt%)/α-Al_2O_3	[40]	0.3	60% C_2H_4, 10% O_2	N	267	1.36		42
Ag (11-13wt%), Cs (68ppm) /α-Al_2O_3	[40]	0.3	10% C_2H_4, 10% O_2	N	267	1.36	6.5	36
Ag (11-13wt%), Cs (68ppm) /α-Al_2O_3	[40]	0.3	10% C_2H_4, 60% O_2	N	267	1.36		50
Ag (11-13wt%), Cs (68ppm) /α-Al_2O_3	[40]	0.3	60% C_2H_4, 10% O_2	N	267	1.36		53
Ag (12wt%)/ α-Al_2O_3	[41]	0.6	25% C_2H_4, 8% O_2, 2ppm EtCl	Y	224	17	10.5	75
Ag (12wt%). Cs (350ppm)/ α-Al_2O_3	[41]	0.6	25% C_2H_4, 8% O_2, 2ppm EtCl	Y	224	17	10.3	80

Ag (12wt%). Cs (350ppm), Re(200ppm)/ α-Al_2O_3	[41]	0.6	25% C_2H_4, 8% O_2, 2ppm EtCl	Y	224	17	10.1	82
Ag (12wt%). Cs (350ppm), Re(200ppm), Mo (150ppm)/ α-Al_2O_3	[41]	0.6	25% C_2H_4, 8% O_2, 2ppm EtCl	Y	224	17	9.8	83
Ag (15wt%) + Cs + Re (Cs,600ppm, Re 400ppm)/ α-Al_2O_3 (coimpregnation)	[42]		30% C_2H_4, 7.5% O_2, 1.85% CO_2, 0.1-0.5ppm Et-diCl	Y	226	17	10	84
Re/Ag(15wt%)-Cs/a-α-Al_2O_3 (Cs (600ppm)-Re(400ppm) sequential impregnation)	[42]		30% C_2H_4, 7.5% O_2, 1.85% CO_2, 0.1-0.5ppm dichloroethane	Y	240	17	7.1	64
Ag(35wt%)/α-Al_2O_3Cs(628ppm), Li (33ppm), Na (42ppm), re(440ppm), [SO4]2- (151ppm), Mn (115ppm)	[43]	1.3	30% C_2H_4, 3% O_2, 0.4% C_2H_6, 1% CO_2, 6.3ppm EtCl	Y	240	5.3	<1.5	87
Ag (11-13wt%), Cu (0.5mol%)/α-Al_2O_3	[40]	0.3	10% C_2H_4, 10% O_2	N	267	1.36	12.2	36
Ag(13.18wt%), Au(0.54wt%)/α-Al_2O_3	[44]	90	6% C_2H_4, 6% O_2	N	255	36	1.8	79
Ag (5wt%, 300nm)/ α-Al_2O_3	[45]	0.7	25% C_2H_4, 8-16% O_2	N	210	17	1.3	72
Ag/NiO_2	[46]		2.5% C_2H_4, 5% O2, 0.5% Ne	N	20	1	6	70
Ir (0.5wt%, single atoms)/a-MnO2	[47]	72	1% C_2H_4/0.5% O_2	N	250	1	75	99
Ir NPs/ a-MnO2	[47]	72	1% C_2H_4/0.5% O_2	N	250	1	4	5
Ag/a-MnO2	[47]	72	1% C_2H_4/0.5% O_2	N	250	1	12	8

Table A6.**6.**

Literature summary of EO catalyst performance adapted from Ref [48] updated with more recent catalyst studies.

Component	Binding Energy (eV)	Full Width Half Max	Fit Shape (G/L)
Electrophilic	529.9-530.3	1.1	50:50
Nucleophilic	528.3-528.7	0.75-0.8	50:50
Ni-philic	529.1-529.5	1.0	50:50

Table A6.7.

Summary of fitting parameters for O 1s XPS spectra in Fig. 6.4; electrophilic oxygen fit with pink traces, nucleophilic fit with red, and Ni-philic fit with blue. Due to the size of the oxygen peaks, O 1s spectra are often fit with a linear background. We also note that the binding energies of the electrophilic and nucleophilic oxygen species agree with literature values [13,49]. Furthermore, we assign the "Ni-philic" oxygen as a Ni-O species, in agreement with literature values for the formation of Ni(II) [50,51]. While these binding energies can overlap with the formation of Ag_2O, we see no evidence for this on the Ag(111) sample even at higher oxygen pressures, nor do we see evidence of Ag_2O formation in the Ag 3d spectra [52,53].

(1) Kresse, G.; Furthmüller, J. Efficiency of Ab-Initio Total Energy Calculations for Metals and Semiconductors Using a Plane-Wave Basis Set. *Comput. Mater. Sci.* **1996**, *6* (1), 15–50. https://doi.org/10.1016/0927-0256(96)00008-0.
(2) Kresse, G.; Hafner, J. Ab Initio Molecular Dynamics for Liquid Metals. *Phys. Rev. B* **1993**, *47* (1), 558–561. https://doi.org/10.1103/PhysRevB.47.558.
(3) Perdew, J. P.; Burke, K.; Ernzerhof, M. Generalized Gradient Approximation Made Simple. **1996**.
(4) Tkatchenko, A.; Scheffler, M. Accurate Molecular van Der Waals Interactions from Ground-State Electron Density and Free-Atom Reference Data. *Phys. Rev. Lett.* **2009**, *102* (7), 073005. https://doi.org/10.1103/PHYSREVLETT.102.073005/FIGURES/2/MEDIUM.
(5) Heyden, A.; Bell, A. T.; Keil, F. J. Efficient Methods for Finding Transition States in Chemical Reactions: Comparison of Improved Dimer Method and Partitioned Rational Function Optimization Method. *J. Chem. Phys.* **2005**, *123* (22), 224101. https://doi.org/10.1063/1.2104507/776452.
(6) Darby, M. T.; Stamatakis, M.; Michaelides, A.; Sykes, E. Charles. H. Lonely Atoms with Special Gifts: Breaking Linear Scaling Relationships in Heterogeneous Catalysis with Single-Atom Alloys. *J. Phys. Chem. Lett.* **2018**, *9* (18), 5636–5646. https://doi.org/10.1021/ACS.JPCLETT.8B01888.
(7) Montemore, M. M.; Medlin, J. W. Site-Specific Scaling Relations for Hydrocarbon Adsorption on Hexagonal Transition Metal Surfaces. *J. Phys. Chem. C* **2013**, *117* (39), 20078–20088. https://doi.org/10.1021/jp4076405.
(8) Nwaokorie, C. F.; Montemore, M. M. Alloy Catalyst Design beyond the Volcano Plot by Breaking Scaling Relations. *J. Phys. Chem. C* **2022**, *126* (8), 3993–3999. https://doi.org/10.1021/acs.jpcc.1c10484.
(9) Park, D. W.; Gau, G. Ethylene Epoxidation on a Silver Catalyst: Unsteady and Steady State Kinetics. *J. Catal.* **1987**, *105* (1), 81–94. https://doi.org/10.1016/0021-9517(87)90010-8.
(10) Jones, T. E.; Wyrwich, R.; Bocklein, S.; Rocha, T. C. R.; Carbonio, E. A.; Knop-Gericke, A.; Schlogl, R.; Gunther, S.; Wintterlin, J.; Piccinin, S. Oxidation of Ethylene on Oxygen Reconstructed Silver Surfaces. *J. Phys. Chem. C* **2016**, *120* (50), 28630–28638. https://doi.org/10.1021/ACS.JPCC.6B10074/ASSET/IMAGES/LARGE/JP-2016-10074D_0006.JPEG.
(11) Chen, C. J.; Harris, J. W.; Bhan, A. Kinetics of Ethylene Epoxidation on a Promoted Ag/α-Al2O3 Catalyst—The Effects of Product and Chloride Co-Feeds on Rates and Selectivity. *Chem. - Eur. J.* **2018**, *24* (47), 12405–12415. https://doi.org/10.1002/chem.201801356.
(12) Kenge, N.; Pitale, S.; Joshi, K. The Nature of Electrophilic Oxygen: Insights from Periodic Density Functional Theory Investigations. *Surf. Sci.* **2019**, *679*, 188–195. https://doi.org/10.1016/J.SUSC.2018.09.009.
(13) Kaichev, V. V.; Bukhtiyarov, V. I.; Hävecker, M.; Knop-Gercke, A.; Mayer, R. W.; Schlögl, R. The Nature of Electrophilic and Nucleophilic Oxygen Adsorbed on Silver. *Kinet. Catal. 2003 443* **2003**, *44* (3), 432–440. https://doi.org/10.1023/A:1024459305551.
(14) Waluyo, I.; Hunt, A. Ambient Pressure X-Ray Photoelectron Spectroscopy at the IOS (23-ID-2) Beamline at the National Synchrotron Light Source II. *Synchrotron Radiat. News* **2022**, *35* (3), 31–38. https://doi.org/10.1080/08940886.2022.2082180/ASSET/BDB66E5A-0587-4FF9-8A92-46D92E6F9330/ASSETS/IMAGES/GSRN_A_2082180_F0005_C.JPG.
(15) Christopher, P.; Linic, S. Shape- and Size-Specific Chemistry of Ag Nanostructures in Catalytic Ethylene Epoxidation. *ChemCatChem* **2010**, *2* (1), 78–83. https://doi.org/10.1002/cctc.200900231.
(16) Skrabalak, S. E.; Wiley, B. J.; Kim, M.; Formo, E. V.; Xia, Y. On the Polyol Synthesis of Silver Nanostructures: Glycolaldehyde as a Reducing Agent. *Nano Lett.* **2008**, *8* (7), 2077–2081. https://doi.org/10.1021/NL800910D/SUPPL_FILE/NL800910D-FILE002.PDF.
(17) Christopher, P.; Linic, S. Shape- and Size-Specific Chemistry of Ag Nanostructures in Catalytic Ethylene Epoxidation. *ChemCatChem* **2010**, *2* (1), 78–83. https://doi.org/10.1002/cctc.200900231.
(18) Skrabalak, S. E.; Au, L.; Li, X.; Xia, Y. Facile Synthesis of Ag Nanocubes and Au Nanocages. *Nat. Protoc. 2007 29* **2007**, *2* (9), 2182–2190. https://doi.org/10.1038/nprot.2007.326.

(19) Hong, J.; Xie, J.; Mirshahghassemi, S.; Lead, J. Metal (Cd, Cr, Ni, Pb) Removal from Environmentally Relevant Waters Using Polyvinylpyrrolidone-Coated Magnetite Nanoparticles. *RSC Adv*. **2020**, *10* (6), 3266–3276. https://doi.org/10.1039/c9ra10104g.
(20) Tientong, J.; Garcia, S.; Thurber, C. R.; Golden, T. D. Synthesis of Nickel and Nickel Hydroxide Nanopowders by Simplified Chemical Reduction. *J. Nanotechnol*. **2014**, *2014*, 6–11. https://doi.org/10.1155/2014/193162.
(21) Chavez, S.; Aslam, U.; Linic, S. Design Principles for Directing Energy and Energetic Charge Flow in Multicomponent Plasmonic Nanostructures. *ACS Energy Lett*. **2018**, *3* (7), 1590–1596. https://doi.org/10.1021/acsenergylett.8b00841.
(22) Vrijburg, W. L.; Van Helden, J. W. A.; Van Hoof, A. J. F.; Friedrich, H.; Groeneveld, E.; Pidko, E. A.; Hensen, E. J. M. Tunable Colloidal Ni Nanoparticles Confined and Redistributed in Mesoporous Silica for CO2 Methanation. *Catal. Sci. Technol*. **2019**, *9* (10), 2578–2591. https://doi.org/10.1039/c9cy00532c.
(23) Khaled, K. F. Electrochemical Behavior of Nickel in Nitric Acid and Its Corrosion Inhibition Using Some Thiosemicarbazone Derivatives. *Electrochimica Acta* **2010**, *55* (19), 5375–5383. https://doi.org/10.1016/J.ELECTACTA.2010.04.079.
(24) Genc, A.; Marlowe, J.; Jalil, A.; Kovarik, L.; Christopher, P. A Versatile Machine Learning Workflow for High-Throughput Analysis of Supported Metal Catalyst Particles. 1–13.
(25) Sokaras, D.; Weng, T. C.; Nordlund, D.; Alonso-Mori, R.; Velikov, P.; Wenger, D.; Garachtchenko, A.; George, M.; Borzenets, V.; Johnson, B.; Rabedeau, T.; Bergmann, U. A Seven-Crystal Johann-Type Hard x-Ray Spectrometer at the Stanford Synchrotron Radiation Lightsource. *Rev. Sci. Instrum*. **2013**, *84* (5), 53102. https://doi.org/10.1063/1.4803669/356922.
(26) Hoffman, A. S.; Singh, J. A.; Bent, S. F.; Bare, S. R. In Situ Observation of Phase Changes of a Silica-Supported Cobalt Catalyst for the Fischerâ€“Tropsch Process by the Development of a Synchrotron-Compatible inÂ Situ/Operando Powder X-Ray Diffraction Cell. *J. Synchrotron Radiat*. **2018**, *25* (6), 1673–1682. https://doi.org/10.1107/S1600577518013942.
(27) Ravel, B.; Newville, M. Synchrotron Radiation ATHENA, ARTEMIS, HEPHAESTUS: Data Analysis for X-Ray Absorption Spectroscopy Using IFEFFIT. *J Synchrotron Rad* **2005**, *12*, 537–541. https://doi.org/10.1107/S0909049505012719.
(28) Hoffman, A. S.; Müller, O.; Hong, J.; Canning, G. A.; Fang, C. Y.; Perez-Aguilar, J. E.; Gates, B. C.; Bare, S. R. Observations of Ethylene-for-CO Ligand Exchanges on a Zeolite-Supported Single-Site Rh Catalyst by X-Ray Absorption Spectroscopy. *J. Phys. Chem. Lett*. **2023**, *14*, 4591–4599. https://doi.org/10.1021/ACS.JPCLETT.3C00349/ASSET/IMAGES/LARGE/JZ3C00349_0005.JPEG.
(29) Patel, D. A.; Kress, P. L.; Cramer, L. A.; Larson, A. M.; Sykes, E. C. H. Elucidating the Composition of PtAg Surface Alloys with Atomic-Scale Imaging and Spectroscopy. *J. Chem. Phys*. **2019**, *151* (16). https://doi.org/10.1063/1.5124687.
(30) Liriano, M. L.; Larson, A. M.; Gattinoni, C.; Carrasco, J.; Baber, A. E.; Lewis, E. A.; Murphy, C. J.; Lawton, T. J.; Marcinkowski, M. D.; Therrien, A. J.; Michaelides, A.; Sykes, E. C. H. Chirality at Two-Dimensional Surfaces: A Perspective from Small Molecule Alcohol Assembly on Au(111). *J. Chem. Phys*. **2018**, *149* (3), 34703. https://doi.org/10.1063/1.5035500/15547254/034703_1_ACCEPTED_MANUSCRIPT.PDF.
(31) Schlosser, D. A.; Yehorova, D.; Kaleem, H.; Maxwell, E. M.; Baker, J. S.; Gillum, M. Z.; DePonte, M. C.; Letchworth-Weaver, K.; Baber, A. E. Effect of Undercoordinated Ag(111) Defect Sites on the Adsorption of Ethanol. *J. Vac. Sci. Technol. Vac. Surf. Films* **2020**, *38* (3), 33213. https://doi.org/10.1116/1.5142020/1065713.
(32) Iyer, K. R.; Bhan, A. Particle Size Dependence of Ethylene Epoxidation Rates on Ag/α-Al2O3 Catalysts: Why Particle Size Distributions Matter. *J. Catal*. **2023**, *420*, 99–109. https://doi.org/10.1016/J.JCAT.2023.02.008.

(33) Keijzer, C. J.; Smulders, L. C. J.; Wezendonk, D.; Willem De Rijk, J.; De Jongh, P. E. Influence of Ag Particle Size and Ag : Al 2 O 3 Surface Ratio in Catalysts for the Chloride-Promoted Ethylene Epoxidation. *Catal. Today* **2024**, *428*, 114447. https://doi.org/10.1016/j.cattod.2023.114447.
(34) Campbell, C. T. Chlorine Promoters in Selective Ethylene Epoxidation over Ag(111): A Comparison with Ag(110). *J. Catal.* **1986**, *99* (1), 28–38. https://doi.org/10.1016/0021-9517(86)90195-8.
(35) Peck, M. A.; Langell, M. A. Comparison of Nanoscaled and Bulk NiO Structural and Environmental Characteristics by XRD, XAFS, and XPS. *Chem. Mater.* **2012**, *24* (23), 4483–4490. https://doi.org/10.1021/cm300739y.
(36) Belskaya, O. B.; Mironenko, R. M.; Gulyaeva, T. I.; Trenikhin, M. V.; Muromtsev, I. V.; Trubina, S. V.; Zvereva, V. V.; Likholobov, V. A. Catalysts Derived from Nickel-Containing Layered Double Hydroxides for Aqueous-Phase Furfural Hydrogenation. *Catalysts* **2022**, *12* (6), 598. https://doi.org/10.3390/CATAL12060598/S1.
(37) Egelske, B. Recent Advances in Catalytic Ethylene Epoxidation: Synthesis, Characterization, and Evaluation. *Theses Diss.* **2021**.
(38) Jingfa, D.; Jun, Y.; Shi, Z.; Xiaohong, Y. Promoting Effects of Re and Cs on Silver Catalyst in Ethylene Epoxidation. *J. Catal. U. S.* **1992**, *138:1* (1), 395–399. https://doi.org/10.1016/0021-9517(92)90033-E.
(39) Goncharova, S. N.; Paukshtis, E. A.; Bal'zhinimaev, B. S. Size Effects in Ethylene Oxidation on Silver Catalysts. Influence of Support and Cs Promoter. *Appl. Catal. Gen.* **1995**, *126* (1), 67–84. https://doi.org/10.1016/0926-860X(95)00036-4.
(40) Jankowiak, J. T.; Barteau, M. A. Ethylene Epoxidation over Silver and Copper–Silver Bimetallic Catalysts: II. Cs and Cl Promotion. *J. Catal.* **2005**, *236* (2), 379–386. https://doi.org/10.1016/J.JCAT.2005.10.017.
(41) Diao, W.; Digiulio, C. D.; Schaal, M. T.; Ma, S.; Monnier, J. R. An Investigation on the Role of Re as a Promoter in Ag-Cs-Re/α-Al2O3 High-Selectivity, Ethylene Epoxidation Catalysts. *J. Catal.* **2015**, *322*, 14–23. https://doi.org/10.1016/j.jcat.2014.11.007.
(42) Ren, D.; Cheng, G.; Li, J.; Li, J.; Dai, W.; Sun, X. X.; Cheng, D. Effect of Rhenium Loading Sequence on Selectivity of Ag–Cs Catalyst for Ethylene Epoxidation. *Catal. Lett.* **2017**, *147* (12), 2920–2928. https://doi.org/10.1007/S10562-017-2211-5/FIGURES/9.
(43) Chen, C. J.; Harris, J. W.; Bhan, A. Kinetics of Ethylene Epoxidation on a Promoted Ag/α-Al2O3 Catalyst—The Effects of Product and Chloride Co-Feeds on Rates and Selectivity. *Chem. - Eur. J.* **2018**, *24* (47), 12405–12415. https://doi.org/10.1002/chem.201801356.
(44) Rojluechai, S.; Chavadej, S.; Schwank, J. W.; Meeyoo, V. Catalytic Activity of Ethylene Oxidation over Au, Ag and Au–Ag Catalysts: Support Effect. *Catal. Commun.* **2007**, *1* (8), 57–64. https://doi.org/10.1016/J.CATCOM.2006.05.029.
(45) Egelske, B. T.; Xiong, W.; Zhou, H.; Monnier, J. R. Effects of the Method of Active Site Characterization for Determining Structure-Sensitivity in Ag-Catalyzed Ethylene Epoxidation. *J. Catal.* **2022**. https://doi.org/10.1016/j.jcat.2022.03.021.
(46) Svintsitskiy, D. A.; Lazarev, M. K.; Slavinskaya, E. M.; Fedorova, E. A.; Kardash, T. Y.; Cherepanova, S. V.; Boronin, A. I. Room Temperature Epoxidation of Ethylene over Delafossite-Based AgNiO2 Nanoparticles. *Phys. Chem. Chem. Phys.* **2023**, *25* (31), 20892–20902. https://doi.org/10.1039/D3CP01701J.
(47) Yang, H.; Wang, X.; Liu, Q.; Huang, A.; Zhang, X.; Yu, Y.; Zhuang, Z.; Li, G.; Li, Y.; Peng, Q.; Chen, X.; Xiao, H.; Chen, C. Heterogeneous Iridium Single-Atom Molecular-like Catalysis for Epoxidation of Ethylene. *J. Am. Chem. Soc.* **2023**, *145* (12), 6658–6670. https://doi.org/10.1021/JACS.2C11380/ASSET/IMAGES/LARGE/JA2C11380_0007.JPEG.
(48) Pu, T.; Tian, H.; Ford, M. E.; Rangarajan, S.; Wachs, I. E. Overview of Selective Oxidation of Ethylene to Ethylene Oxide by Ag Catalysts. *ACS Catal.* **2019**, 10727–10750. https://doi.org/10.1021/acscatal.9b03443.

(49) Bukhtiyarov, V. I.; Prosvirin, I. P.; Kvon, R. I. Study of Reactivity of Oxygen States Adsorbed at a Silver Surface towards C2H4 by XPS, TPD and TPR. *Surf. Sci.* **1994**, *320* (1–2), 2–5. https://doi.org/10.1016/0039-6028(94)00562-1.
(50) Uhlenbrock, S.; Scharfschwerdt, C.; Neumann, M.; Illing, G.; Freund, H. J. The Influence of Defects on the Ni 2p and O 1s XPS of NiO. *J. Phys. Condens. Matter* **1992**, *4* (40), 7973–7978. https://doi.org/10.1088/0953-8984/4/40/009.
(51) Mcintyre, N. S.; Cook, M. G. X-Ray Photoelectron Studies on Some Oxides and Hydroxides of Cobalt, Nickel, and Copper. *Anal. Chem.* **1975**, *47* (13), 2208–2213. https://doi.org/10.1021/ac60363a034.
(52) Hoflund, G. B.; Weaver, J. F.; Epling, W. S. Ag Foil by XPS. *Surf. Sci. Spectra* **1994**, *3* (2), 151–156. https://doi.org/10.1116/1.1247777.
(53) Schön, G.; Tummavuori, J.; Lindström, B.; Enzell, C. R.; Enzell, C. R.; Swahn, C.-G. ESCA Studies of Ag, Ag2O and AgO. *Acta Chem. Scand.* **1973**, *27* (January), 2623–2633. https://doi.org/10.3891/acta.chem.scand.27-2623.

Appendix to Chapter 7

Materials and Methods

Temperature programmed desorption (TPD)

TPD experiments were conducted in an ultra-high vacuum (UHV) chamber with a base pressure $>1\times10^{-10}$ mbar equipped with a Hidden Hal RC 201 mass spectrometer capable of advancing to within 1 mm of the Ag(111) crystal surface. The crystal was cleaned with cycles of Ar^+ ion sputtering (~2 μA drain current, 1.0 keV beam energy) and annealing to 725 K. Temperatures were measured with a K-type thermocouple welded to the back of a crystal. The crystal was heated resistively via its support wires, and cooled with liquid nitrogen. NiAg(111) surface alloys were prepared by deposition of Ni (Goodfellow, 99.99%) via electron beam evaporation (Omicron, EFM 3) onto a Ag(111) crystal held at 473 K. Exposures of O_2 (Middlesex, 99.999%) were performed with a precision leak valve. Ni coverage was calculated by using the CO trace area referenced to a known ethanol monolayer coverage. [1,2]

X-ray photoemission spectroscopy (XPS)

Ambient pressure XPS was performed at beamline 23-ID-2 (IOS) of the National Synchrotron Light Source II (NSLS- II) at Brookhaven National Laboratory.[3] All experiments were performed on a Ag(111) crystal cleaned with Ar^+ ion sputtering and annealing to 900 K until XPS spectra were free from impurities. High purity O_2 (Matheson, 99.994%) was introduced to the chamber via precision leak valve while the sample was heated with a pyrolytic boron nitride heater. Temperature was measured with a K-type thermocouple mounted between the Ag(111) crystal and the heater. NiAg(111) alloys were prepared similarly by evaporating a Ni rod (Goodfellow, 99.99%) with a SPECS EBE-4 e-beam evaporator.

For the XPS data in Fig. 7.1 the sample was exposed to incremental Langmuir (1^{-6} torr for 1 second) doses of O_2 at 325 K. Upon saturation, the same sample was then heated at a rate of 40 K/min, then held at each temperature for ~20 min while the XPS spectra were collected this (Fig 7.3A). Ag(111) and NiAg(111) surfaces in Fig 7.2A and C were both annealed to 900 K (Ni was deposited after this final anneal step) and immediately exposed to 0.2 Torr O_2 at 325 K before heating to 433 K still under ambient pressure conditions. The sputtered Ag(111) sample was prepared by

completing the same 900 K anneal as with the other two samples followed by an additional 3 minutes of sputtering as described previously for standing cleaning cycles. This sample was then exposed to 0.2 Torr O_2 at 325 K before heating to 433 K still under ambient pressure conditions. Finally, Fig 7.3D was doped with Ni as with previous samples and exposed to 10 mtorr O_2 at 475 K before being cooled and returned to UHV where it was stepwise annealed, and spectra were taken at temperature.

Photon energies of 1090, 760, and 500 eV were used to generate photoelectrons with kinetic energies of ~200 eV for the Ni 2p, O 1s, and C 1s core levels, respectively, to maintain similar probing depths. Reference Ag 3d spectra were taken at each photon energy. Spectra were corrected with respect to the Fermi edge and metallic Ag 3d binding energy. We observed four oxygen species with discrete binding energies; one attributed to nucleophilic oxygen with binding energy ~ 528.4 eV, one associated with a Ni bound oxygen species ~529.3 eV, one associated with electrophilic oxygen ~530.1 eV, and one associated with subsurface oxygen ~531.1 eV. XPS data was analyzed with CasaXPS and fit with a linear background; each species was assigned and fit according to literature values for the different types of oxygen as described in previous chapters.

All spectra were corrected with a relative sensitivity factor (RSF) for each photon energy used. Where necessary, peak intensity was corrected for the decreased electron inelastic mean free path (IMFP) resulting from increased chamber pressure. Monolayer coverages were calculated with respect to a monolayer of Ag(111). To do this the $Ag3d_{5/2}$ spectra were first corrected for spin orbit splitting and RSF as well as IMFP as the Ag 3d reference spectra were taken at photon energies more surface sensitive to C 1s and O 1s species. The fraction of the total Ag 3d intensity attributed to the surface layer of Ag, 0.19, 0.23, 0.35, was calculated using the electron escape depth for each photon energy, 1090, 760 and 500 eV, respectively; and these values were used to extract a monolayer reference for coverage calculations.

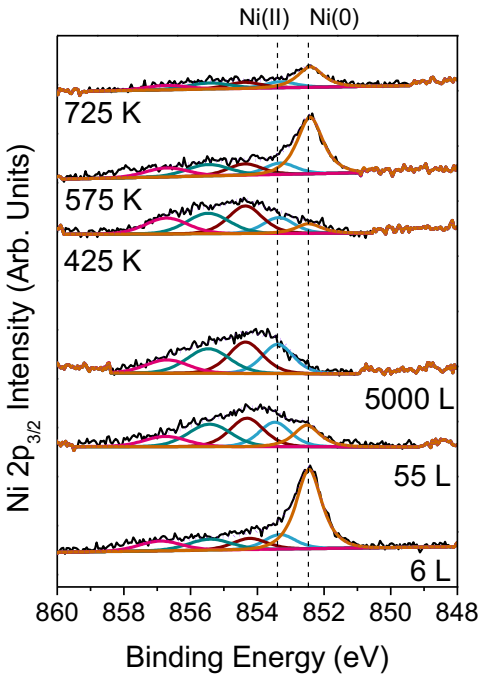

Figure A7.1. The shift in oxidation state of Ni in Ag(111) during oxygen uptake and release. Ni $2p_{3/2}$ spectra of NiAg(111) as it is exposed to ultra low doses of oxygen show the transition from metallic sites (orange fit) to a more oxidized, Ni(II) oxidation state, as larger oxygen doses are introduced to the sample. Subsequent annealing of this very mildly oxidized surface shows as oxygen desorbs from the surface some metallic Ni sites return before the intensity is lost as Ni migrates out of detection range of XPS.

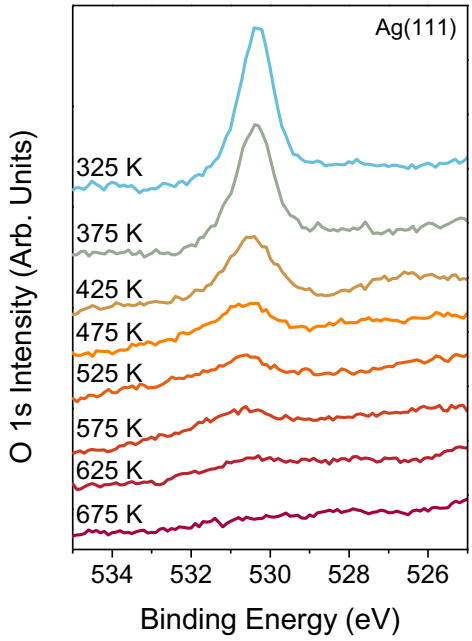

Figure A7.2 Desorption of oxygen from Ag(111) as a function of temperature. Ag(111) is exposed to 100 mTorr O_2 at 475 K and returned to UHV where it is then annealed stepwise from 325 K to 675 K where it no oxygen is detected. There is no shift in oxygen species as the surface is annealed.

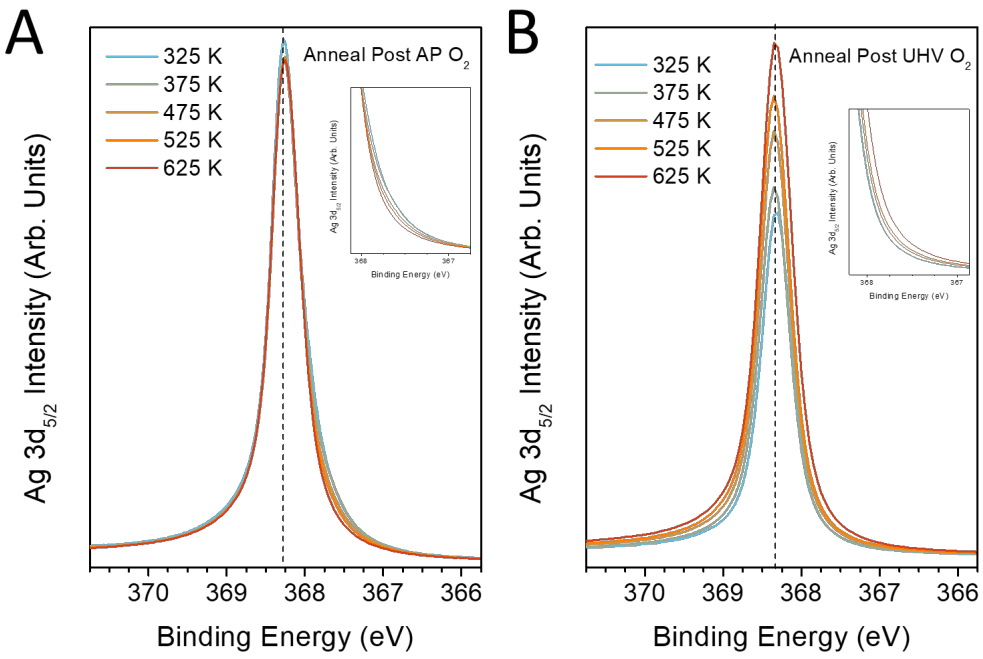

Figure A7.3. A comparison of peak shape of Ag as strongly and moderately oxidized NiAg(111) is annealed. (A) After 10 mTorr exposure to O_2 there is ~10x the oxygen coverage on NiAg(111) in Fig 7.3D than Fig 7.3A. This oxygen coverage is predominately electrophilic oxygen which does not shift the oxidation state of Ag, however there is a slightly widening of the peak shape that is associated with the early formation of a lower binding energy shoulder associated with nucleophilic oxygen and the affiliated Ag reconstructions. As the surface is annealed the Ag spectra narrows and becomes more symmetrical as can be seen in the inset. **(B)** After more mild oxidation NiAg(111) that has only been exposed to 5000 L of O_2 the highest coverage O species is still Ni-philic and as such the peak shape for the Ag $3d_{5/2}$ spectra remains metallic. There is some slight variation in FWHM of these spectra but no obvious trend as oxygen is desorbed beyond an increase in Ag intensity.

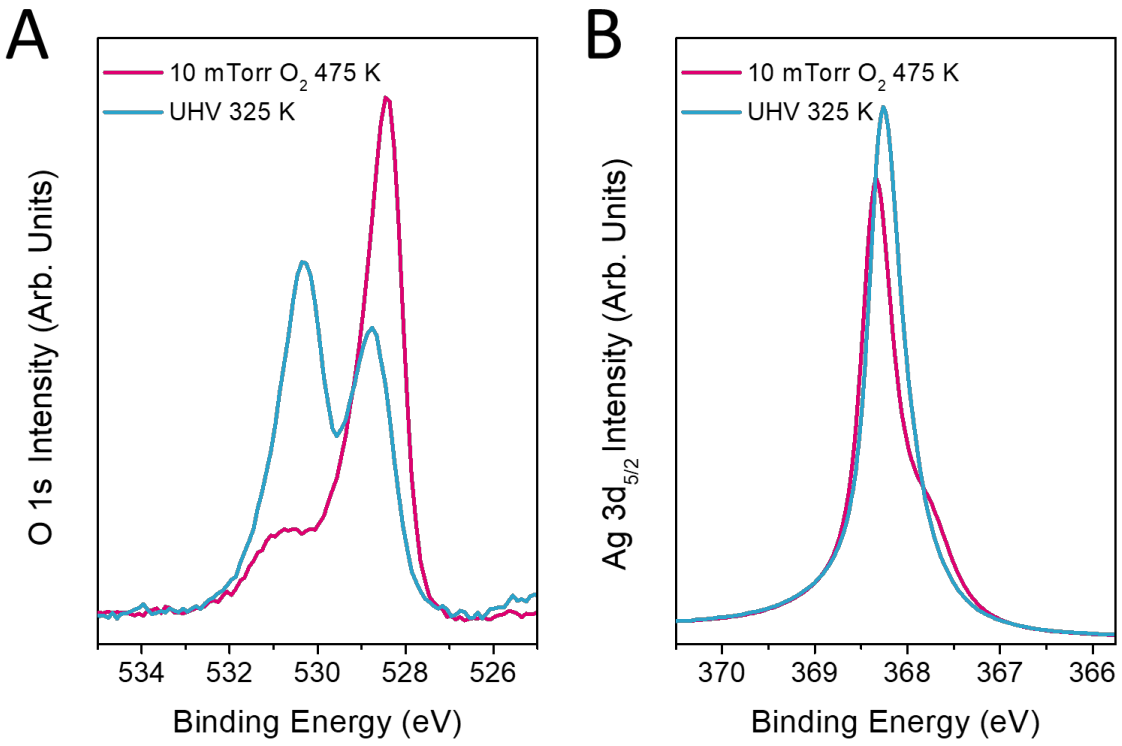

Figure A7.4. The effect of cooling on a significantly reconstructed NiAg(111) sample. NiAg(111) was exposed to 10 mTorr O_2 and heated to 475 K where it was allowed to equilibrate for ~20 minutes. At this elevated temperature (pink traces) the O 1s **(A)** spectra show predominately nucleophilic oxygen (~528. 3 eV) and the signature shoulder appears in the Ag $3d_{5/2}$ spectra **(B)**. This sample was retuned to UHV and allowed to cool to 325 K (blue traces) where there is a significant decrease in nucleophilic oxygen in the O 1s spectra a a loss of the signature reconstructed shoulder in the Ag $3d_{5/2}$ trace. This demonstrates that the formation of nucleophilic oxygen on NiAg(111) is somewhat reversible as a function of temperature even after AP O_2 exposures.

References

(1) Liriano, M. L.; Larson, A. M.; Gattinoni, C.; Carrasco, J.; Baber, A. E.; Lewis, E. A.; Murphy, C. J.; Lawton, T. J.; Marcinkowski, M. D.; Therrien, A. J.; Michaelides, A.; Sykes, E. C. H. Chirality at Two-Dimensional Surfaces: A Perspective from Small Molecule Alcohol Assembly on Au(111). *Journal of Chemical Physics* **2018**, *149* (3), 34703. https://doi.org/10.1063/1.5035500/15547254/034703_1_ACCEPTED_MANUSCRIPT.PDF.

(2) Schlosser, D. A.; Yehorova, D.; Kaleem, H.; Maxwell, E. M.; Baker, J. S.; Gillum, M. Z.; DePonte, M. C.; Letchworth-Weaver, K.; Baber, A. E. Effect of Undercoordinated Ag(111) Defect Sites on the Adsorption of Ethanol. *Journal of Vacuum Science & Technology A: Vacuum, Surfaces, and Films* **2020**, *38* (3), 33213. https://doi.org/10.1116/1.5142020/1065713.

(3) Waluyo, I.; Hunt, A. Ambient Pressure X-Ray Photoelectron Spectroscopy at the IOS (23-ID-2) Beamline at the National Synchrotron Light Source II. *Synchrotron Radiation News* **2022**, *35* (3), 31–38. https://doi.org/10.1080/08940886.2022.2082180/ASSET/BDB66E5A-0587-4FF9-8A92-46D92E6F9330/ASSETS/IMAGES/GSRN_A_2082180_F0005_C.JPG.

Appendix to Chapter 9

X-ray photoemission spectroscopy (XPS)

Ambient pressure XPS was performed at beamline 23-ID-2 (IOS) of the National Synchrotron Light Source II (NSLS- II) at Brookhaven National Laboratory [1]. All experiments were performed on a Ag(111) crystal cleaned with Ar^+ ion sputtering and annealing to 900 K until XPS spectra were free from impurities. Temperature was measured with a K-type thermocouple mounted between the Ag(111) crystal and the heater. NiAg(111) alloys were prepared similarly by evaporating a Ni rod (Goodfellow, 99.99%) with a SPECS EBE-4 e-beam evaporator. Ni coverage was calculated by using the corrected Ni 2p peak area referenced to a saturated oxygen surface as well as with reference to a monolayer of Ag(111). High purity O_2 (Matheson, 99.994%) and C_2H_4 (Matheson, 99.95%) were introduced to the chamber using precision leak valves while the sample was heated with a pyrolytic boron nitride heater. Photon energies of 1090, 760, and 500 eV were used to generate photoelectrons with kinetic energies of ~200 eV for the Ni 2p, O 1s, and C 1s core levels, respectively, to maintain similar probing depths. Reference Ag 3d spectra were taken at each photon energy. Spectra were corrected with respect to the Fermi edge and metallic Ag 3d binding energy. XPS data was analyzed with CasaXPS and fit with a linear background; each species was assigned and fit according to literature values for the different types of oxygen as described in previous chapters.

All spectra were corrected with a relative sensitivity factor (RSF) for each photon energy used. Where necessary, peak intensity was corrected for the decreased electron inelastic mean free path (IMFP) resulting from increased chamber pressure. Monolayer coverages were calculated with respect to a monolayer of Ag(111). To do this the $Ag3d_{5/2}$ spectra were first corrected for spin orbit splitting and RSF as well as IMFP as the Ag 3d reference spectra were taken at photon energies more surface sensitive to C 1s and O 1s species. The fraction of the total Ag 3d intensity attributed to the surface layer of Ag, 0.19, 0.23, 0.35, was calculated using the electron escape depth for each photon energy, 1090, 760 and 500 eV, respectively; and these values were used to extract a monolayer reference for coverage calculations.

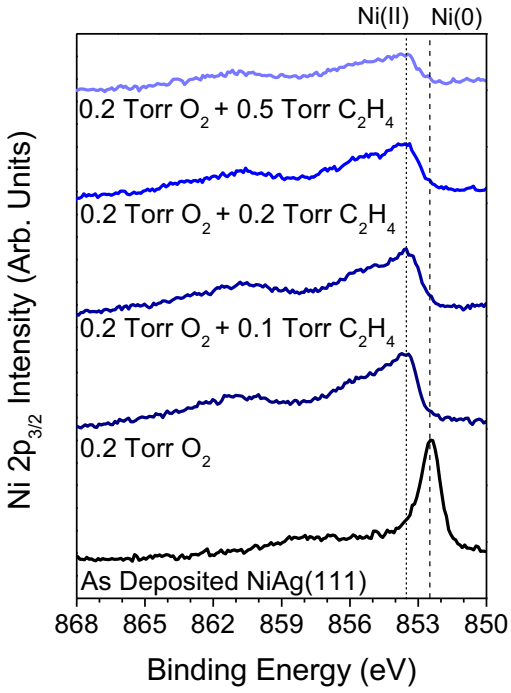

Figure A9.1. Binding energy shift of Ni $2p_{3/2}$ spectra as oxygen and ethylene are introduced. As deposited, the Ni spectra in Ag(111) remains narrow and distinctly metallic in peak shape and binding energy (~852.7 eV), upon introduction of oxygen the peak shape and binding energy shift to the broader features associated with Ni(II) formation. As ethylene is introduced, the BE of the Ni remains consistent with a Ni(II) oxidation state despite a decrease in surface coverage with higher ethylene partial pressures.

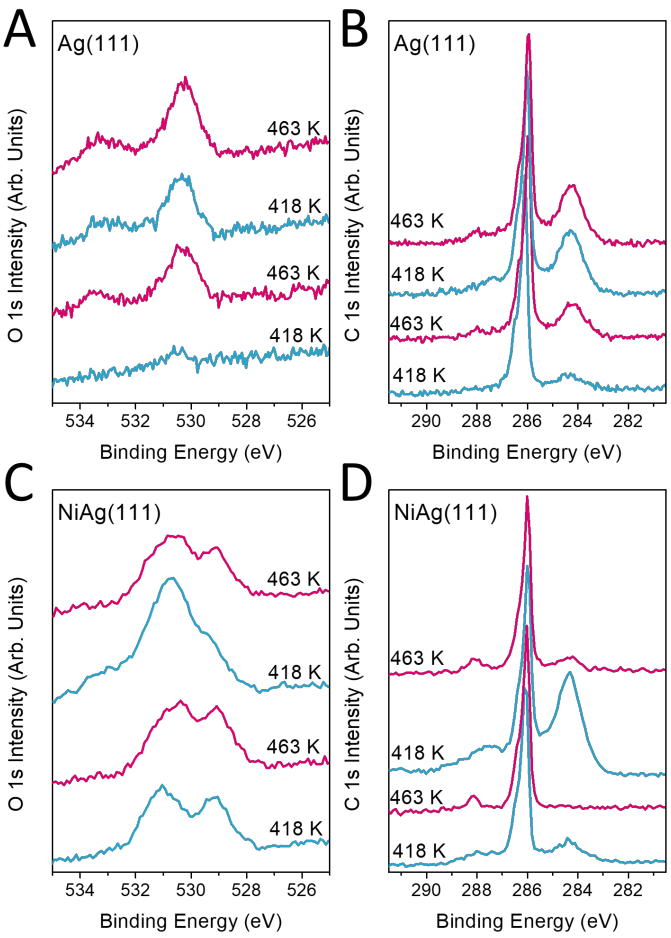

Figure A9.2 A comparison of surface species on Ag(111) and NiAg(111) under epoxidation conditions as a function of temperature. On Ag(111) cooling to 418 K initially results in a nearly flat O 1s trace **(A)** and with no signs of carbonate (~288.1 eV) in the C 1s spectra **(B),** however there is an increase in similar adsorbates to when ethylene only is introduced to the surface (Fig A9.3). After this initial uptake in c-c/ethylene species even though heating and cooling cycles this lower BE species continues to grow in intensity. O 1s spectra reveal the addition of higher BE species often associated with adsorbates like water and CO_2. NiAg(111) shows greater reversibility of these c-c/ethylene species which increase in coverage at lower temperatures and decrease with heating **(D).** Changes in the O 1s spectra for the NiAg(111) sample **(C)** remain more subtle but similarly show increases in higher BE species at lower temperatures.

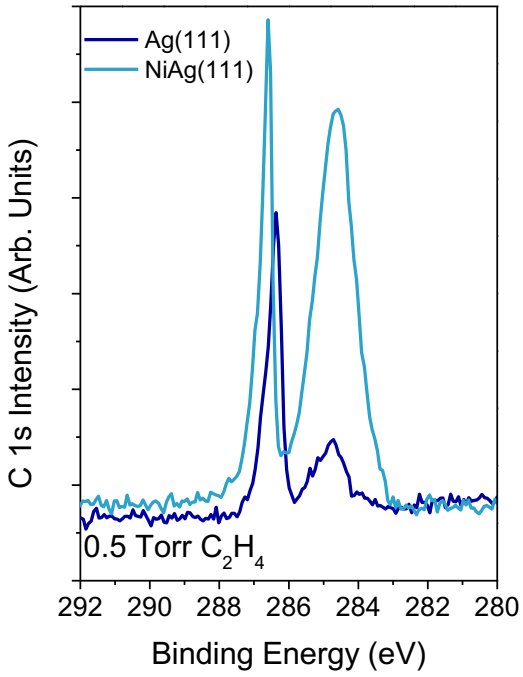

Figure A9.3. C 1s spectra of Ag(111) and NiAg(111) under 0.5 Torr C_2H_4. Exposure of clean Ag(111) and NiAg(111) to only ethylene reveals a distinctly igher coverage in ethylene and low binding energy carbon species on NiAg(111) (light blue) compared to Ag(111) (dark blue). The FWHM of the light blue trace suggest there are several adsorbate species and this binding energy region is associated with carbon-carbon bonding, while higher BE regions of the C 1s are often associated with oxygen containing species. Hence, we assign these lower BE species as ethylene/c-c adsorbates. The binding energies for both spectra were corrected with respect to the fermi edge, however the shift in the gas phase ethylene feature (sharp central peak) do not shift with surface based corrections as they are independent of the sample.

References

(1) Waluyo, I.; Hunt, A. Ambient Pressure X-Ray Photoelectron Spectroscopy at the IOS (23-ID-2) Beamline at the National Synchrotron Light Source II. *Synchrotron Radiat. News* **2022**, *35* (3), 31–38. https://doi.org/10.1080/08940886.2022.2082180/ASSET/BDB66E5A-0587-4FF9-8A92-46D92E6F9330/ASSETS/IMAGES/GSRN_A_2082180_F0005_C.JPG.